IMPERIAL COLLEGE LONDON

Faculty of Natural Sciences

Fluid Dynamics in Nanoscale Systems with Amorphous Surfaces and the Interaction of Nanoparticles with Surfactant Layers

Matthew Groombridge

Chemical Physics Section, Department of Chemistry

Doctoral Thesis (PhD Degree)

MMXII

Declaration

I confirm that this work: "Fluid Dynamics in Nanoscale Systems with Amorphous Surfaces and the Interaction of Nanoparticles with Surfactant Layers" and the material presented within it is entirely my own. References to the work of other researchers are numbered in the text and noted in an appendix at the end of the report.

Name of Student: Matthew Groombridge.

Name of Supervisor: Professor Nick Quirke.

Abstract

The flow properties of fluids confined within nanoscale pores have been investigated. This study attempts to increase the understanding of some of the factors which affect flow over amorphous surfaces. Direct comparisons are made between experimental data and theoretical systems. Equilibrium and non-equilibrium methods are used to calculate the slip coefficient and a relaxation time, which is related to the interfacial friction. This is shown to be a simple and reliable way of predicting flow behaviour across a wide range of systems with different structures. Other methods, such as those based on Maxwell's model, are found to be less reliable in systems with very rough surfaces.

Enhanced flow rates, as found in some experimental systems, would have enormous benefits in a nanofluidic device. The flow dynamics in a variety of systems with different surface roughnesses and chemical compositions have been determined. The flow of water and decane fluids over a variety of carbon surfaces have been studied. Flow over PDMS surfaces with varying levels of oxidation has also been analysed. Enhancements are found to be lower than those predicted experimentally.

There is a wide interest in the effects of inhalation of nanoparticles on lung tissues. In this work, the interactions of several environmentally interesting nanoparticles (fullerenes and titanium dioxide) with a model lung membrane have been simulated. The trajectories and interactions of the nanoparticles with the membranes are studied. Hydrophobic particles are found to sit amongst the lipid tails, hydrophillic particles nearer the water/lipid interface. Although no particles are found to cross freely into the water layer, an interesting effect is noted whereby water molecules are seen to leave the water phase of the membrane and coat the surface of hydrophilic nanoparticles. For the largest nanoparticles this creates a bridge across the membrane from the water phase to the vacuum.

Contents

1 Introduction **10**

1.1 Microfluidics 10

1.2 Towards Nanofluidic Devices 12

1.2.1 Properties of Carbon Nanotubes 13

Simulated Flow through Carbon Nanotubes 13

Experimental Flow through Carbon Nanotubes 15

1.2.2 Flow through Amorphous Carbon Nanopipes 17

1.2.3 PDMS Nanostructures 18

2 The Interaction of Nanoparticles with Biological Membranes **21**

2.1 Possible Medical Applications of Nanoparticles 21

2.1.1 Nanoneedles and Trans-membrane Transport 21

2.1.2 Lung Membranes and the Inhalation of Nanoparticles 22

3 Fluid Flow Through Nanoscale Channels **25**

3.1 Fluid Dynamics Theory 25

3.2 Interfacial Friction and the Slip Coefficient 28

3.2.1 Maxwell Theory of Slip 30

3.2.2 Equilibrium Calculation of the Slip Coefficient 33

3.2.3 The Slip Coefficient from Non-Equilibrium Systems 34

3.2.4 Other Methods of Calculation 35

3.2.5 Tangential Force Measurements 36

4 Molecular Dynamics Simulations **38**

4.1 System Trajectory 38

4.2 Ensembles . . . 40
4.2.1 Simulating the NVT Ensemble . . . 40
4.2.2 Simulating the NPT Ensemble . . . 41
4.3 Forces within the System . . . 41
4.3.1 Solid-Solid Forces . . . 42
4.3.2 Intermolecular Forces . . . 42
Ewald Summation . . . 43
4.3.3 Intramolecular Forces . . . 44
4.4 Microscopic Fluid Dynamics . . . 46
4.4.1 Stress Tensor Calculation . . . 47
4.4.2 Diffusion/Viscosity Calculation . . . 48
4.5 Flow Generation . . . 49

5 Molecular Models **51**
5.1 Carbon Model . . . 51
5.1.1 Tersoff-Brenner Potential . . . 52
5.2 PDMS Model . . . 55
5.3 Fluid Models . . . 57
5.3.1 Water Model . . . 57
5.3.2 Decane Model . . . 60
5.4 Fluid-Carbon Interactions . . . 62
5.5 Fluid-PDMS Interactions . . . 63
5.6 Fluid Flow Simulation Parameters . . . 64

6 Results I - Fluid Flow in Nanopores **66**
6.1 Carbon Slit Pores . . . 66
6.1.1 Characterisation of the Surfaces . . . 67
6.1.2 Equilibrium Molecular Dynamics Simulations (EMD) . . . 71
6.1.3 Non-Equilibrium Molecular Dynamics Simulations (NEMD) . . . 77
6.1.4 Graphene Surfaces . . . 79
6.1.5 Diamond Surfaces . . . 80
6.1.6 Mobile Diamond Surfaces . . . 82
6.1.7 Amorphous Carbon Surfaces . . . 83

Width d=6nm Pore . . . 87
Reflecting Particle Membrane Generated Flow Data . . . 89
Effects of Confinement . . . 91
6.1.8 Modification of System Parameters . . . 93
Effect of Varying Fluid Pressure . . . 93
Effect of Varying Wall/Fluid Interactions . . . 93
6.1.9 Modification of Graphite Surfaces . . . 94
6.1.10 Hydrogenated Carbon Surfaces . . . 97
6.1.11 Carbon-Decane Slit Pore Systems . . . 97
Equilibrium Simulations . . . 98
Non-Equilibrium Simulations . . . 98
6.2 Cylindrical Pore Geometries . . . 99
6.2.1 Carbon Nanotubes . . . 99
6.2.2 Multi-walled Nanotube with Defects . . . 101
6.2.3 Different Carbon Densities . . . 102
6.2.4 Amorphous Carbon Cylinder . . . 103
6.2.5 Effect of Nitrogen Bubbles . . . 104
6.3 PDMS/Water Systems . . . 105
6.3.1 Characterisation of the Surfaces . . . 105
6.3.2 Equilibrium Molecular Dynamics Simulations (EMD) . . . 109
6.3.3 Non-equilibrium Molecular Dynamics Simulations (NEMD) . . . 111
6.4 Data Summary . . . 116

7 Modelling the Membrane 118

7.1 Models of Biological Membranes . . . 118
7.1.1 Previous Simulation Work . . . 118
7.1.2 DPPC Model . . . 119
7.1.3 Nanoparticle Models . . . 120
7.2 Initial Equilibration . . . 123

8 Results II - Interaction of Nanoparticles with Biomembranes 128

8.1 Bilayer NPT . . . 128
8.1.1 Fullerene Nanoparticles . . . 128

8.1.2 Titanium Dioxide Nanoparticles - Potential I 132
r=0.6nm 132
r=1.5nm 132
8.1.3 Titanium Dioxide Nanoparticles - Potential II 134
r=0.6nm 134
r=1.5nm 136
8.2 Monolayer Systems 142
8.3 Approach of Nanoparticles through the Water Phase 144
8.4 Energy/Force Measurements 148

9 Conclusions **155**
9.1 Suggestions for Future Work 159

A Published and Submitted Papers **160**

B Acknowledgments **170**

Bibliography **171**

List of Tables

1.1 Summary of the Experimental Flow Data 18

5.1 Tersoff-Brenner Potential Parameters 53
5.2 Bond Lengths and Angles for the PDMS atoms 57
5.3 Constituent Atoms For Each Surface 57
5.4 Potential parameters for the SPC/E water atoms 57
5.5 Potential parameters for the Decane atoms 61
5.6 Characterisation of the Fluid Models 61
5.7 Interaction Parameters for the Carbon-Fluid Sites 63
5.8 Non bonded potential parameters for the PDMS system 63

6.1 Characterisation of the Carbon Surfaces 69
6.2 Graphene Slit Pore NEMD Data 80
6.3 Diamond Slit Pore NEMD Data 81
6.4 Mobile Diamond Surface Slit Pore NEMD Data 82
6.5 Water-Carbon 3nm NEMD Flow Data 85
6.6 6nm Carbon-Water Data 87
6.7 EMD Data for the Amorphous Carbon Slit-Pores 88
6.8 Water-Carbon 3nm RPM NEMD Flow Data 89
6.9 Water-Carbon 4nm RPM NEMD Flow Data 90
6.10 Water-Carbon 6nm RPM NEMD Flow Data 90
6.11 Water-Carbon 9nm RPM NEMD Flow Data 90
6.12 Water-Carbon 12nm RPM NEMD Flow Data 90
6.13 EMD Data for the Smaller Width Amorphous Carbon Slit-Pores 91
6.14 h=1nm Slit Pore NEMD Data 91

6.15 h=1.5nm Slit Pore NEMD Data . . . 92
6.16 h=2nm Slit Pore NEMD Data . . . 92
6.17 Modified Fluid Density Slit Pore NEMD Data . . . 93
6.18 Variable Wall/Fluid Interaction EMD Data . . . 94
6.19 Relaxation Times for the Modified Graphite Surfaces . . . 96
6.20 Potential Parameters in the System . . . 97
6.21 Relaxation Times for the hydrogenated surfaces . . . 97
6.22 Decane/Carbon EMD Data . . . 98
6.23 Decane d= 3.0nm Slit Pore NEMD Data . . . 99
6.24 Decane d= 6.0nm Slit Pore NEMD Data . . . 99
6.25 Carbon Nanotube d=3nm NEMD Data . . . 101
6.26 Carbon Nanotube d=6nm NEMD Data . . . 101
6.27 EMD Data for the MWNT with Varying Defect Percentages . . . 101
6.28 Roughness data for the alternative density surfaces . . . 102
6.29 EMD Flow data for the alternative density surfaces (d=6nm Cylindrical) . . . 103
6.30 d=3nm Amorphous Carbon Cylinder NEMD Flow Data . . . 104
6.31 Characterisation of the PDMS Surfaces . . . 106
6.32 Details of the Boundary Layer (Relative to Center of Pore) . . . 109
6.33 EMD Data for the PDMS Slit-Pores . . . 110
6.34 Flow data for the S_0 PDMS-Water system . . . 114
6.35 Flow data for the S_1 PDMS-Water system . . . 114
6.36 Flow data for the S_2 PDMS-Water system . . . 115
6.37 Collected Simulation data for the Water Simulations . . . 116

7.1 Non bonded potential parameters for the DPPC Molecule . . . 121
7.2 Buckingham Non bonded potential parameters for the Initial TiO_2 Model . . . 121
7.3 Non bonded potential parameters for the TiO_2 . . . 122
7.4 Characterisation of the Nanoparticles . . . 123

8.1 The Average Positions of the Nanoparticles . . . 142
8.2 The Energies for the Nanoparticles . . . 148

Chapter 1

Introduction

1.1 Microfluidics

Nanofluidic technology has many potential applications in chemistry, biology and medicine. Microfluidic or Lab-on-a-chip technology has already found uses in biomolecular separations [1], DNA analysis [2, 3] and cell manipulation [4], for example. A microfluidic device is one which has channels with a dimension smaller than 1mm within it. They have major advantages in terms of sample handling, reagent mixing, separation and detection when compared to macroscale analogues.

Advantages arise due to the high surface to volume ratio of microfluidic devices which allows for superior heat dissipation from within the channels. The lower sample/reagent and power consumption of the device also pose a significant advantage, with picolitre sample volumes often being sufficient for analysis/synthesis purposes. Superior analytical performance in terms of speed, efficiency and control of the process can be achieved.

These devices have the potential to be used in medical environments [5] for the on the spot analysis of samples. This would greatly increase sample turnover and cut the diagnosis time for patients. The techniques and materials used in the fabrication process are relatively inexpensive and the devices can therefore be disposed of after one use, reducing risk of patient contamination.

Applications also include environmental testing where the on-the-spot analysis of soil samples in the field to quickly determine contamination and can reduce the response time for spills of hazardous material [6]. This is because their small size allows for high portability. Another

area which could potentially benefit is organic synthesis, where combinatorial methods could be made more efficient by the introduction of microfluidic devices which have the capability to use smaller sample sizes.

Most early microfluidic devices were fabricated in silicon or glass which requires etching channels into their surfaces and therefore can be relatively expensive and time consuming. The use of polymeric materials for the manufacture of these devices offers a significant advantage in that the channels can be moulded, rather than etched. One of the main polymeric materials used in microfluidic systems for the manufacture of channels in a device is PDMS (Polydimethylsiloxane) [7]. The use of this material has several benefits: it is easily moulded, is durable and chemically inert and is cheap and non-toxic. It can also be used in biological systems for the manipulation of samples containing DNA, blood and proteins, due to its high biocompatibility. PDMS has a low glass transition temperature, has a high degree of chain flexibility and is optically transparent.

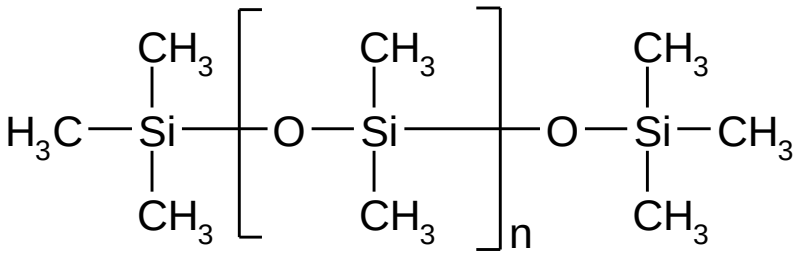


Figure 1.1: PDMS Structure

One disadvantage of using polymers rather than glass or silicon is that the surface structure and chemistry of polymers is less well defined and therefore needs to be carefully considered and controlled. Polymers can also be incompatible with some organic solvents. The PDMS surface is hydrophobic and small channels are resistant to filling by water, but it is believed that during plasma treatment of PDMS surfaces (part of the curing process) active species from the oxygen plasma attack the silicon atoms and substitute Si-C bonds for Si-O bonds [8]. On the surface Si–CH_3 groups are replaced with Si-OH groups. This can alter the properties of the PDMS surface causing it to become more hydrophilic after the introduction of these silanol groups, reducing the water-PDMS contact angle thus improving the wettability of the surface by water, making the filling of small channels more favourable. This is obviously advantageous in some situations, e.g., capillary filling, though the long term stability of the oxidised surface is unknown. Over time the hydrophobicity is restored, although techniques have been developed

to delay the recovery [9].

The ability to control the wettability by plasma treatment suggests the possibility of driving fluids through nanostructured materials using wettability gradients.

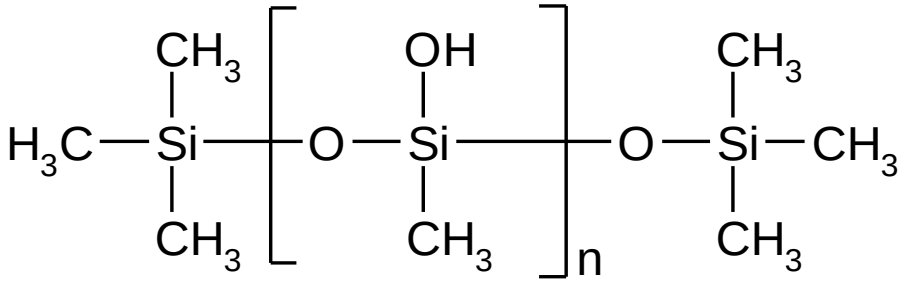


Figure 1.2: Oxidised PDMS Structure

One popular method for the fabrication of microfluidic systems in PDMS is using soft lithography [10]. This involves first creating a positive relief or master using photolithography which then gives the required pattern of channels. From the master, channels in the PDMS are created by replica moulding (casting the polymer and then curing). High definition channels in PDMS can be formed using replica moulding because the PDMS is elastomeric and is easily released from the mould without being damaged.

An example of a microfluidic system fabricated in PDMS using replica moulding was one developed for capillary electrophoresis separation [11].

1.2 Towards Nanofluidic Devices

The advantages gained through the use of microfluidic devices should theoretically be amplified a thousand times in a nanofluidic device. However, at the nanoscale additional interactions, which can largely be ignored at larger scales play a far greater part in the physical properties of the system. Interfacial effects are much more important on smaller scales, the interface being a larger proportion of the system.

For the design of a nanofluidic device a detailed understanding of the molecular transport through the system is important. The transport of fluids is greatly affected by the interfacial friction force in the system. The narrow pore widths give rise to large flow resistances and thus fluids require large forces in order to be pumped through the tube. The flow of fluids in

nanopores and the interaction of the fluid with the nanopore walls has been the subject of much research recently and both theoretical [12] and simulation [13, 14] studies have been carried out. The relation between the molecular properties of an interface and the hydrodynamic boundary conditions is an intriguing one which has not yet been answered properly for non-model systems, but one which is vital to the understanding of experimental flow through nanopores.

Sub-10nm structures where significant deviations from continuum fluid dynamics are seen are difficult to produce experimentally. One exception and possible candidate for nanofluidic flow devices, which has duly attracted a lot of interest, is the carbon nanotube.

1.2.1 Properties of Carbon Nanotubes

Since their discovery and characterisation in 1991 [15], research into the properties of carbon nanotubes has been extensive. Their structure is that of a rolled up sheet of graphene, with radii ranging from 0.5nm to above 5.0nm and lengths up to the milimeter range [16]. Production is usually via Catalytic Vapour Deposition (CVD) from a hydrocarbon gas. Carbon nanotubes are categorised using the graphene sheet lattice vectors (n, m). The diameter of the nanotube is then given by:

$$d = \frac{a_{C-C}}{\pi}\sqrt{n^2 + nm + m^2} \tag{1.1}$$

The nanotubes can be metallic or semi-conducting depending on these vectors. Carbon nanotubes are viewed as potential building blocks for nanoscale devices due to their efficient transport of fluid as well as their ease of synthesis. Much work (both experimental and simulation) has thus been undertaken on the flow of fluids through these nanotubes, as discussed in the following sections. It has also been shown possible [17] to connect two carbon nanotubes together using a heating process which leads to the possibility of engineering structures and pipes for the flow of fluids in devices.

Simulated Flow through Carbon Nanotubes

Surprisingly due to the hydrophobic nature of carbon, spontaneous imbibition of water into carbon nanotubes was seen in simulations [18]. This effect was thought to be due to strong

hydrogen bonding between water molecules driving the formation of a depletion layer next to the solid surface. Capillary flow at the macroscale is described by the Washburn equation, which relates the filling rate (penetration length as a function of time) of a capillary to the interfacial pressure difference (given by the Laplace equation). The penetration length (L) is proportional to the square root of the time ($t^{1/2}$) in this case. In carbon nanotubes very rapid imbibition occurs initially which does not follow this relation as the penetration length is found to be proportional to t^1. This initial rapid uptake of fluid drops to the Washburn equation-like behaviour at longer time scales [19]. The diffusion mechanism of water within a nanotube has also been investigated and was suggested to be single-file $\left(r^2 \propto t^{1/2}\right)$ in the smallest width nanotubes [20] rather than the normal Fickian mechanism ($r^2 \propto t$).

It was determined through simulation studies that fluids inside carbon nanopores experience a very low interfacial friction [13] - therefore fluid flow through carbon nanotubes is expected to be extremely rapid. A simulation study published by Joseph and Aluru [21] found flow enhancements of around 2000 times in a (16,16) carbon nanotube and suggested that this fast transport is partly due to a depletion layer at the solid fluid interface, rather than due to the smoothness of the carbon nanotube surface as previously thought. This enhancement was in line with experimental expectations. Both mechanisms suggest that enhancement is caused by a significant amount of liquid slip at the interface. Other work suggests a migration of gases to the interface resulting in a low viscosity boundary layer creating a velocity jump at the boundary [22]. A number of simulations of graphene/water give a range of slip lengths from 30nm [23] to 80nm [24] or even nearer 500nm [21]. Reasons suggested for this variation are the fitting procedure [23] or the large velocity gradient at the wall [25]. Some simulation work has suggested that slip lengths are actually lower than those seen in experiments and suggest errors in the experiment due to miscalculation of flow parameters, e.g. miscalculation of flow area or the presence of additional external driving force [23]. Water flow in carbon nanotubes is therefore expected to obey the slip-modified Hagen-Poiseuille relation. Slip flow is desirable as it leads to uniform profiles and reduces the time spent in the pore, which can be important for controlling chemical reactions.

Water structure at the interface and its relation to flow behaviour are still not well understood. It was suggested in a study in 2008 [26] that the effective radius of the imbibing fluid increases with flow rate. This is because at higher rates fluid molecules do not have time to adjust to

the equilibrium positions due to the wall potential. It has also been found that defects in the nanotube wall and the presence of impurities can significantly change the rate of water flow through it and that smooth walls are required for the fastest flow rates [27]. Larger carbon nanotubes generally contain more defects and thus this is expected to hamper flow.

At the nanoscale fluid viscosity can vary from its bulk value. In one study [28] the viscosity of water was found to decrease with radius (from $\approx 8.0\times10^{-4}$Pas in d=5nm to $\approx 6.5\times10^{-4}$Pas in d=2nm) and also to decrease with increasing flow rate. The slip length is also found to increase in the more confined systems (from ≈30nm in d=5nm to ≈100nm in d=2nm). The average number of hydrogen bonds for a water molecule in the bulk is around four. Due to confinement effects the average number could be reduced and it has been found that the diffusion of water is lower in confined geometries [29].

Simulation studies have also looked at the pumping of fluids through carbon nanotubes. In one such study gas flow was generated using travelling waves on the surface of the nanotube [30]. In another, Decane pumping was seen upon stimulation of the radial breathing mode of the nanotube [31]. This method could also be used to determine water/tube potentials.

Experimental Flow through Carbon Nanotubes

Experimentally it is found that Carbon nanotubes can be wetted by liquids with surface tensions less than around 150mN/m [32]. Water at 72mN/m is well below this. Surface chemistry and structure can have a big effect on the wettability. For example, a low water-carbon contact angle is sometimes seen due to hydrogen bonds between the water molecules and impurities such as carbonyl groups introduced during the manufacturing process.

The enhanced flow, predicted by simulation, was first demonstrated experimentally in 2005 by Majumder et al [33]. Pressure driven flow was measured by weighing the mass of transported liquid through the tubes during a fixed period of time. Dramatically enhanced flow was seen. The transport of fluids through multi-walled carbon nanotube membranes with tube diameter, d=7nm was measured during a fixed period of time and flow rates five orders of magnitude above those expected were seen for pressure driven flow (Enhancement=61,404, Slip Length=53,728nm). Later smaller d=2nm tubes were also tested experimentally [34], but smaller flow enhancements were found. In other work using slightly larger pores (d=40nm systems) [35],

no water-glass slip was found but significant deviations from that expected were seen for decane (l_s=14nm). For large diameter tubes liquid flow followed continuum laws [36].

Some attempts were made by Majumder et al [33] to ensure the fluid was flowing through the center of the pore by using 10nm gold nanoparticles as a control. For water Majumder [33] reported an enhancement of 61,404 times but Holt [34] report enhancement of only 2,000 to 8,000 times in the smaller pores, which is opposite to that expected for a confinement effect from simulation studies. Flow rates are proportional to the fourth power of pore radius, which means any miscalculation of radius introduces large errors. Majumder [33] found decane flows slower than water, opposite to that of the macroscale pipes, suggesting the enhancement may be caused by the structure of the water molecules and hydrogen bonding effects within the pores.

A depletion layer can be seen in experimental work through X-ray reflectivity measurements of the interface between water and an alkane-like surface. The thickness of this thermodynamically driven depletion layer is of the order of one water molecule. This depletion layer was seen for contact angles above around 100° but not below this [37], which agrees with simulation interpretations. The behaviour of the fluid will be affected by the interfacial interactions much more in a nanoscale system and the exact surface structure will play a large part in determining the flow behaviour. It has been found previously through simulation studies that there is some orientation of the fluid parallel to a nanotube surface. The oxygen atoms in the water molecules are found to preferentially sit over the middle of the graphene rings [38], which cannot happen for an amorphous surface.

Several factors may limit transport in reality, e.g. structural defects such as dislocations/faults or obstacles caused by particles blocking the flow. Later experimental studies suggest lower slip coefficients. The slip length of water flow on graphite determined through the damping of an AFM tip at the interface is predicted to be somewhat lower at l_s=8nm with a water graphite contact angle of 74°. Other papers suggest lower rates [39] which found no significant deviations from classical behaviour.

Experiments introducing fluorescent nanoparticles into sub-micron (r=750nm) carbon nanopipes using capillary imbibition [40] have been performed. Inducing flow by pumping using electric field gradients or ultrasound has also been shown possible [30]. These types of experiments show that the manipulation and transport of fluids or particles is possible in these nanoscale pores, which will be important for the construction of nanofluidic devices.

1.2.2 Flow through Amorphous Carbon Nanopipes

Carbon nanopipes have been produced experimentally by chemical vapour deposition of carbon from a hydrocarbon gas onto a template [41]. They are generally larger than carbon nanotubes and the carbon is amorphous rather than a well ordered graphitic stucture. Carbon formed by catalytic vapour deposition tends to be hydrophobic due to C-H groups on the surface.

To form the nanopipes an aluminium oxide template is placed in a furnace and a hydrocarbon gas, e.g. ethylene, is passed over it. Carbon is deposited on the surface of the aluminium oxide. The pipe diameters range from 50 to 200nm, but an internal diameter as low as 6nm has been reported [42]. The walls of the pipes are usually around 5-20nm thick and will contain amorphous carbon. The Aluminium Oxide template can be removed with Sodium Hydroxide, leaving the pipes intact, while also increasing hydrophilicity.

These templated tubes can have advantages relative to carbon nanotubes grown on a catalyst particle as the pore size and length are easier to control.

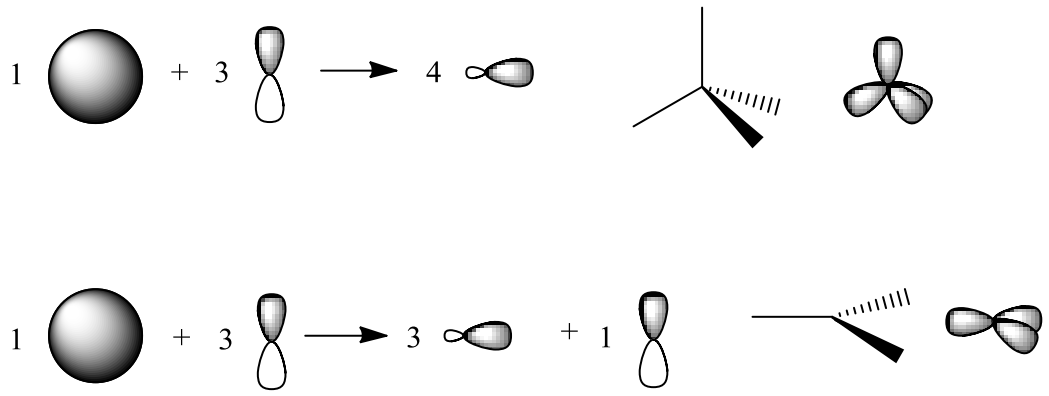


Figure 1.3: Carbon Hybridisation

Amorphous carbon is an allotrope of carbon which does not have any crystalline structure. Microscopically it is the ratio of threefold graphitic sp^2 bonds to tetrahedral diamond-like sp^3 bonds (figure 1.3) which controls the macroscopic properties of the amorphous carbon such as density and hardness. The type of amorphous carbon depends largely on the production method. Amorphous carbon deposits produced by the vapour deposition of hydrocarbons have a high hydrogen content and are soft with a low density [43]. TEM studies also suggest that there may

be a variety of nano-aligned graphene pieces in the structure [44].

The flow rate for water, decane and ethanol through a sample of these nanopipes has previously been measured and found to be several orders of magnitude greater than expected from macroscale fluid dynamics [45]. It is though less enhanced (Enhancement=22-34, Slip Length=113-177nm) than that seen in carbon nanotubes. A syringe pump was used to force each fluid through a membrane of CVD deposited carbon nanopipes. The pressure was measured and the flow rate measured by collecting the fluid passed. The inner diameter of the tubes was measured by SEM.

The experimental data for the flow enhancements through the various nanotubes and nanopipes are summarised in table 1.1.

System	Water		Decane		Ethanol	
	ε	l_s (nm)	ε	l_s (nm)	ε	l_s (nm)
d=2nm Nanotube [34]	4950	890	-	-	-	-
d=7nm Nanotube [33]	61404	53728	3941	3448	32143	28124
d=43nm Nanopipe [46]	34	177	45	237	25	129

Table 1.1: Summary of the Experimental Flow Data

1.2.3 PDMS Nanostructures

As mentioned previously PDMS is a very popular material for use in microscale devices. Some experimental work has been undertaken to try to produce nanoscale features in PDMS and other polymers. One such method has been proposed for growing polymeric nanotubes [47]. The tubes are grown on an Aluminium oxide template. Such polymeric nanotubes are light weight, low cost and can have a variety of physical and chemical properties which carbon nanotubes do not. They could be used in molecular probe technologies and could be applied in DNA carriage, for example. Research into their synthesis and properties is therefore very desirable. The growth of these nanotubes can be difficult to control though, so research has also been conducted looking at the nanoscale equivalents of the microscopic methods for generating channels.

Nanochannels can theoretically be introduced into polymeric materials using soft lithographic methods or photolithography [48]. Photolithographic methods for the patterning of substrates include extreme UV lithography, which has a resolution limit due to diffraction. Electron beam lithography can create smaller patterns but is still limited by scattering and is generally quite slow.

Using standard replica moulding the lowest possible channel widths reported are around 20nm to 30nm, somewhat lower than the pore widths intended to be looked at in this project. These limits represent the restrictions of producing the master moulds using electron-beam lithography, which have the aforementioned limits in resolution and uniformity of patterning.

A paper published in 2004 used single-walled carbon nanotubes to perform polymer imprint lithography [49]. Firstly single-walled carbon nanotubes were grown onto a substrate using CVD, and then PDMS was poured onto this substrate and cured, resulting in the features being replicated in the PDMS layer. The size of the channels formed in the PDMS were directly related to the width of the carbon nanotubes, resulting in channels as low as 2nm in width. This method shows great promise in generating nanochannels in PDMS and gives channels of width comparable to those studied in this report.

A potentially interesting utilisation of PDMS material on the nanoscale would be via the plasma oxidation of its surface to drive fluids spontaneously through the nanochannels. This would be advantageous as it reduces the need for pumping. The possibility of droplet movement due to a surface tension gradient was first experimentally demonstrated by Chaudhury and Whitesides [50]. Water was made to run up a wettability gradient upon a silicon surface which had been modified by varying exposure to a silane vapour. Motion of a droplet on a surface will result if there is an imbalance of the surface tension forces acting on opposite sides of the drop. The two main ways of controlling surface wettability are either the chemical modification of the surface or an alteration of its roughness.

In order to modify the surface properties of PDMS, various techniques can be utilised that involve physical or chemical treatments or a combination of both. Previous studies report that oxygen plasma treatment propagates deep under the polymer surface (about several hundred nanometers) and causes chemical changes in the surface region of PDMS: polar functional groups containing hydroxyl groups (Si-OH groups) are introduced into its surface, leading to the hydrophilic surface. Its surface characteristics though gradually reverse and the surface recovers its hydrophobicity after a short time [51].

The untreated PDMS shows hydrophobic behaviour and poor wettability with an 110° water drop contact angle. After oxygen plasma treatment, the contact angle decreases with plasma power as well as treatment time. It can reduce to as little as 10°. Recovery is believed to occur due to migration of low molar mass species from the bulk to the surface. A promising

method for the delay of the hydrophobic recovery is through thermal aging of the PDMS prior to plasma exposure [9]. Lower molecular weight species can be volatised and removed from the bulk through thermal aging. A PDMS network without these species will retain its hydrophilicity for a much longer time. Therefore by exposing a section of heat treated PDMS to varying degrees of plasma oxidation along its length should create a wettability gradient and the spontaneous transport of fluid along it.

In summary, there is much exciting work taking place and there are many questions still to answer in the move towards nanofluidic devices. Carbon-based systems in the form of the carbon nanotube provide a very low friction interface which could be used for rapid transport. There is though great variation in the values obtained for the magnitude of this enhancement in experimental work. Also, proof that nanoscale channels can be fabricated in PDMS is evidence that the systems looked at in this project are practically possible and theoretical research into their flow properties could prove valuable in the eventual fabrication of nanofluidic devices based upon this material which is already commonly used on the microscale. Such nanopores would also have many potential uses for the delivery and manipulation of fluids.

Chapter 2

The Interaction of Nanoparticles with Biological Membranes

2.1 Possible Medical Applications of Nanoparticles

2.1.1 Nanoneedles and Trans-membrane Transport

One of the most interesting potential applications of carbon nanotubes and nanopipes is in the emerging field of nanomedicine. The permeation of a cell membrane is required for a drug molecule to reach its biological target. The primary role of this membrane is the separation of internal cellular structures from the outside. Membranes are constructed from layers of phospholipids held together non-covalently. The phospholipids have a hydrophilic head group and a hydrophobic tail. In a bilayer the head groups, which are usually solvated, occupy 1nm each side and the hydrocarbon tails around 3nm in total.

There are mechanisms for the transport of materials across the membrane. Membrane channels, pores and transport proteins provide pathways for the transport of atoms or molecules across cellular membranes. The incorporation of artificial channels such as nanotubes into membranes has many potential uses. Their diameters are much smaller than typical cells. They can be used to deliver drugs to the interior of cells with the benefits that they can potentially target individual cells and access locations that macroscale needles cannot. Nanotubes can be filled with specific drug molecules and such filling has been previously studied [27]. It has also been proven in experimental work that a nanotube can penetrate the membrane of a cell without

damaging it - carbon nanopipes with nanometer scale diameters were used to controllably inject fluorescent dye molecules into cells [52].

Controlling the interactions between the nanotube and membrane or nanotube and drugs could be theoretically achieved through functionalising the tubes but the surface modification of carbon materials is difficult. The chemical modification of carbon nanotubes has been researched with some success in altering the carbon surface, e.g. direct fluorination or addition of C-O bonds [53]. Also some studies of the surface modification of mesoporous carbon using diazonium compounds have been carried out [54]. The oxidation of carbon using acids can also be used, which adds functional groups such as carboxylic acids to the carbon surface. This method though has drawbacks due to the low surface reactivity of carbon and the damage sustained to the carbon. Surface modification is interesting as it has potential applications for the control of filling and release of materials from within nanopipes in drug delivery applications. A review of the effect of nanoparticle surface properties on the interactions with the cell and endocytic pathways has been published [55].

2.1.2 Lung Membranes and the Inhalation of Nanoparticles

As well as the transport of nanoparticles across membranes, there is also much interest in the inhalation of nanoparticles in the lungs. Inhaled particles have been shown to pose health risks. Nanoparticles can induce inflammation in the pulmonary system [56]. Historically asbestos was discovered to have negative effects and carbon nanotubes are predicted to behave similarly. In-vivo experiments [57] have shown that nanotubes can induce a response similar to that of asbestos fibres. Carcinogenicity of asbestos fibres is found to be largest when exposed to longer ($> 20\mu$m) fibres because macrophages cannot engulf larger fibres. Radioactive particles have also been found to enter the bloodstream in humans when inhaled [58]. More recently, the negative effects of graphene nanoplatelets were reported [59]. The size and planar shape of the particles were predicted to possess unusual aerodynamic effects. Fullerene particles are present in diesel soot [60].

Titanium dioxide nanoparticles have been shown experimentally to cross airways [61]. Titanium dioxide nanoparticles, inhaled as an aerosol, entered lung tissue by diffusion and were found to not be membrane bound in many cases. Hydroxyapatite particles (90nm diameter) have been found to inhibit surfactant function in experimental studies by increasing the compressibility of

the layer [62]. This effect was believed to be due to the removal of proteins from the surfactant layer by the particle. The nanoparticles ended up covered in adsorbed protein molecules. The exact mechanisms of the nanoparticle-lung interactions on a molecular level though are still unknown.

In the lungs, the surfaces of the alveoli are covered with a layer of surfactant which controls surface tension during breathing. An example of an alveolus is shown below in figure 2.1. Unlike cell membranes the surface of the lung is a monolayer, which changes shape during breathing. Its main function is to reduce the surface tension of the air/fluid interface. It stabilises the alveolar interface during the compression and expansion phases and reduces the work required during the cycle. A low surface tension is required upon compression (after exhalation) to ease re-expansion.

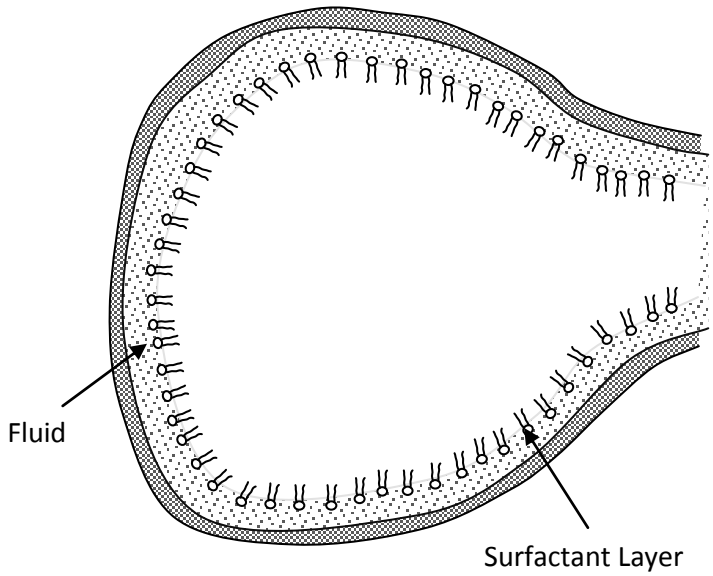


Figure 2.1: Alveolar Structure

The chemical composition of the lung surfactant has been previously analysed [63]. 80% of the layer is found to be Phosphatidylcholine and 70% of this is in the saturated form, Dipalmitoylphosphatidylcholine (DPPC). Other large constituents are Phosphatidylglycerol, which is negatively charged and accounts for around 10% of the membrane and Cholesterol around 5%. These lipids are pictured in the figure 2.2. Samples of human lung surfactant have also been analysed for their composition of electrolytes [64]. They were found to have a Na^+ concen-

tration of 83.1 mmol/dm^3, a K^+ concentration of 27.3 mmol/dm^3 and a Cl^- concentration of 74.1 mmol/dm^3. These correspond to concentrations of around 0.05 ions/nm^3. There are also a number of proteins in lung surfactant.

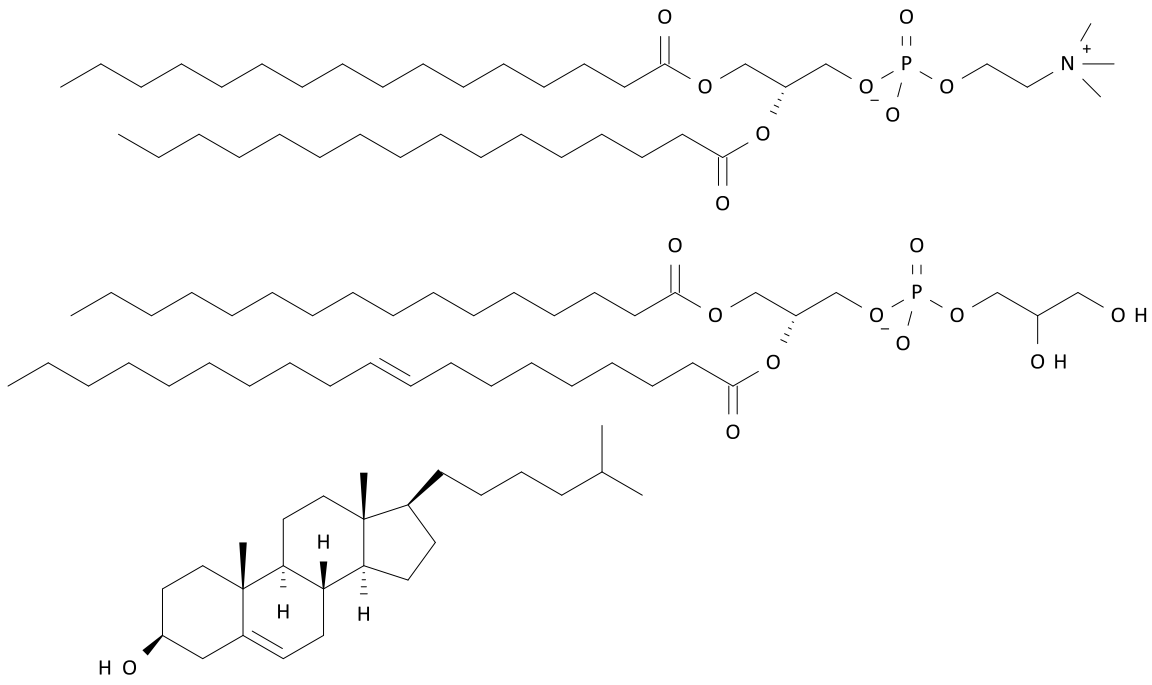


Figure 2.2: Molecular Structures of the DPPC, POPG and Cholesterol Lipids

Understanding the exact nature of the interaction of nanoparticles with the lung surface and if the nanoparticles adversely affect the operation of the pulmonary surfactant during the breathing cycle are poorly understood on the nanoscale, yet are very important from an environmental toxicology perspective. More work therefore needs to be done in this area.

Chapter 3

Fluid Flow Through Nanoscale Channels

3.1 Fluid Dynamics Theory

Classical fluid dynamics is based upon an assumption of a continuum and the associated conservation laws of mass, momentum and energy. Viscous fluid flow for a non-compressible Newtonian fluid is generally described by the Navier-Stokes equations [65], which arise from the considerations of the conservation of momentum and Newton's second law. In the x direction:

$$\rho F_x - \frac{\partial \sigma_{xx}}{\partial x} + \frac{\partial \tau_{xy}}{\partial y} + \frac{\partial \tau_{xz}}{\partial z} = \frac{\partial}{\partial t}\left(\rho u_x\right) + \frac{\partial}{\partial x}\left(\rho {u_x}^2\right) + \frac{\partial}{\partial y}\left(\rho u_x u_y\right) + \frac{\partial}{\partial z}\left(\rho u_x u_z\right) \tag{3.1}$$

Where u is velocity, ρ is the fluid density and τ and σ are stresses. Upon the assumption of a Newtonian linear viscosity this reduces to:

$$F_x - \frac{1}{\rho}\frac{\partial P}{\partial x} + \eta\left(\frac{\partial^2 u_x}{\partial x^2} + \frac{\partial^2 u_x}{\partial y^2} + \frac{\partial^2 u_x}{\partial z^2}\right) = \frac{\partial u_x}{\partial t} + u_x\frac{\partial u_x}{\partial x} + u_y\frac{\partial u_x}{\partial y} + u_z\frac{\partial u_x}{\partial z} \tag{3.2}$$

Where η is the viscosity coefficient of the fluid, P the pressure acting on the fluid and g is the gravitational constant. The pressure is defined as the trace of the stress tensor. The fluid can be driven by either gravity (ρg) or a pressure gradient ($-dP/dx$).

$$P = \frac{1}{3}\left(\sigma_{xx}+\sigma_{yy}+\sigma_{zz}\right) \tag{3.3}$$

The Navier-Stokes equation can be solved for a simple Newtonian fluid under gravity driven flow to give the parabolic solution for flow in a slit pore:

$$u_x\left(z\right) = \frac{\rho g_x}{2\eta}\left(h^2 - z^2\right) + u_x\left(z_w\right) \tag{3.4}$$

Or for pressure driven flow:

$$u_x\left(z\right) = -\frac{1}{2\eta}\frac{\partial P}{\partial x}\left(h^2 - z^2\right) + u_x\left(z_w\right) \tag{3.5}$$

Where z is the distance from the middle of the tube, h is half the width of the pore and $u_x\left(z_w\right)$ is the slip velocity (the velocity at the walls of the tube, $u_x\left(z_w\right) = {u_x}^f\left(z_w\right) - {u_x}^w$). From this solution it can be seen that $u_x\left(z\right)$ is a maximum in the center of the pore (when z is 0). This gives a flow profile of the form shown in figure 3.1.

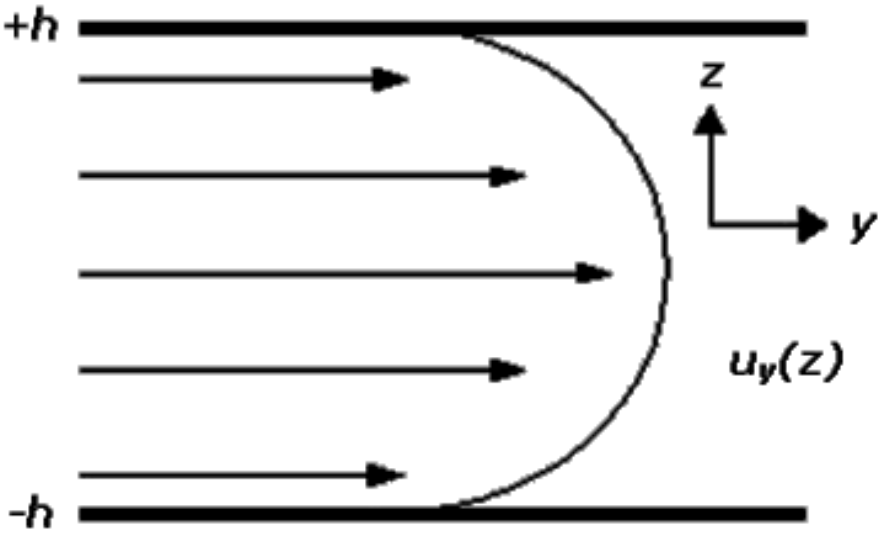


Figure 3.1: Flow Profile

The shear (strain) rate (γ) is given as the gradient of the velocity profile, which is linear in z:

$$\gamma = \frac{\partial u_x(z)}{\partial z} = -\frac{\rho g z}{\eta} \tag{3.6}$$

The equation for the flow profile leads to expressions for the average velocity (u_{av}) and the volumetric flow rate (Q):

$$u_{av} = \langle u_x(z) \rangle = \frac{1}{h}\int_0^h u_x(z)\,dz = \frac{1}{3\eta}\rho g_x h^2 + u_x(z_w) \tag{3.7}$$

$$Q = A_{yz}u_{av} = (2h)^2\left[-\frac{1}{3\eta}\frac{\partial P}{\partial x}h^2 + u_x(z_w)\right] = -\frac{4h^4}{3\eta}\frac{\partial P}{\partial x} + 4h^2 u_x(z_w) \tag{3.8}$$

The Hagen-Poiseuille law (equation 3.8) shows that there is a strong dependence between tube width and flow rate (h^4). Application of this equation to nanoscale flows in carbon nanotubes and nanopipes predicts much lower flow rates than are actually seen, i.e., there is an enhancement of flow on the nanoscale.

For a cylindrical pore the flow profile and average velocity are given by (R is the tube radius):

$$u_x(r) = \frac{\rho g_x}{4\eta}\left(R^2 - r^2\right) + u_x(r_w) \tag{3.9}$$

$$u_{av} = \langle u_x(r) \rangle = \frac{1}{\pi R^2}\int_0^R u_x(r)\,2\pi r dr = \frac{\rho g_x R^2}{8\eta} + u_x(r_w) \tag{3.10}$$

Simple hydrodynamic theory also predicts a parabolic temperature profile, where the thermal conductivity is assumed to be constant across the width of the pore. The viscous heat is proportional to the square of the local strain rate. Due to these local temperature inhomogeneities a heat flux as described by Fourier's law is expected:

$$T(z) = T(z_w) + \frac{\eta\gamma(z)^2}{2\kappa}\left(h^2 - z^2\right) \tag{3.11}$$

At the macroscopic level microscopic effects between the walls of a tube and the fluid can be largely ignored. On the nanoscale though, these interactions can dominate the flow through the tube. The Knudsen number (equation 3.12) is defined as the ratio of the mean free path in the

system ($\overline{v}$ is the average molecular velocity) to the length scale (L), which gives a measure of how valid continuum theory will be in the system.

$$Kn = \frac{\lambda}{L} = \frac{2\eta}{\rho \overline{v} L} \tag{3.12}$$

Another quantity from fluid dynamics which is useful as a measure of the turbulence of flow is the Reynolds number which is the ratio of the inertial to drag forces in the system (equation 3.13).

$$Re = \frac{\rho h u_{av}}{2\eta} \tag{3.13}$$

The Navier-Stokes predictions have been found to break down in channel widths below five molecular diameters or when the density/temperature variations in the system are comparable to the mean free path [66]. Due to anisotropy in the system there is a region a few molecular diameters wide where the bulk equations break down. The Navier-Stokes equations assume averaging over a scale larger than the mean free path of the molecules. Far away from the solid surface the momentum transport is described by the Navier-Stokes equations. Temperature profiles have also been found to not follow their predicted shape [67]. The shear stress oscillates around a linear profile and the velocity profile showed a deviation from its normal parabolic shape and showed points of inflexion where the strain rate is zero. These effects have led some to suggest that position dependent equations may be necessary to describe the situation correctly in some cases such as that in equation 3.14 for the viscosity [68].

$$\eta(z) = -\frac{\sigma_{xz}(z)}{\partial u_x(z)/\partial z} \tag{3.14}$$

3.2 Interfacial Friction and the Slip Coefficient

In solving fluid flow problems in a macroscopic system, non-slip boundary conditions are often applied to simplify the problem. This condition involves assuming the fluid velocity at the walls of the system is zero, i.e. there is no relative motion between the fluid and wall.

On the nanoscale though the slip velocity can be significant. This slip velocity is defined in

terms of the slip coefficient, l_s, which is the distance from the wall that the extrapolated velocity profile, as seen in figure 3.2, goes to zero. Wall slip is fairly common for gases but rarer for dense liquids. It is calculated as the ratio of the fluid velocity at the wall and the shear rate at the wall (equation 3.15).

$$l_s = \frac{u_x\left(z_{\text{wall}}\right)}{\partial u_x\left(z_{\text{wall}}\right)/\partial z} \tag{3.15}$$

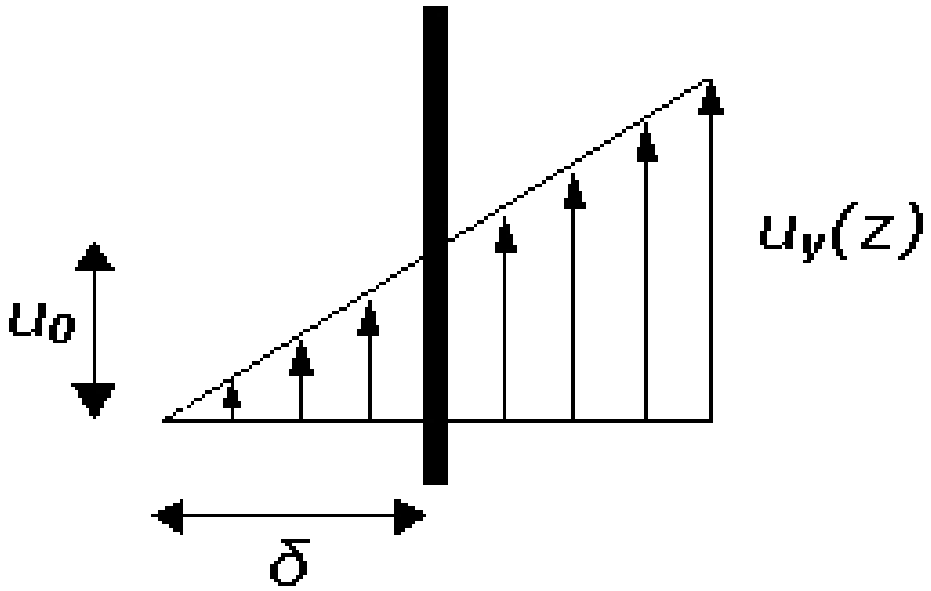


Figure 3.2: Definition of Navier Slip Coefficient

The slip length is further seen to be related to the stress at the wall and the shear viscosity:

$$u_x\left(z_{\text{wall}}\right) = l_s \frac{\partial u_x\left(z_{\text{wall}}\right)}{\partial z} = \left(\frac{l_s}{\eta}\right)\sigma_{xz}\left(z_{\text{wall}}\right) \tag{3.16}$$

The enhancement (ε) of the Hagen-Poiseuille flow due to the presence of slip is given by equations 3.17 and 3.18 for the slit and cylindrical pores respectively. Q_S is the flow with slip and Q_N is normal non-slip Hagen-Poiseuille flow.

$$\varepsilon = \frac{Q_S}{Q_N} = 1 - \frac{3\eta u_x\left(z_w\right)}{h^2(\partial P/\partial x)} = 1 + \frac{3l_s}{h} \tag{3.17}$$

$$\varepsilon = \frac{Q_S}{Q_N} = 1 + \frac{8l_s}{R} \tag{3.18}$$

Simulation studies have indicated a wide range of different boundary conditions at the wall are possible [69]. Experimental work has used optical/rheological techniques, e.g. fluorescence labelling/surface force apparatus [70] methods to determine non-zero slip lengths. The assumption of non-slip boundary conditions, which is fine for macroscopic flows, is not valid on the nanoscale, where the large surface area to volume ratio of the system means interfacial effects are much more important. Fluids which slip at solid walls have a lower resistance to flow and are thus desirable in physical applications.

Experimentally the slip coefficient can be calculated from the measured flow and pressure gradient (equation 3.19).

$$l_s = \frac{R}{4} - \frac{2\eta\left(\frac{Q_M}{N_p}\right)}{\left(\frac{\partial P}{\partial x}\right)\pi R^3} \tag{3.19}$$

Where Q_M is the measured flow rate and N_p the number of carbon pores. The number of pores and their average radius are measured using TEM. In experiments, a pressure is applied and the amount of fluid transported through the pores is collected. From this a flow rate can be determined and thus the enhancement and slip coefficient can be estimated. Underestimating the number of pores or the radius of the pores will lead to an overestimate in the slip coefficient.

3.2.1 Maxwell Theory of Slip

Collisions of fluid atoms with the wall transfer momentum to it and momentum lost by the fluid is gained by the wall. This momentum exchange at the surface can be described through the use of a scattering kernel and the extent of the exchange is related to the interfacial frictional resistance.

The phenomenon of slip was first defined at the atomic scale by James Clerk Maxwell in 1879 [71]. The amount of slip was shown to be dependent on the molecular structure of the surface and to the proportion of molecules diffusely reflected by the surface compared to those specularly reflected. The model only allows for these two types of collision event.

Thermalised molecules are adsorbed by the surface and then released in random directions at a later stage (diffuse reflection), thus losing all of their momentum in the direction of flow. They are released according to Knudsen's cosine law [72], which states that the direction in which the molecule is released is independent of the direction of approach and is proportional to $\cos\theta$ (θ is the angle formed normal to the surface). All other molecules are perfectly reflected and rebound elastically according to the laws of incidence and reflection (specular reflection).

If a molecule collides with the surface with incident velocity in the direction of flow v_{xi} and is specularly reflected with velocity v_{xf} then the change in momentum upon collision is given by:

$$m\triangle v_x = m\left(v_{xf} - v_{xi}\right) \tag{3.20}$$

The fraction of molecules having a velocity, v_{xi} is $f\left(v_{xi}\right)dv_{xi}$ and the total quantity of molecules incident on a unit area of the surface in a given time is $\rho_i v_{zi}$, therefore the total force acting on a unit area of the surface is:

$$F_{\text{tot}} = \int_{-\infty}^{\infty} \rho_i v_{zi} m\triangle v_x f\left(v_{xi}\right) dv_{xi} \tag{3.21}$$

Thermalised molecules, on the other hand, transfer 100% of their momentum to the wall:

$$F_{\text{therm}} = \int_{-\infty}^{\infty} \rho_i v_{zi} m v_{xi} f\left(v_{xi}\right) dv_{xi} \tag{3.22}$$

Maxwell's coefficient (α) is the proportion of molecules thermalised by the surface, i.e., the proportion of momentum transferred to the wall:

$$\alpha = \frac{F_{\text{tot}}}{F_{\text{therm}}} = \frac{\int_{-\infty}^{\infty} \rho_i v_{zi} m\triangle v_x f\left(v_{xi}\right) dv_{xi}}{\int_{-\infty}^{\infty} \rho_i v_{zi} m v_{xi} f\left(v_{xi}\right) dv_{xi}} \tag{3.23}$$

Terms cancel to give:

$$\alpha = \frac{\int_{-\infty}^{\infty} \triangle v_x dv_{xi}}{\int_{-\infty}^{\infty} v_{xi} dv_{xi}} = \frac{v_{in} - v_{out}}{v_{in}} \tag{3.24}$$

This equation (3.24) defines the Maxwell coefficient of slip, and gives a means to determine it

from a molecular dynamics simulation. By analysing the velocity profiles of particles colliding with the wall, the incident and reflected velocities can be determined and the accommodation coefficient calculated. This method has previously been applied to simulations of flow through carbon nanotubes [13]. The slip velocity based on Maxwell's coefficient is then given by:

$$u_s = \left(\frac{2-\alpha}{\alpha}\right) \frac{\partial u_x \left(z_{\text{wall}}\right)}{\partial z} \tag{3.25}$$

The slip length is further related to this coefficient through formula 3.26 originally derived by Maxwell [71]:

$$l_s = \lambda \left(\frac{2}{\alpha} - 1\right) \tag{3.26}$$

Where λ is the value of the mean free path in the system. This equation provides a direct link between Maxwell's theory of slip and the hydrodynamic equations shown earlier, which has many potential practical uses when analysing/modelling a system under flow.

For a no-slip condition the net velocity at the wall from rebounding molecules should be zero, i.e. 50% $-v_x$, 50% $+v_x$ from complete thermalisation and subsequent Knudsen cosine release. On the other hand when no molecules are themalised $v_{in} = v_{out}$, i.e. 100% of molecules move downstream and perfect slip is seen. Maxwell's coefficient is related to the amount of momentum transfer at the wall/fluid interface and the fraction of molecules diffusely reflected by the surface. As the coefficient increases the slip length decreases, tending towards stick boundary conditions (zero slip velocity). Conversely as Maxwell's coefficient decreases the slip length tends toward infinity and perfect slip is seen (the velocity profile is flat). In previous studies of the nature of collisions at the wall [73] it has been seen that in systems with a low fluid-wall interaction that most collisions are specular but that at higher interaction strengths multiple collision events between the wall and fluid can occur. Furthermore [74] it was seen that in fact no collisions are either completely specular or diffuse and that a fraction of momentum is lost upon each collision depending on the geometry and that the coefficient therefore represents the average fraction of momentum lost per collision.

3.2.2 Equilibrium Calculation of the Slip Coefficient

Since Maxwell's original work a method to calculate the slip length from equilibrium systems via an assessment of the interfacial friction has been developed [75]. The Langevin equation, based on Newton's second law, can be used to describe the equation of motion for an individual particle undergoing Brownian diffusion, in terms of the average frictional force ($-\gamma v$) it experiences and a random time-dependant noise term, $F(t)$. The friction coefficient in the system, γ is known from hydrodynamics.

$$m\frac{dv\left(t\right)}{dt} = -\gamma v\left(t\right) + F\left(t\right) \tag{3.27}$$

Multiplying (3.27) by $v(0)$ and summing over all of the molecules in the system gives the linear first order differential equation:

$$M\frac{dC_c\left(t\right)}{dt} = -\gamma C_c\left(t\right) \tag{3.28}$$

The autocorrelation function, $C_c(t)$, is dependant on the average velocity over all particles, $u\left(t\right)$.

$$C_c\left(t\right) = \left\langle u\left(t\right) u\left(0\right)\right\rangle, \qquad u\left(t\right) = \frac{1}{N}\sum_{i=1}^{N} v_i\left(t\right) \tag{3.29}$$

Equation 3.28 can be solved simply using standard analytical methods to give the collective velocity autocorrelation function in exponential form:

$$C_c\left(t\right) = C_c\left(t\right)\exp\left(-\frac{\gamma t}{M}\right) \tag{3.30}$$

From Boltzmann statistics $C_c(0)$ can be defined as:

$$C_c\left(0\right) = \left\langle u\left(0\right) u\left(0\right)\right\rangle = u\left(0\right)^2 = \frac{k_B T}{M} \tag{3.31}$$

Setting the relaxation time of the velocity autocorrelation function as $\tau = M/\gamma$ gives:

$$C_c(t) = \frac{k_B T}{M} \exp\left(-\frac{t}{\tau}\right) \tag{3.32}$$

This relaxation time can further be related to Maxwell's coefficient to give (f_0 is the collision frequency):

$$\alpha = \frac{N}{f_0 \tau} \tag{3.33}$$

For model systems previously studied the two methods agree [76].

3.2.3 The Slip Coefficient from Non-Equilibrium Systems

This relaxation time can also be determined from non-equilibrium simulations [77]. The flow of fluid through a nanopore is a balance between two forces: 1) the external driving force acting on fluid particles and 2) the frictional force exerted by the wall on the moving fluid. The sum of the gravitational force applied is given by:

$$F_g = \sum_{i=1}^{N} m_i g = Mg \tag{3.34}$$

The frictional force is known from Stokes' Law, which gives an equation for the viscous resistance experienced. This drag force is proportional to the velocity, but opposite in direction. As defined above, $\tau = M/\gamma$, therefore:

$$F_f = -\gamma u_{av} = -\frac{M u_{av}}{\tau} \tag{3.35}$$

Setting the two equations equal to each other,

$$u_{av} = \tau g \tag{3.36}$$

This equation links the average fluid velocity, the external force and the relaxation time. For a pressure driven flow the equation is:

$$u_{av} = -\frac{\tau}{\rho}\frac{dP}{dx} \tag{3.37}$$

It can be further shown that the slip length is related to the relaxation time and the gravitational force to give equation 3.38 for slit pores:

$$l_s = \frac{\tau\eta}{\rho h} - \frac{h}{3} \tag{3.38}$$

Or for a cylindrical pore:

$$l_s = \frac{2\tau\eta}{\rho R} - \frac{R}{4} \tag{3.39}$$

3.2.4 Other Methods of Calculation

The slip coefficient can be calculated in simulations from a method based on the fluctuation-dissipation theorem, which relates the relaxation of equilibrium fluctuations to that of an external perturbation. In this case the autocorrelation function of the x-component of the force acting on the fluid due to the wall is related to the slip coefficient [78].

$$l_s = \frac{\eta}{\gamma} = \frac{A_{xy}}{k_B T}\int_0^\infty \langle F_x(t)\, F_x(0)\rangle dt \tag{3.40}$$

$F_x(t)$ is the x-component of the stress exerted by the wall on the fluid. A_{xy} is the surface area. At high shear rates the Navier slip boundary condition was shown to break down in systems using frozen walls [79] and follow a relationship of the form in equation 3.41 below, which leads to unbounded slip at high shear rates:

$$l_s = {l_s}^0\left(1 - \frac{\gamma}{\gamma_c}\right)^{-1/2} \tag{3.41}$$

There is a critical shear rate (γ_c) above which the slip length is non-linear. Further work though indicated this could be due to the use of a rigid wall model which neglects momentum transfer between the wall and the fluid [80]. It is thus important when using frozen walls to ensure a linear regime is being sampled. Flexible walls do not show the same behaviour. Experimental

work has suggested that for rough surfaces the slip coefficient is constant as the flow rate varies, but this was not the case for smooth surfaces [81]. Two mechanisms have been proposed for slip [82] – individual hopping between equilibrium positions along the surface or the movement of the entire layer.

It has also been suggested from simulation work that the slip length follows a relationship of the form in equation 3.42, where the slip coefficient increases for small pore radii and is essentially constant above this [23]. C is a fitting parameter. Slip lengths were found to increase significantly below nanotube diameters of 3nm.

$$l_s = {l_s}^{\infty} - \frac{C}{r^3} \tag{3.42}$$

The liquid motion is opposed by a force proportional to the relative velocity between wall and fluid. The larger the friction due to intermolecular interactions between the fluid and the solid, the smaller the slip length is seen to be. An investigation of the relation between slip length and contact angle was published by Varanov et al [83]. This was followed by another paper [84] which proposed a semi-empirical relationship (equation 3.43) between wetting angle, θ and slip coefficient for smooth hydrophobic surfaces.

$$l_s \propto (\cos\theta + 1)^{-2} \tag{3.43}$$

When the wall fluid interaction, ε_{wf} is large there is significant momentum transfer at the wall. Contributing factors to larger slip include poor interfacial wettability or weak molecular attraction between phases, high shear rates and the smoothness of the solid surface. Nucleation of gas bubbles at the interface could also play a part in producing slip boundary conditions. The determination of the effect of nanoscale parameters and the dependence of slip on the shear rate at the interface are important.

3.2.5 Tangential Force Measurements

The slip length can also be determined from a direct calculation of the stress at the interface. Viscous momentum transport between the fluid and the solid is due to a boundary layer of fluid at the interface, which results in a resistance to flow. The Navier slip model assumes that the

amount of slip at the wall is proportional to the tangential component of the stress tensor at the solid surface ($\sigma_{xz}(z_{\text{wall}})$) [85]. The tangential force per unit area is given by dividing the integral of the tangential force across the boundary layer (${f_x}^w$) by the area of the interface (A_{xz}).

$$\frac{{F_x}^w}{A_{xz}} = \frac{1}{A_{xz}} \int_{z_0}^{z_0+l} {f_x}^w(z)\, dz = -\left(\frac{\eta}{l_s}\right) {v_x}^{\text{slip}} = \eta \frac{\partial u_x(z_{\text{wall}})}{\partial z} \tag{3.44}$$

The tangential wall force exerted on the water molecules in the boundary layer next to the fluid-solid interface can be calculated in a molecular dynamics simulation by separating the force each fluid molecule experiences into fluid-fluid and fluid-wall components. The slip velocity is calculated as the average of the velocity of all the molecules within the boundary layer in the direction of flow. This is the velocity that the fluid slips relative to the solid. When a slip velocity is present the wall exerts a frictional opposing force on the boundary layer fluid, which is the rate of momentum transport from the fluid to the wall due to collisions. This force represents a time averaged effect of wall-fluid interactions.

Models suggest that the friction coefficient is due to two effects which resist flow – Lennard-Jones interactions between the wall/ fluid and surface characteristics/roughness [86]. The wall-fluid interactions are determined by the structure of the potential energy surface near the wall $V(x, y, z)$, which is itself determined by the potential energy parameters within the system. It has been seen [87] that the wall can generate order in the fluid parallel to the walls which plays a significant part in the boundary conditions.

The previously discussed equations for the determination of slip boundary conditions and results using them have for the most part only been tested in simplified systems. For example through the use of model fluids, e.g. gases or single site model particles flowing over surfaces, which have themselves either been simplified through being fixed or being smooth. There are very few studies which attempt to model flow dynamics over realistic amorphous surfaces that would be found in experimental systems. This is one key theme of this work. The many different slip coefficients observed in both experiments and simulations also need explaining.

Chapter 4

Molecular Dynamics Simulations

4.1 System Trajectory

The simulations of the systems in this work were carried out using molecular dynamics. This method involves the solution of Newton's equations of motion for each molecule in the system and then following their spatial trajectories. These trajectories can then be linked to macroscale properties using statistical mechanics. Non-equilibrium simulation techniques are commonly used in the study of nanofluidics.

A molecular system has a configuration space spanned by a set of generalised coordinates $\{q_1, q_2 \dots q_i\}$. The trajectory of the system through this configuration space $\{q_1(t), q_2(t) \dots q_i(t)\}$ is determined via Hamilton's principle, which minimises the action integral (equation 4.1).

$$S = \int_{t_1}^{t_2} \mathcal{L}\left(q_i, \dot{q}_i\right) dt = \int_{t_1}^{t_2} \left(K\left(q_i, \dot{q}_i\right) - V\left(q_i\right)\right) dt \tag{4.1}$$

Where $\mathcal{L}$ is the Langrangian. This minimisation leads to the Lagrangian equations of motion (equation 4.2) for each degree of freedom of the system ($\lambda_\alpha a_{\alpha i}$ represent any constraints).

$$\frac{d}{dt}\left(\frac{\partial \mathcal{L}}{\partial \dot{q}_i}\right) - \frac{\partial \mathcal{L}}{\partial q_i} = \lambda_\alpha a_{\alpha i} \tag{4.2}$$

This can also be reformulated to give Hamilton's equations which describe the time evolution of the coordinates and momenta of each degree of freedom in the system.

$$\dot{q} = \frac{\partial \mathcal{H}}{\partial p_i}, \qquad \dot{p} = -\frac{\partial \mathcal{H}}{\partial q_i} \tag{4.3}$$

The Hamiltonian function is given by the sum of the kinetic and potential energies:

$$\mathcal{H} = K\left(q_i, \dot{q}_i\right) + V\left(q_i\right) = \frac{p^2}{2m} + V(r) \tag{4.4}$$

The evolution of the system through phase space is symplectic and described by Liouville's theorem, requiring that the phase space volume occupied by a system evolving according to Hamilton's equations of motion be preserved in time (equation 4.5).

$$\frac{df}{dt} = \frac{\partial f}{\partial t} + \sum_{i=1}^{N} \left(\dot{q}_i \frac{\partial f}{\partial q_i} + \dot{p}_i \frac{\partial f}{\partial p_i} \right) = 0 \tag{4.5}$$

From this equation and the definition of the Hamiltonian function the Liouville operator (iL) can be defined, which will give the evolution of the system from its initial state.

$$\dot{f} = iLf \quad \text{where} \quad iL = \sum_{i=1}^{N} \left(\frac{p_i}{m_i} \frac{\partial}{\partial q_i} + F_i \frac{\partial}{\partial p_i} \right) \tag{4.6}$$

Application of this operator to the initial coordinates and momenta of the system gives the evolution of a system of particles through space. The solution is the Velocity Verlet algorithm [88], which has the advantages of being symplectic and time-reversible and has good energy conserving properties.

$$\dot{q}\left(t + \frac{\delta t}{2}\right) = \dot{q}\left(t\right) + \frac{\delta t}{2m} F\left[q\left(t\right)\right] \tag{4.7}$$

$$q\left(t + \delta t\right) = q\left(t\right) + \delta t \, \dot{q}\left(t + \frac{\delta t}{2}\right) \tag{4.8}$$

$$\dot{q}\left(t + \delta t\right) = \dot{q}\left(t + \frac{\delta t}{2}\right) + \frac{\delta t}{2m} F\left[q\left(t + \delta t\right)\right] \tag{4.9}$$

The dynamics of this microscopic system can be linked to macroscopic properties through the

use of statistical mechanics. Properties of a system can be calculated either via a time average or as an ensemble average. The time average is the average of a series of measurements of a property as the system evolves in time:

$$\langle A \rangle = \frac{1}{\tau} \sum_{t=1}^{\tau} A\left(q, p, t\right) \tag{4.10}$$

The ensemble average ($\langle A \rangle$) is an average over a series of systems weighted by their probability of occurring. If the system is ergodic these two averages should be equal.

$$\langle A \rangle = \int f(q,p) A(q,p) dqdp \tag{4.11}$$

The distribution of points in phase space ($f\left(q,p\right)$) for the canonical ensemble (NVT) is given by the Boltzmann formula:

$$f\left(q,p\right) dqdp = \frac{\exp\left(-\beta H\left(q,p\right)\right)}{\sum_i \exp\left(-\beta H\left(q,p\right)\right)} dqdp \tag{4.12}$$

4.2 Ensembles

4.2.1 Simulating the NVT Ensemble

The Nose-Hoover Thermostat [89] is used in this work to ensure the system is operating within the canonical ensemble. Nose's Hamiltonian is of the form:

$$\mathcal{H}_{NVT} = \sum_i \frac{p_i^2}{2m_i s^2} + \phi\left(q\right) + \frac{{p_s}^2}{2Q_s} + \left(X+1\right) k_B T \ln s \tag{4.13}$$

Where s is a scaling factor, p_s is its momentum and Q_s is its 'mass'. X represents the number of degrees of freedom. This modifies the standard Hamiltonian equations of motion by scaling the time, therefore reproducing the canonical probability density. The equations of motion for the system are given by the solution of Hamilton's equations:

$$\dot{q_i} = \frac{p_i}{m_i s^2}, \quad \dot{p_i} = F\left(q_i\right), \quad \dot{s} = \frac{p_s}{Q}, \quad \dot{p_s} = \sum \frac{p_i^2}{m_i s^3} - \frac{\left(X+1\right) k_B T}{s} \tag{4.14}$$

As dt= sdt', the time can be rescaled to give the real time:

$$\dot{q}_i = \frac{p_i}{m_i s}, \quad \dot{p}_i = sF\left(q_i\right), \quad \dot{s} = \frac{sp_s}{Q}, \quad \dot{p_s} = \sum \frac{p_i^2}{m_i s^2} - \left(X+1\right) k_B T \tag{4.15}$$

These equations can then be converted to a more convenient form (Hoover [90]):

$$\ddot{q}_i = \frac{\dot{p}_i}{m_i s} - \left(\frac{p_i}{m_i s}\right)\frac{\dot{s}}{s} = \frac{F\left(q_i\right)}{m} - \frac{\dot{q}_i p_s}{Q} = \frac{F\left(q_i\right)}{m} - \xi \dot{q}_i \tag{4.16}$$

Where ξ is a friction coefficient, which evolves in time according to $\dot{\xi}$:

$$\xi = \frac{p_s}{Q}, \quad \dot{\xi} = \frac{\sum m_i \dot{q}_i{}^2 - \left(X+1\right) k_B T}{Q} \tag{4.17}$$

4.2.2 Simulating the NPT Ensemble

Alternatively, an NPT ensemble in which the pressure, as well as the temperature, is fixed on average can be obtained by allowing the volume of the system (V) to change [91]. The Hamiltonian in this case is:

$$\mathcal{H}_{NPT} = V^{-2/3} \sum_i \frac{p_i^2}{2m_i s^2} + \phi\left(V^{1/3} q\right) + \frac{{p_s}^2}{2Q_s} + \frac{{p_V}^2}{2Q_V} + \left(X+1\right) k_B T \ln s + P_{ext} V \tag{4.18}$$

4.3 Forces within the System

The total intermolecular potential energy of the system is given by the sum of three different contributions, v_{ff}, v_{ss} and v_{sf} which represent the interaction potentials for the fluid-fluid, solid-solid and solid-fluid interactions respectively.

$$V = \sum_{j>i}^{N_f} v_{ff}(i,j) + \sum_{j>i}^{N_s} v_{ss}(i,j) + \sum_{j>i}^{N_f, N_s} v_{sf}(i,j) \tag{4.19}$$

4.3.1 Solid-Solid Forces

In some previous simulation work it has been suggested that fixing the solid surface can reduce the computational time without significant change to the results [87]. Other work suggests this leads to incorrect results especially at high shear rates [80]. Tethering wall atoms to their lattice sites allows them to move and interact during collisions, whilst maintaining sufficient rigidity to contain the fluid. The force due to such a harmonic tethering potential is given by equation 4.20 [92]:

$$F\left(r\right) = -k\left(r\left(t\right) - r_{eq}\right) \tag{4.20}$$

Where k is a spring constant which determines the rigidity of the solid. This spring constant must be small enough to allow sufficient thermal motion and heat transfer but large enough to maintain wall solidity. Using this method has one possible advantage that the wall atoms rather than the fluid atoms could be thermostated thus allowing a more experimentally realistic heat conduction to the walls.

4.3.2 Intermolecular Forces

The fluid properties will depend on the intermolecular potential energy interactions which are technically defined by the equations of quantum mechanics. Calculations of this type though would be impractical in simulations of condensed matter systems for long time scales, so approximations have to be made [93]. Atoms are commonly treated as spheres and their interactions modelled as empirical analytic functions. The Lennard-Jones potential [94] is used to model the Van der Waals interactions, due to the fluctuating charge densities between atoms. This potential contains terms for both attractive and short-range repulsive effects and is given by equation 4.21.

$$U(r_{ij}) = 4\varepsilon\left[\left(\frac{\sigma}{r_{ij}}\right)^{12} - \left(\frac{\sigma}{r_{ij}}\right)^{6}\right] \tag{4.21}$$

The interaction energy has a minimum at $r = 2^{1/6}\sigma$. The Buckingham potential, which treats the repulsion slightly differently, is given by:

$$U(r_{ij}) = A\ \exp\left(\frac{r_{ij}}{\rho}\right) - \frac{C}{{r_{ij}}^6} \tag{4.22}$$

The Coulomb interaction is used to calculate electrostatic interactions between charged groups within the system, here in a form which ensures the potential and force are both zero at the interaction cut-off (r_c):

$$U(r_{ij}) = \frac{q_i q_j}{4\pi\varepsilon_0}\ \left[\frac{1}{r_{ij}} + \frac{r_{ij}}{{r_c}^2} - \frac{2}{r_c}\right] \tag{4.23}$$

Ewald Summation

Truncating the Coulombic force can result in errors and artificial behaviour in the system. The popular Ewald Sum method [95] can be used for a more accurate treatment. This splits the Coulomb potential into two sums, one in real space (r) and the other in reciprocal space (k). α determines the relative width of the real/reciprocal space functions.

$$U = \frac{2\pi}{V}\sum_{k\neq 0} Q\left(k\right) S\left(k\right) S\left(-k\right) - \frac{\alpha}{\sqrt{\pi}}\sum_i\sum_a {q_{ia}}^2 + \frac{1}{2}\sum_i\sum_a\sum_{j\neq i} q_{ia}\sum_b q_{jb}\frac{erfc\left(\alpha r_{iajb}\right)}{r_{iajb}} \tag{4.24}$$

$$\text{where} \quad S(k) = \sum_i\sum_a q_{ia}\exp\left(ik\cdot r_a\right) \tag{4.25}$$

$$\text{and} \quad Q(k) = \frac{\exp\left(-k^2/4\alpha^2\right)}{k^2} \tag{4.26}$$

$$\text{with} \quad k = 2\pi\left(l/L_x, m/L_y, n/L_z\right) and \left|k^2\right| \leq \left|k^2_{max}\right| \tag{4.27}$$

For slab-like systems, which are only 2D periodic, an adjustment term to the potential [96] can be used to correct for effects caused from the use of the 3D Ewald Sum (in this case for the z-dimension, with dipole moment M_z).

$$U = \frac{2\pi}{V} M_z^2 = \frac{2\pi}{V} \sum_i q_i {z_i}^2 \tag{4.28}$$

4.3.3 Intramolecular Forces

The potential energy of each molecule in the system can be represented by a series of terms which include approximations for the various effects a molecule experiences (equation 4.29).

$$U_{tot}\left(d_{ij}, \theta_{ijk}, \phi_{ijkl}, r_{ab}\right) = u_{bond}\left(d_{ij}\right) + u_{bend}\left(\theta_{ijk}\right) + u_{tors}\left(\phi_{ijkl}\right) + u_{\mathrm{NB}}\left(r_{ab}\right) \tag{4.29}$$

Forces within the molecule (e.g. bond stretching or bending) can be treated analytically to give functions which are harmonic about an equilibrium value.

The harmonic bond potential (u_{bond}) can be used to describe bond stretching around the equilibrium value, d_0:

$$U\left(d_{ij}\right) = \frac{1}{2} k (d_{ij} - d_0)^2 \tag{4.30}$$

The harmonic angle potential (u_{bend}) can be used to describe bond bending around an equilibrium value, θ_0:

$$U\left(\theta_{ijk}\right) = \frac{1}{2} k (\theta_{ijk} - \theta_0)^2 \tag{4.31}$$

The triple cosine torsional interaction potential is used for dihedral rotation about a bond where ϕ is the angle between the planes ijk and jkl (i, j, k and l are consecutive adjacent atoms):

$$U(\phi_{ijkl}) = \frac{1}{2} A_1 (1 + \cos\phi\ ) + \frac{1}{2} A_2 (1 - \cos 2\phi\ ) + \frac{1}{2} A_3 (1 + \cos 3\phi\ ) \tag{4.32}$$

Alternatively lengths/angles within the molecule can be constrained. In this study the bond lengths are constrained using the SHAKE algorithm [97]. This iteratively adjusts the bond lengths back to their required lengths after having been moved using the integration algorithm. The constraint is of the form:

$$\sigma_{ij} = (r_i - r_j)^2 - {d_{ij}}^2 = 0 \tag{4.33}$$

The movement of the atoms at each step is adjusted iteratively until the bond length is close to its required value according to:

$$q_i(t + \delta t) = {q_i}'(t + \delta t) + \frac{\delta t^2}{2m_i} \sum \lambda_{ij}(t) \underline{r}_{ij}(t) \tag{4.34}$$

Where the constraining force is given by:

$$\lambda_{ij}(t) = \frac{{d_{ij}}^2 - r_{ij}(t + \delta t)^2}{\delta t^2 ({m_i}^{-1} + {m_j}^{-1}) r_{ij}(t) \cdot r_{ij}(t + \delta t)} \tag{4.35}$$

Velocity values are also constrained using the Rattle algorithm [98] by the requirement:

$$\frac{d}{dt}(r_i(t) - r_j(t))^2 = (r_i(t) - r_j(t))(\dot{r}_i(t) - \dot{r}_j(t)) = 0 \tag{4.36}$$

Velocity values are therefore adjusted at each step according to:

$$\dot{q}_i(t + \delta t) = {\dot{q}_i}'(t + \delta t) + \frac{\delta t^2}{2m_i} \sum \gamma_{ij}(t + \delta t) \underline{r}_{ij}(t + \delta t) \tag{4.37}$$

Where the constraining force is given by:

$$\gamma_{ij}(t + \delta t) = \frac{2x_{ij} \cdot (v_j(t) - v_i(t))}{\delta t ({m_i}^{-1} + {m_j}^{-1}) r_{ij}(t)} \tag{4.38}$$

In a typical molecular dynamics simulation step, forces between atoms are computed at integral time steps and from these particle velocities can be calculated using the velocity Verlet algorithm. These can then be used to update the particle positions subject to any constraints and the thermostat. Once a steady state has been reached, the properties of the system can be determined using statistical mechanical methods.

4.4 Microscopic Fluid Dynamics

The equations of fluid dynamics can also be derived from statistical mechanical principles [99] as originally shown by Irving/Kirkwood [100]. Equations expressing mass conservation and momentum conservation are obtained. The mass density ($\rho(r,t)$) at time, t is given by:

$$\rho\left(r,t\right)=\sum_{i}m_{i}\delta\left(r-r_{i}\left(t\right)\right) \tag{4.39}$$

Integrating this over a volume element gives the mass within that space. The momentum density is defined similarly:

$$\rho\left(r,t\right)u\left(r,t\right)=\sum_{i}m_{i}\dot{r_{i}}\delta\left(r-r_{i}\left(t\right)\right)=\sum_{i}\left(m_{i}v_{i}\delta\left(r-r_{i}\left(t\right)\right)+\rho\left(r,t\right)u\left(r,t\right)\right) \tag{4.40}$$

The rate of change of mass density is given by:

$$\frac{\partial}{\partial t}\rho\left(r,t\right)=\sum_{i}m_{i}\frac{\partial r_{i}}{\partial t}\frac{\partial}{\partial r_{i}}\delta\left(r-r_{i}\left(t\right)\right)=-\frac{\partial}{\partial r}\sum_{i}m_{i}\dot{r_{i}}\delta\left(r-r_{i}\left(t\right)\right)\therefore\frac{\partial}{\partial t}\rho\left(r,t\right)=-\frac{\partial}{\partial r}\rho\left(r,t\right)u\left(r,t\right) \tag{4.41}$$

The rate of change of momentum density is given by:

$$\frac{\partial}{\partial t}\rho\left(r,t\right)u\left(r,t\right)=-\frac{\partial}{\partial r}\sum_{i}m_{i}\dot{r}_{i}\dot{r}_{i}\delta\left(r-r_{i}\left(t\right)\right)+\sum_{i}m_{i}\ddot{r}_{i}\delta\left(r-r_{i}\left(t\right)\right) \tag{4.42}$$

This then reduces to:

$$\frac{\partial}{\partial t}\rho\left(r,t\right)u\left(r,t\right)=-\frac{\partial}{\partial r}\sum_{i}\left(m_{i}v_{i}v_{i}\delta\left(r-r_{i}\left(t\right)\right)+\rho\left(r,t\right)u\left(r,t\right)u\left(r,t\right)\right)+\sum_{i}F_{i}\delta\left(r-r_{i}\left(t\right)\right) \tag{4.43}$$

Upon symmetrising the force summation between pairs of molecules this becomes:

$$\frac{\partial}{\partial t}\rho(r,t)u(r,t) = -\frac{\partial}{\partial r}\sum_i \left(m_i v_i v_i \delta(r - r_i(t)) + \rho(r,t)u(r,t)u(r,t)\right) + \frac{1}{2}\sum_{i,j} r_{ij}F_{ij}\int_0^1 d\lambda\delta(r - r_i - \lambda r_{ij}) \tag{4.44}$$

From comparison to the macroscopic formula the microscopic representation of the pressure tensor can be seen as:

$$\sigma(r,t) = \sum_i m_i v_i v_i \delta(r - r_i(t)) - \frac{1}{2}\sum_{i,j} r_{ij}F_{ij}\int_0^1 d\lambda\delta(r - r_i - \lambda r_{ij}) \tag{4.45}$$

The temperature can also be defined using the number density as:

$$\frac{3}{2}n(r,t)\,k_B T(r,t) = \sum_i^N \frac{1}{2} m_i v_i v_i \delta(r - r_i(t)) \tag{4.46}$$

4.4.1 Stress Tensor Calculation

The expression for the stress tensor above can be divided into kinetic and potential contributions:

$$\sigma(r,t) = \sigma^K(r,t) + \sigma^V(r,t) \tag{4.47}$$

Where the kinetic contribution is:

$$\sigma^K(r,t) = \sum_i m_i \left(\frac{p_i}{m_i} - v(r,t)\right)\left(\frac{p_i}{m_i} - v(r,t)\right)\delta(x_i - r(t)) \tag{4.48}$$

And the potential contribution is:

$$\sigma^V(r,t) = -\frac{1}{2}\sum_i \sum_{i\neq j} (x_i - x_j) F_{ij}\delta(x_i - r(t)) \tag{4.49}$$

The potential contribution at the wall for the stress over the boundary layer can be calculated as a force acting across a surface (A_{xz}):

$$\sigma_{xz}{}^V(r,t) = \frac{1}{A_{xz}}\sum_{(i,j)} F_{ij,x} \tag{4.50}$$

The pressure on the nanoscale though is found to have large fluctuations and is very sensitive to the number of molecules [25], thus long simulation times are required to obtain an accurate value.

4.4.2 Diffusion/Viscosity Calculation

The translational motion of the fluid molecules can be measured through the diffusion coefficient (D). This can be calculated either as an autocorrelation function of the center of mass velocities of the molecules in the system or as the mean square deviation in their position (equation 4.51).

$$D = \frac{1}{3}\int_0^\infty dt \left\langle v_x\left(t+dt\right) v_x\left(t\right)\right\rangle = \frac{1}{6Nt}\sum_i^N \left\langle \left|r_i\left(t\right) - r_i\left(0\right)\right|^2 \right\rangle \tag{4.51}$$

The viscosity (η) is another important quantity in these systems. It can be calculated from the Newtonian definition of shear viscosity, which linearly relates the stress to the shear rate (equation 4.52). This formula only applies at low shear rates for Newtonian fluids.

$$\sigma_{xy} = -\eta\frac{\partial v_x}{\partial y} \tag{4.52}$$

A Green-Kubo formula for the shear viscosity in the system can also be derived [101]. The shear viscosity is related to correlations of fluctuations in the stress tensor (equation 4.53).

$$\eta = \frac{V}{k_B T}\int_0^\infty dt \left\langle \sigma_{xy}\left(t+dt\right)\sigma_{xy}\left(t\right)\right\rangle \tag{4.53}$$

Other methods for calculating the viscosity include an Einstein type method or that proposed by Hess/Evans [102, 103]. It has also been calculated from the diffusion coefficient (equation 4.54) [104].

$$\eta = \frac{k_B T}{2\pi a D} \tag{4.54}$$

Viscosity can be measured directly through the shearing stress between the wall and the fluid (equation 4.52). It has also been calculated previously through analysing the deceleration of a flowing fluid within a pore [28]. The fluid was accelerated to a certain flow rate and the

deceleration (d) monitored once the external force had been removed.

$$\sigma_{xz}(0) = \frac{Nmd}{2\pi RL} \tag{4.55}$$

This was then linked to the viscosity via the volumetric flow rate.

4.5 Flow Generation

The systems can be driven away from equilibrium through the use of several methods in order to give non-equilibrium dynamics. It is important to ensure that the field is small enough to get a linear system response. Poiseuille flow can be generated through the application of a gravitational acceleration force to each atom within the system ($m_i g$). The applied external acceleration can be held constant throughout the simulation and the field strength determined through trial and error or it can be varied during the simulation to achieve a desired flow velocity through a feedback mechanism [25]:

$$g_i = \frac{m_i}{\delta t}\left({V_{com}}^0 - V_{com}\right) \tag{4.56}$$

The use of a gravitational type force though is not necessarily the most desirable way to model pressure driven flow as it requires forces far beyond those used in experimental work (which are generally due to a pressure gradient) and may produce artificial effects, such as heating, in certain regions of the system (e.g. next to the wall). Also in a non-homogeneous system the effects on local flow behaviour at the wall induced through a constant external gravitational field may be different to those generated from a pressure gradient. Shear rates in simulations are orders of magnitude larger than those employed in experimental studies. Several other mechanisms for the generation of flow have therefore been suggested.

The fluidised piston model was proposed in 2006 [105] to drive a fluid using a pressure gradient. The flow is driven by separating the system into two regions – one which is subject to an external field and the second downstream from which data is sampled. This though has the disadvantage that the system size is increased, requiring longer processing times.

Another method [106] which uses a reflecting particle membrane can generate flow by allowing

particles to move unrestricted in one direction across an artificial membrane, but only allowing a certain percentage to cross the other way. This creates a pressure gradient across the system ($\partial P/\partial x$), which is more in keeping with an experimental set-up where fluid enters and leaves a channel under a pressure difference $P_{in} - P_{out} > 0$. The magnitude of this gradient can be varied by modifying the probability of reflection at the membrane. Fluid is driven in the direction of the unrestricted barrier. There is also very little additional computational effort required.

Both the RPM method and an external gravitational force have been utilised in this work to generate non-equilibrium flow.

Chapter 5

Molecular Models

In simulation work it is important to choose realistic potential energy functions in order to obtain reliable results. The models used for the solid carbon and PDMS surfaces and the fluids flowing across them shall now be discussed.

5.1 Carbon Model

There are three potential methods for forming the amorphous carbon surface to be used in the flow studies:

1. Freezing a Molten Carbon Sample
2. Modelling Vapour Deposition Process
3. Reverse Monte Carlo

Freezing a molten carbon sample is one of the most popular ways and is the method used originally by Tersoff in 1986 [107]. Most models are formed by the freezing of a molten carbon sample. A carbon sample is equilibrated at 5000K for 0.5ps where the liquid is highly diffusive. The liquid sample is then cooled to 300K over 0.5ps using a velocity rescaling algorithm. The coordination in the finished sample (i.e. the sp^2/sp^3 ratio) is determined by counting the number of atoms lying within 0.185nm of an atomic site. In order to achieve the correct hydrogen content in the surface, the H:C ratio in the liquid can be controlled by comparison with experiment.

In another method efforts to simulate the vapour deposition process have been undertaken by Neyts et al. in Belgium [108]. Hydrocarbon radical species collide with a surface and a hydrogenated amorphous carbon layer is formed.

The initial surface can either be a freshly generated crystal structure or a previously generated amorphous carbon surface and the lower layers are kept fixed. The species fired at the surface can be chosen from a number of fragments/atoms. The chosen fragment is then placed above the substrate at a randomly determined position and allowed to move towards the substrate, by increasing its z-velocity, where it interacts with the surface potential. A Berendsen thermostat is used to control the temperature of the surface. Atoms and fragments not bound to the surface are removed after impact. The fragments/molecules used in the simulation included C_2H_2, C_2, CH and C/H. Again, the coordination in the finished sample can be determined by counting the number of atoms lying within 0.185nm of an atomic site. In order to achieve the correct hydrogen content in the surface, the total C:H ratio in all the deposited fragments can be predetermined.

Alternatively reverse Monte Carlo methods [109] can be used to produce a structural model of amorphous carbon which is accurate compared to experiment. They work by randomly moving atoms and then accepting the move if the structure is closer to the experimental one or rejecting it if it is not until an equilibrium value is reached.

In this work the melting/freezing method was chosen as it was the simplest and easiest to control factors such as the proportion of hydrogen. Generation using vapour deposition leads to very diffuse and rough surfaces and no-pair correlation function exists to compare the surface in order to conduct a reverse Monte-Carlo simulation.

5.1.1 Tersoff-Brenner Potential

Classical potentials have advantages over quantum methods for large systems and long simulation times. For carbon though it is important to allow for variable bonding situations, which do not feature in a simple Lennard-Jones potential. An example of a classical potential which has the ability to model these effects are the Tersoff style empirical bond order potentials. Terms reflecting the local coordination of each atom are used to modify the strength of interactions (b_{ij}). Each pair of covalently bonded atoms then interacts via the modified potential, equation 5.1 (the chemical binding energy) :

$$E_b\left(r_{ij}\right) = \sum_i \sum_j \left(U^R\left(r_{ij}\right) - b_{ij} U^A\left(r_{ij}\right) \right) \tag{5.1}$$

The attractive (U^A) and repulsive (U^R) potential terms are given by equations 5.2 and 5.3 respectively.

$$U^A\left(r_{ij}\right) = f^c\left(r_{ij}\right) \sum_{n=1,3} B_n e^{-\beta_n r_{ij}} \tag{5.2}$$

$$U^R\left(r_{ij}\right) = f^c\left(r_{ij}\right) \left(1 + \frac{Q}{r_{ij}}\right) A e^{-\alpha r_{ij}} \tag{5.3}$$

Q, A, B_n, α and β_n are empirical parameters presented in table 5.1.

B_1=12388.79eV	β_1=4.7205A^{-1}	Q =0.31346A
B_2=17.56741eV	β_2=1.43321A^{-1}	A =10953.544eV
B_3=30.71493eV	β_3=1.38269A^{-1}	α =4.76539A^{-1}

Table 5.1: Tersoff-Brenner Potential Parameters

b_{ij} is the bond order between atoms i and j. It varies as the coordination of the two interacting atoms varies. It is this which adjusts the potential via several terms (equation 5.4) according to the bonding environment.

$$b_{ij} = \frac{1}{2}\left[{b_{ij}}^{\sigma-\pi} + {b_{ji}}^{\sigma-\pi}\right] + {b_{ij}}^{\pi} \tag{5.4}$$

The bond order parameter, b_{ij}, depends on the local coordination and bond angles for the atoms i and j. This term is larger for stronger bonds. As shown below in figure 5.1, the bond energy varies for single, double and triple bonds. The triple bond has the greatest minimum.

The ${b_{ij}}^{\sigma-\pi}$ terms give the (sigma) covalent bond interactions. They form the main contribution to the bond order. ${b_{ij}}^{\sigma-\pi}$ is the effect of the neighbours of atom i on the ij bond and vice versa for ${b_{ji}}^{\sigma-\pi}$.

$${b_{ij}}^{\sigma-\pi} = \left[1 + \sum_{k(\neq i,j)} f^c\left(r_{ik}\right) G\left(\cos\theta_{ijk}\right) e^{\lambda_{ijk}} + P_{ij}\left({N_i}^C, {N_i}^H\right)\right]^{-1/2} \tag{5.5}$$

$G(\cos\theta_{ijk})$ is a term dependent on bond angles. P_{ij} is a spline. The quantities ${N_i}^C$ and ${N_i}^H$

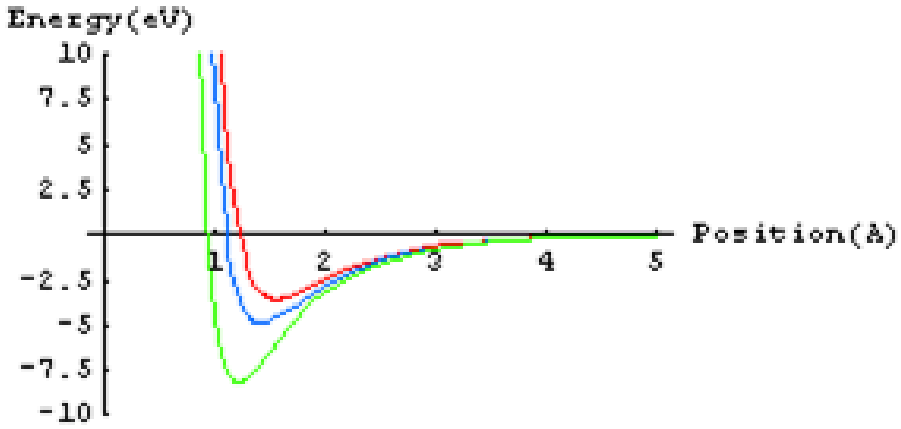


Figure 5.1: Potential energy curves for single, double and triple bonds using the potential

represent the number of hydrogen atoms and carbon atoms that are neighbours of the atom, i.

The ${b_{ij}}^{\pi}$ terms describe the pi bonding interactions and allow for any radical character (RC) in conjugated systems and include effects due to the dihedral angles (DH) for any carbon-carbon double bonds. In all of the above equations the function $f^c(r_{ij})$ limits the range of the covalent interactions.

The Tersoff-Brenner potential is not included in the commonly used DL_POLY, NAMD or GROMACS simulation packages and so was developed independently. The derivative of the potential formula was calculated and then converted to a computational algorithm using the C++ language. This code was then tested extensively on a number of systems to ensure it was operating correctly. A diamond lattice, a carbon nanotube and a benzene molecule were all modelled and shown to be stable and have bond lengths and energies comparable to those in the original paper. This code is included as an appendix at the back of this report.

In this work the wall is usually fixed during flow simulations for simplicity, meaning the solid-solid potential is constant and can be removed from the calculation. In some cases though in addition to its use during the initial formation of the amorphous surfaces the Tersoff-Brenner potential was also used when the wall atoms are not frozen in place to model carbon-carbon interactions within the surface.

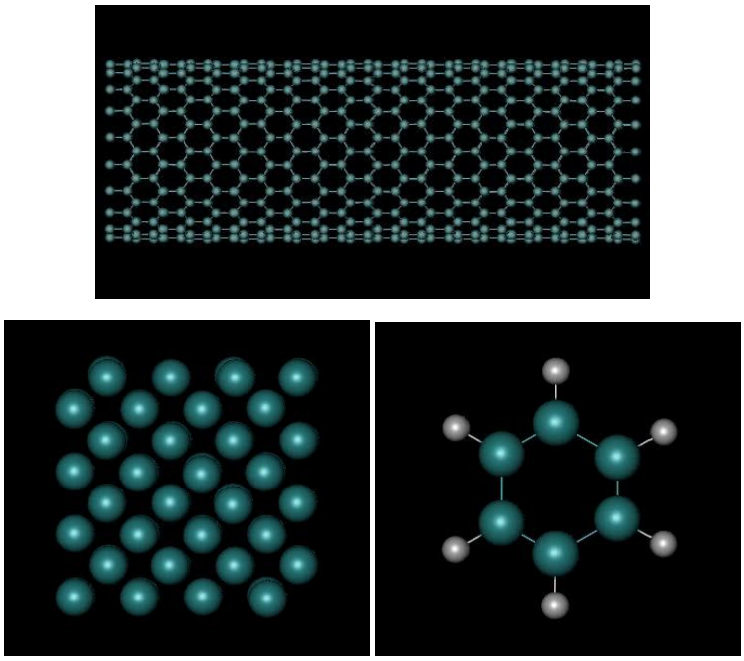


Figure 5.2: Models of the Diamond, Nanotube and Benzene tested

5.2 PDMS Model

The PDMS structure was obtained from Schneemilch [110], which was based on the model proposed by Smith et al [111] using classical parameters derived from ab initio quantum mechanical methods. In their paper the geometry of the PDMS and the partial charges on the individual atoms were calculated using a HF/6-31G(2d) method. The dynamics of the model were tested using molecular dynamics and self-diffusion coefficients, viscosities and structure factors were found to give good agreement with experimental values.

This PDMS surface (with no oxidation) was produced by compressing a linear PDMS chain with a backbone of 198 Silicon and 199 Oxygen atoms gradually between elastic boundaries at high temperature to give a surface with dimensions $x = 2.70$nm, $y = 2.70$nm, $z = 4.00$nm. Two other surfaces to imitate the effects of oxidation on the PDMS surface were derived by replacing Si-CH_3 groups on the surface with Si-OH groups. One surface was created with 16 replacements (8 on each surface of the PDMS) and another with 32 replacements (16 on each side of the PDMS). Groups were replaced closest to the surface first. The partial charges on the Silicon and Oxygen atoms in the PDMS chain are adjusted to maintain charge neutrality. The composition of all the surfaces and the simulation parameters for the PDMS atoms are described

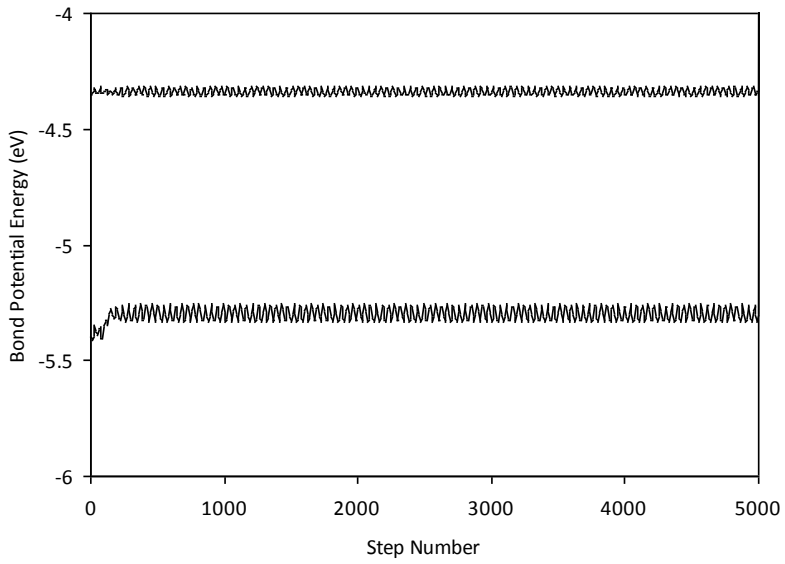


Figure 5.3: The Bond energies for the C-C and C-H bonds within the Benzene molecule

in greater detail in tables 5.2 and 5.3 below.

These surfaces have been used in the study of the wetting properties of PDMS [110]. The PDMS/Water contact angle and the line tension were measured. For the untreated surface a contact angle of 124° was measured, for the 16 oxidised, 100° and for the 32 oxidised, 76°. These values show that the surfaces become more hydrophilic upon oxidation and that the water droplets have a higher tendency to spread out and wet the surface, which agrees with that found experimentally with plasma treatment.

Water droplets on polymer surfaces have also previously been studied using molecular dynamics simulation by Hirvi et al [112]. The contact angles of water droplets on polyethylene and poly(vinylchloride) surfaces were measured.

For the flow simulations the PDMS slab was cut in half. These two halves were then placed at the top and bottom of a simulation cell. The surface atoms were fixed in position during simulations.

Bond Type	Equilibrium Bond Length (nm)
Si-O	0.165
Si-C	0.188
C-H	0.109

Angle Type	Equilibrium Bond Angle (°)
Si-O-Si	137.63
O-Si-O	105.56
O-Si-C	109.82
C-Si-C	112.44
Si-C-H	111.09
H-C-H	107.77

Table 5.2: Bond Lengths and Angles for the PDMS atoms

Atom Type	Mass (amu)	Charge (e)	Number In S_0	Number In S_1	Number In S_2
Si1	28.0	0.7608	192	178	166
Si2	28.0	0.6792	4	4	4
Si3	28.0	1.0219	0	12	20
Si4	28.0	1.2830	0	2	6
O1	16.0	-0.4620	194	168	148
O2	16.0	-0.5038	0	22	34
O3	16.0	-0.5455	0	2	6
O4	16.0	-0.5872	0	2	6
O5	16.0	-0.5300	0	16	32
C	12.0	-0.5604	396	380	364
H1	1.02	0.1370	1188	1140	1092
H2	1.02	0.2060	0	16	32

Table 5.3: Constituent Atoms For Each Surface

5.3 Fluid Models

5.3.1 Water Model

The SPC/E model for water [113] was chosen above other models such as TIP3P [114] as it gives the best results for the bulk properties of water whilst remaining a relatively simple model, thus improving computational efficiency. The model has a fixed oxygen-hydrogen bond length of r_{OH} = 0.1nm, and a fixed angle of $\angle$ HOH = 109.47°, and uses Lennard-Jones parameters of σ = 0.3166nm and ε = 0.650 kJmol^{-1}. Positive charges are placed on the hydrogen atoms with q_H = +0.4238e and a negative charge of q_O = -0.8476e is placed on the oxygen atom. The water molecules are set to be rigid and their bond lengths constrained using the SHAKE algorithm. The phase behaviour of this model is not qualitatively correct though and the freezing temperature is 60K too low [115].

Site	σ (nm)	ε (kJmol^{-1})	q(e)
O	0.3166	0.650	-0.8476
H	-	-	+0.4238

Table 5.4: Potential parameters for the SPC/E water atoms

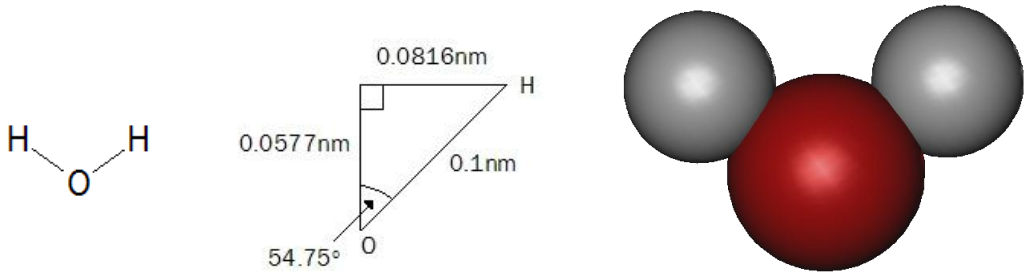


Figure 5.4: The Water Molecule

The viscosity of bulk water using this model has been calculated through the Green-Kubo relation [103]. Shown in figure 5.5 below is the autocorrelation function of the off-diagonal components of the stress tensor ($\langle\sigma_{xy}(t)\sigma_{xy}(0)\rangle$). Integrating over the length of the curve (100ps) gives the viscosity of a pure water system to be 6.3×10^{-4}Pas, which is around that expected for this model [116], but somewhat lower than the value in an experimental system (8.9×10^{-4}Pas). The self-diffusion coefficient is calculated from the mean-square displacement of the center of mass using the Einstein relation to be 2.95×10^{-9} m^2s^{-1}. Previous analysis [117] of the model gives the diffusion coefficient to be around 2.9×10^{-9} m^2s^{-1}. At 298K, the experimental value of the diffusion coefficient is 2.3×10^{-9} m^2s^{-1}. The average potential energy of the water molecule is found to be -46.662kJ/mol, also in agreement with other simulation work.

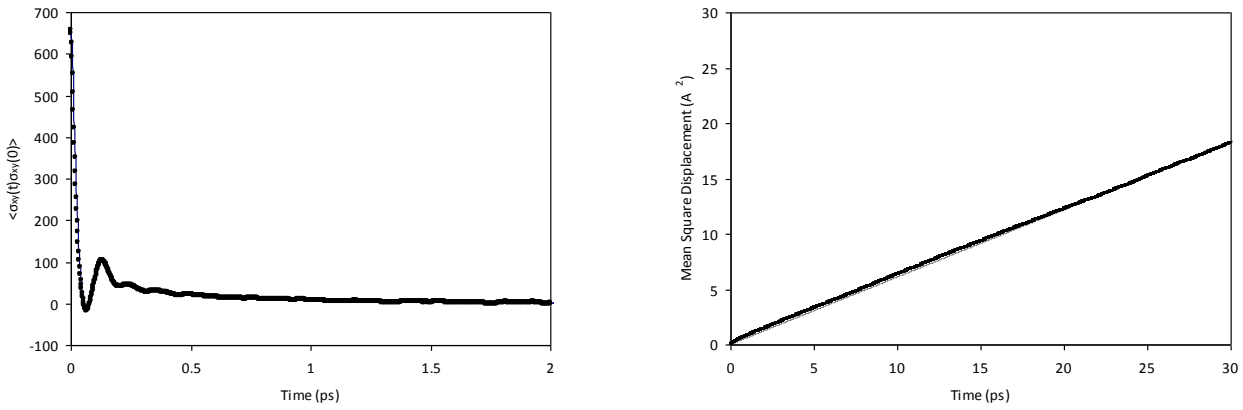


Figure 5.5: Autocorrelation Function of Stress Tensor and MSD for the Water Model

The surface tension is calculated as the difference in the normal and tangential pressures at

the interface (equation 5.7). The local pressures were calculated using both the Harasima [118] and Kirkwood [119] methods which use slightly different ways of splitting the stress into local components. The Harasima method is required to split the reciprocal space sum when using Ewald summation in both cases, but the Kirkwood method was preferred for the short range calculation due to the enhanced averaging provided. The Kirkwood formula for splitting the stress is given below (equation 5.6).

$$P_N(z) = -\left\langle \frac{1}{V_s} \sum_{i>j}^{N} \frac{|z_{s1} - z_{s2}|}{|z_{ij}|} \frac{{z_{ij}}^2}{r_{ij}} \frac{dU(r_{ij})}{dr_{ij}} \right\rangle \tag{5.6}$$

$$\gamma = \frac{1}{2} \int_{-\infty}^{\infty} [P_N(z) - P_T(z)] dz \tag{5.7}$$

An interfacial water system was generated from a bulk liquid configuration by expanding the boundaries in the z-dimension. The density profile follows the form of equation 5.8 and is pictured in figure 5.6.

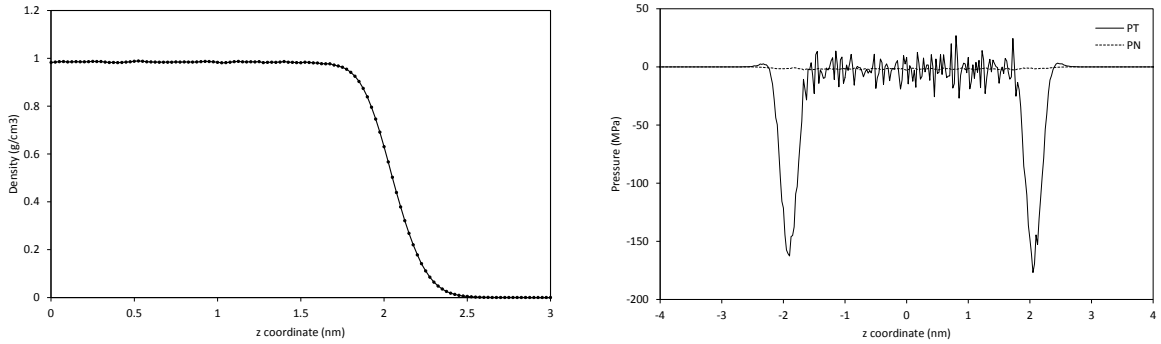


Figure 5.6: The Density and Pressure Distribution in the Interfacial Water System

$$\rho(z) = \frac{1}{2}(\rho_l + \rho_v) - \frac{1}{2}(\rho_l - \rho_v) \tanh\left[\frac{(z - z_0)}{d}\right] \tag{5.8}$$

Integration of the stress profile gives the surface tension of the water model to be around 5.1×10^{-3}mN/m. There is a wide variation in the literature values reported for the SPC/E surface tension [120], but the figure obtained is within the range.

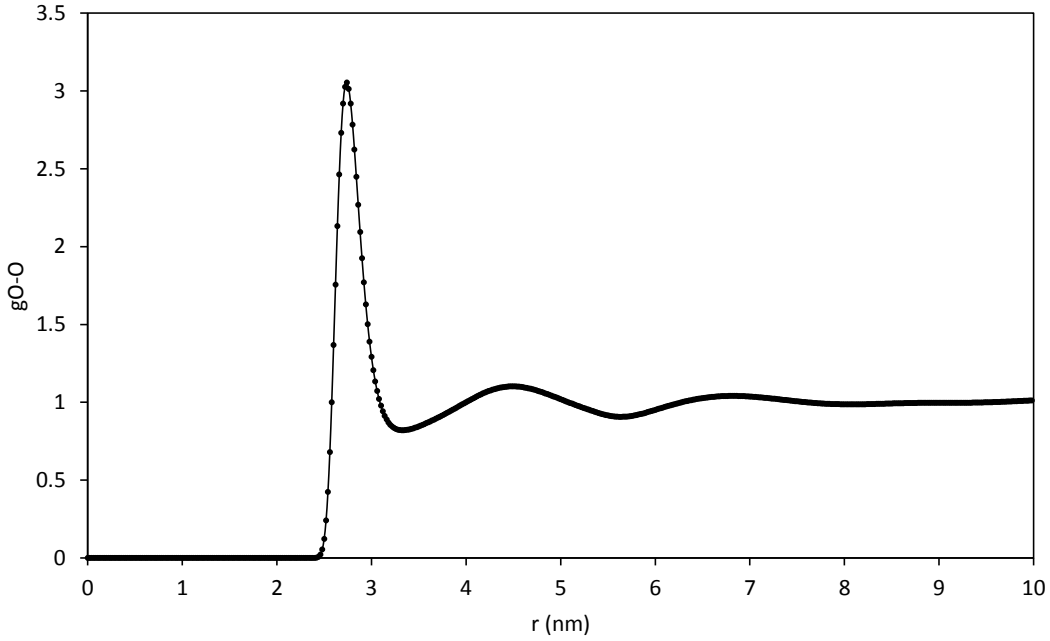


Figure 5.7: The O-O Radial Distribution Function for the SPC/E Model

5.3.2 Decane Model

A united-atom model which assumes that every CH_3 and CH_2 group in the decane model can be treated as a single interaction site was used [121]. Ignoring the Hydrogen atoms significantly reduces the computational time. Bond bending and dihedral rotations are allowed, but the bond lengths are fixed at 0.153nm.

The bond bending potential energy is represented by equation 4.31 where k_θ=519.66kJmol^{-1}rad^{-1} and the equilibrium bond angle, θ_0=114°. The torsional potential is given by equation 4.32 where A_1=2.9517kJmol^{-1}, A_2=-0.56697kJmol^{-1} and A_3=6.5793kJmol^{-1}.

Several sets of Lennard-Jones parameters based on different cut-offs appear in the original paper. Lennard-Jones parameter values for those used are shown below in table 5.5. Two different cut-off values were used, but in the simulations a 1.1nm cut-off was chosen as it seemed to give better results for the bulk properties.

Characterisation of the Diffusion coefficients, the Surface Tensions and the Viscosities of each of these bulk models was carried out and compared with the experimental quantities, these are summarised in table 5.6.

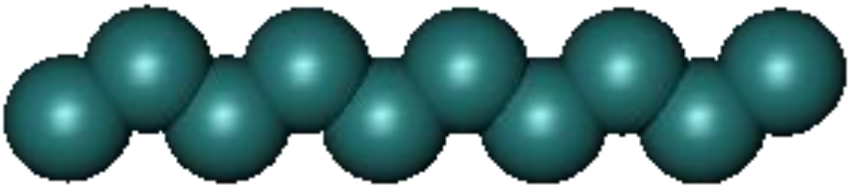


Figure 5.8: The Decane Model

Site	r_{cut} (nm)	σ (nm)	ε (kJmol^{-1})	q(e)
CH_3	0.8	0.393	1.3809	0.000
CH_2	0.8	0.393	0.5693	0.000
CH_3/CH_2	0.8	0.393	0.8866	0.000
CH_3	1.1	0.393	1.0589	0.000
CH_2	1.1	0.393	0.4366	0.000
CH_3/CH_2	1.1	0.393	0.6799	0.000

Table 5.5: Potential parameters for the Decane atoms

Fluid	D ($\times 10^{-9}$m^{2}s^{-1})	η ($\times 10^{-4}$Pas)	γ ($\times 10^{-4}$mN/m)
Water	3.043	5.845	51.039
Water EWD	2.896	6.289	51.738
Water Expt	2.30 [122]	8.941 [104]	72.050 [123]
Decane (r_c =0.8nm)	4.240	3.877	22.449
Decane (r_c =1.1nm)	4.537	4.174	23.554
Decane Expt	1.380 [124]	8.612 [125]	23.950 [126]

Table 5.6: Characterisation of the Fluid Models

5.4 Fluid-Carbon Interactions

Carbon-Fluid interactions are also based on the Lennard-Jones potential and are derived from the Lorentz-Bertholot mixing rules (equations 5.9).

$$\sigma_{ij} = \frac{1}{2}\left(\sigma_i + \sigma_j\right), \qquad \varepsilon_{ij} = \sqrt{\varepsilon_i \varepsilon_j} \tag{5.9}$$

Where i = C and j = H or O for water.

For graphite a number of water contact angles have been recorded [127]. Several values are in the range 80-90°, but also some are as low as 40°. The variation is suggested to be caused by imperfections or impurities. To choose a suitable water-carbon potential the macroscopic experimental contact angle of a droplet of water (5μL) on a flat section of vapour deposited carbon was determined (figure 5.9). Using computer analysis software the contact angle was found to be 84°, which is similar to previous graphite-water contact angles. Due to this similarity water-carbon Lennard-Jones parameters from a potential optimised for carbon-water interactions (Werder et al. [127]) were used.

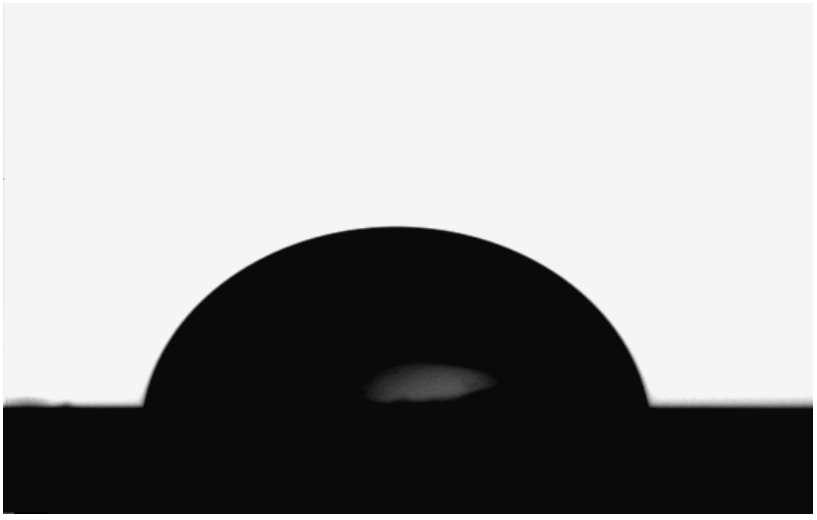


Figure 5.9: Water drop on Amorphous Carbon Surface

The decane-carbon potential has been used previously [121] and was shown to be consistent

with known experimental data for decane on carbon.

The fluid-solid interaction parameters are summarised in table 5.7.

Interaction	σ (nm)	ε (kJmol^{-1})
C(Surface)-C(Surface)	0.340	0.2330
C(Surface)-O(Water)	0.319	0.3920
C(Surface)-CH_3(Decane) (r_{cut}=0.8nm)	0.3665	0.5672
C(Surface)-CH_2(Decane) (r_{cut}=0.8nm)	0.3665	0.3642
C(Surface)-CH_3(Decane) (r_{cut}=1.1nm)	0.3665	0.4967
C(Surface)-CH_2(Decane) (r_{cut}=1.1nm)	0.3665	0.3189

Table 5.7: Interaction Parameters for the Carbon-Fluid Sites

5.5 Fluid-PDMS Interactions

PDMS-Water interactions are based on the Buckingham potential and derived from mixing rules. The parameters required for the interaction of each atom type with the oxygen atom on the water molecule (OW) are given in table 5.8 below. The water hydrogen atoms (HW) interact only electrostatically with the PDMS surface.

Atom Type	A (kJmol^{-1})	ρ(Å)	C (kJmol^{-1}Å^6)
Si1-Si4	258491.7	0.3063	5814.9
O1-O4	317331.3	0.2581	2090.7
O5	317334.2	0.2775	3927.9
C	140967.3	0.2952	2650.1
H1,H2	59316.6	0.2694	548.1

Table 5.8: Non bonded potential parameters for the PDMS system

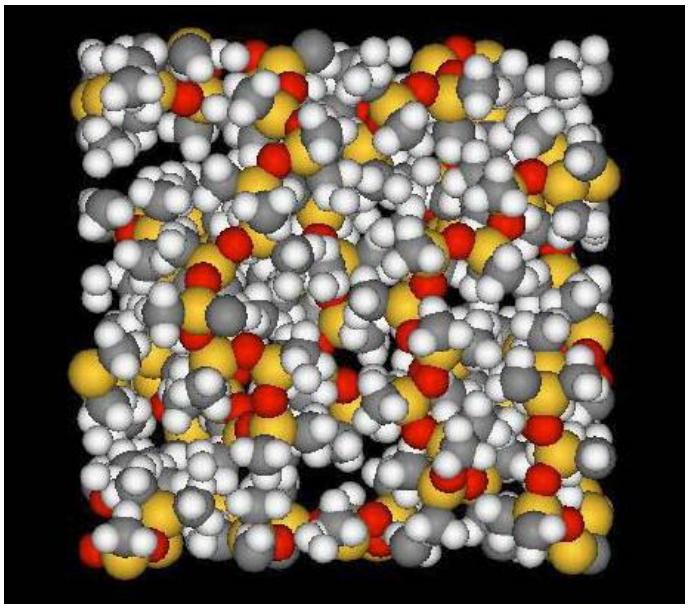


Figure 5.10: The PDMS Surface

5.6 Fluid Flow Simulation Parameters

The simulations were all carried out within the canonical ensemble (NVT). The temperature was set to 300K and the Nose-Hoover thermostat (equation 4.16) used to maintain this temperature. The velocity Verlet integration scheme (equation 4.7) was used to update the trajectories with an integration time of 2fs. Periodic boundary conditions were applied to the system. The Nose-Hoover relaxation time was set to 0.05ps, which determines the mass of the heat bath and thus the strength of the temperature control. In most simulations the standard deviation in the temperature is around ±3K and the pressure ±5MPa.

When using the potential functions cut-offs were applied to simplify the calculations with $u(r_{ij}) = 0$ for $r_{ij} > r_{cut}$, where $r_{cut} = 1.0\text{nm}$ ($\approx 3\sigma_{wf}$). Cell division of the simulation box and neighbour lists were used in order to achieve greater computational efficiency when calculating intermolecular forces. Ewald summation (equation 4.24) was used to calculate Coulombic forces with α=0.25 and k_x, k_y and k_z around 5 typically. Extra vacuum was added between the two outer surfaces and equation 4.28 was used in order to reduce self interaction in the z-dimension.

The molecular dynamics formulae (Chapter 4) were converted to computational algorithms using

the C++ language and then tested on some standard systems, a sample of this force code can be seen in the appendix. The DL_POLY [128] molecular dynamics program was also used for some initial simulations, with modifications made to the program source code in order to calculate and output the necessary results. VMD [129] was used to generate molecular models of the system and videos of the simulation. Simulations were run on Intel Xeon E5345 2.33GHz processors in machines supplied by IBM. Flow simulations were integrated for around 5-10ns which took 2-3 weeks in most cases.

Chapter 6

Results I - Fluid Flow in Nanopores

6.1 Carbon Slit Pores

The fluid-flow equations were tested and the slip coefficients calculated for a number of systems of experimental interest. The relations between equilibrium and non-equilibrium dynamics were considered and in order to compare results with experiment, several different carbon surfaces were simulated. Graphene was simulated as a rigid planar sheet, with a fixed C-C bond length of 0.142nm. A crystalline diamond surface was also simulated. Two surfaces were created for the graphene and diamond systems and these placed at the $\pm$z-coordinate needed to give the desired internal diameter. Fluid was added to the space between the surfaces to liquid density and then the number of water molecules adjusted to achieve an atmospheric pressure.

An amorphous carbon surface was also formed by melting the diamond lattice and gradually freezing it again once molten. The initial $5.0 \times 5.0 \times 2.0$ nm^3 lattice of 6000 carbon atoms was raised in temperature to 10,000K and then left for 50,000 steps at this elevated temperature. The system was cooled gradually over 200,000 steps and then once back to 300K left to equilibrate for a further 500,000 steps and subsequently the atoms frozen into position. The slab of amorphous carbon was cut in half and the fluid added to liquid density at room temperature in between the two blocks which had been set at the required distance apart. Many different pore widths have been looked at with 1nm being the smallest (which is approximately 3σ) and 42nm the largest – which is on par with the experimental size.

6.1.1 Characterisation of the Surfaces

Firstly the structure of each surface was explored using a probe water molecule. Measurements of the surface's roughness were performed by scanning a water molecule over the surface and finding its equilibrium position according to the force it experiences normal to the surface as a function of x and y coordinate. The water molecule was oriented with the oxygen atom pointing towards the surface. The force follows a '12-6 potential' style shape, i.e. it reaches a minimum and then becomes repulsive. The point at which it changes sign from negative to positive corresponds to the minimum in the potential and this point was taken as the surface location. A picture of the whole surface was derived by repeating this procedure at x and y positions 0.05nm apart above the surface.

The average equilibrium position of a water molecule across the surface was then taken to be the average of the point of the potential minimum between the probe molecule and the carbon atoms at an array of grid points across each surface and the roughness the standard deviation in this position.

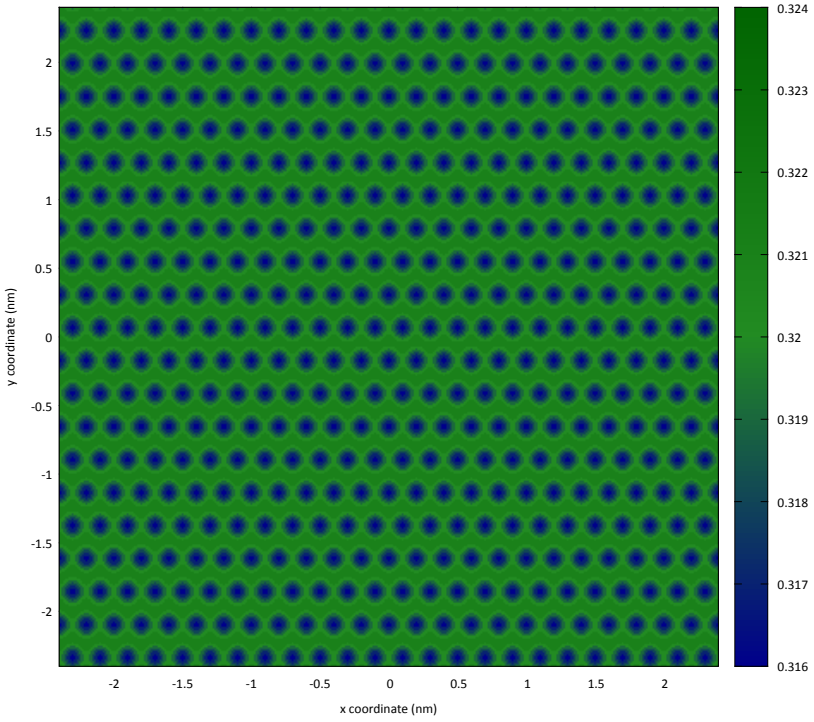


Figure 6.1: The Graphene Surface

The roughness values for graphene, diamond and the amorphous surface were measured in this way. The graphene surface was found to be extremely smooth, having a very regular structure

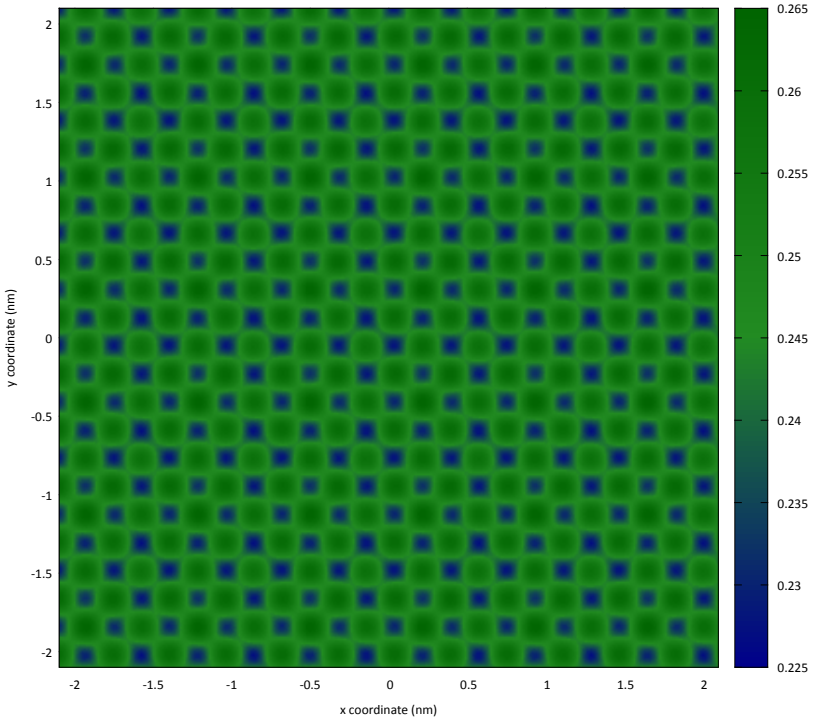


Figure 6.2: The Diamond Surface

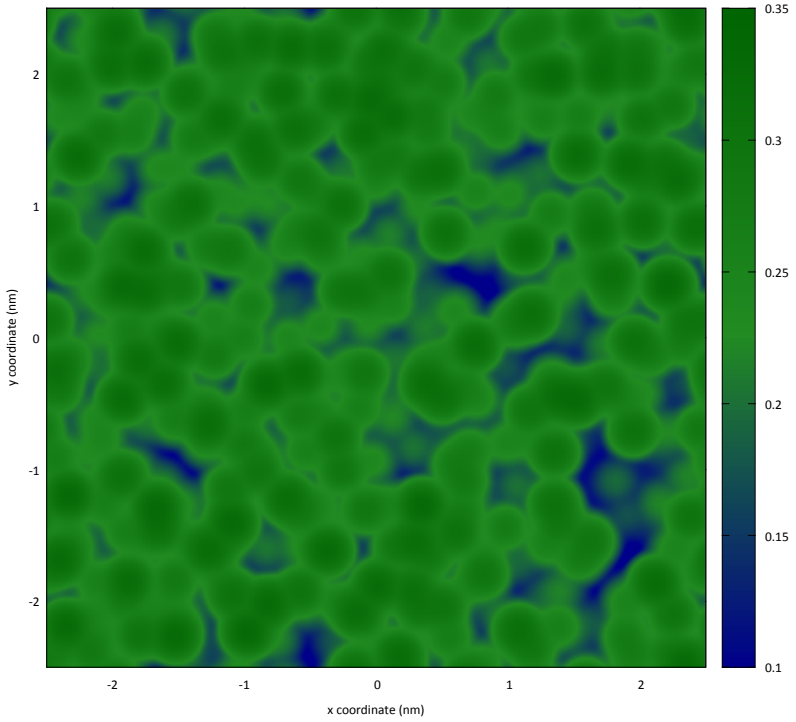


Figure 6.3: The Amorphous Carbon Surface

with few surface features apart from small minima above each ring. The profile for graphene is shown in figure 6.1 as the surface of minimum potential, with surface dimensions of $L_x = 4.8$nm and $L_y = 4.8$nm. The plot for the diamond surface is still very regular (figure 6.2) but

shows a roughness value of 0.008nm, five times that of the graphene. In this case $L_x = 4.3$nm and $L_y = 4.3$nm. The amorphous carbon surface is much rougher than the other two, with a roughness value of 0.042nm obtained which is thirty times that of graphene and five times that of diamond. The amorphous carbon surface structure is shown in figure 6.3. The dimensions of the carbon slab in this case are $L_x = 5.0$nm and $L_y = 5.0$nm giving a total surface area of 25.0nm^2.

Surface	Average Position (nm)	Standard Deviation (nm)
Graphene	0.3195	0.0014
Diamond	0.2468	0.0081
Amorphous Carbon	0.2486	0.0419

Table 6.1: Characterisation of the Carbon Surfaces

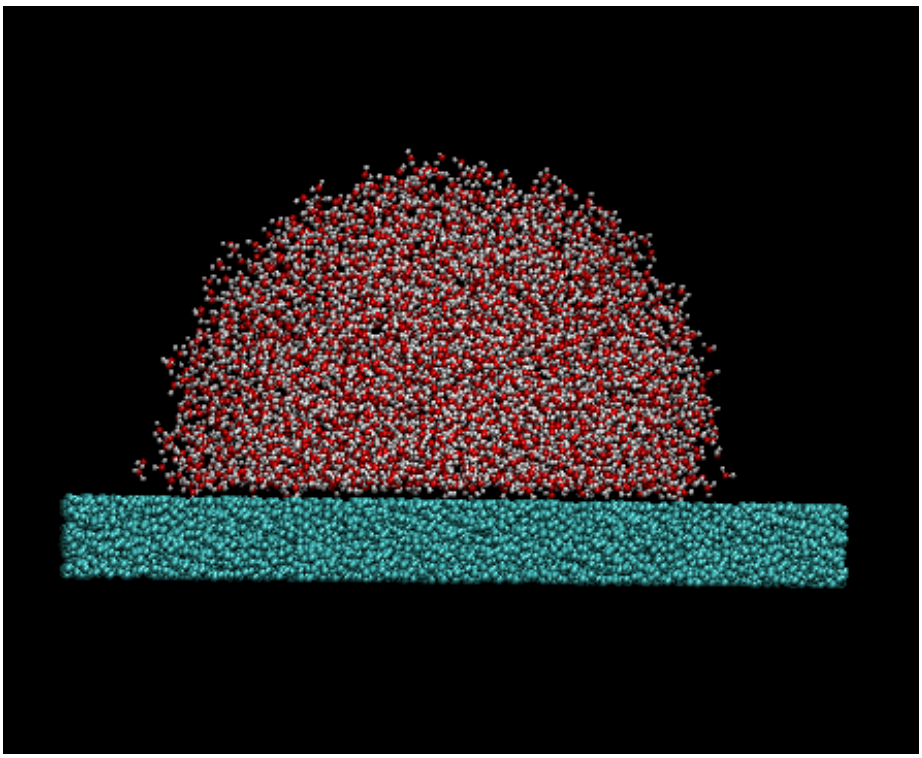


Figure 6.4: Water drop on Amorphous Carbon Surface

The contact angles for water droplets on these surfaces were also calculated. A droplet of 4000 water molecules on the surface was simulated (figure 6.4) and the radial density profile determined (figure 6.5). From this the interface can be examined and a plot of the average equimolar dividing surface (figure 6.6) is used to calculate the contact angle trigonometrically via a straight line fit. The radius of the drop is around 3nm. As the interaction between the fluid/solid becomes weaker, so the contact angle of the liquid on the substrate increases. Figure 6.5 below shows the density of the droplet which has been averaged radially over several hundred

thousand steps. At the equimolar dividing surface (in this case 0.5g/cm^3) it can be seen that the contact angle is around 95°. Graphite is seen to be slightly more hydrophilic than the diamond and amorphous surfaces.

These values for the contact angle have not been corrected for the line tension (equation 6.1), which was found in previous water/carbon droplet studies [127] to be positive and around 0.25 nJ. The contact angle will also be affected by the roughness of the surface.

$$\cos\theta \ = \cos\theta_\infty \ - \frac{\tau}{r\gamma_{lv}} \tag{6.1}$$

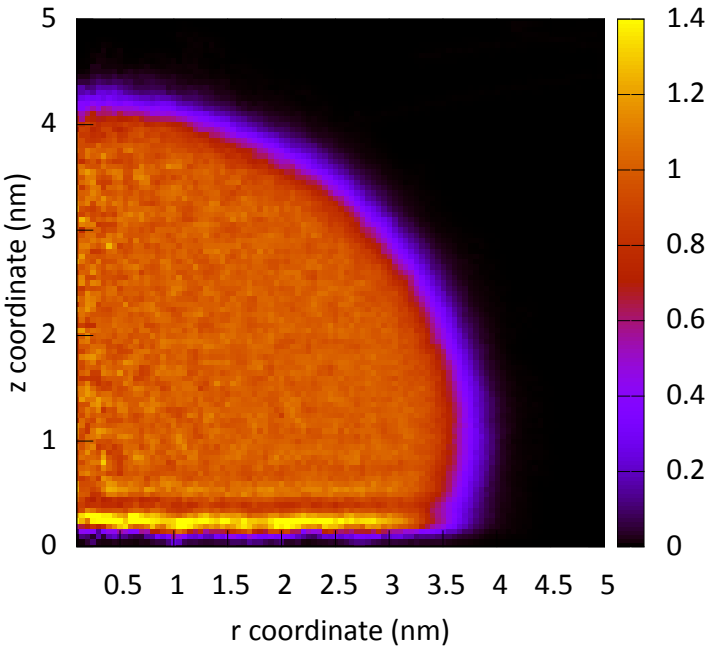


Figure 6.5: Simulated Water drop on Amorphous Carbon Surface

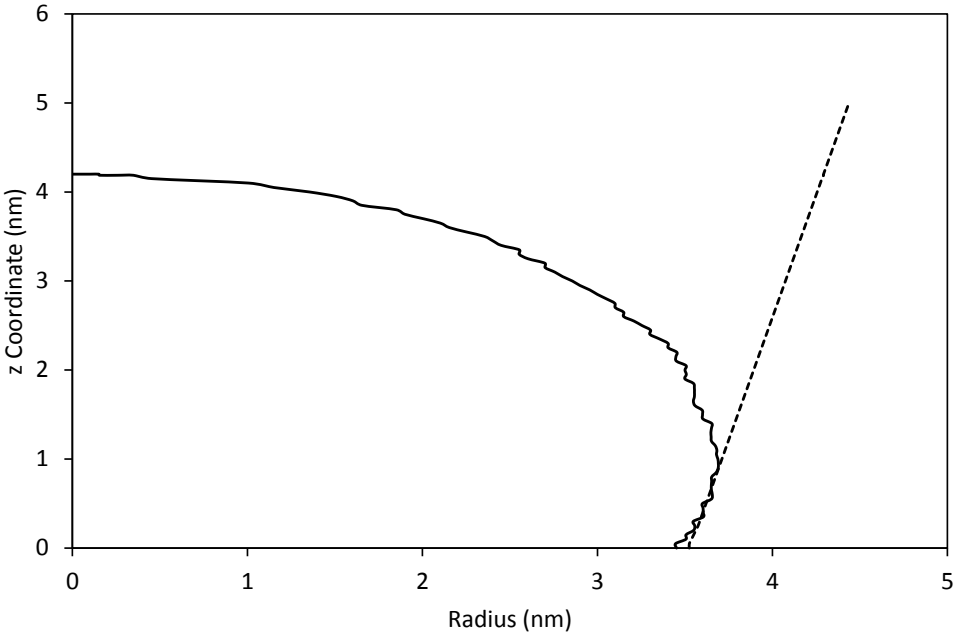


Figure 6.6: The Fit to the EMDS for the Determination of Contact Angle

6.1.2 Equilibrium Molecular Dynamics Simulations (EMD)

Equilibrium simulations were carried out in these water/carbon pores. After equilibration for 500,000 steps the simulations were run for 2,500,000 steps (5ns) at a rate of around 7000 steps per hour of CPU time using a 2.5GHz Intel Xeon processor. Profiles of the fluid properties along the z-axis were obtained by dividing the pore volume into N bins of dimension $L_x \times L_y \times (L_z/N)$. These bins were chosen to have a volume of 5.0 × 5.0 × 0.05 nm^3. The properties in each bin were then calculated by summing the necessary physical quantity in the bin and then weighting by the number density within the bin.

$$P(r,t) = \frac{\sum_{i \epsilon bin}^{N} P_i(r,t)\,\delta(r - r_i(t))}{\sum_{i \epsilon bin}^{N} n_i(r,t)\,\delta(r - r_i(t))} \tag{6.2}$$

After equilibration a density profile across the pore was determined. The density profile exhibits two regions - bulk like uniform density in the center of the pore and a non-uniform interfacial region next to the walls. Near the wall, the fluid experiences a potential from the wall and responds to this, the water molecules preferentially occupy positions within the minimum of this potential. The average potential energy per water molecule is shown in figure 6.7, this

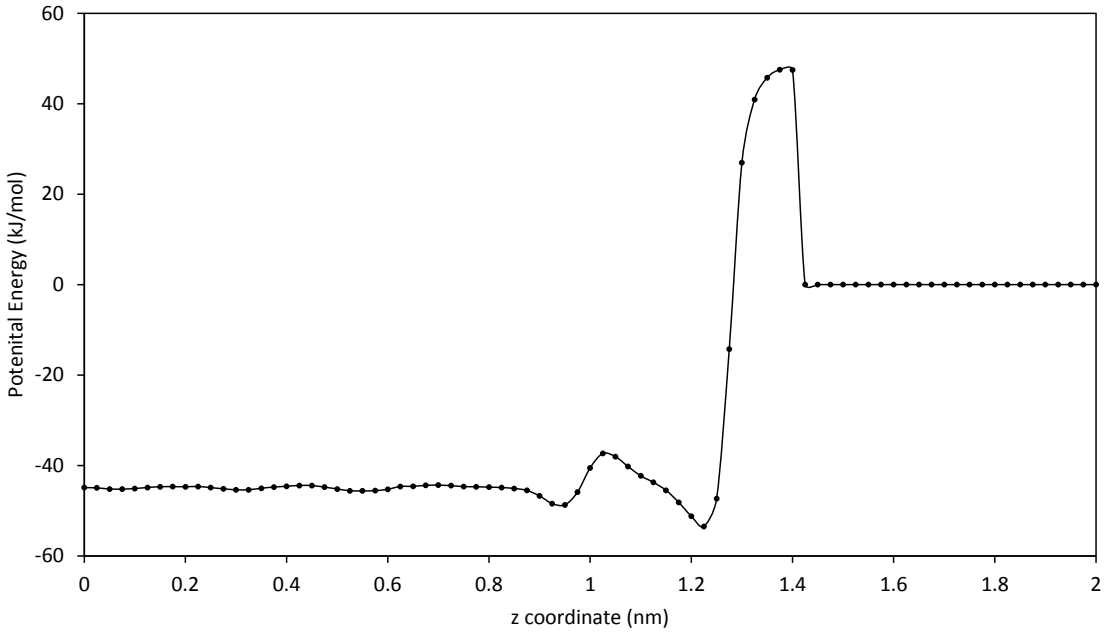


Figure 6.7: The Potential Energy per Molecule Along the z-axis

demonstrates the inhomogeneity in the pore and shows a sharp increase in potential energy at the walls. An example of the density profile of the fluid along the axis perpendicular to the surface of the pore is depicted in figure 6.8 for the amorphous carbon system. The density varies along the z axis and is thus not constant (an assumption used in the Navier-Stokes equations).

The boundary layer is defined as the region below the first minimum in the density profile and the start of the solid. The boundary layer is therefore about 0.4nm wide in the amorphous carbon pore pictured (figure 6.8). In the carbon-water systems studied there is little penetration of water below the surface layer. In fact, a depletion layer is seen (about 0.2nm) with very little water next to the surface. It has been seen previously [130] that the hydrodynamic position of the wall is located inside the fluid typically one atomic distance away from the outer layer of solid atoms. For smoother surfaces the boundary layer is a little shorter.

The dimension of the fluid is therefore ill-defined in the z direction due to this depletion layer. This effect is minimal for macroscale systems but has a big effect on the flow dimensions on the nanoscale. In the carbon/water systems due to this depletion layer the actual flow diameter is lower than the distance between the two surfaces. The value of h in the simulations is therefore taken to be from the center of the pore to the equimolar dividing surface (EMDS). This point

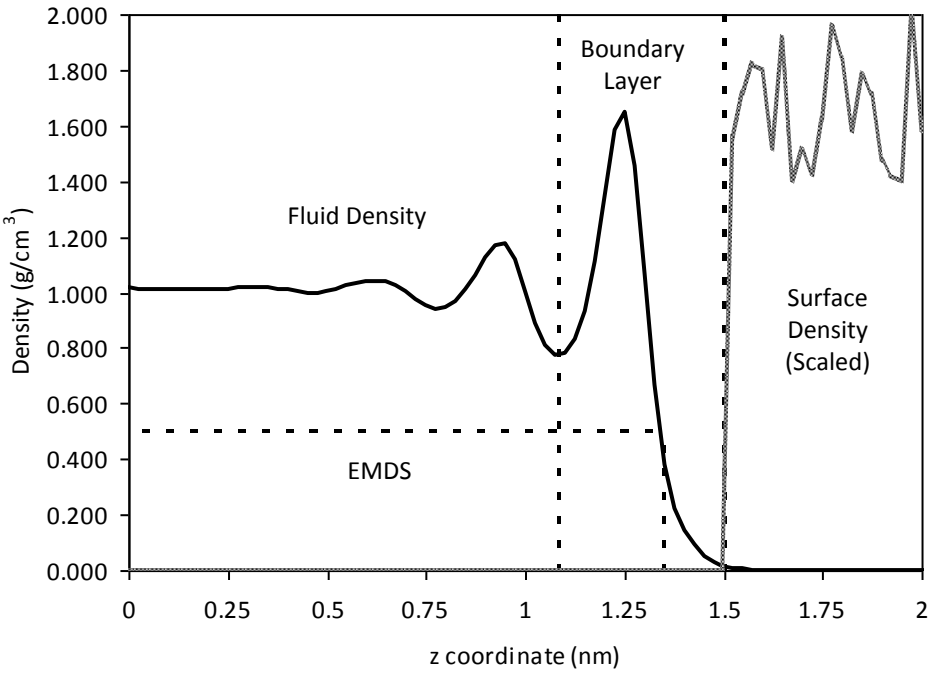


Figure 6.8: Fluid Density profile showing the EMDS and the calculation of h

is defined to be where the fluid density drops to half of its value in the bulk (figure 6.8). The fluid volume was also taken to be the area of the walls multiplied by this value of h in the z dimension.

In the equilibrium simulations the velocity of the center of mass of the fluid fluctuates as the simulation progresses as depicted below in figure 6.9. Over the course of the simulation though, as no external force has been applied, the center of mass velocity should be normally distributed about zero, as proven in figure 6.10. The rate of this fluctuation is related to the friction at the interface and leads to a relaxation time (equation 3.32), which can be calculated from an analysis of the decay of the collective velocity autocorrelation function (figure 6.11).

Further, using these relaxation times the slip length in the pores can be predicted under flow conditions using equation 3.38.

The pressure in the pore was obtained as a function of z using a similar procedure to that for the interfacial water system earlier. The pressure distribution in the system is sharply peaked at the interface reflecting the peak in the density, as shown in figure 6.12 for the graphene system. This inhomogeneity and sharp increase at the interface have been suggested as potentially useful in enhancing reactivity in miniaturised systems [131].

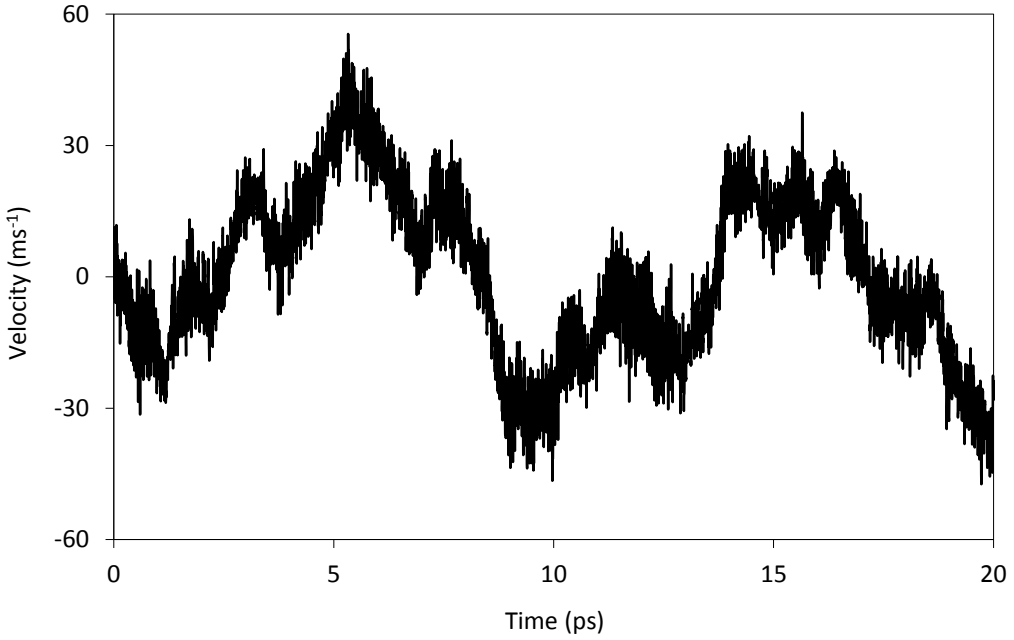


Figure 6.9: The Fluctuations in the Center of Mass velocity in the system

As shown earlier the velocity of the center of mass fluctuates with time. An attempt was made to collect velocity profiles of the fluid when the center of mass velocity was moving in certain directions, which should be equivalent to a system under flow conditions. An attempt to calculate Maxwell's coefficient using equation 3.24 was also made. To test this several different velocity bounds were looked at and velocity profiles for molecules colliding with the wall and a velocity profile for all molecules as a function of z coordinate derived in each case. Flow profiles can be obtained but they are not parabolic. In a normal non-equilibrium simulation the center of mass velocity is constant and therefore there is no acceleration, this is not the case in the equilibrium simulation, the center of mass velocity varies and so the acceleration is always changing.

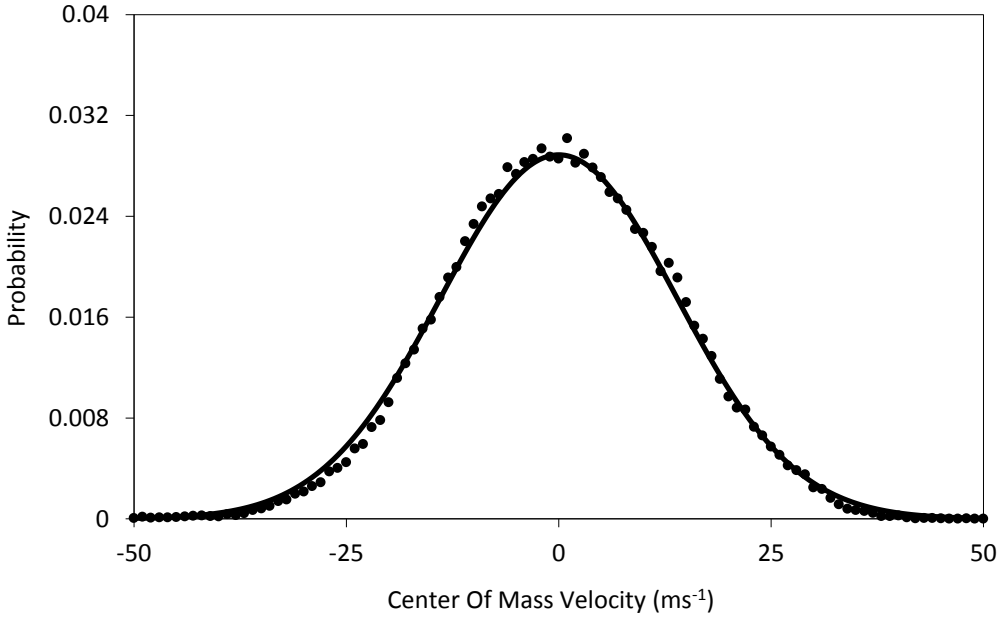


Figure 6.10: The distribution of velocities is Gaussian

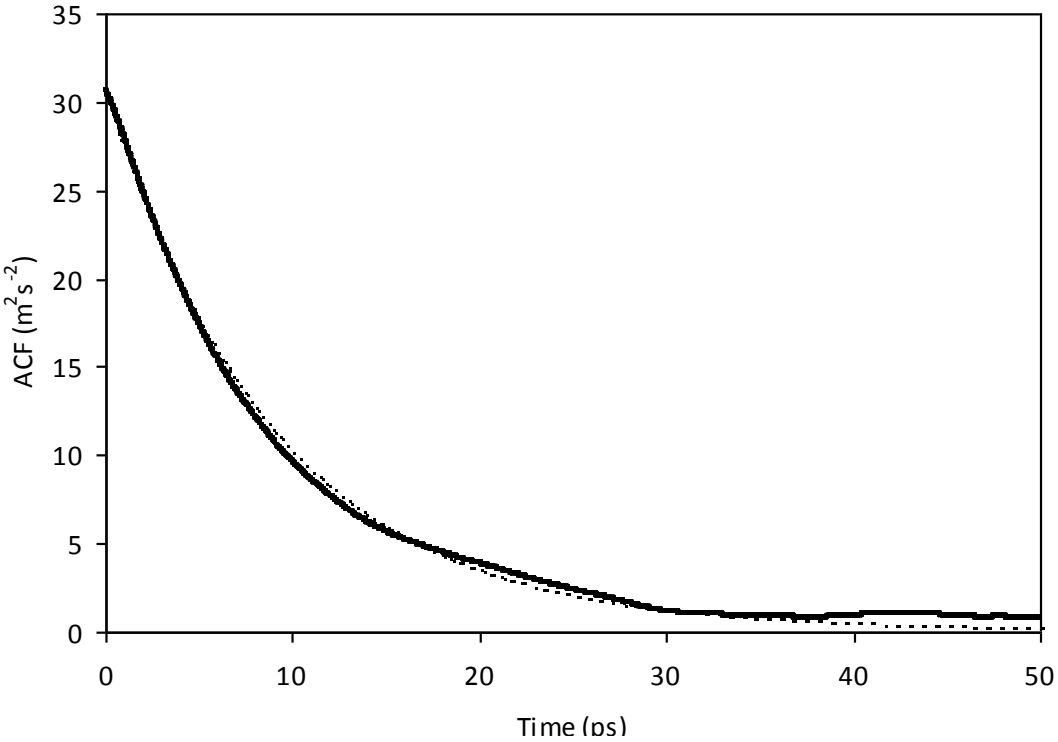


Figure 6.11: The velocity autocorrelation function in the 6nm Water system with fit

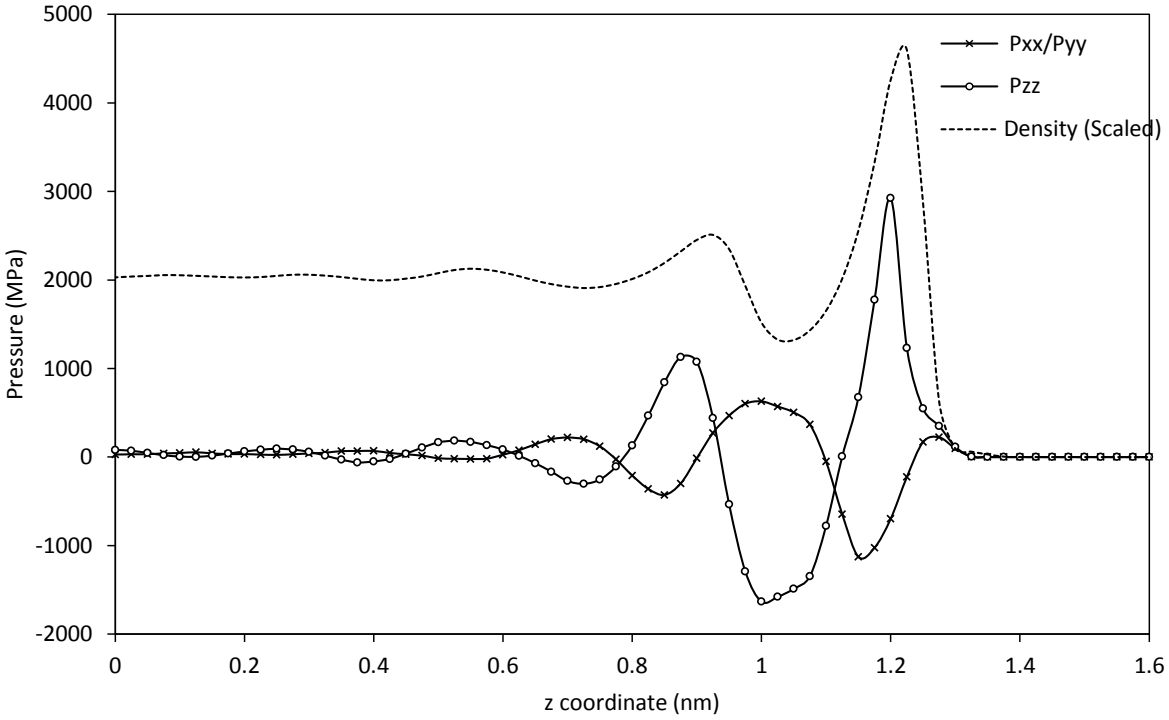


Figure 6.12: The Pressure Profile in the Graphene System

6.1.3 Non-Equilibrium Molecular Dynamics Simulations (NEMD)

The systems were also perturbed from an equilibrium state using an external field. Flow simulations in each pore were firstly conducted under the influence of a uniform gravitational field. Each simulation was run for at least 2,500,000 steps, i.e. 5ns, after 500,000 equilibration steps. During NEMD simulations, when an external gravitational field was employed to induce flow, the streaming velocity was subtracted before application of the thermostat.

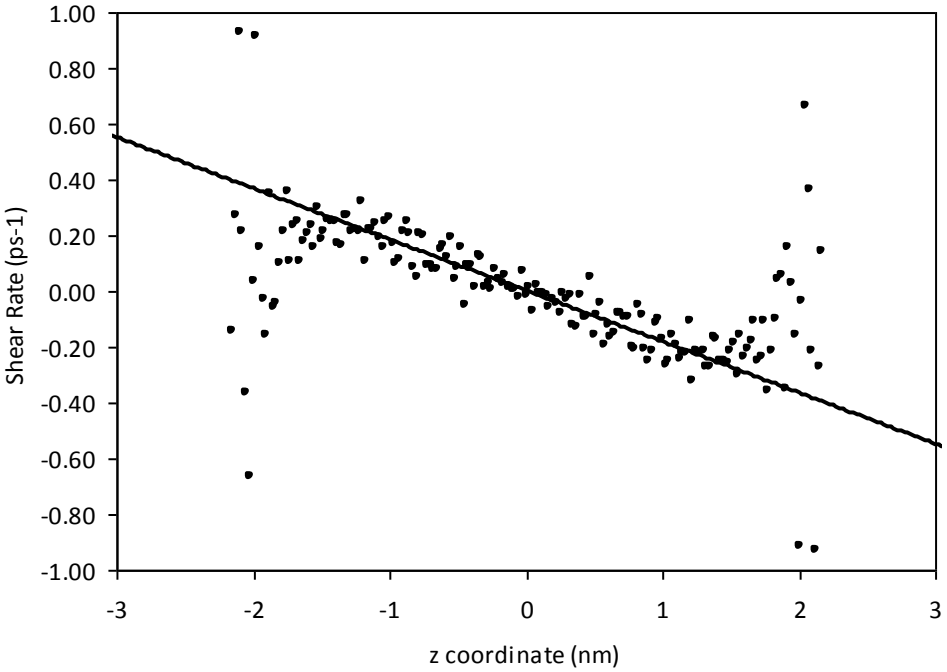


Figure 6.13: The shear rate across the pore in the 4nm Amorphous Carbon system

Gravitational field values were typically chosen in the range 0.01 to 0.05 $\times 10^{14}$ ms^{-2} to maintain mean flow velocities in the range from 3ms^{-1} to 40ms^{-1}, which varied depending on the surface and were much lower for graphene. At these flow rates the velocity profile is parabolic, the flow is linear (figure 6.22) and the viscosity of the water can be calculated by fitting a parabolic expression for the laminar flow profile. A steady state has been reached when there is a balance between shear forces and the external force. These values are high enough to generate an accurate profile whilst minimising fluctuations due to thermal noise. The thermal velocity of water is around 340ms^{-1} at 300K, much higher than fluid velocities in experiments. Average velocities less than 3ms^{-1} are difficult to obtain in the time scales used in these simulations as very long simulation times are required due to these thermal fluctuations, and higher flow rates cause

non-linear effects. The mean fluid velocities in experiments are around 0.0002ms^{-1} [45]. The fact that the flow rate is linear as a function of the external force means that the conclusions found here should be equally applicable to the lower flow rates which would be found in an experiment. The Reynolds number was found to be around 0.1 in a typical simulation, well within a laminar flow regime.

The local shear rate has been determined from the gradient of the velocity profile data and of its fit and shown below in figure 6.13. It is linear in the center of the pore as expected from the earlier equation, but shows non-linearity at the interfaces.

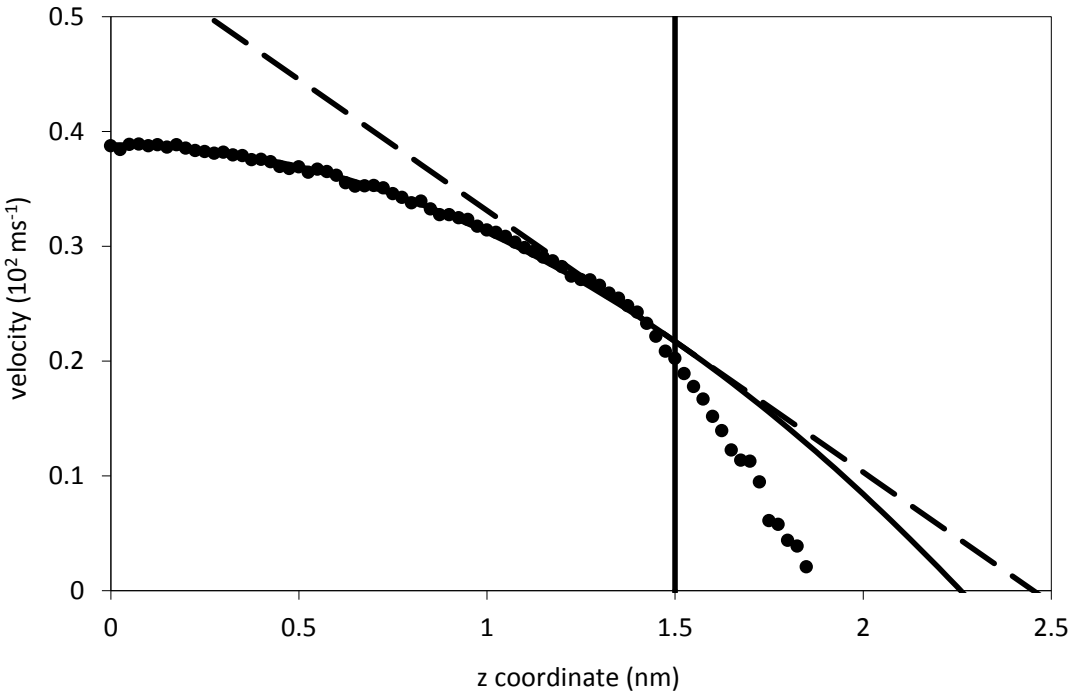


Figure 6.14: The Slip Coefficient calculation

The velocity profiles inside the pores were obtained by dividing the z-axis into bins and summing the velocity in each according to equation 6.3. These are shown in figure 6.21 for a range of values of the external gravitational force in the amorphous system. The simulated profiles fit the expected classical equation except in the regions closest to the wall, therefore fits were only performed using data from the center of the pore where the density is constant. Volumetric flow rates were found by integrating the velocity profile over the cross-sectional area. The methodology for determining the slip coefficient is displayed in figure 6.14. The gradient of the velocity profile at the wall is determined and the slip coefficient calculated from this.

$$u_{slab}(x) = \frac{1}{M} \sum_{i \epsilon slab} m_i v_{ix} \tag{6.3}$$

The relaxation time of the center of mass velocity in the pore is linked to the average flow velocity in the non-equilibrium simulations by equation 3.36. Relaxation times have been calculated for each value of gravitational field strength and averaged.

A collision is defined as occurring when the z component of the particles center of mass velocity reverses during a timestep and the particles center of mass position is close to the wall. When a collision occurs the previous 250 particle positions and the next 250 particle velocities are stored and then averaged over all colliding particles to achieve the temporal profiles. The velocity profiles of particles colliding with the wall exhibited a single peak in velocity approximately 0.05 ps before collision. After collision the particles lost a fraction of their streaming velocity due to the collision with the wall, before regaining it through viscous drag force exerted by the boundary layer. The difference in the peak streaming velocities before and after collision is then related to the Maxwell coefficient through equation 3.24.

6.1.4 Graphene Surfaces

A graphene pore of width 3nm was simulated first. 2036 water molecules were added between the two sheets to give a pore of width 3nm at atmospheric pressure, which is pictured (figure 6.15).

Graphene is an example of an extremely smooth surface and the data obtained reflect this. The EMD relaxation time of the center of mass velocity is very long with a value of 147.65ps suggesting very low interfacial friction. The slip length calculated from formula 3.38 was then 69.66nm. The NEMD flow profiles are found to be essentially flat rather than curved (figure 6.16). The flatness of the profile makes it difficult to obtain a perfect fit to the data and very small deviations in the fitting parameters make a big difference to the overall slip coefficient. The average slip coefficient from the NEMD flow profile data is shown in table 6.2 and was found to be 71.22nm, in good agreement with the EMD value. A slip length of this size would give a flow enhancement of around 150 times compared to non-slip flow.

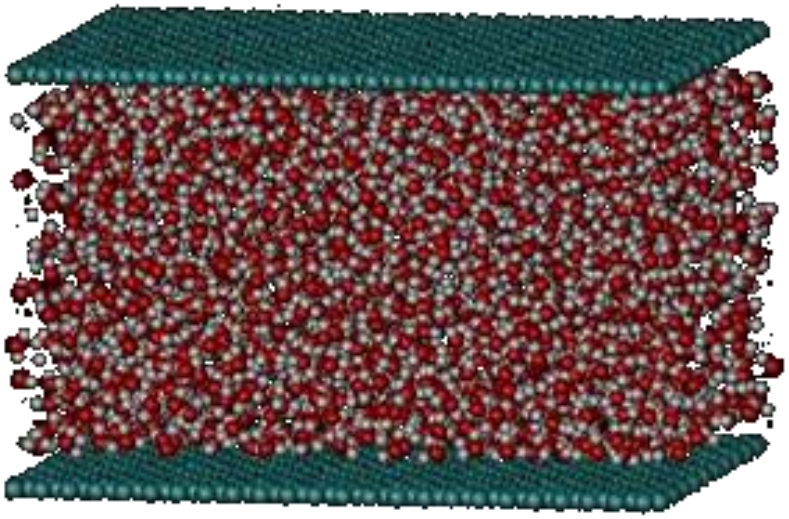


Figure 6.15: The Graphene System

g (10^{14}ms^{-2})	u_{av} (ms^{-1})	u_s (ms^{-1})	l_s (nm)	η (10^{-4} Pas)	τ (ps)	Q (10^{-17}m^{3}s^{-1})	ε
0.001	15.2796	15.2133	74.514	6.367	152.80	22.003	150.03
0.0015	21.6743	21.6092	71.858	6.484	144.50	31.211	144.72
0.002	28.1351	28.0426	65.680	6.089	140.67	40.051	132.36
0.003	46.3110	46.1736	72.808	6.149	154.37	66.687	146.62
Average	-	-	71.215	6.272	148.085	-	143.43
St Dev	-	-	3.850	0.185	6.572	-	7.70

Table 6.2: Graphene Slit Pore NEMD Data

6.1.5 Diamond Surfaces

Another allotrope of carbon, diamond was investigated next. The roughness is four times higher and the surface density is also increased relative to the graphene. For anisotropic surfaces fluid flow was generated in two different directions in order to test the effect. The pore diameter, d was again equal to 3nm. The number of water molecules added was 1713 in this case. The EMD slip coefficient and relaxation time were found to be much smaller than those for graphene at l_s=3.09nm and τ=7.01ps. The flow profile is seen to have a parabolic shape. NEMD data (table 6.3) gives similar values to the EMD again.

An attempt was also made to calculate Maxwell's coefficient in this system using equation 3.24. The velocity profiles of colliding particles exhibited an increase in velocity approximately 0.05ps

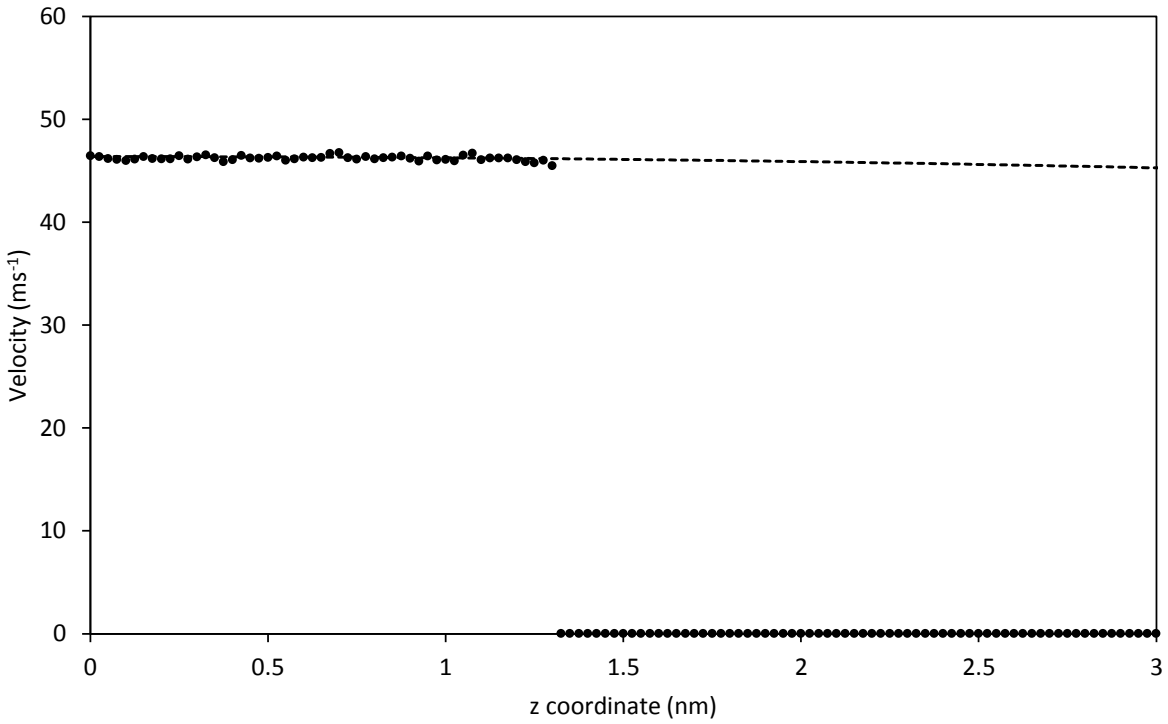


Figure 6.16: The Graphene Flow Profile

before collision with the wall, due to acceleration through the depletion layer. After the collision the fluid molecules, on average, lost a fraction of their streaming velocity before regaining it when rejoining the boundary layer fluid. The difference in the peak streaming velocities before and after collision is related to the Maxwell coefficient through equation 3.24, which in this case gives a value of 0.0478, which is relatively low. An example of one of these profiles is shown in figure 6.17.

g (10^{14}ms^{-2})	ΣF_{wf} (pN)	u_{av} (ms^{-1})	u_s (ms^{-1})	l_s (nm)	η (10^{-4} Pas)	τ (ps)	Q (10^{-17}m^{3}s^{-1})	ε
0.02(x)	-53.056	14.792	12.808	2.906	6.126	7.396	19.082	6.812
0.03(x)	-77.040	22.676	19.648	2.920	6.019	7.559	29.252	6.840
0.04(x)	-102.584	30.275	26.156	2.858	5.899	7.569	39.055	6.716
0.05(x)	-127.429	39.904	35.191	3.089	5.986	7.423	51.476	7.178
0.03(y)	-76.734	22.717	19.524	2.753	5.710	7.572	29.305	6.506
0.04(y)	-103.713	29.169	25.217	2.872	6.149	7.292	37.628	6.744
0.05(y)	-130.940	38.921	33.719	2.917	5.839	7.784	50.208	6.834
Average	-	-	-	2.902	5.961	7.513	-	6.804
St Dev	-	-	-	0.104	0.157	0.159	-	0.201

Table 6.3: Diamond Slit Pore NEMD Data

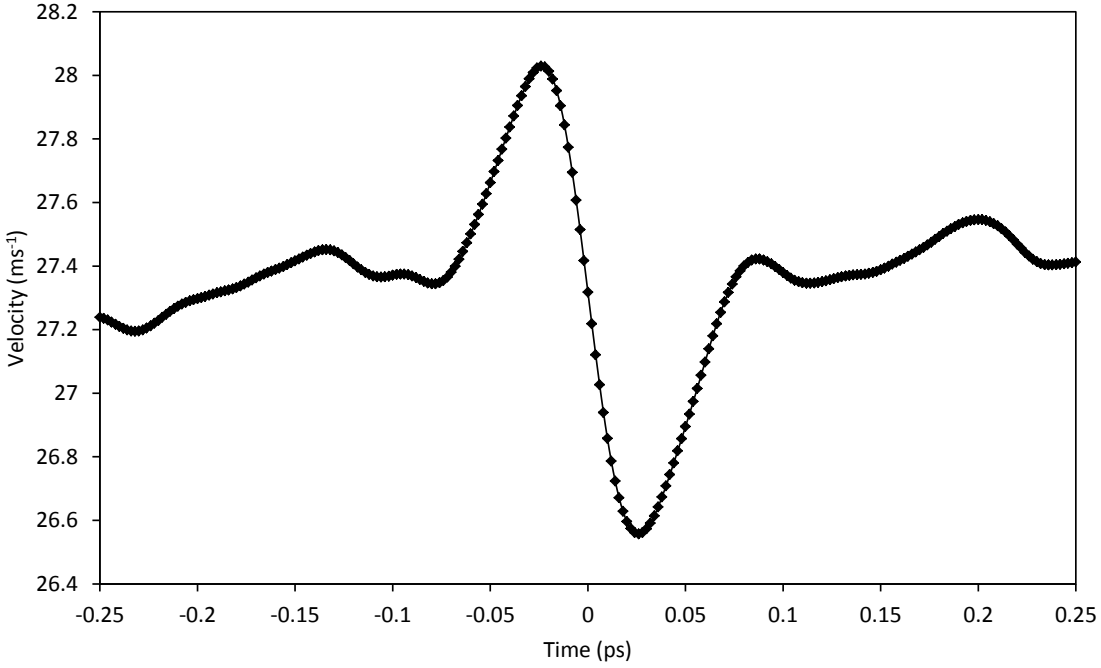


Figure 6.17: Tangential Velocity Profile in the 3nm Diamond System

6.1.6 Mobile Diamond Surfaces

The same Diamond systems were also modified to allow the surface atoms to move. The Tersoff-Brenner potential was used for the Carbon-Carbon interactions and a small tethering force was added to each atom to ensure the integrity of the surface was maintained. The solid atoms and water molecules were coupled to two separate Nose-Hoover NVT thermostats with τ=0.05ps and T=300K. Both EMD and NEMD simulations were again conducted. The relaxation time in the EMD case was found to be 8.284ps and the slip coefficient 3.579nm. The NEMD results are shown in table 6.4. A modest increase in the relaxation times and the slip coefficients are seen relative to the frozen surfaces.

g (10^{14}ms^{-2})	ΣF_{wf} (pN)	u_{av} (ms^{-1})	u_s (ms^{-1})	l_s (nm)	η (10^{-4} Pas)	τ (ps)	Q (10^{-17}m^{3}s^{-1})	ε
0.025	-63.732	19.862	17.370	3.021	5.652	7.945	25.622	7.042
0.03	-76.883	23.062	20.576	3.724	7.029	7.688	29.750	8.448
0.035	-89.479	27.978	24.444	3.113	6.017	7.994	36.092	7.226
0.04	-102.213	32.477	28.134	2.915	5.595	8.119	41.895	6.830
0.05	-127.869	41.222	36.471	3.454	6.393	8.244	53.176	7.908
Average	-	-	-	3.245	6.197	7.998	-	7.491
St Dev	-	-	-	0.335	0.709	0.209	-	0.671

Table 6.4: Mobile Diamond Surface Slit Pore NEMD Data

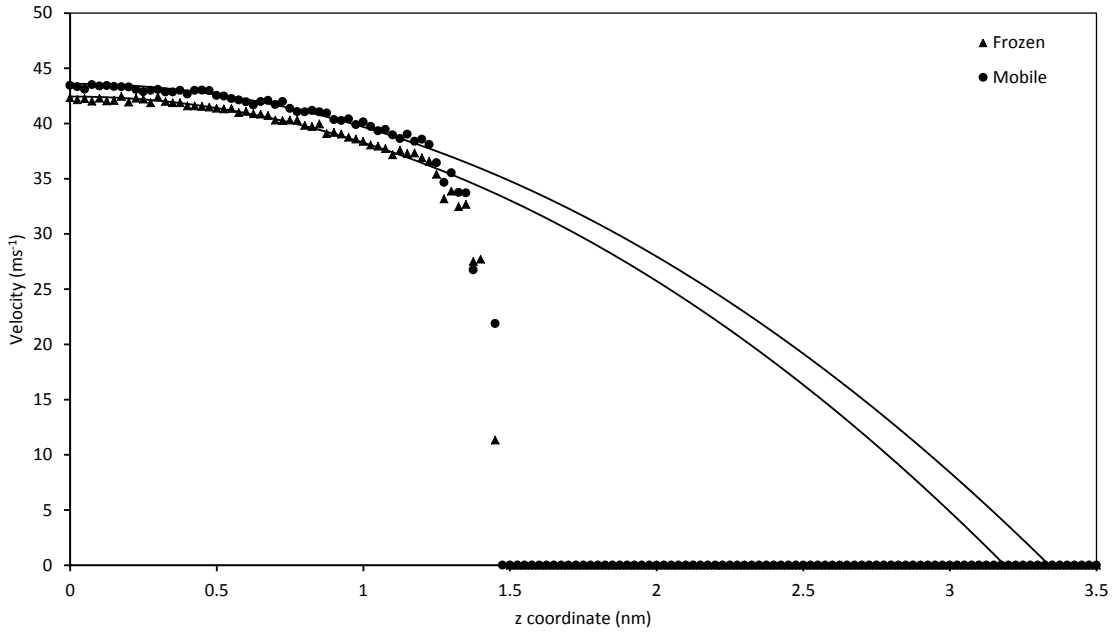


Figure 6.18: A Comparison of the Flow Profiles for g=0.05×10^{14}ms^{-2} for the Frozen and Mobile Surfaces

Figure 6.18 shows the effect of unfreezing the surface in the NEMD case - the velocity profile is shifted upwards slightly and the slip length increases. On average for both methods the relaxation time was found to increase by 12.1% and the slip coefficient to increase by 13.7%. Due to this small difference between the two cases it was decided for future simulations that frozen surfaces would be used due to advantages gained through reduced overheads and therefore reduced simulation times. Using a mobile surface doubled the processor time per ns due to the required calculation of the additional surface-surface interactions.

6.1.7 Amorphous Carbon Surfaces

The amorphous surfaces were set 3nm apart and the number of water molecules adjusted to 2309. A picture of the initial simulation cell is shown in the figure 6.20. Several pore widths were investigated for this system. The relaxation time and slip coefficient were found to be further reduced relative to graphene/diamond. In this case they were found to be τ=3.153 ps and l_s=1.226 nm.

Viscosity values have again been calculated from the fits to the profiles. The average value obtained is 6.3 $\pm$ 0.3 $\times10^{-4}$ Pa.s, which compares favourably with the value of 6.4 $\times10^{-4}$ Pa.s

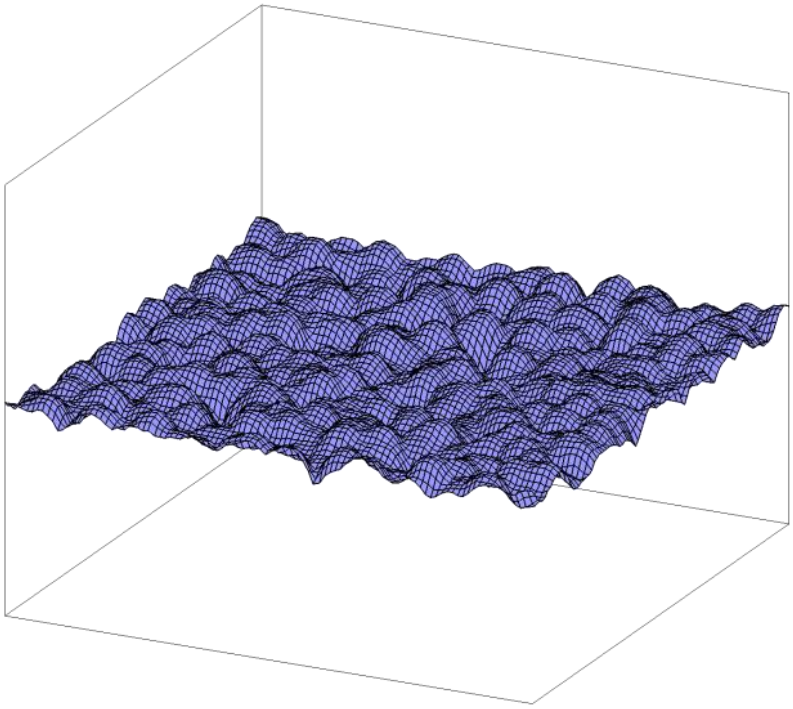


Figure 6.19: 3D Plot of the Amorphous Carbon Surface

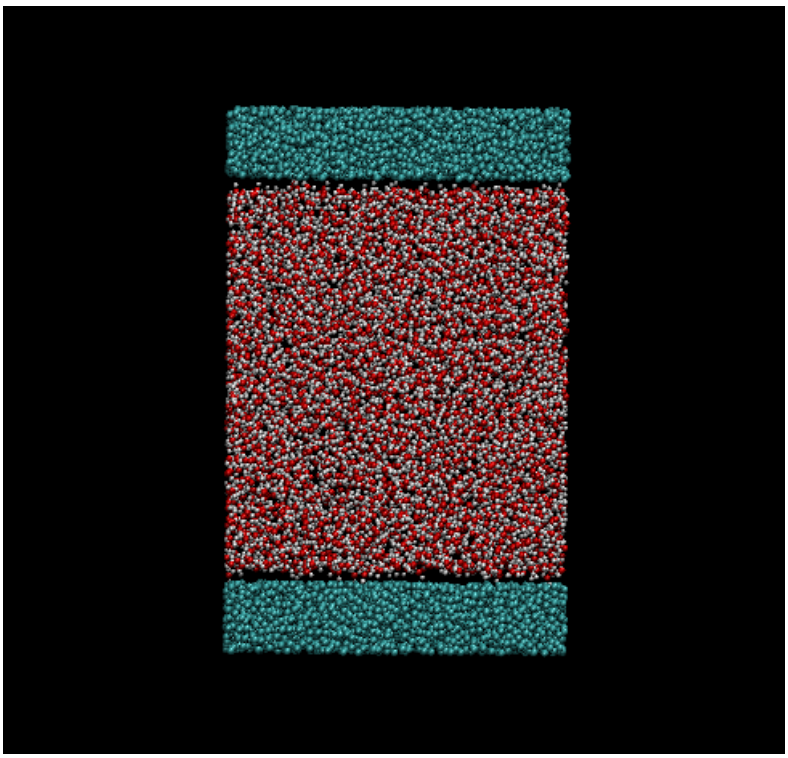


Figure 6.20: The h=6nm Amorphous Carbon Slit Pore

reported in previous simulation studies for SPC/E water [116]. The viscosity values at each external force value are shown in figure 6.23 below. At the shear rates employed the viscosity is constant and thus the fluid is behaving as a Newtonian fluid. Slip lengths have also been

calculated from the velocity profile data and are shown in figure 6.23. The average velocity values for a certain external force value are a hundred times lower than the corresponding flow over a graphitic surface.

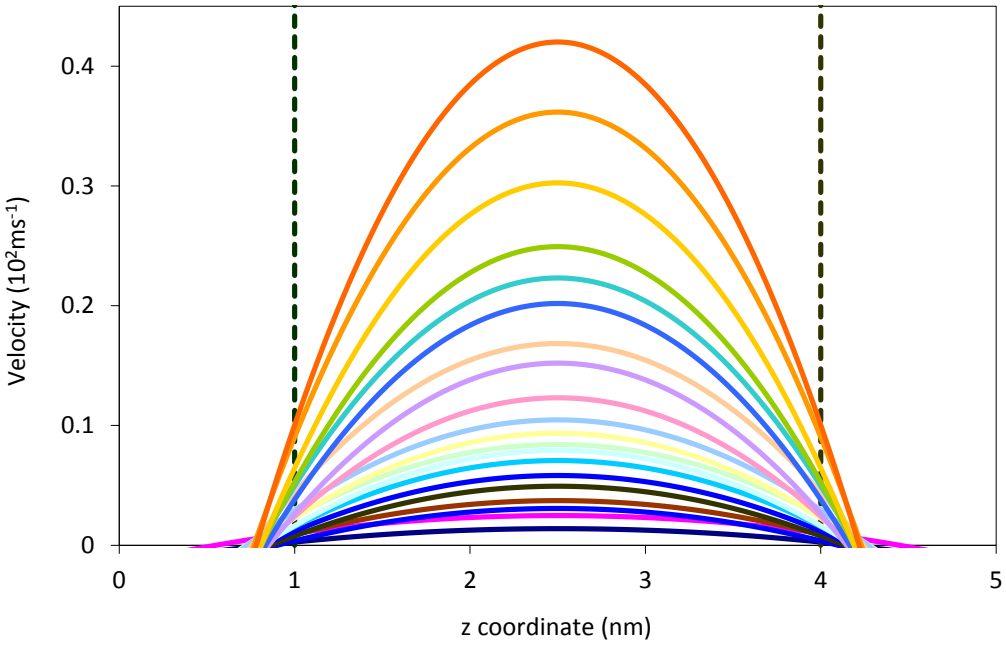


Figure 6.21: The Velocity profiles in the Amorphous Carbon System

In this case it is found that there is very little scatter in the flow profile data, meaning that slip coefficients would be relatively unchanged by varying the viscosity/fit.

g (10^{14}ms^{-2})	ΣF_{wf} (pN)	u_{av} (ms^{-1})	u_{max} (ms^{-1})	u_s (ms^{-1})	l_s (nm)	η (10^{-4} Pas)	τ (ps)	Q (10^{-17}m^{3}s^{-1})	ε
0.010	-34.0956	3.4025	3.9421	2.5791	1.1408	6.129	3.4025	5.1037	3.2816
0.015	-51.2075	4.7851	5.6141	3.5200	1.0087	5.985	3.1901	7.1776	3.0174
0.020	-68.115	6.6633	7.7803	4.9588	1.0565	5.922	3.3316	9.9949	3.1130
0.025	-85.1525	8.3421	9.5957	6.4293	1.2273	6.596	3.3368	12.5132	3.4546
0.030	-102.198	10.1682	11.7752	7.7159	1.1462	6.174	3.3923	15.2523	3.2924
0.035	-119.217	11.8729	13.7524	9.0051	1.1437	6.159	3.2920	17.8094	3.2946
0.040	-136.315	13.1679	15.0714	10.2631	1.2924	6.950	3.2919	19.7518	3.5848
0.045	-153.116	14.5793	16.8968	11.0428	1.1371	6.422	3.2398	21.8689	3.2742
Average					1.1445	6.292	3.3218		3.2891
St Dev					0.0886	0.345	0.0768		0.1773

Table 6.5: Water-Carbon 3nm NEMD Flow Data

The average value of the relaxation time found in the NEMD simulations (figure 6.24) compares well to the EMD value. It is constant over the range of the external field magnitudes. Furthermore the slip lengths derived from a fit to the flow profile agree favourably with those predicted

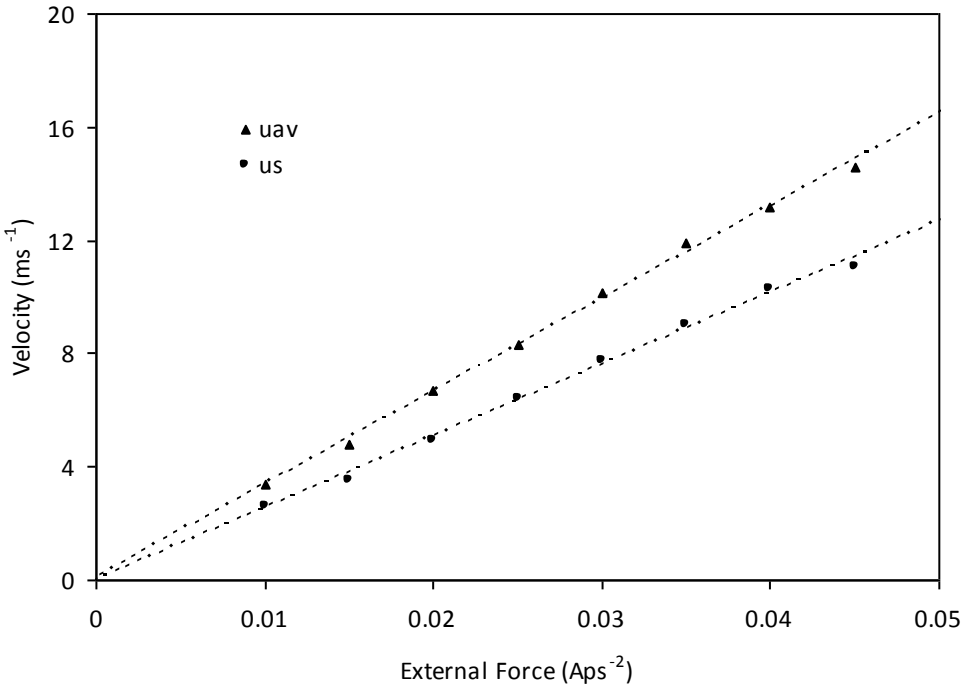


Figure 6.22: Average velocity and slip velocity values as a function of external force (3nm Water system)

by equation 3.38. These results are summarised in table 6.5.

The tangential force has been calculated as a function of z according to equation 6.4 and is plotted in figure 6.25 with the water density and a scaled velocity profile. The total tangential force exerted by the wall is defined as the integral of this. This tangential force is seen to drop to zero after 0.5nm from the wall, which is much less than the cut-off radius of 1.0nm. The force acts across the entire boundary layer and is seen to peak around the equimolar dividing surface. There is no significant change seen in the shape of the curve as the external force and thus flow rate increase, just an increase in magnitude. The magnitude of the external driving force is also not seen to have much effect on the shape of the density profile.

$$F_{slab}(x) = \frac{1}{M} \sum_{i \epsilon slab, j \epsilon wall} F_{ijx} \tag{6.4}$$

When trying to calculate Maxwell's coefficient in these systems with amorphous surfaces the peaks in the velocity profiles for particles colliding with the wall such as those obtained for diamond were less well pronounced. There was still some consistency in the values though and an average for Maxwell's coefficient of α=0.08656 $\pm$0.01492 was found, approximately double

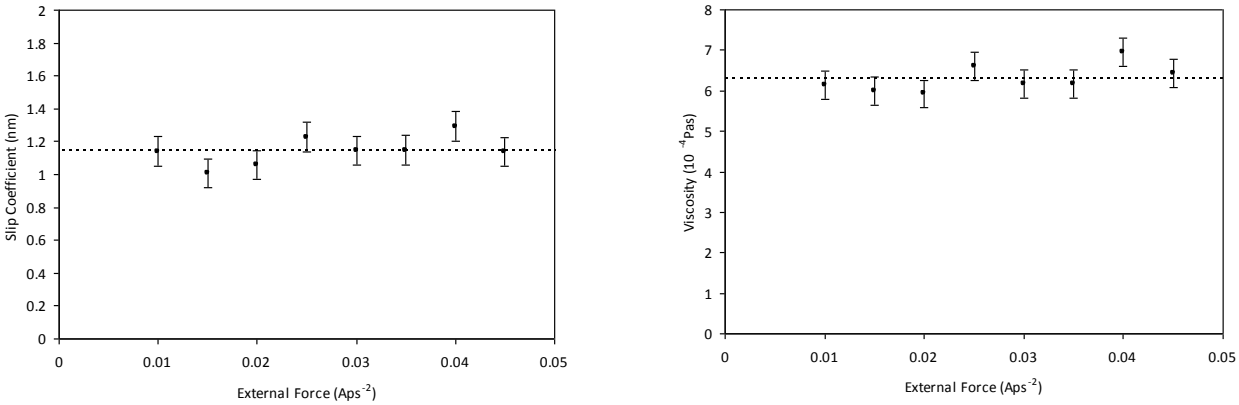


Figure 6.23: Slip coefficient and viscosity as a function of external force (3nm Water system)

that for the diamond, highlighting the increased thermalisation and momentum transfer with the rougher surface.

Width d=6nm Pore

A pore twice the width of the original was also investigated using a constant gravitational field non-equilibrium simulation. The z-dimension was doubled and the number of water molecules adjusted accordingly. The relaxation times are much longer and flow rates are higher for a given external field value than in the 3nm width case. The slip coefficient though is constant.

g (10^{14}ms^{-2})	ΣF_{wf} (pN)	u_{av} (ms^{-1})	u_{max} (ms^{-1})	u_s (ms^{-1})	l_s (nm)	η (10^{-4} Pas)	τ (ps)	Q (10^{-17}m^{3}s^{-1})	ε
0.010	-71.8825	8.9694	10.7219	7.2372	1.0057	6.343	8.9694	26.9082	2.0057
0.015	-107.888	14.0789	17.8861	12.3043	1.1062	5.940	9.3859	42.2367	2.1062
0.020	-143.648	18.9707	22.5216	15.4608	1.0946	6.261	9.4854	56.9121	2.0946
0.025	-179.666	24.1013	28.5955	19.6592	1.1027	6.184	9.6405	72.3039	2.1027
0.030	-215.425	28.1280	33.4701	22.8477	1.0641	6.243	9.3760	84.3840	2.0641
0.035	-251.126	34.5111	41.1548	27.9442	1.0360	5.857	9.8603	103.5333	2.0360
0.040	-286.691	39.6207	46.7312	32.5925	1.1857	6.254	9.9058	118.8621	2.1857
Average					1.0976	6.152	9.5898		2.0976
St Dev					0.06444	0.169	0.3614		0.0644

Table 6.6: 6nm Carbon-Water Data

The slip lengths for other pore widths were then calculated. The equilibrium results are shown in table 6.7 below for a range of widths. The slip coefficient is independent of pore width. The relaxation time increases as the pore width increases due to the decrease in influence that the surface has within the system.

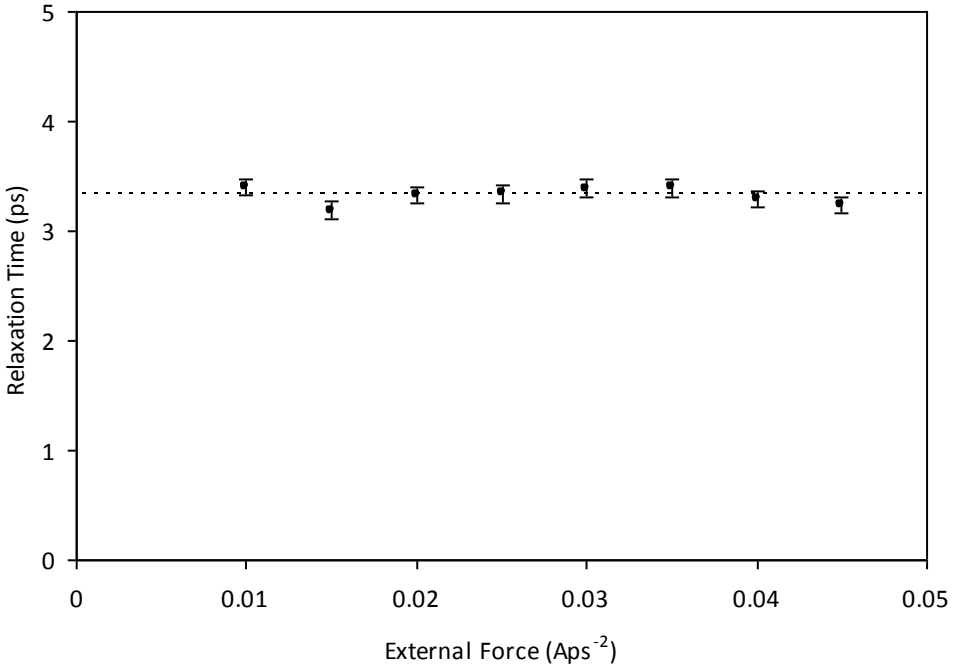


Figure 6.24: Tau values as a function of external force (3nm Water system)

Pore Diameter (nm)	τ_{EMD} (ps)	l_s (nm)
3.0	3.1525	1.2264
4.0	5.0339	1.0690
6.0	9.1650	1.0176
9.0	17.3741	1.0870
12.0	29.3051	1.2265

Table 6.7: EMD Data for the Amorphous Carbon Slit-Pores

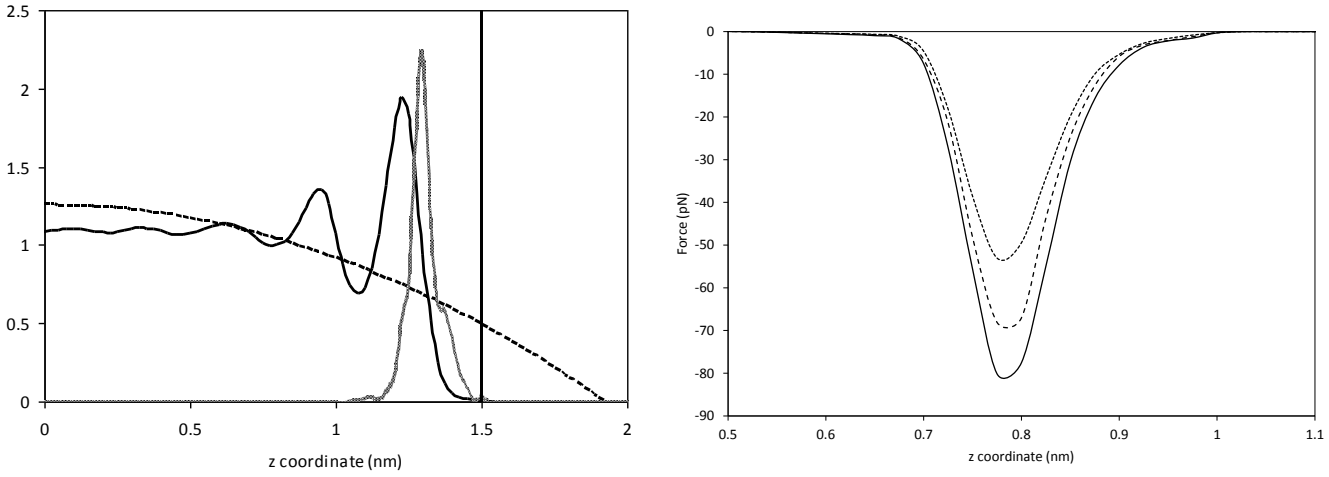


Figure 6.25: Tangential Force with water density and at varying external force values in the 3nm Carbon system

Reflecting Particle Membrane Generated Flow Data

Non-equilibrium simulations were also conducted using the RPM method for the generation of flow in the pores, which is seen to work well. Data is comparable to the external field method but is more variable. Shown below in figure 6.26 is the pressure across the length of the pore and the resulting flow profile obtained in the x direction for the case where the reflection probability is 60%. The pressure is seen to drop linearly across the center of the pore as required.

For the 6nm pore the pressure gradient was found to be too high in some cases resulting in non-linearity of the velocities. These results have been excluded from the averages. It is important to ensure that the response is linear, otherwise the slip coefficient and relaxation time start to diverge, as is seen in this data.

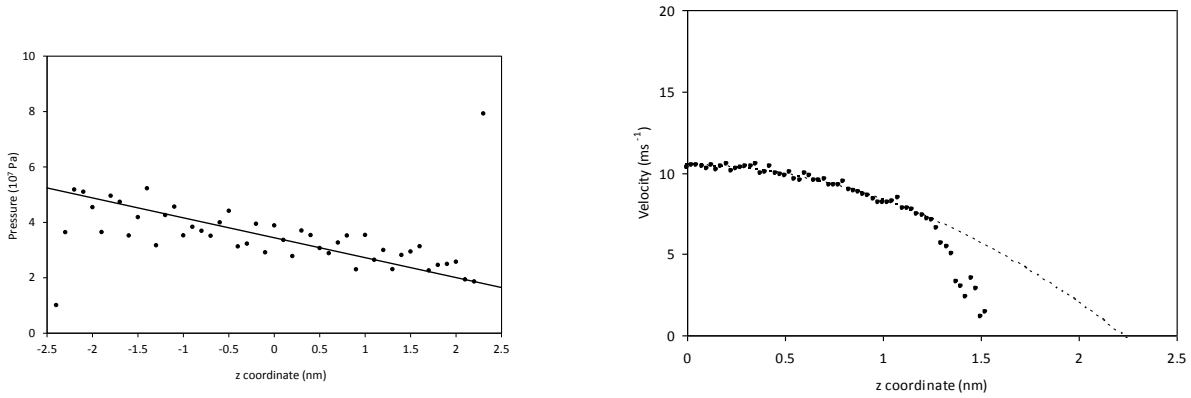


Figure 6.26: Stress Profile along Pore and Flow Profile for RPM System (p=0.6)

p	ΣF_{wf} (pN)	dP/dx (10^{15}Pa/m)	u_{av} (ms^{-1})	u_s (ms^{-1})	l_s (nm)	η (10^{-4} Pas)	τ (ps)	Q ($10^{-17}m^3s^{-1}$)	ε
0.10	-94.065	2.5084	9.0245	6.8448	1.1439	5.927	3.5977	13.5367	3.2878
0.15	-143.133	3.8169	14.4763	10.8238	1.0769	5.382	3.7927	21.7145	3.1538
0.20	-189.798	5.0613	19.1137	14.7519	1.2353	5.976	3.7765	28.6706	3.4706
0.25	-237.223	6.3259	23.8363	18.1313	1.1582	5.711	3.7680	35.7545	3.3164
0.30	-282.204	7.5254	29.1585	22.3873	1.2066	5.724	3.8747	43.7378	3.4132
0.35	-328.402	8.7574	34.2324	26.6927	1.2950	5.982	3.9089	51.3486	3.5901
Average					1.2314	5.871	3.8354		3.4628
St Dev					0.1093	0.326	0.1489		0.2186

Table 6.8: Water-Carbon 3nm RPM NEMD Flow Data

p	ΣF_{wf} (pN)	dP/dx (10^{15}Pa/m)	u_{av} (ms^{-1})	u_s (ms^{-1})	l_s (nm)	η (10^{-4}Pas)	τ (ps)	Q ($10^{-17}m^3s^{-1}$)	ε
0.05	-63.649	1.2730	6.8864	4.6091	1.0586	5.5602	5.4097	13.7728	2.5879
0.10	-126.815	2.5363	14.4949	10.1225	1.2141	5.7698	5.7150	28.9898	2.8212
0.15	-188.089	3.7618	21.0584	14.2897	1.1052	5.5280	5.5979	42.1168	2.6578
0.20	-245.214	4.9043	27.6899	18.8801	1.1222	5.5373	5.6461	55.3798	2.6833
0.25	-305.209	6.1042	34.4132	23.6579	1.1524	5.6454	5.6376	68.8264	2.7286
0.30	-355.372	7.1074	42.1972	29.7617	1.2558	5.6851	5.9370	84.3944	2.8837
Average					1.1514	5.6210	5.6572		2.7271
St Dev					0.0727	0.0961	0.1714		0.1091

Table 6.9: Water-Carbon 4nm RPM NEMD Flow Data

p	ΣF_{wf} (pN)	dP/dx (10^{15}Pa/m)	u_{av} (ms^{-1})	u_s (ms^{-1})	l_s (nm)	η (10^{-4}Pas)	τ (ps)	Q ($10^{-17}m^3s^{-1}$)	ε
0.05	-95.879	1.2784	12.5774	6.4141	1.0084	6.0197	9.83849	37.7322	2.0084
0.10	-186.803	2.4907	25.5435	13.852	1.1545	6.1828	10.2555	76.6305	2.1545
0.15	-270.045	3.6006	38.0784	20.8963	1.1863	6.0817	10.5756	114.2352	2.1863
0.20	-348.944	4.6526	49.4811	28.1351	1.2896	6.3256	10.6352	148.4433	2.2896
0.25	-418.112	5.5748	61.2239	36.0583	1.4059	6.4291	10.9822	183.6717	2.4059
Average					1.1597	6.1525	10.3262		2.1597
St Dev					0.1162	0.1336	0.36538		0.1162

Table 6.10: Water-Carbon 6nm RPM NEMD Flow Data

p	ΣF_{wf} (pN)	dP/dx (10^{15}Pa/m)	u_{av} (ms^{-1})	u_s (ms^{-1})	l_s (nm)	η (10^{-4}Pas)	τ (ps)	Q ($10^{-17}m^3s^{-1}$)	ε
0.05	-29.487	0.2620	4.2597	2.0284	1.0831	6.6451	16.2556	19.1687	1.7221
0.1	-57.753	0.5133	8.1894	3.3935	0.8218	6.0567	15.9534	36.8523	1.5479
0.15	-113.190	1.0061	17.7871	8.7699	1.1655	6.3137	17.6787	80.0419	1.7770
0.2	-165.764	1.4734	26.2467	13.2033	1.2169	6.392	17.8134	118.1102	1.8113
0.25	-214.001	1.9022	34.5302	17.6712	1.2636	6.3844	18.1526	155.3859	1.8424
0.3	-266.075	2.3651	41.9673	21.7665	1.3016	6.6248	17.7443	188.8529	1.8677
Average					1.0718	6.3519	16.9253		1.7146
St Dev					0.1756	0.2423	0.9573		0.1170

Table 6.11: Water-Carbon 9nm RPM NEMD Flow Data

p	ΣF_{wf} (pN)	dP/dx (10^{15}Pa/m)	u_{av} (ms^{-1})	u_s (ms^{-1})	l_s (nm)	η (10^{-4}Pas)	τ (ps)	Q ($10^{-17}m^3s^{-1}$)	ε
0.02	-78.738	0.5249	14.4414	5.0255	0.9351	6.0222	27.5116	21.6621	2.8702
0.04	-147.574	0.9838	27.7168	11.1356	1.1891	6.4095	28.1724	41.5752	3.3782
0.05	-180.945	1.2063	33.1036	12.9284	1.1324	6.4589	27.4423	49.6554	3.2648
0.06	-211.117	1.4074	40.4147	16.5732	1.2325	6.3771	28.7149	60.6221	3.4650
0.07	-241.705	1.6114	46.1969	19.5209	1.3003	6.5253	28.6694	69.2954	3.6006
0.08	-269.552	1.7971	51.0737	21.3978	1.2802	6.5414	28.4214	76.6106	3.5604
Average					1.2065	6.3408	28.6729		3.4130
St Dev					0.1248	0.2801	1.4399		0.2496

Table 6.12: Water-Carbon 12nm RPM NEMD Flow Data

Effects of Confinement

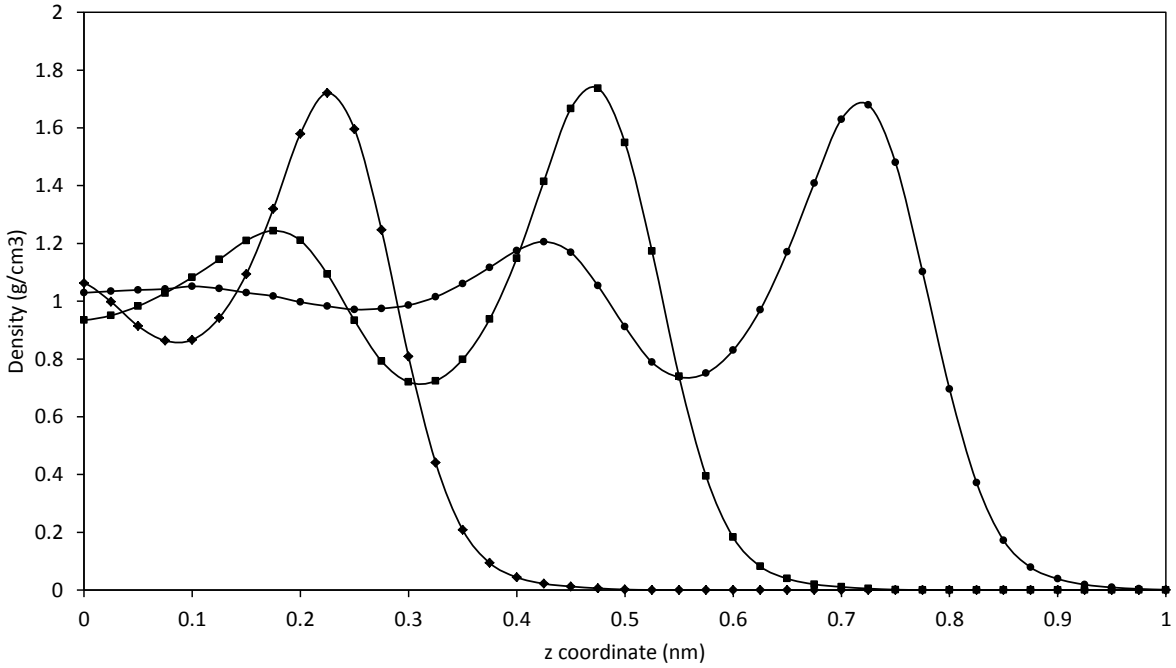


Figure 6.27: The Density Profiles in the Confined Systems

Pore Diameter (nm)	τ_{EMD} (ps)	l_s (nm)
1.0	0.6138	1.3259
1.5	1.0897	1.1367
2.0	1.6223	1.0417

Table 6.13: EMD Data for the Smaller Width Amorphous Carbon Slit-Pores

g (10^{14}ms^{-2})	u_{av} (ms^{-1})	u_s (ms^{-1})	l_s (nm)	η (10^{-4} Pas)	τ (ps)	Q (10^{-17}m^{3}s^{-1})	ε
0.30	13.7401	13.0162	1.4983	8.6331	0.4581	17.724	9.989
0.40	19.4075	18.3121	1.3930	7.6072	0.4852	25.036	9.358
0.50	25.0863	23.8139	1.5597	8.1874	0.5017	32.361	10.358
0.60	31.6963	30.1923	1.6279	8.3114	0.5283	40.088	11.037
Average	-	-	1.5309	8.1846	0.4933	-	10.1859
St Dev	-	-	0.1170	0.4284	0.0294	-	0.7020

Table 6.14: h=1nm Slit Pore NEMD Data

Smaller width pores were tested to see if any significant enhancement is seen similar to that in carbon nanotubes [28]. The h=1nm system has only three water layers (figure 6.27). The number of water molecules after equilibration are d=1nm N_{wat}=661, d=1.5nm N_{wat}=1083 and d=2nm N_{wat}=1496. Much larger external forces are required to generate flow rates in the more confined spaces. As is shown in figure 6.27, as the level of confinement increases the amount

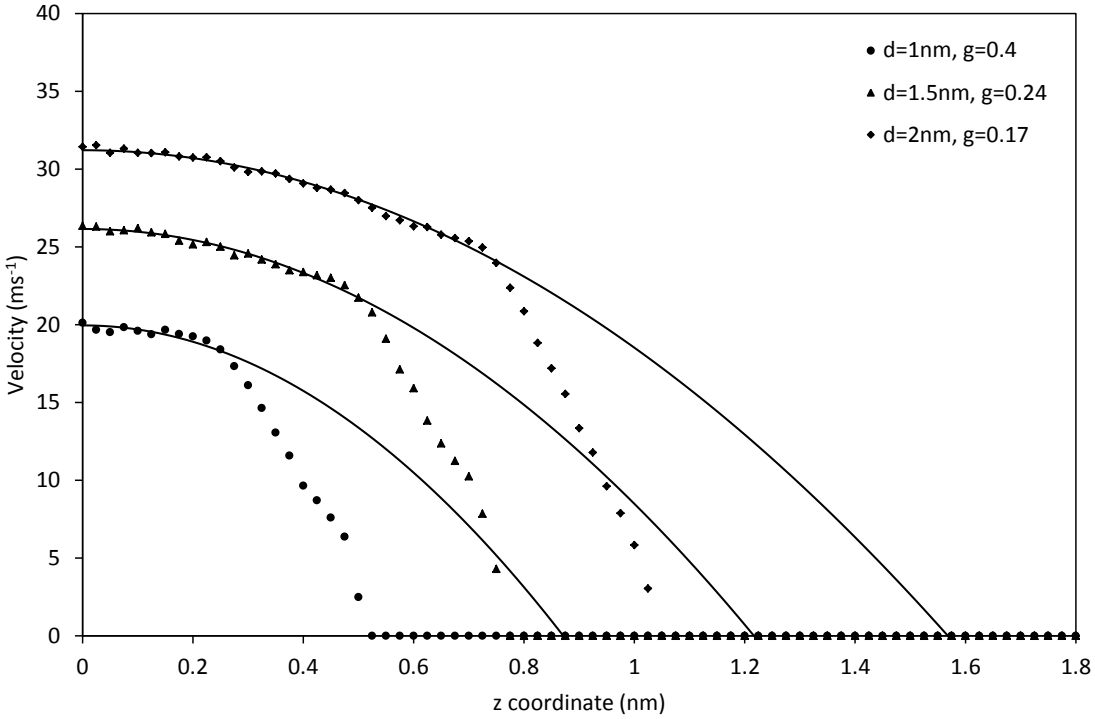


Figure 6.28: A Comparison of the Flow Profiles in the Confined Systems

g (10^{14}ms^{-2})	u_{av} (ms^{-1})	u_s (ms^{-1})	l_s (nm)	η (10^{-4} Pas)	τ (ps)	Q (10^{-17}m^{3}s^{-1})	ε
0.12	11.5886	9.9224	1.0916	7.2613	0.9657	14.949	5.3664
0.18	17.0447	14.2501	1.0199	7.7294	0.9469	21.987	5.0796
0.24	24.3714	20.8094	1.0711	6.7941	1.0155	31.439	5.2844
0.28	29.3318	25.0260	1.0656	6.5570	1.0476	37.838	5.2624
Average	-	-	1.0621	7.0855	0.9939	-	5.2182
St Dev	-	-	0.0302	0.5195	0.0460	-	0.1209

Table 6.15: h=1.5nm Slit Pore NEMD Data

g (10^{14}ms^{-2})	u_{av} (ms^{-1})	u_s (ms^{-1})	l_s (nm)	η (10^{-4} Pas)	τ (ps)	Q (10^{-17}m^{3}s^{-1})	ε
0.08	12.4551	9.8288	0.9981	6.4986	1.5569	16.067	3.9943
0.11	17.5457	13.9769	1.0443	6.5751	1.5951	22.634	4.1329
0.14	22.4589	17.8198	1.0243	6.4380	1.6042	28.972	4.0729
0.17	28.5069	23.0917	1.1371	6.6972	1.6769	36.774	4.4113
Average	-	-	1.0509	6.5522	1.6083	-	4.1529
St Dev	-	-	0.0605	0.1118	0.0501	-	0.1814

Table 6.16: h=2nm Slit Pore NEMD Data

of fluid flowing through the center of the pore and undergoing parabolic flow is reduced. The fit is performed only over the central portion of the pore undergoing parabolic flow (figure 6.28). Agreement is still found between EMD and NEMD but only modest increases in the slip coefficient are seen in the smallest system.

EMD data are shown in figure 6.13. NEMD data are shown in tables 6.14, 6.15 and 6.16.

6.1.8 Modification of System Parameters

As none of these systems gave slip coefficients/flow enhancements close to those predicted experimentally, it was decided to vary some of the parameters in these simulated systems, such as the pressure and potential energy functions to see if any better agreement could be reached and how much variation would be needed to achieve larger flow rates.

Effect of Varying Fluid Pressure

The pressure in the system was changed by modifying the density of the fluid. Non-equilibrium simulations using a gravitational field strength fixed at 0.02 $\times 10^{14}\text{ms}^{-2}$ were undertaken. As can be seen in table 6.17, even at low densities, the slip coefficient is only slightly enhanced.

N	$\langle P \rangle$ (MPa)	ΣF_{wf} (pN)	u_{av} (ms^{-1})	u_s (ms^{-1})	l_s (nm)	η (10^{-4} Pas)	τ (ps)	Q ($10^{-17}\text{m}^3\text{s}^{-1}$)	ε
2000	-30.147	-60.037	16.995	14.693	2.664	4.525	8.231	25.549	6.328
2250	-11.174	-67.420	7.364	5.197	1.326	5.602	3.644	11.046	3.652
2300	-1.886	-68.905	6.259	4.328	1.079	5.828	3.235	9.388	3.158
2350	8.746	-70.489	5.249	3.349	0.793	6.392	2.504	7.874	2.586
2400	21.115	-72.026	4.637	2.880	0.723	6.777	2.223	6.956	2.446
2450	34.839	-73.226	4.036	2.155	0.534	6.943	1.939	6.054	2.068
2500	50.279	-74.871	3.943	1.677	0.345	6.867	1.876	5.915	1.690

Table 6.17: Modified Fluid Density Slit Pore NEMD Data

Effect of Varying Wall/Fluid Interactions

As a potential source of error in the system, the wall/fluid interaction was also varied to see what effect this would have on the results. Equilibrium simulations were undertaken in a number of systems with different C-OW Lennard-Jones interaction energies. Again it is seen in table 6.18 that only in extreme cases does the slip coefficient become significantly enhanced. As the solid-fluid interaction strength increases it is noted that the decay of the correlation function becomes progressively less ideal (figure 6.30), suggesting that fluid adsorbed at the interface does not behave as that in the bulk.

This data also does not fit a $(1 + \cos\theta)^{-2}$ relationship of the type suggested in reference [84].

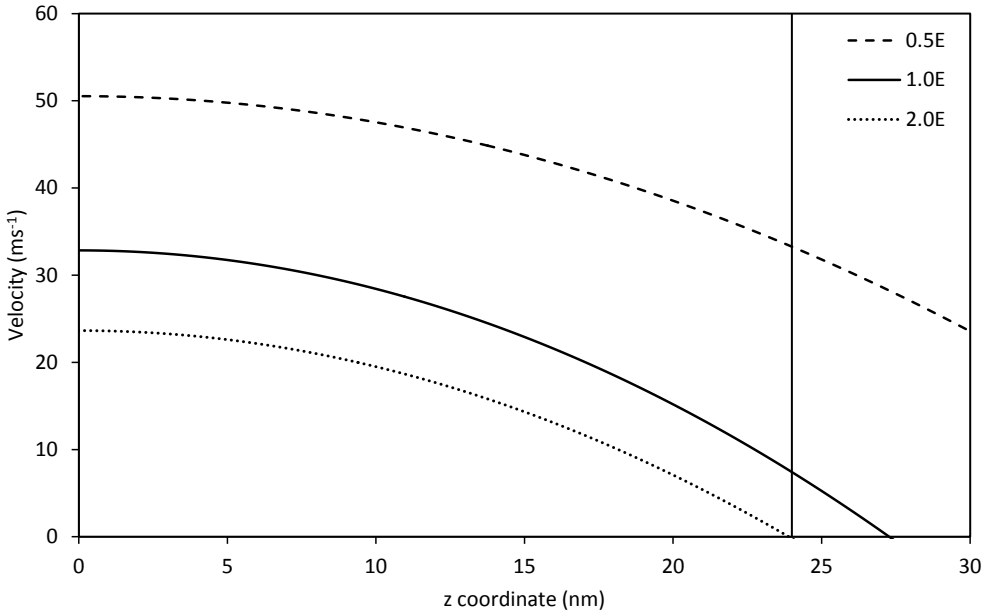


Figure 6.29: Flow Profiles with Varying Fluid-Solid Interaction Parameters

$\varepsilon/\varepsilon_0$	N_{wat}	ρ_{max} (g/cm^3)	δ (nm)	τ (ps)	l_s (nm)	γ (10^{-11}kgs^{-1})	ε -	θ (°)
0.05	2090	0.985	0.25	51.950	24.369	0.120	49.738	130.7
0.25	2142	1.024	0.23	16.337	7.513	0.392	16.026	122.6
0.50	2218	1.187	0.21	7.825	3.485	0.848	7.970	117.3
0.75	2268	1.402	0.20	4.529	1.925	1.497	4.850	108.8
1.00	2309	1.586	0.19	3.153	1.156	2.262	3.312	98.0
1.25	2344	1.724	0.18	2.317	0.879	3.024	2.758	89.6
1.50	2374	1.877	0.17	1.831	0.648	3.876	2.296	79.2
1.75	2399	1.972	0.17	1.506	0.494	4.764	1.988	71.9
2.00	2422	2.050	0.16	1.322	0.407	5.479	1.814	60.3

Table 6.18: Variable Wall/Fluid Interaction EMD Data

6.1.9 Modification of Graphite Surfaces

In order to produce some surfaces with a greater variety of roughness values the positions of atoms within a graphitic surface were modified in various ways. An initial system with four graphite sheets was used and surface atoms were randomly moved in the x and y directions, the z dimension and a combination of both. Also some surfaces with defects were produced by randomly removing surface atoms. The roughness values of the surfaces were then calculated as before. Equilibrium simulations were used to calculate the slip coefficient. These results are shown in table 6.19.

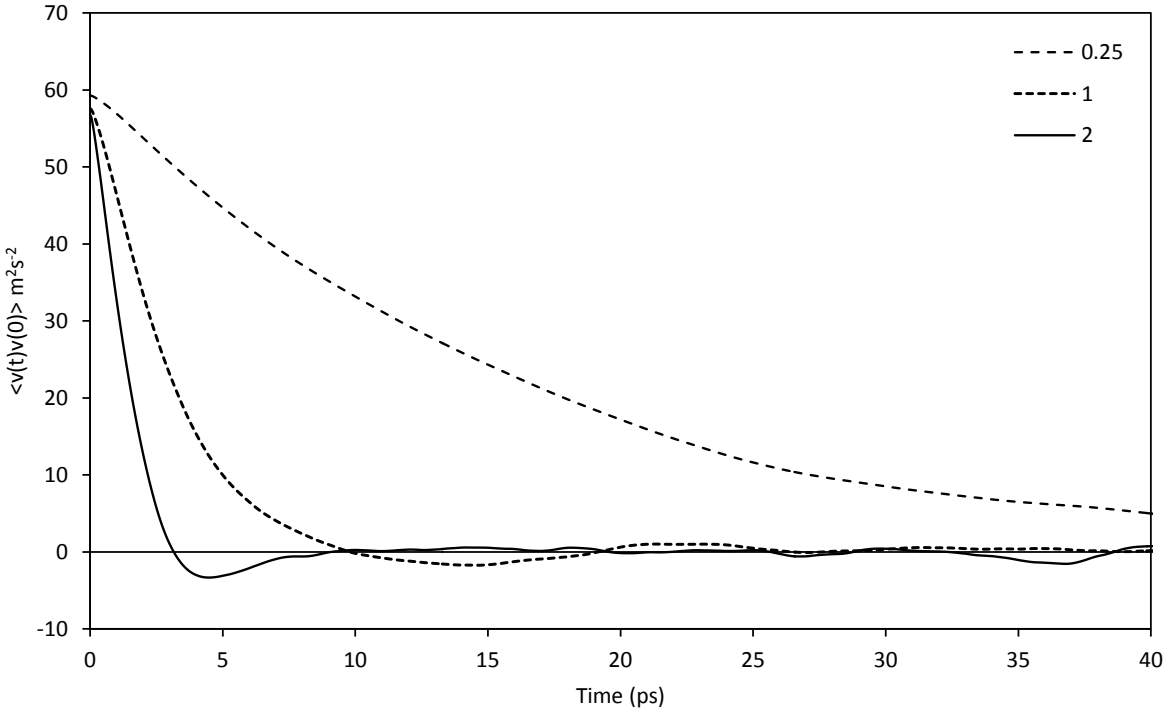


Figure 6.30: The Autocorrelation Function with Varying Solid Interaction Parameters

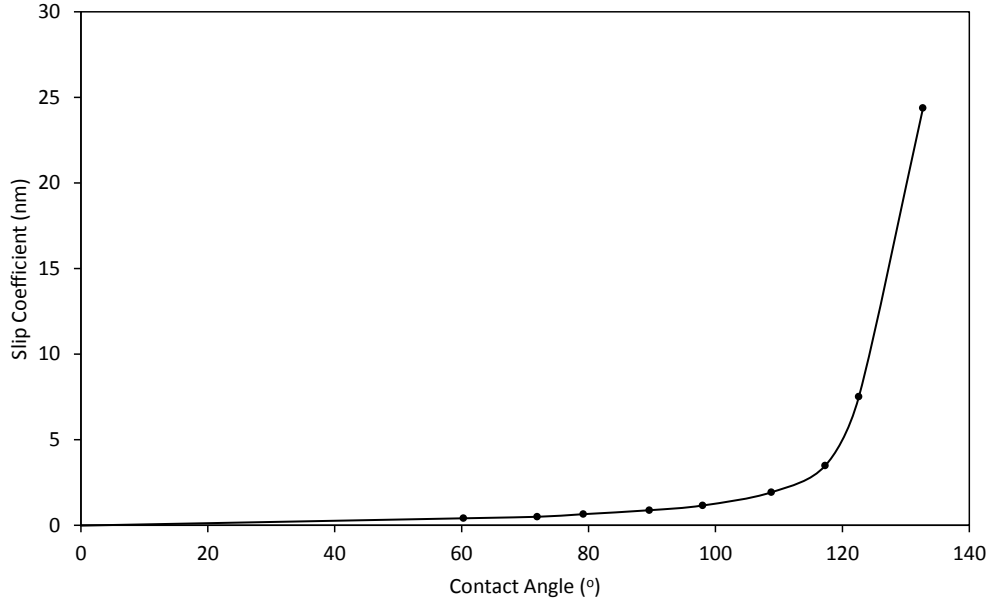


Figure 6.31: Slip Coefficient as a Function of Wall Interaction Strength

Surface	Roughness (nm)	τ_{EMD} (ps)	l_s (nm)
x/y Var. ±1.0	0.0017	150.29	70.911
z Var. ±0.25	0.0016	134.36	63.371
z Var. ±0.5	0.0022	103.37	48.702
z Var. ±0.75	0.0030	76.85	36.156
z Var. ±1.0	0.0037	37.02	17.301
z Var. ±1.5	0.0070	17.37	8.004
z Var. ±2.0	0.0102	8.97	4.028
x/y/z Var. ±0.5	0.0041	48.44	22.705
Defect 1%	0.0021	101.34	47.746
Defect 2%	0.0026	70.198	33.005
Defect 3%	0.0027	62.99	29.594
Defect 4%	0.0029	59.56	27.971
Defect 5%	0.0037	42.89	20.084
Defect 10%	0.0053	27.71	12.897

Table 6.19: Relaxation Times for the Modified Graphite Surfaces

6.1.10 Hydrogenated Carbon Surfaces

In reality the amorphous carbon surfaces formed from the vapour deposition of hydrocarbons will potentially contain a large amount of hydrogen. To investigate the effect of this on flow behaviour some hydrogen atoms were added to the amorphous carbon lattice. Hydrogen Lennard-Jones parameters are lower than carbon and so would be expected to reduce the average interaction energy with the surface.

Interaction	ε (kJmol^{-1})	σ (nm)
HS-HS	0.125	0.250
CS-CS	0.275	0.350
OW-OW	0.650	0.317
CS-OW (1)	0.424	0.330
HS-OW	0.285	0.280
CS-OW (2)	0.392	0.319

Table 6.20: Potential Parameters in the System

To test the effects on the flow data of hydrogen substitution in the surface, the original carbon model was used and a certain percentage of the carbon atoms randomly replaced with hydrogen. Four such systems were generated and an equilibrium calculation of the relaxation time performed. The results are shown in the table 6.21. The relaxation time and slip coefficient increase slightly upon addition of hydrogen due to the increasing hydrophobicity of the surface as the percentage of hydrogen increases but not by enough to significantly change the slip coefficient.

%H	Density (g/cm^3)	τ_{EMD} (ps)	l_s (nm)
10	2.939	3.5502	1.1791
20	2.690	3.5844	1.1948
30	2.441	4.0951	1.4292
40	2.192	4.3885	1.5638

Table 6.21: Relaxation Times for the hydrogenated surfaces

6.1.11 Carbon-Decane Slit Pore Systems

In experimental testing of the transport through carbon nanopipes the flow of a number of fluids through the pores was undertaken and all were found to give significant enhancements over the expected flow rates [33]. A decane-carbon system was therefore set up in the same way as the water-carbon system. Decane molecules were added between two carbon surfaces to liquid density (0.720 gcm^{-3}), the pressure adjusted to atmospheric, and then equilibrated.

Width 3nm and 6nm pores were looked at containing 219 and 452 decane molecules respectively. The peaks in the density plot in this system are seen to be sharper than for the water system, suggesting that the decane molecules are more attracted to the interface than the water due to the potential function.

Equilibrium Simulations

Relaxation time values were determined from the collective velocity correlation function decay curves in the same manner as for the water-carbon systems. Values are shown in table 6.22 below.

Pore Diameter (nm)	N_{dec}	τ_{EMD} (ps)	l_s (nm)	ε
3.0	219	1.7020	0.4697	1.939
6.0	452	4.4076	0.4197	1.419

Table 6.22: Decane/Carbon EMD Data

Non-Equilibrium Simulations

Non-equilibrium simulations were also performed with these systems. Agreement between the equilibrium and non-equilibrium equations is still found in these smaller pores.

The decane data show lower relaxation times and slip coefficients than for water, in agreement with the experimental work of Majumder et al. [33] but not that of Whitby et al. [46]. The flow enhancements are correspondingly even lower for decane than in the water case.The slip coefficient and relaxation times are approximately halved.

A width d=42nm pore, which has a diameter close to that used in the experimental work, was also produced with 3283 decane molecules. The lower density and united-atom nature of the decane model allowed the simulation of the larger system, which was not practical in the water case due to processing time constraints. Due to the low viscosity of this model though and the large width of the pore, the flow profile in the system was not parabolic throughout and the central region showed a uniform velocity profile. This made determination of the flow parameters difficult and agreement between EMD and NEMD was not found.

g (10^{14}ms^{-2})	u_{av} (ms^{-1})	u_s (ms^{-1})	l_s (nm)	η (10^{-4} Pas)	τ (ps)	Q (10^{-17}m^{3}s^{-1})	ε
0.05	8.1169	3.6536	0.368	4.941	1.509	12.175	1.736
0.06	9.7303	4.9285	0.462	5.511	1.519	14.595	1.924
0.07	11.3765	5.1661	0.374	4.971	1.512	17.065	1.748
0.08	12.7138	5.5713	0.391	4.934	1.475	19.071	1.782
0.09	15.0141	7.0726	0.401	4.998	1.556	22.521	1.802
Average	-	-	0.3992	5.071	1.514	-	1.798
St Dev	-	-	0.0375	0.247	0.029	-	0.075

Table 6.23: Decane d= 3.0nm Slit Pore NEMD Data

g (10^{14}ms^{-2})	u_{av} (ms^{-1})	u_s (ms^{-1})	l_s (nm)	η (10^{-4} Pas)	τ (ps)	Q (10^{-17}m^{3}s^{-1})	ε
0.02	11.0824	3.2604	0.382	4.679	4.586	33.247	1.382
0.025	13.2886	3.9565	0.489	5.569	4.517	39.865	1.489
0.03	14.9459	4.5132	0.391	4.996	4.087	44.837	1.391
0.035	17.9023	5.0356	0.372	5.347	4.279	53.706	1.372
0.04	20.2465	5.8142	0.383	5.447	4.241	60.739	1.383
Average	-	-	0.4034	5.207	4.342	-	1.403
St Dev	-	-	0.0483	0.364	0.206	-	0.048

Table 6.24: Decane d= 6.0nm Slit Pore NEMD Data

6.2 Cylindrical Pore Geometries

Pores in real experimental systems predominantly have a cylindrical geometry. Some examples of cylindrical systems were simulated in order to test the cylindrical versions of the equations and the flow dynamics over these curved surfaces.

6.2.1 Carbon Nanotubes

A (22,22) and a (45,45) nanotube were formed which give nominal diameters of 2.98nm and 6.102nm. C-C Bond lengths were fixed at 0.142nm. The nanotubes were formed with an axial length of L_x = 10nm (the flow dimension). Nanotube diameter, d=3.0nm contains 1855 water molecules, whilst diameter d=6.1nm has 8782 water molecules after equilibration.

The nanotube exhibits a very strong layering next to the walls as shown in the two-dimensional density plot, figure 6.33. Similarly to graphene, very high relaxation times are found (τ=69.321ps for d=3nm, τ=130.512ps for d=6nm), with slip lengths of 65.288nm and 55.080nm respectively. The relaxation time is halved compared to graphene for the 3nm system, but the slip coefficient has a slightly lower but similar value, suggesting minimal curvature effects in these systems. Flow data for the nanotubes are shown below in tables 6.25 and 6.26. The flow enhancement

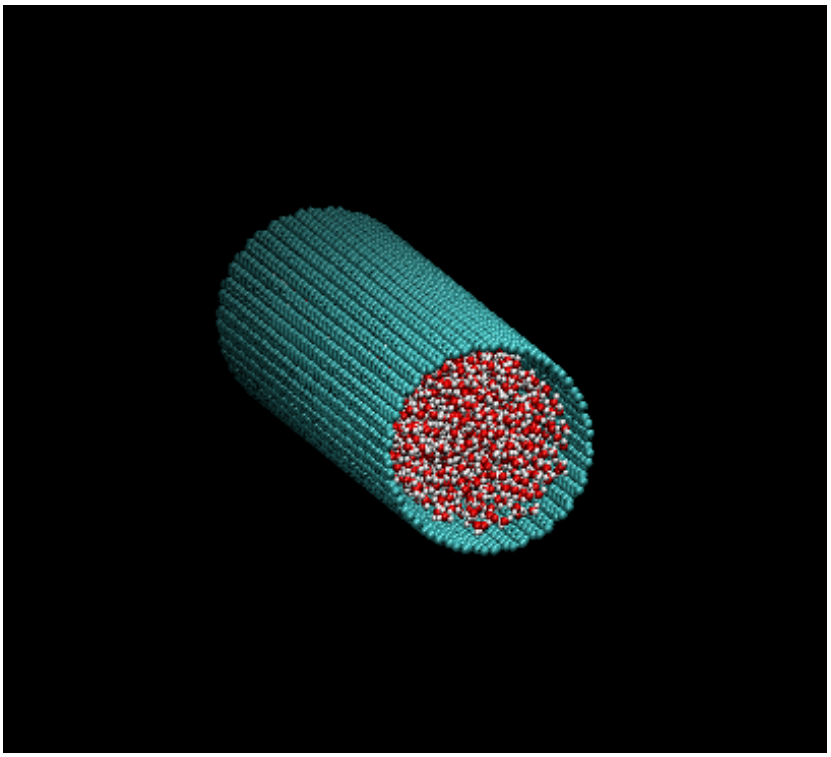


Figure 6.32: The d=3nm CNT System

due to the high slip coefficients found is around 350 in the r=1.5nm system and 140 in the r=3.0nm system. These are between ten and a hundred times lower than the values predicted experimentally.

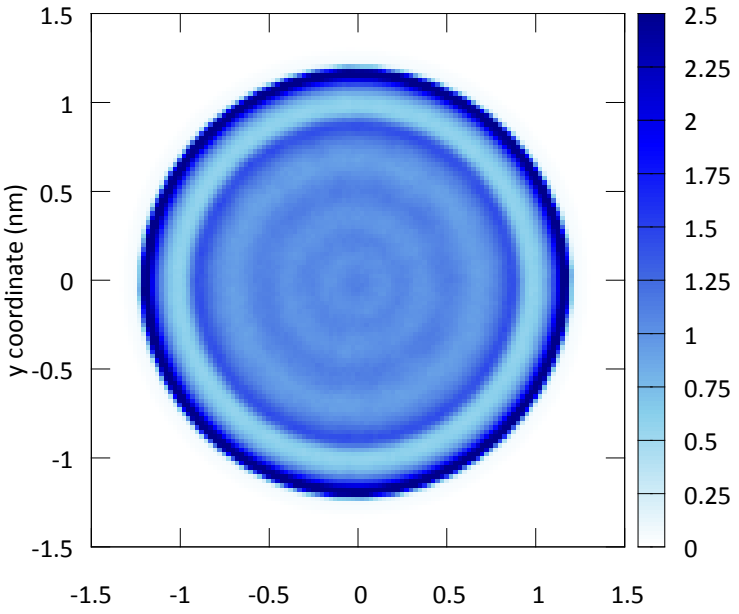


Figure 6.33: The 2D Density Profile in the Carbon Nanotube System

g (10^{14}ms^{-2})	u_{av} (ms^{-1})	u_s (ms^{-1})	l_s (nm)	η (10^{-4} Pas)	τ (ps)	Q (10^{-17}m^{3}s^{-1})	ε
0.002	13.828	13.649	63.536	5.819	69.139	9.774	339.858
0.003	20.119	19.879	68.938	6.502	67.064	14.052	368.669
0.0035	23.808	23.808	61.432	5.819	68.021	16.828	328.637
0.004	28.881	28.337	68.071	6.486	71.780	20.415	364.045
Average	-	-	65.494	6.175	69.001	-	350.303
St Dev	-	-	3.598	0.370	2.038	-	9.595

Table 6.25: Carbon Nanotube d=3nm NEMD Data

g (10^{14}ms^{-2})	u_{av} (ms^{-1})	u_s (ms^{-1})	l_s (nm)	η (10^{-4} Pas)	τ (ps)	Q (10^{-17}m^{3}s^{-1})	ε
0.002	25.322	24.386	49.581	5.794	126.61	71.159	133.216
0.0025	30.043	29.008	54.191	6.772	120.17	84.945	145.509
0.003	37.431	36.107	52.734	6.353	124.77	105.834	141.624
0.004	50.765	48.993	53.438	6.326	126.91	143.535	143.501
Average	-	-	52.486	6.311	124.62	-	140.963
St Dev	-	-	2.026	0.401	3.110	-	2.701

Table 6.26: Carbon Nanotube d=6nm NEMD Data

6.2.2 Multi-walled Nanotube with Defects

The effect of degree of roughness and the extent of the drop off with defect percentage were tested. A three shelled multi-walled nanotube (MWNT) of internal diameter 3.0nm, with interlayer dimension 0.34nm, was taken and then a certain percentage of atoms removed from its surface randomly in order to simulate defects in the lattice and to vary the roughness. It is found that even with only 5% of carbon sites removed, the slip length is halved.

Defect Percentage	τ_{EMD} (ps)	l_s (nm)	$\gamma_{EMD}(10^{-12}\text{kgs}^{-1})$
0.0	75.918	69.395	0.2991
2.1	46.695	42.553	0.4863
4.7	36.971	33.621	0.6142
8.9	16.682	14.985	1.3613
13.2	15.431	13.836	1.4716
16.9	13.416	11.985	1.6927
21.2	7.897	6.916	2.8756
24.9	7.133	6.214	3.1836

Table 6.27: EMD Data for the MWNT with Varying Defect Percentages

It can be seen that the relaxation time drops rapidly and the friction coefficient increases with increasing roughness. There is though expected to be a limit to this effect as further removals of atoms would be expected to reduce the density of the surface and thus the force exerted by the wall, reducing resistance to flow.

6.2.3 Different Carbon Densities

The roughness of the vapour deposited surfaces used in the experimental work has previously been measured using atomic force microscopy [132]. These found the surface roughness to be in the range 0.09nm to 0.40nm, which shows that the simulated carbon surface was still somewhat smoother than experiment would suggest. Some carbon surfaces with different densities have also been generated from freezing a molten carbon sample at different densities ranging from 1.5gcm^{-3} to 3.0gcm^{-3}. Plots showing the surface structure for the various densities are shown in figure 6.34. Fluid molecules flowing over a rough surface are expected to lose more tangential momentum than those flowing over a smooth surface thus reducing the slip length. The roughness values are shown in table 6.28 below. The less dense the surface the rougher it becomes.

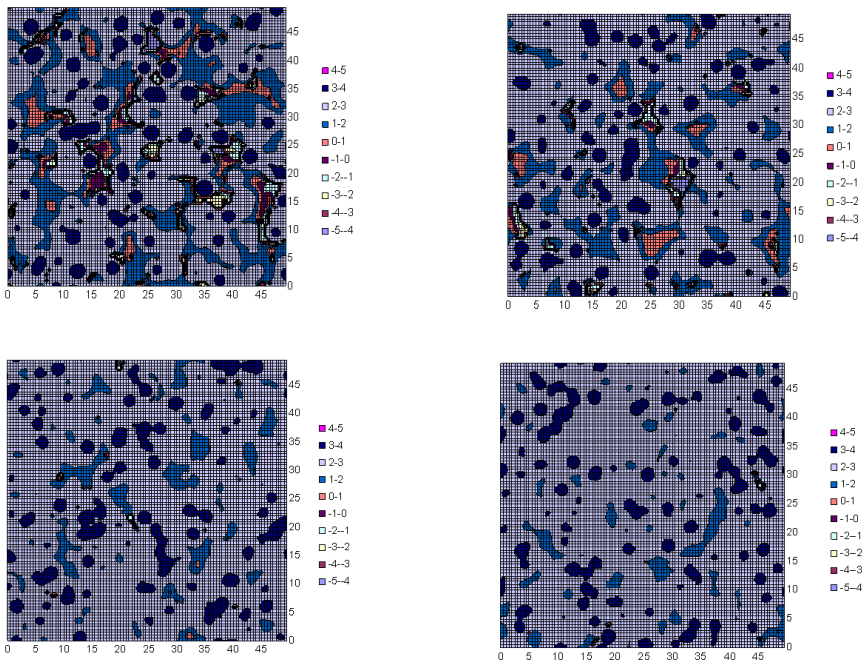


Figure 6.34: Surface plots for different carbon surface densities (1.5-3.0 g/cm^3)

Density (g/cm^3)	Average Position (nm)	Standard Deviation (nm)
1.5	0.196	0.141
2.0	0.225	0.106
2.5	0.254	0.048
3.0	0.258	0.040

Table 6.28: Roughness data for the alternative density surfaces

As shown in table 6.29, a reduction in the slip length is found as the roughness increases.

Density (g/cm^3)	τ_{EMD} (ps)	l_s (nm)
2.0	2.3135	0.2642
2.25	2.5035	0.3768
2.5	2.6982	0.4615
2.75	2.9301	0.5976
3.0	3.6538	0.9181

Table 6.29: EMD Flow data for the alternative density surfaces (d=6nm Cylindrical)

6.2.4 Amorphous Carbon Cylinder

In order to simulate this configuration a 3nm radius cylindrical pore was formed by cutting a cylinder from the middle of a large slab of amorphous carbon which had been formed in the same manner as before. All atoms along the x-axis within a radius of 1.5nm of the center were removed. This pore was then filled with water and its flow behaviour under an external gravitational field investigated. In order to simulate a more realistic density a 2.5g/cm^3 sample of atomic carbon was used to form the amorphous carbon tube.

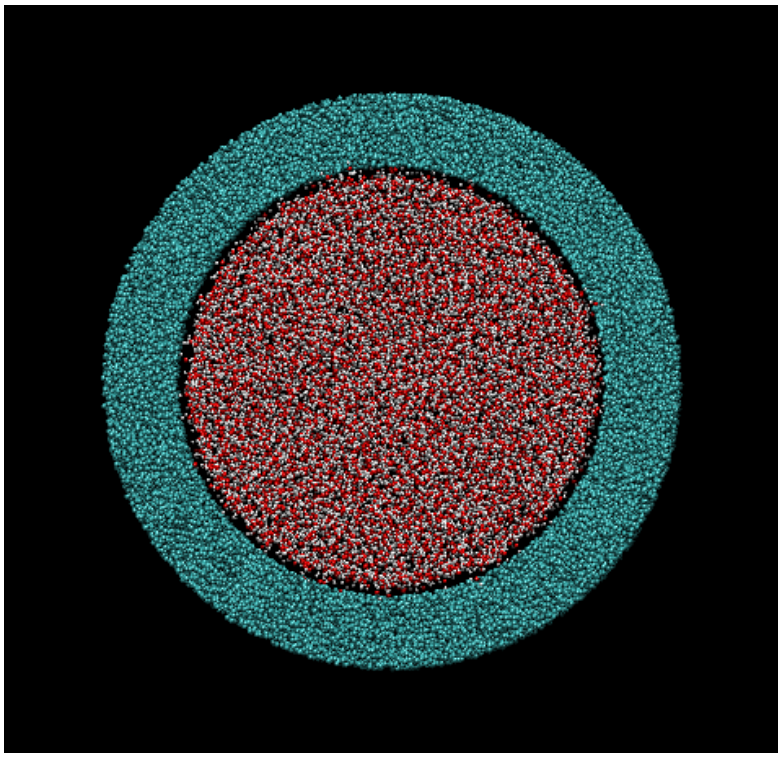


Figure 6.35: The r=3nm Amorphous Tube

The fluid interactions with the wall in both the smooth carbon nanotube case and the amorphous carbon pore were compared through analysing the density profiles of the water (figure 6.36). The water in the carbon nanotube shows a much greater degree of ordering next to the interface and is peaked further from the wall suggesting a larger depletion layer, which could offer some

explanation for the extremely high flow rates.

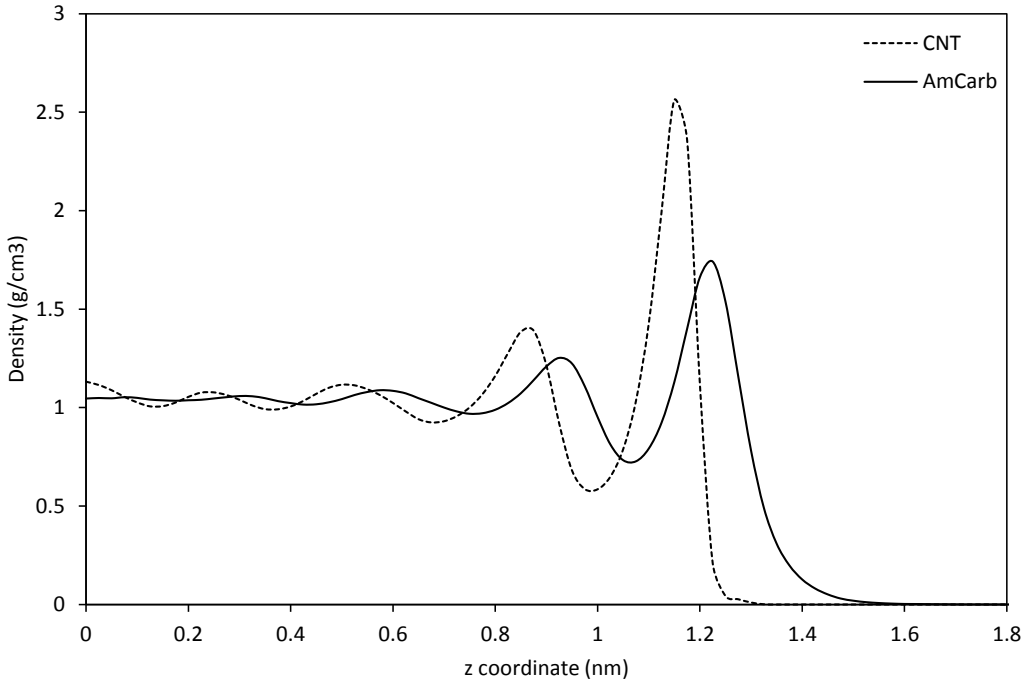


Figure 6.36: Density Profile Comparison Between Amorphous Tube/CNT

It was found that the flow rates decrease compared to the slit-pore geometry for a similar driving force. The slip coefficients are again slightly smaller in the cylindrical system suggesting the effect of increasing the amount of surface/fluid contact increases the frictional effect. The relaxation time in the equilibrium case was 1.197 ps giving a slip coefficient of 0.762 nm. Non-equilibrium flow data for the amorphous tubes are shown below in table 6.30.

g (10^{14}ms^{-2})	u_{av} (ms^{-1})	u_s (ms^{-1})	l_s (nm)	η (10^{-4} Pas)	τ (ps)	Q (10^{-17}m^{3}s^{-1})	ε
0.08	10.908	4.909	0.682	6.945	1.364	7.710	4.637
0.12	17.243	7.630	0.661	6.502	1.437	12.188	4.525
0.16	24.111	10.536	0.647	6.138	1.507	17.043	4.451
0.20	29.579	11.860	0.602	6.857	1.479	20.908	4.211
Average	-	-	0.648	6.611	1.447	-	4.456
St Dev	-	-	0.034	0.369	0.062	-	0.181

Table 6.30: d=3nm Amorphous Carbon Cylinder NEMD Flow Data

6.2.5 Effect of Nitrogen Bubbles

The possibility of nitrogen bubbles affecting the flow of a fluid experimentally has been raised. This was simulated by adding a small amount of nitrogen to the system. It was modelled as a

diatomic molecule using the Lennard-Jones parameters found in reference [133]. The nitrogen is seen to accumulate at the interface (figure 6.37) but not make a significant difference to the magnitude of the slip coefficient. In the non-equilibrium case upon separating the velocity profile into components subtle differences are seen in the relative velocities - the nitrogen at the interface moves slower than the water molecules.

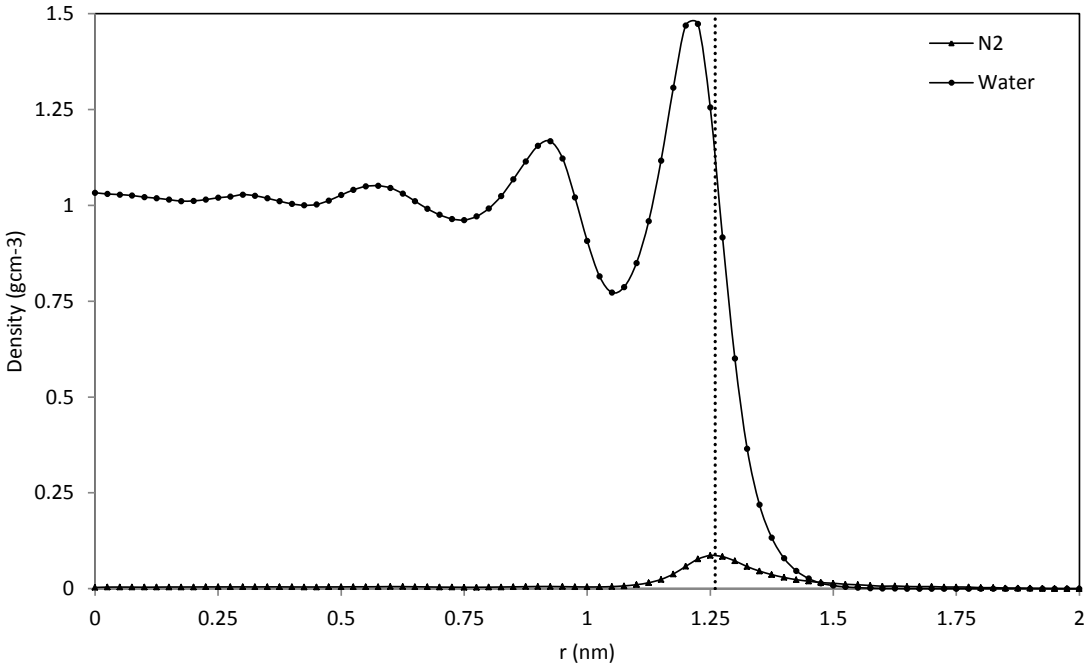


Figure 6.37: The Density Profile for the Nitrogen-Water System

6.3 PDMS/Water Systems

A model of the polymer PDMS was also used to calculate slip lengths as it is commonly used in real systems and there is much experimental interest in the surface properties. It offers a much rougher surface than the previous carbon based ones.

6.3.1 Characterisation of the Surfaces

The solid surfaces were again analysed in order to make comparisons of their structure and roughness. To estimate surface roughness the equilibrium position of a water molecule at an array of grid points across the surface was calculated as the minimum in the potential energy

of the interaction between the probe molecule and the PDMS atoms. The roughness was then defined as the standard deviation in this position.

These r.m.s. roughness values are shown in table 6.31. The S_1 surface shows a large increase in roughness compared to the S_0 surface since the methyl groups closest to the surface are replaced in the initial oxidation step. The further replacements on the S_2 surface occur over 0.1nm below the surface, leaving the topography of the outer surface unchanged while beginning to form pits and cracks. The surface structures are shown in figure 6.38 for the S_0 surface, figure 6.39 for the S_1 surface and figure 6.40 for the S_2 surface. These are much rougher than the carbon surfaces used, being around ten times greater than that of the amorphous carbon. The average positions are also below that of the nominal surface used during the formation of the pore.

Surface	Average Position (nm)	Standard Deviation (nm)
S_0	-0.3071	0.2219
S_1	-0.1431	0.2492
S_2	-0.1332	0.3126

Table 6.31: Characterisation of the PDMS Surfaces

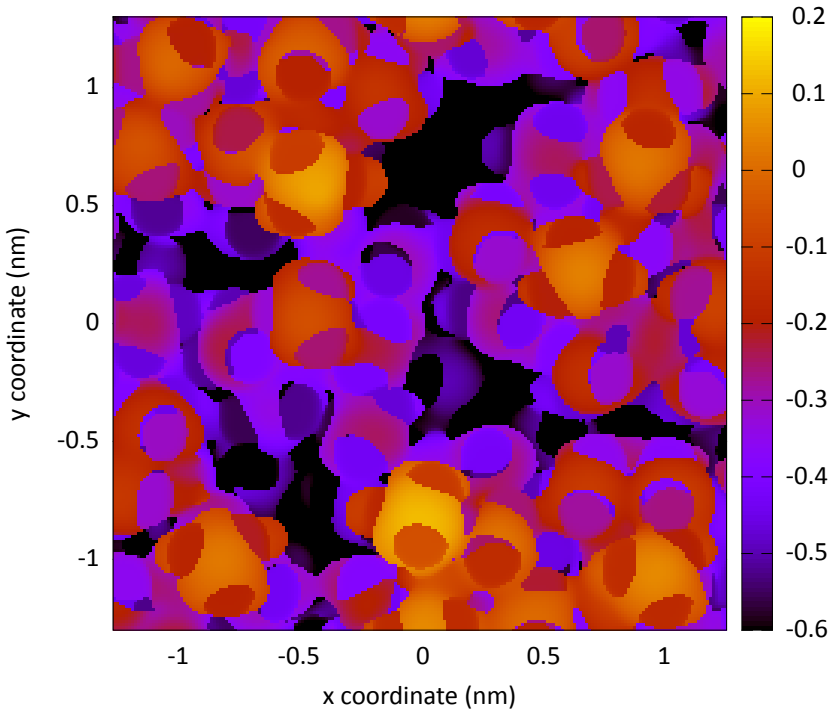


Figure 6.38: The S_0 PDMS Surface

Density profiles along the axis of the nanopore were obtained using 2.7 × 2.7 × 0.025 nm^3 rectangular bins for the three systems. The center of mass of the water molecule was used as a reference. Peaks are again seen next to the walls, which correspond to the average of the

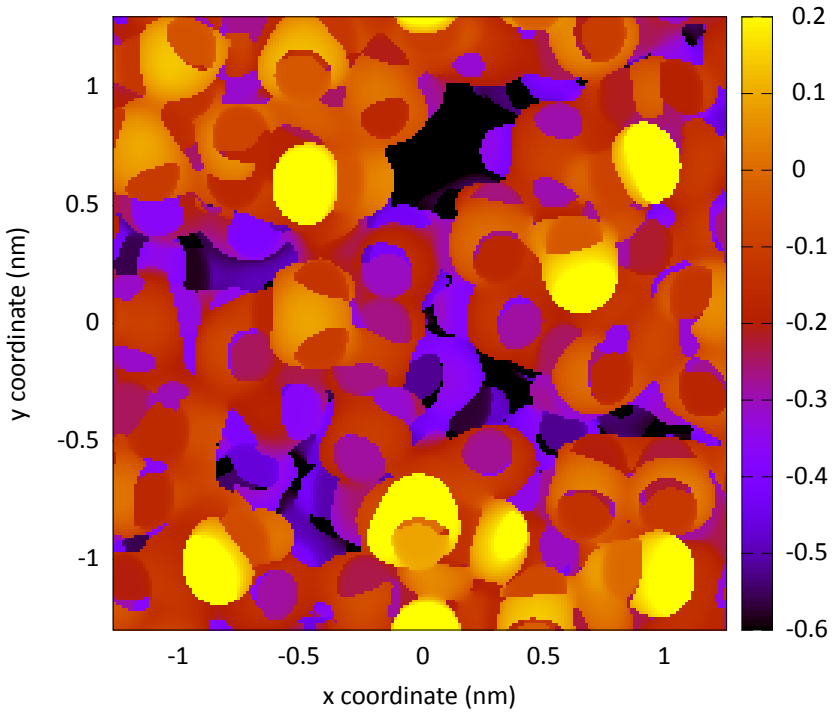


Figure 6.39: The S_1 PDMS Surface

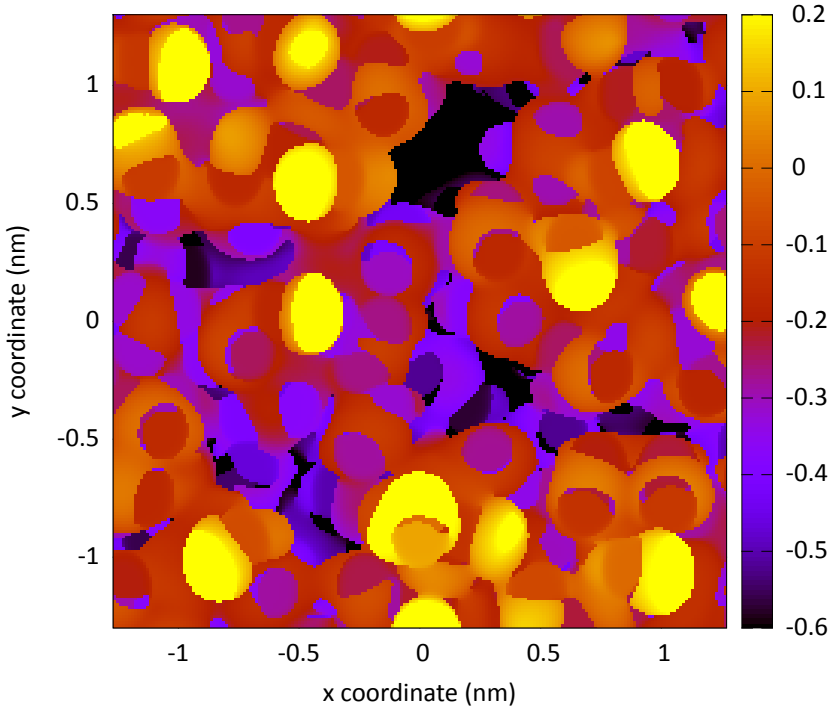


Figure 6.40: The S_2 PDMS Surface

potential minimum at the interface felt by the water molecules next to the wall. They represent the position of the first adsorbed water monolayer in the system. A second, smaller set of peaks is seen, which correspond to the second adsorption layer. As the surfaces are rough, the density

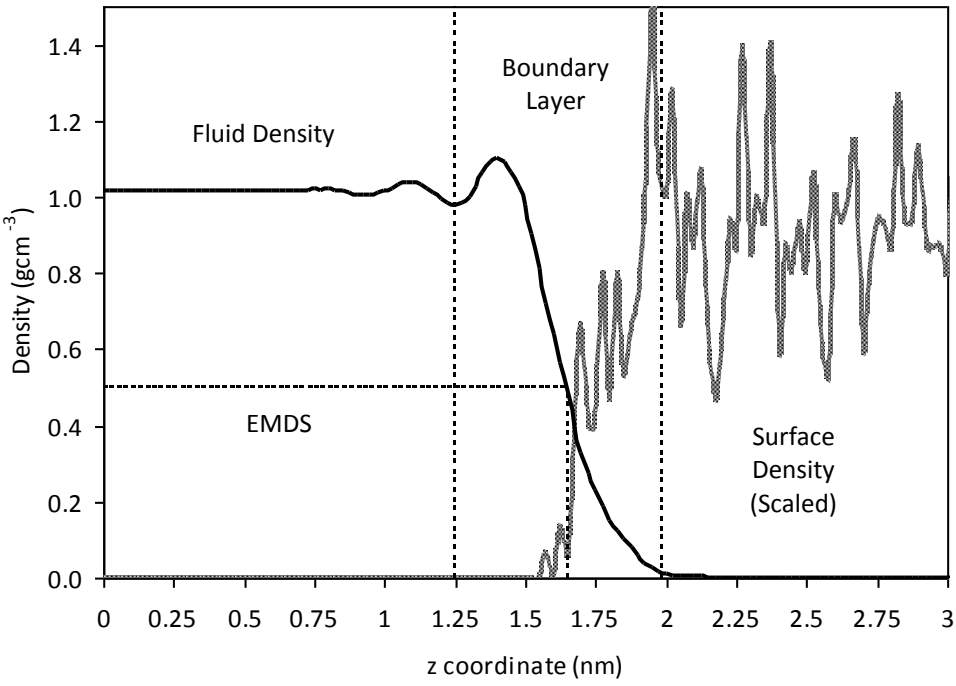


Figure 6.41: Fluid density profiles with the PDMS surface added for the Untreated surface

profiles are not as well defined as for fluid packing against a hard, smooth wall or when compared to the carbon systems. For these more hydrophilic surfaces a larger wall/fluid attractive force induces a higher density at the interface.

The density profiles along the axis perpendicular to the surface of each pore are depicted in figure 6.42. As the pore walls are mirror images of each other the data are averaged over both surfaces. From the density profiles it is seen that the effective volume of the pore decreases with oxidation.

The boundary layer is defined as the region below the first minimum in the density (figure 6.41). The boundary layer is quite diffuse, compared with that typically observed on a regular surface, and is up to 0.75 nm wide in the S_0 pore. The position of the simulation cell boundary during the initial creation of the PDMS surface is at 1.5 nm. It is therefore evident that a significant amount of penetration of the surface by water molecules is occurring.

Table 6.32 shows the position of the equimolar dividing surface (EMDS), the position of the peak density and the position of the first minimum in the density profile in the PDMS systems. All water molecules below this minimum are considered to be part of the boundary layer next to the wall. The width is decreased upon oxidation and the surface roughness increases. There

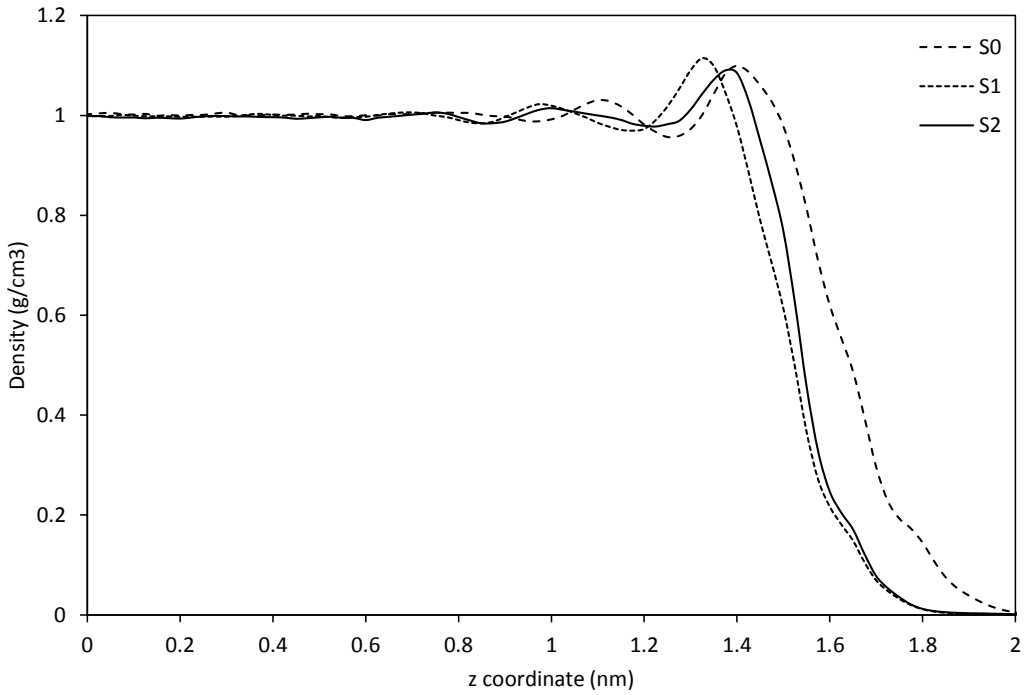


Figure 6.42: Fluid density Profiles for the three Surfaces

is no substantial difference seen in the magnitude of the density of water at the interface.

Surface	EMDS (nm)	Peak (nm)	Minimum (nm)
S_0	1.650	1.400	1.265
S_1	1.525	1.325	1.175
S_2	1.540	1.375	1.225

Table 6.32: Details of the Boundary Layer (Relative to Center of Pore)

6.3.2 Equilibrium Molecular Dynamics Simulations (EMD)

The rate of fluctuation of the center of mass is related to the interfacial friction, as shown earlier in equation 3.30. Taking the time autocorrelation function of the center of mass velocity and fitting to equation 3.32 leads to the relaxation time for these systems.

The collective velocity autocorrelation functions as calculated for each pore are shown in figure 6.43. This function decays faster with increasing degree of oxidation, suggesting that the interfacial friction increases. The relaxation times are displayed in table 6.33. Using these relaxation times the slip coefficient in the pores can again be predicted under flow conditions using equation 3.38. These PDMS pores all have very low slip coefficients suggesting near no-slip conditions at the wall. This will have consequences if PDMS nanopores are ever used in a device, as flow

rates would be very low due to the high interfacial frcition.

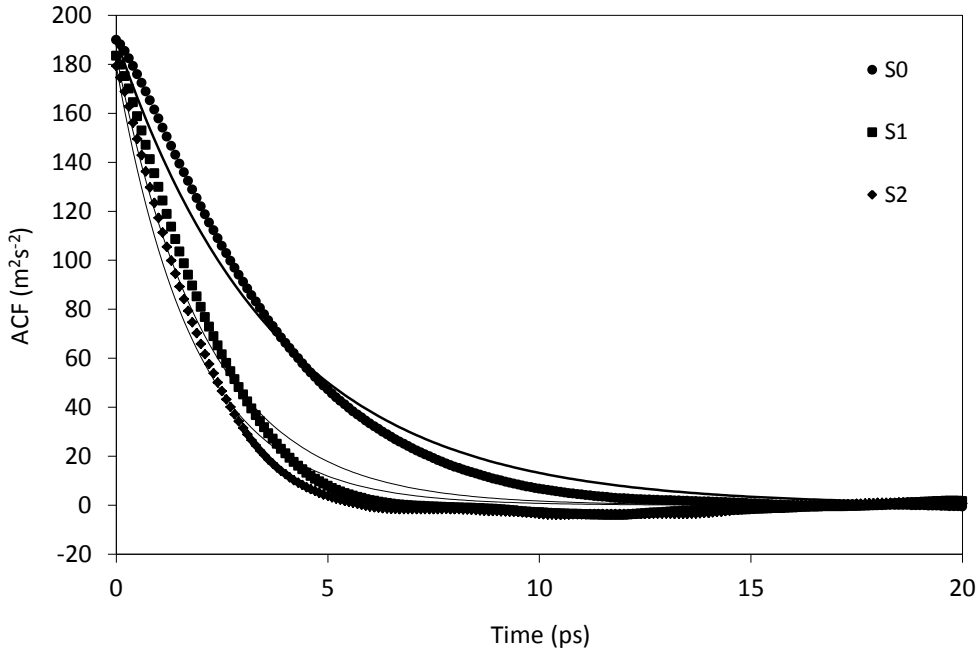


Figure 6.43: Autocorrelation functions for each of the PDMS surfaces

System	τ_{EMD} (ps)	l_s (nm)
S_0	1.915	0.166
S_1	1.401	0.085
S_2	1.377	0.047

Table 6.33: EMD Data for the PDMS Slit-Pores

The fits for these correlation functions for these cases are not very well aligned with the original data and the exponential decay is not ideal. Again some regions of the curve are negative, as seen previously in figure 6.30 for the strong carbon-wall interaction suggesting that some of this effect is due to interfacial water. Thus, to see if a better fit could be obtained molecules closest to the wall were excluded from the calculation of the center of mass velocity at each step as they could be negatively affecting the average. Different amounts of the surface layer of the fluid were excluded and a fit of the autocorrelation function performed for each.

It was found that a better fit could indeed be obtained for the S_0 pore but at the expense of agreement between EMD/NEMD results. A comparison is shown in figure 6.44. The intercept increases as mass is excluded. In the S_1/S_2 pores little improvement was seen in fit quality.

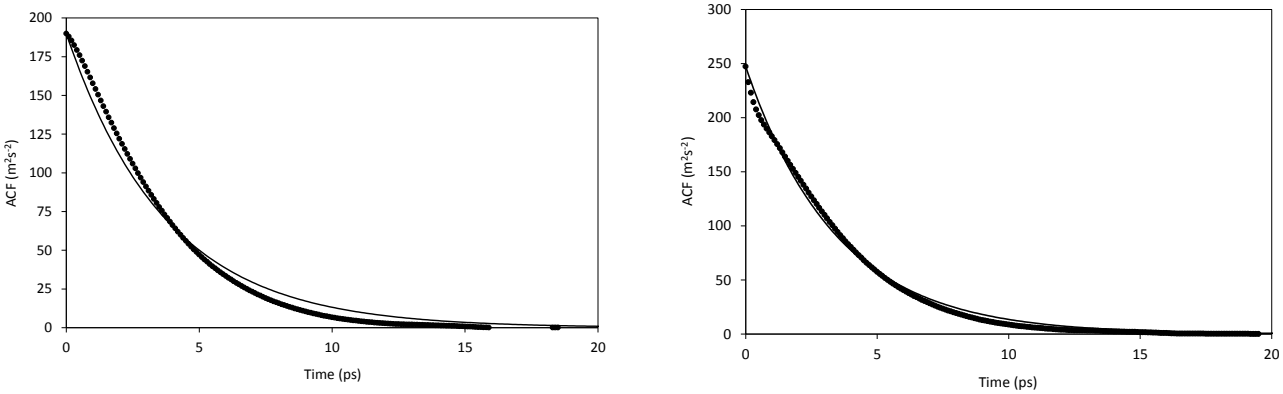


Figure 6.44: Comparing the best fit and the original fit (PDMS S_0)

6.3.3 Non-equilibrium Molecular Dynamics Simulations (NEMD)

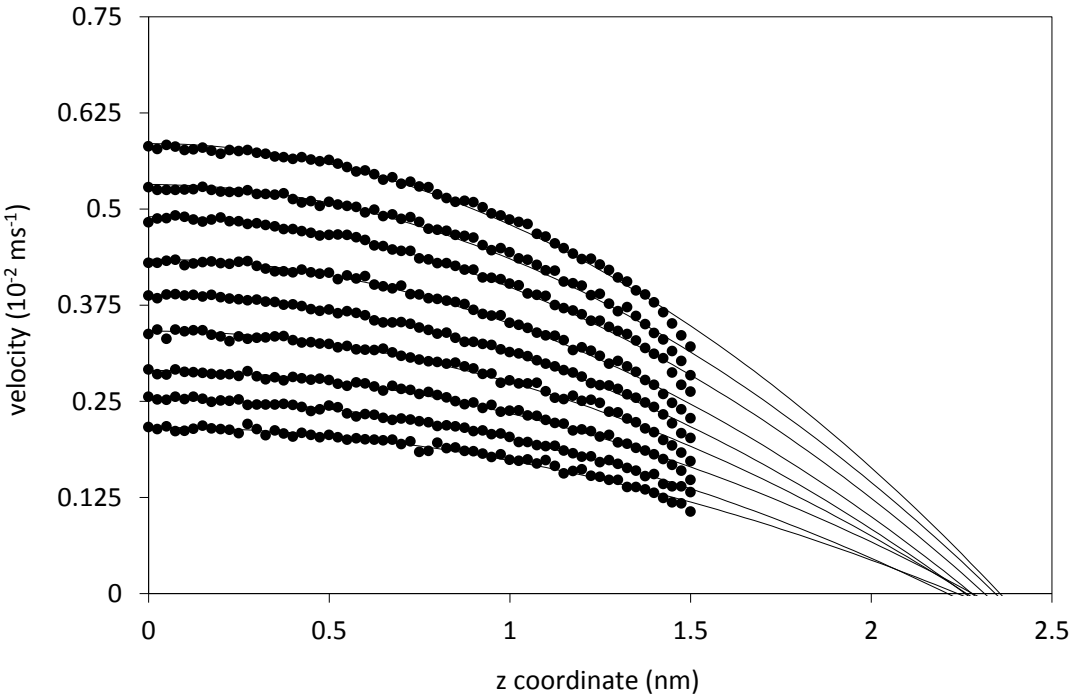


Figure 6.45: Velocity profiles in the PDMS system (S_0)

The systems were also studied under the influence of a gravitational force. Firstly a suitable value for the external driving force was determined. This involved trying different values for the gravitational field strength in the x-direction to find the best figure. For each value a velocity profile across the length of the pore in the z direction was determined and this then fit to equation 3.4, to determine the peak velocity and slip lengths. Above 0.2×10^{14} ms^{-2} plug flow

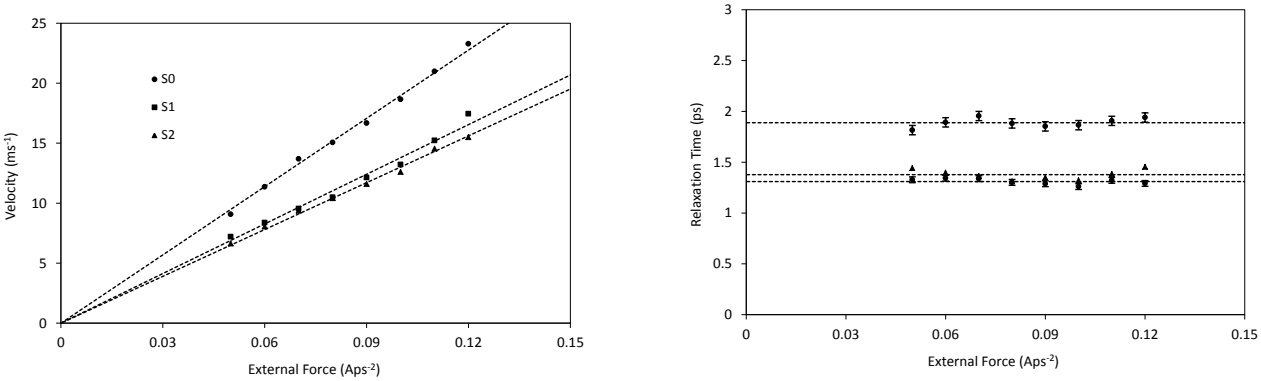


Figure 6.46: The NEMD relaxation time and slip coefficient as a function of external force for each system

is seen. The region between 0.2 and 0.01×10^{14} ms^{-2} shows values which have constant slip coefficients - this is the region where the external force/ frictional force balance and the slip length is relatively independent of external force. Using this value flow simulations across each of the systems (untreated, 16 oxidised replacements and 32 oxidised replacements) were carried out.

Flow simulations in each pore were conducted under the influence of an external field. The velocity profiles inside the S_0 pore are shown in figure 6.45 for a range of values of the external gravitational force. Gravitational field values were chosen to be 0.05, 0.06, 0.07, 0.08, 0.09, 0.10, 0.11 and 0.12 $\times10^{14}$ ms^{-2}. At these flow rates the velocity profile is parabolic, and the viscosity of the water can be calculated by fitting a parabolic expression to the laminar flow profile. The value obtained is $6.5 \pm 0.3 \times 10^{-4}$ Pa.s, which compares favourably with the value of 6.4×10^{-4} Pa.s reported in previous simulation studies for SPC/E water [116]. Also shown in figure 6.47 are flow profiles for a chosen value of external force (0.09×10^{14} ms^{-2}) for each pore. It can be seen that the flow rate is substantially reduced in the oxidised pores.

The relaxation time in the pore is linked to the average flow velocity by equation 3.36. Relaxation times have been calculated using this formula for each value of gravitational field strength. The average compares well to the EMD value for all three systems. Furthermore the slip lengths derived from a fit to the flow profile agree favourably with those predicted by equation 3.38. These low slip coefficients and enhancements suggest that the flow could be reasonably described as 'no-slip' over these highly amorphous surfaces, unlike in the carbon systems.

Molecules in the boundary layer were monitored during the simulation as they underwent col-

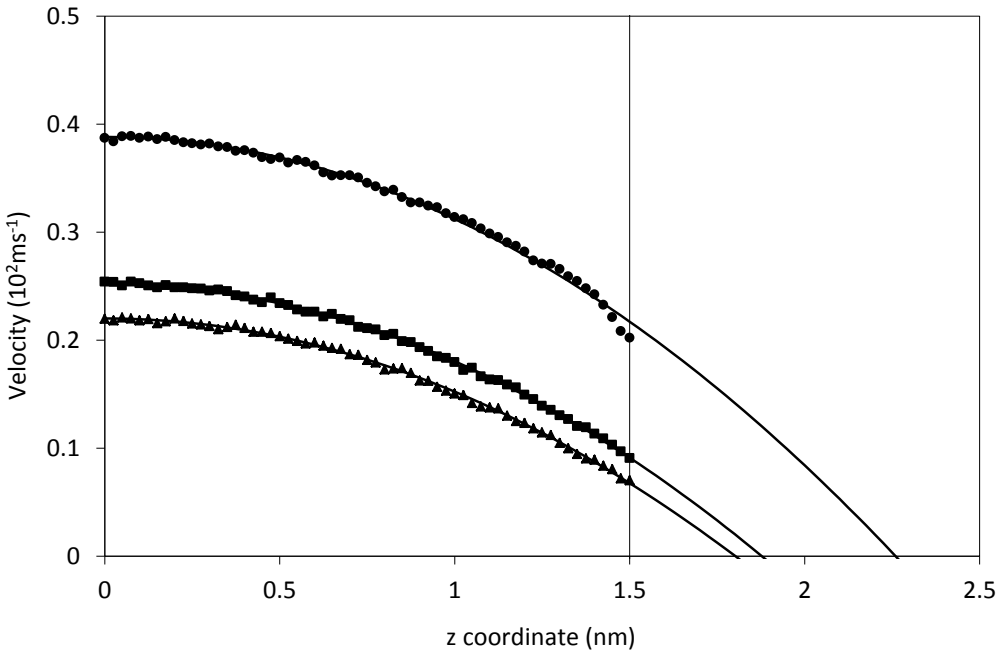


Figure 6.47: Velocity profiles in each system at the same external force

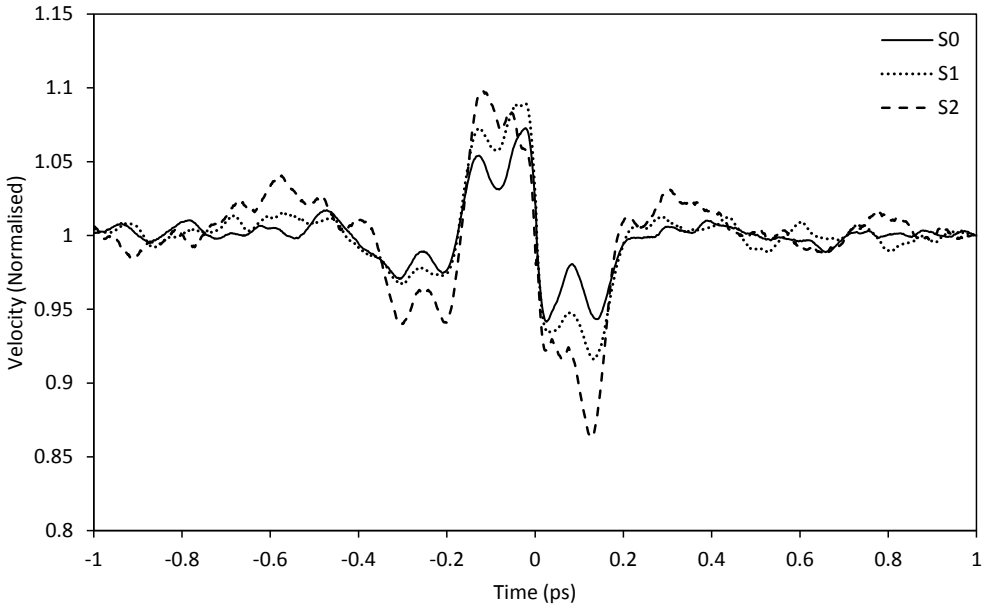


Figure 6.48: The Velocity of Colliding Particles in the PDMS System

lisions with the wall, as defined by equation 3.24. The component of the molecular velocity in the direction of flow was averaged for all colliding molecules as a function of the time before and after each collision. The average temporal streaming velocities are shown for each PDMS pore

g (10^{14}ms^{-2})	ΣF_{wf} (pN)	u_{av} (ms^{-1})	u_{max} (ms^{-1})	u_s (ms^{-1})	l_s (nm)	η (10^{-4}Pas)	τ (ps)
0.05	-61.77	9.0763	11.8763	3.9077	0.1459	6.617	1.8153
0.06	-74.115	11.3546	14.9050	4.8009	0.1360	6.262	1.8924
0.07	-86.469	13.6810	17.9599	5.7828	0.1359	6.062	1.9544
0.08	-98.782	15.0499	19.5498	6.7438	0.1693	6.588	1.8812
0.09	-111.097	16.6708	21.5468	7.6704	0.1863	6.839	1.8523
0.10	-123.443	18.6456	24.2368	8.3251	0.1671	6.628	1.8646
0.11	-135.713	20.9748	27.2533	9.3856	0.1684	6.492	1.9068
0.12	-148.141	23.2803	30.3592	10.2134	0.1566	6.282	1.9400
Average					0.1582	6.471	1.8884
St Dev					0.0107	0.251	0.0458

Table 6.34: Flow data for the S_0 PDMS-Water system

g (10^{14}ms^{-2})	ΣF_{wf} (pN)	u_{av} (ms^{-1})	u_{max} (ms^{-1})	u_s (ms^{-1})	l_s (nm)	η (10^{-4}Pas)	τ (ps)
0.05	-57.206	7.2039	10.3273	2.6183	0.08657	5.932	1.4408
0.06	-68.686	8.3753	11.6532	3.5628	0.11802	6.783	1.3959
0.07	-80.058	9.5469	13.4213	3.8589	0.09567	6.695	1.3638
0.08	-91.491	10.4894	14.9512	3.9385	0.06780	6.644	1.3112
0.09	-102.972	12.1282	17.1229	4.7950	0.08681	6.677	1.3476
0.10	-114.392	13.2129	18.5522	5.1269	0.08252	6.813	1.3213
0.11	-125.975	15.2179	21.4522	6.0647	0.08996	6.538	1.3834
0.12	-137.373	17.4518	24.3274	7.3569	0.11386	6.467	1.4543
Average					0.09265	6.569	1.3773
St Dev					0.01394	0.282	0.0519

Table 6.35: Flow data for the S_1 PDMS-Water system

in figure 6.48. The profiles were also normalised by dividing by the slip velocity.

In contrast to earlier studies of flow over crystalline surfaces of low roughness, for all the PDMS surfaces studied here clear peaks were not seen thus making the determination of u_{in} and u_{out} more difficult. For the PDMS profiles shown in figure 6.48 there are two distinct peaks evident in the temporal streaming velocity profiles before and after collision. This suggests that there are two types of collision occurring. The collision times, measured from peak to peak, are approximately 0.1 ps for the fast collision and 0.3 ps for the slower collision. The fast collision is relatively unaffected by oxidation whereas the amount of velocity lost in the slower collision increases as the degree of oxidation is increased. One conclusion that may be drawn is that the faster collisions are occurring at low affinity points on the surface and are essentially repulsive and therefore rapid. The slower collisions, on the other hand, occur at sites of high affinity whose number increase as hydroxyl groups replace methyl groups during oxidation. Not all repulsive collisions are necessarily specular with respect to the plane of the surface, due to the roughness.

g (10^{14}ms^{-2})	ΣF_{wf} (pN)	u_{av} (ms^{-1})	u_{max} (ms^{-1})	u_s (ms^{-1})	l_s (nm)	η (10^{-4}Pas)	τ (ps)
0.05	-57.924	6.6379	9.3936	2.3415	0.05612	6.724	1.3276
0.06	-69.634	8.0571	11.5307	2.6414	0.03452	6.401	1.3429
0.07	-81.149	9.3683	13.5444	2.8574	0.01609	6.211	1.3383
0.08	-92.779	10.4122	14.7919	3.5839	0.04853	6.769	1.3015
0.09	-104.451	11.594	16.5088	3.9315	0.04409	6.786	1.2882
0.10	-115.844	12.6061	17.1331	4.1662	0.04948	7.313	1.2606
0.11	-127.636	14.5415	20.6123	5.0765	0.05287	6.714	1.3220
0.12	-139.075	15.4938	22.0543	5.2655	0.04473	6.778	1.2912
Average					0.04330	6.712	1.3090
St Dev					0.01277	0.321	0.0285

Table 6.36: Flow data for the S_2 PDMS-Water system

It would appear that some molecules are being trapped inside the rough surface and reversing direction upon collision. This effect was averaged out over all flow directions but also seems to contribute to the reduction of the peak velocity before collision.

To obtain a reliable value for Maxwell's coefficient using equation 3.24 a large number of collisions with the wall at various collision velocities and angles are required to achieve the clear peaks seen for the earlier smooth surfaces. For the extremely rough PDMS surfaces though, this method cannot be used due to the multiple peaks being superimposed on top of each other and inseparable. As shown earlier in figure 6.48 the velocity profiles of particles colliding with the wall are very complicated and have multiple peaks. Different flow directions across an amorphous surface will show a wide variation in the magnitude of Maxwell's coefficient and the non-equilibrium and equilibrium Maxwell coefficient values obtained will not be in agreement. For model systems the two methods agree [76]. The equilibrium definition of Maxwell's coefficient samples all flow directions across the surface and for a highly isotropic surface such as the PDMS only looking at non-equilibrium flow in one direction may not be sufficient to gain agreement due to the many possible collision events/geometries.

In Maxwell's model collisions are assumed to be relatively simple (just two distinct types), but the roughness of the surfaces complicates the definition of a collision and more complex collision events than the theory allows may be occurring. The model was developed for gases not liquids. Increased numbers of collisions which do not fit Maxwell's theory may be occurring in the condensed phase, with fluid-fluid interactions to consider as well as fluid-wall. An attempt was made to achieve a cleaner plot by narrowing the definition of a collision (i.e. a z-reversal) to only those where the wall/fluid force is significant or by restricting the region where collisions

are included. This does improve the data in some cases but a universal improvement is not seen across all simulations. Multiple collision events with the wall due to trapped molecules could be occurring or fluid-fluid interactions could be responsible for the disagreement, which are not taken into account in Maxwell's model which was derived for low-density gases.

6.4 Data Summary

A wide range of different surfaces have been simulated and the only ones found to have any significant enhancement relative to the expected flow rates are the smooth graphitic ones. Many different parameters within the systems were varied but no enhancements are close to those found experimentally. Poor flow behaviour through nanoscale pores will make construction of nanofluidic devices very difficult. This data shows that significantly enhanced flow on the nanoscale will be very difficult to achieve, as experimental surfaces are rarely smooth. It is also obvious from this data that the flow behaviour is dictated by factors far more complicated than just the interaction strength and that the surface structure and roughness play a large part in the dynamics. In fact they seem to have a much larger effect than the nature and composition of the surface. The slip coefficient for the amorphous carbon surface is also found to be fairly constant over a range of different pore widths.

Pore	h/r (nm)	Kn	rough (nm)	C.A. (°)	τ_{EMD} (ps)	τ_{NEMD} (ps)	$l_{s\mathrm{EMD}}$ (nm)	$l_{s\mathrm{NEMD}}$ (nm)	ε
Graphene	3.0	0.773	0.0014	84	147.648	148.085	69.661	71.215	143.430
Diamond	3.0	0.773	0.0081	96	7.009	7.514	3.099	2.902	6.804
Diamond (mob)	3.0	0.773	0.0081	96	8.284	7.998	3.579	3.245	7.491
AmCarb	1.0	3.479	0.0419	98	0.665	0.493	1.326	1.531	10.186
AmCarb	1.5	1.897	0.0419	98	1.089	0.994	1.137	1.062	5.248
AmCarb	2.0	1.227	0.0419	98	1.622	1.608	1.042	1.051	4.153
AmCarb	3.0	0.773	0.0419	98	3.153	3.322	1.226	1.145	3.371
AmCarb	4.0	0.564	0.0419	98	5.034	5.672	1.069	1.151	2.665
AmCarb	6.0	0.364	0.0419	98	9.115	9.589	1.018	1.097	2.058
AmCarb (RPM)	6.0	0.364	0.0419	98	9.115	10.326	1.018	1.159	2.089
AmCarb (RPM)	9.0	0.246	0.0419	98	17.374	16.925	1.087	1.072	1.719
AmCarb (RPM)	12.0	0.183	0.0419	98	29.305	28.673	1.227	1.207	1.609
CNT	3.0	0.802	0.0014	84	69.320	69.001	65.288	65.494	350.303
CNT	6.0	0.364	0.0014	84	130.512	124.615	55.080	52.486	140.963
S_0 PDMS	3.0	0.663	0.2219	124	1.915	1.888	0.166	0.158	1.316
S_1 PDMS	3.0	0.706	0.2492	100	1.401	1.377	0.085	0.093	1.186
S_2 PDMS	3.0	0.701	0.3126	76	1.377	1.309	0.047	0.044	1.088

Table 6.37: Collected Simulation data for the Water Simulations

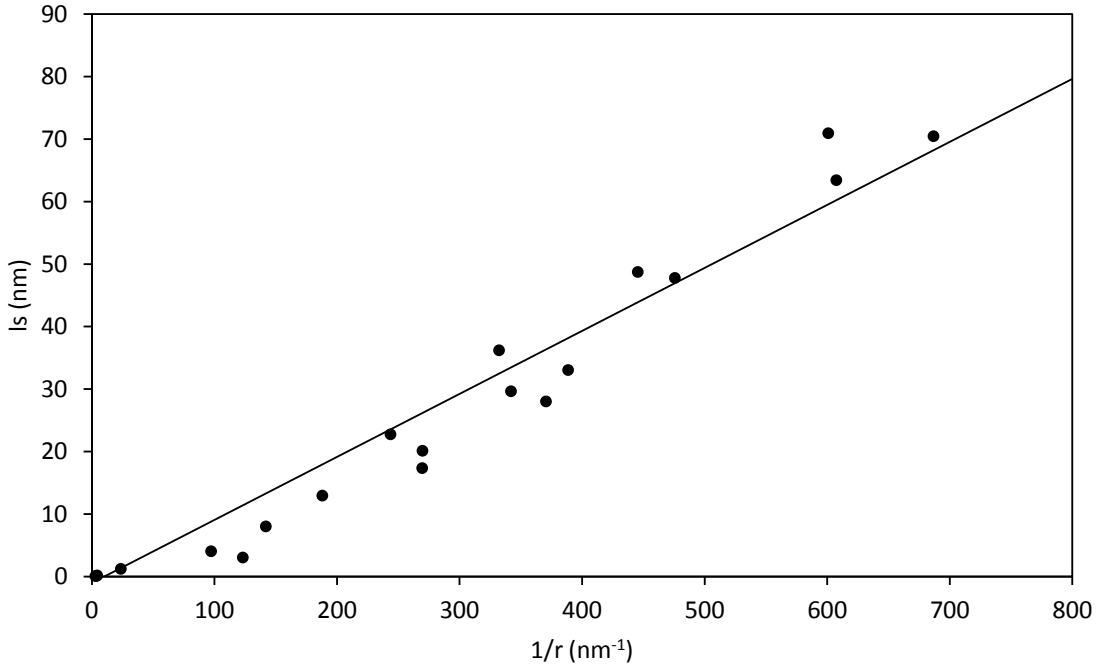


Figure 6.49: Slip Coefficient as a Function of Roughness with Fit

All the data for the various surfaces are collected in table 6.37. A plot of this data and that in table 6.19 showing the slip coefficient versus the inverse of the roughness is plotted in figure 6.49. A linear fit with the slip coefficient inversely proportional to the roughness is also included in the plot. This gives a reasonable fit to the slip coefficient data collected in the simulations, suggesting that across this sample of surfaces the slip coefficient is universally inversely proportional to the roughness. It also suggests that the slip length in the graphene or carbon nanotube systems are roughly as expected due to the extreme smoothness of the surfaces rather than to other effects. In this work a wide range of roughnesses have been used, ranging from the very rough PDMS with low slip and the extremely smooth graphene with a large slip coefficient. Experimentally it will be difficult to produce surfaces with higher smoothness than this, suggesting a limit to any possible flow enhancement.

Chapter 7

Modelling the Membrane

7.1 Models of Biological Membranes

7.1.1 Previous Simulation Work

Several pieces of previous simulation work have looked at the interactions between model membranes and nanotubes. Coarse grained studies of the interaction between both a 0.5nm length hydrophobic tube and a tube possessing hydrophilic ends with a Dipalmitoylphosphatidylcholine (DPPC) membrane have been undertaken [134]. The free energy of water conduction through the tubes was compared with water permeation across the lipid bilayer. The hydrophilic tube was found to conduct water more efficiently as the hydrophilic ends of the tube stabilised the tube in the bilayer. Water diffusion through single-walled nanotubes (SWNT) inserted into phospholipid membranes has also been studied previously using non-equilibrium molecular dynamics with electric fields [135].

Permeation of molecules across cell membranes occurs by transport through the aqueous phase outside the membrane, subsequent diffusion across the bilayer and then movement to another aqueous phase on the other side. Permeability coefficients of small organic molecules (benzene, ethanol and water) across a DPPC bilayer have been previously calculated using simulation work [136].

A greater understanding of the interaction of nanomaterials with biological entities is important for toxicological purposes. The translocation of the fullerene, C_{60} and its hydroxylated derivative $C_{60}(OH)_{20}$ across a model cell membrane have been looked at. Pristine C_{60} can jump into the

bilayer but the $C_{60}(OH)_{20}$ can barely penetrate [137]. The adsorption of the C_{60} into the bilayer is driven by the hydrophobic interactions between the C_{60} and the lipid tails. It was also predicted in this study that complete translocation across the bilayer would take around 2ms, well beyond the range of molecular dynamics simulation. Clumps of fullerene nanoparticles crossing a bilayer membrane have also been previously simulated [138]. A study has also looked at the interaction of charged gold nanoparticles with a lipid bilyer membrane [139]. The forces required to drive nanoparticles of different shapes and sizes across a bilayer have also been calculated [140].

Most previous simulation work has focused on the interactions between a bilayer and nanoparticles as would be the situation when looking at transport across a normal cell membrane. Some studies though have looked more specifically to simulate a monolayer lung membrane. One such paper, published in 2008 [141] looked at the surfactant film interacting with a carbon fragment. NVT simulation work of the passage of fullerenes across a model lung surfactant layer has also previously been looked at [142]. C_{60} particles are seen to remain in the head group region for the duration of the simulation, whereas hydroxylated particles move further into the layer and sit at the interface.

Previous simulations have primarily focused on relatively small nanoparticles around the size of fullerenes [143]. To analyse larger systems and nanoparticles, mesoscale methods such as coarse-graining must typically be used. This though can eliminate atomic-scale resolution of the dynamics. In this work the range and size of particles interacting with the membrane has been extended. A much larger (diameter 3nm) particle has also been simulated atomistically, as well as several smaller particles, in order to study some of the effects of nanoparticles at biological interfaces. These particles are of environmental interest as fullerenes have been found in petrol soot and titanium dioxide is used in a number of consumer products.

7.1.2 DPPC Model

Bilayers contain a large number of different proteins/phospholipids but the most common constituent is DPPC. The most commonly used molecular model for DPPC is that proposed by Berendsen in 1994 [144]. Comparison of molecular dynamics results with experimental data (bilayer repeat distance, surface are per lipid, tail order parameters, etc) showed this to be a realistic model. Saturated 16 carbon atom chains are attached to a zwitterionic head group,

with amide/phosphate functionality (figure 7.1). United atom sites are used for the CH_3 and CH_2 groups to simplify the model by the removal of the Hydrogen atoms.

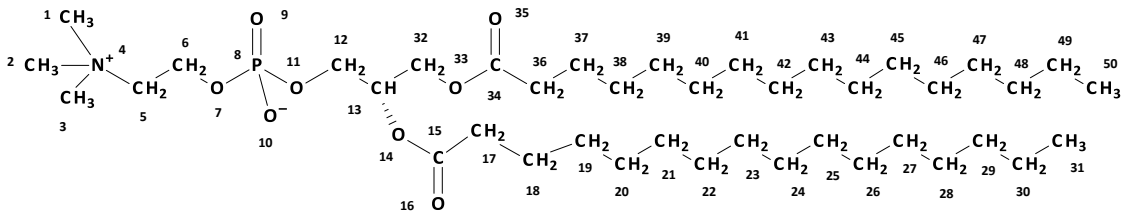


Figure 7.1: DPPC Structure

The structure factor of the monolayer is defined as the average orientation of the lipid tails with respect to the normal (z-axis).

$$S_{ij} = \frac{1}{2} \langle 3 \cos(\theta_i) \cos(\theta_j) - \delta_{ij} \rangle \tag{7.1}$$

The area per lipid in the monolayer is another quantity commonly used to characterise the system.

$$A_L = \frac{L_x L_y}{N_{Lipid}} \tag{7.2}$$

Parameters for the DPPC model were taken from Berger [145], which is an extension of the GROMOS force field. The SPC/E model [113] was used for the water molecules.

7.1.3 Nanoparticle Models

The fullerene (C_{60}) nanoparticle is modelled as a rigid sphere with a C-C bond length of 0.146nm. The hydroxylated form is the same, but with 20 -OH groups added randomly to carbon sites. The C-O and O-H bond lengths were 0.140 and 0.095nm respectively and the C-O-H angle was 106.3°. Partial charges and Lennard-Jones parameters are displayed in table 7.3.

Titanium Dioxide spheres at initial radii of 0.6nm, 1.0nm and 1.5nm were cut from a rutile lattice. They were then allowed to relax for 200ps to create an amorphous surface, using the Buckingham interaction parameters in table 7.2 [146]. These were found to be the best available

Numbers	Group	Name	σ (nm)	ϵ (kJ/mol)	charge (e)
1-3	CH_3	LC3	0.396	0.606	0.40
4	N	LNL	0.325	0.711	-0.50
5	CH_2	LH2	0.391	0.606	0.30
6	CH_2	LC2	0.380	0.606	0.40
7	O	LOS	0.300	0.711	-0.80
8	P	LP	0.374	0.836	1.70
9-10	O	LOM	0.296	0.878	-0.80
11	O	LOS	0.300	0.711	-0.70
12	CH_2	LC2	0.380	0.606	0.40
13	CH_1	LH1	0.380	0.334	0.30
14	O	LOS	0.300	0.711	-0.70
15	C	LC	0.375	0.438	0.70
16	O	LO	0.296	0.606	-0.70
17	CH_2	LP2	0.396	0.380	0.00
18-30	CH_2	LP2	0.396	0.380	0.00
31	CH_3	LP3	0.396	0.570	0.00
32	CH_2	LC2	0.380	0.606	0.50
33	O	LOS	0.300	0.711	-0.70
34	C	LC	0.375	0.438	0.80
35	O	LO	0.296	0.606	-0.60
36	CH_2	LP2	0.396	0.380	0.00
37-49	CH_2	LP2	0.396	0.380	0.00
50	CH_3	LP3	0.396	0.570	0.00

Table 7.1: Non bonded potential parameters for the DPPC Molecule

for classical molecular dynamics during a comparative study [147]. These parameters have also been used previously to simulate titanium dioxide nanoparticles [148]. Internally the structure of the nanoparticle remains crystalline. The atoms were then fixed in position relative to each other using constraints and the SHAKE algorithm during the simulations with the lipid membrane.

Atom Type	mass (a.m.u.)	A (kJ/mol)	ρ (Å)	C (kJ/molÅ^6)	charge (e)
Ti-Ti	47.8670	3003381.9	0.154	506.4	+2.196
Ti-O	-	1636556.8	0.194	1215.3	-
O-O	15.9994	1137144.0	0.234	2916.7	-1.098

Table 7.2: Buckingham Non bonded potential parameters for the Initial TiO_2 Model

The Van der Waals parameters and partial charges used for the interactions between the nanoparticle and the membrane are summarised in table 7.3. Two different models were used for the Titanium Dioxide, one with the quantum mechanically determined partial charges used during the initial formation of the nanoparticles and the other with reduced partial charges to give a better agreement with the experimental contact angle [149]. These models give contact angles with water of around 45° and 75° respectively. UFF Lennard-Jones parameters [150] were cho-

sen for the Van der Waals interactions. Lennard-Jones interactions with the lipid atoms were then determined using mixing-rules.

Atom Type	mass	σ (nm)	ϵ (kJ/mol)	charge (e)
C	12.011	0.3361	0.4057	0.0 / +0.5
O	15.999	0.2626	1.7249	-0.8
H	1.008	-	-	+0.3
Ti (I)	47.8670	0.2829	0.0712	+0.650
O (I)	15.9994	0.3930	0.2512	-0.325
Ti (II)	47.8670	0.2829	0.0712	+2.196
O (II)	15.9994	0.3930	0.2512	-1.098

Table 7.3: Non bonded potential parameters for the TiO_2

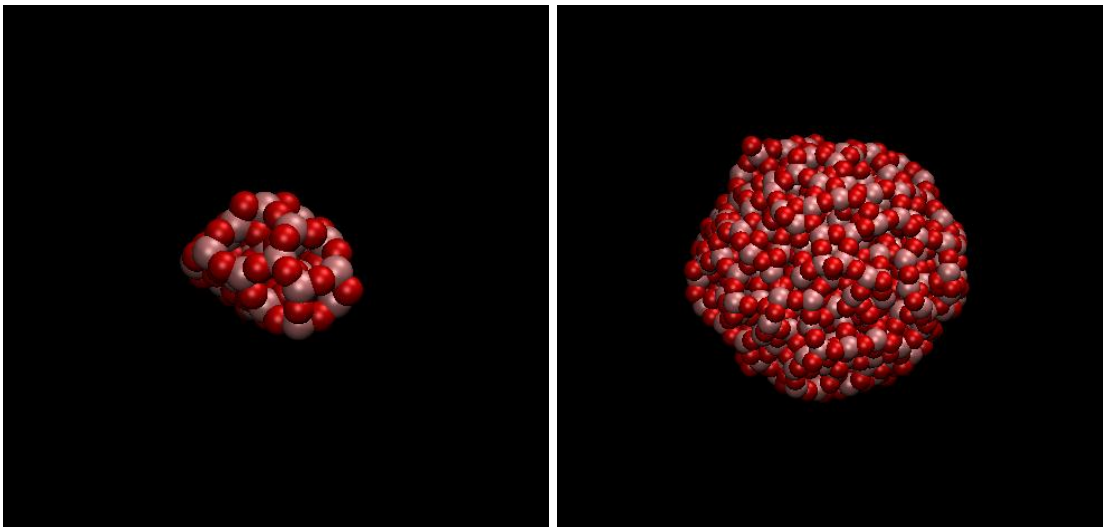


Figure 7.2: The Titanium Dioxide Nanoparticles

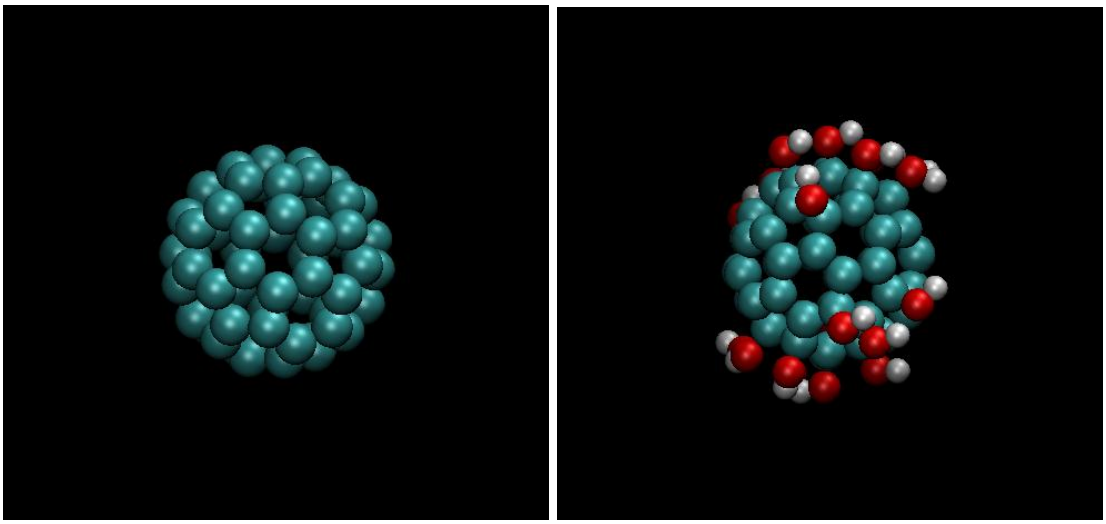


Figure 7.3: The Fullerene Nanoparticles

The nanoparticles were then characterised. For the fullerenes the radius is the position of the furthest atom from the center of mass. Due to the amorphous nature of the TiO_2 particles, they

are not perfectly spherical. The radius was thus defined as the radius from the center of mass at which 95% of the total mass is contained. These radii, and the resulting surface areas and volumes are shown in table 7.4.

Nanoparticle	Radius (nm)	Surface Area (nm^2)	Volume (nm^3)
TiO_2 Small	0.629	4.9718	1.0424
TiO_2 Large	1.543	29.9186	15.3882
C_{60}	0.351	1.5482	0.1811
$C_{60}(OH)_{20}$	0.525	3.4636	0.6061

Table 7.4: Characterisation of the Nanoparticles

7.2 Initial Equilibration

The published bilayer configuration of Berendsen and Tieleman [151], as modified previously [142], was used as a basis for the model of the lung surface. This was achieved by inverting the initial bilayer to produce a system with two vacuum-lipid interfaces. This system was then expanded relative to the original configuration, in order to accommodate the larger nanoparticle. The x and y dimensions were doubled to x=12.8nm, y=12.8nm. The z dimension was 18.0nm, allowing a large amount of vacuum between the two lipid surfaces. The number of DPPC molecules is 512 (256 per layer) and the number of water molecules is 14552. This configuration is shown in figure 7.4.

GROMACS [152] was used to perform the simulations. The simulations were run in parallel using MPI on 8-processor machines with 2.33GHz Intel Xeon processors. Integration times of around 1ns per day were achieved. A Berendsen thermostat [153] was used to fix the temperature at 310K and the lipid molecules and water phase were coupled separately. Particle Mesh Ewald [154] was used for the calculation of electrostatic forces.

Preliminary work was first carried out within the NVT ensemble. Ions were added to the system in the ratios/quantities suggested experimentally (24 Na^+, 8 K^+ and 32 Cl^-) and the system allowed to equilibrate for 20ns. A density profile along the z-axis is shown for this equilibrated system (figure 7.5). This density profile has also been separated into head/tail units in figure 7.6 which shows the separation of the system into two different regions. Approximately 1nm of charged head groups reside next to the 3nm long water layer. Next to the head groups, and exposed to a vacuum, are the uncharged lipid tails which spread for a further 1.5nm.

Average Diffusion coefficients were calculated for the two components and were found to be $1.886\times10^{-9}\mathrm{m}^2\mathrm{s}^{-1}$ for the water molecules and $0.135\times10^{-9}\mathrm{m}^2\mathrm{s}^{-1}$ for the DPPC molecule.

A second system was generated by removing one of the lipid monolayers, giving one lipid-vacuum interface and one water-vacuum interface, thus allowing the nanoparticles to approach from a different direction. Extra water molecules were added. The number of DPPC molecules in this configuration is therefore 256 and the number of water molecules is now increased to 25800. Due to the size of these systems a simulation rate of approximately 0.2ns per processor per day was achievable.

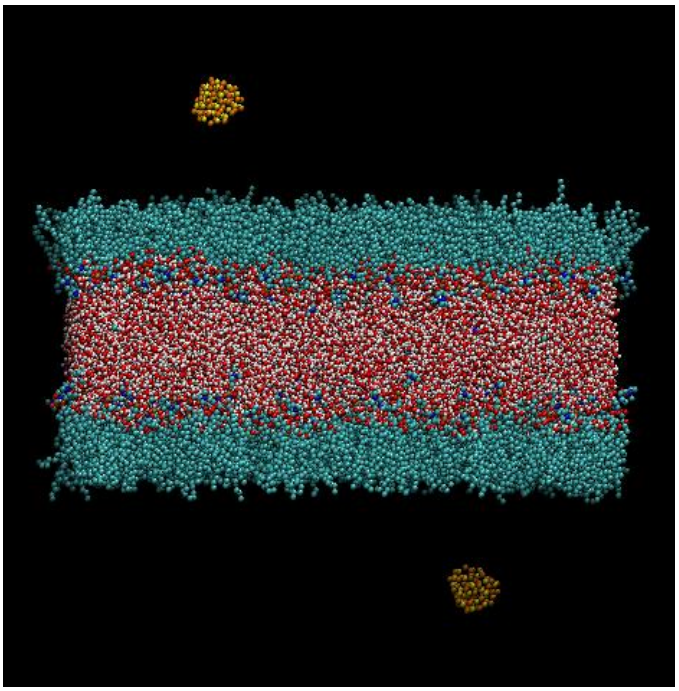


Figure 7.4: The Bilayer System with the Smallest TiO_2 Nanoparticles

During equilibration, the trajectories of the ions were tracked. Sodium ions are seen to congregate at the interface, but the Chloride and Potassium ions remain within the water phase, showing only a slight increase at the interface (figure 7.7). This is similar to the behaviour found in previous bilayer simulations with ions [155]. Diffusion coefficients after equilibration were found to be $0.248\times10^{-9}\mathrm{m}^2\mathrm{s}^{-1}$ for Sodium, $1.339\times10^{-9}\mathrm{m}^2\mathrm{s}^{-1}$ for Potassium and $1.303\times10^{-9}\mathrm{m}^2\mathrm{s}^{-1}$ for Chloride, further suggesting association of the Na^+ ions at the interface.

In order to allow the area of the membrane to fluctuate along the plane of the membrane in the x/y dimensions, the NPT ensemble was chosen for the simulations. The external pressure

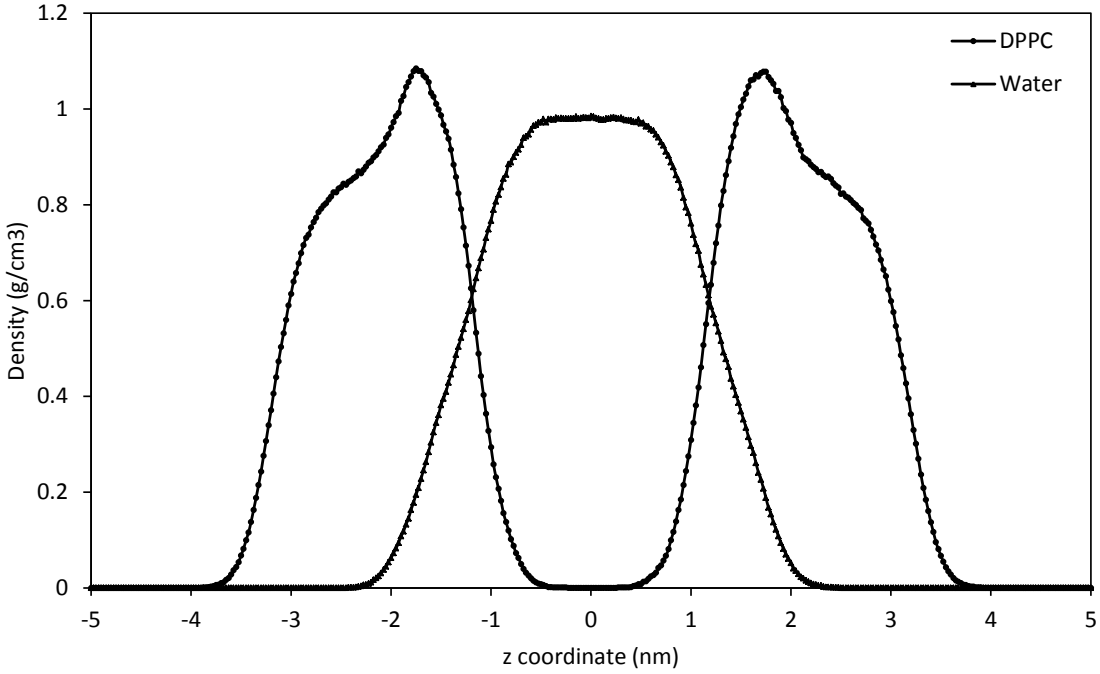


Figure 7.5: The Density Profile in the Bilayer System (Center of the Water Phase is at z=0nm, with peaks in the Lipid Density at z=±2nm)

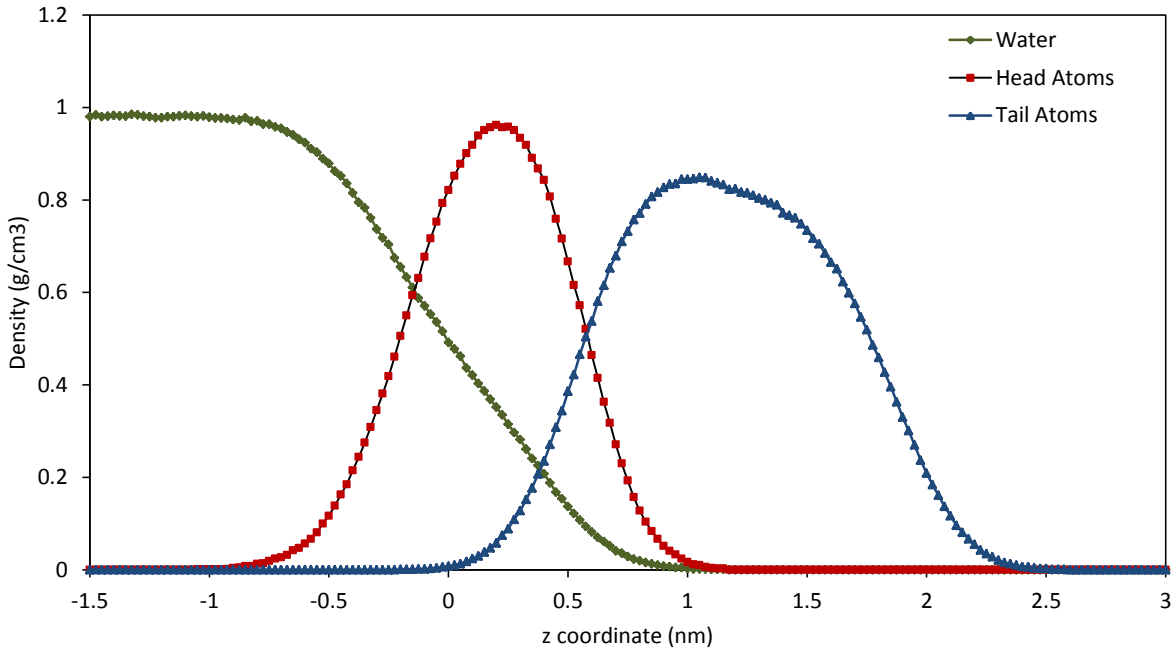


Figure 7.6: The Distribution of Head and Tail Atom Types (Middle of water phase at z=-1.5nm, water EMDS at z=0nm and start of the lipid tails at z=2nm)

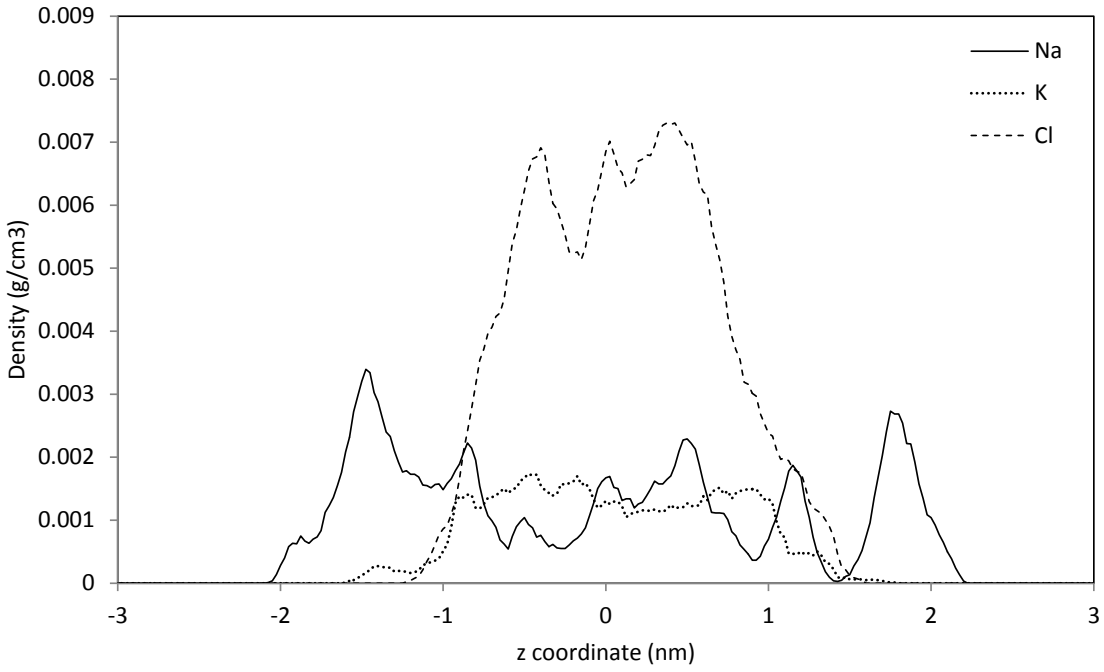


Figure 7.7: The Distribution of Ions in the Bilayer System

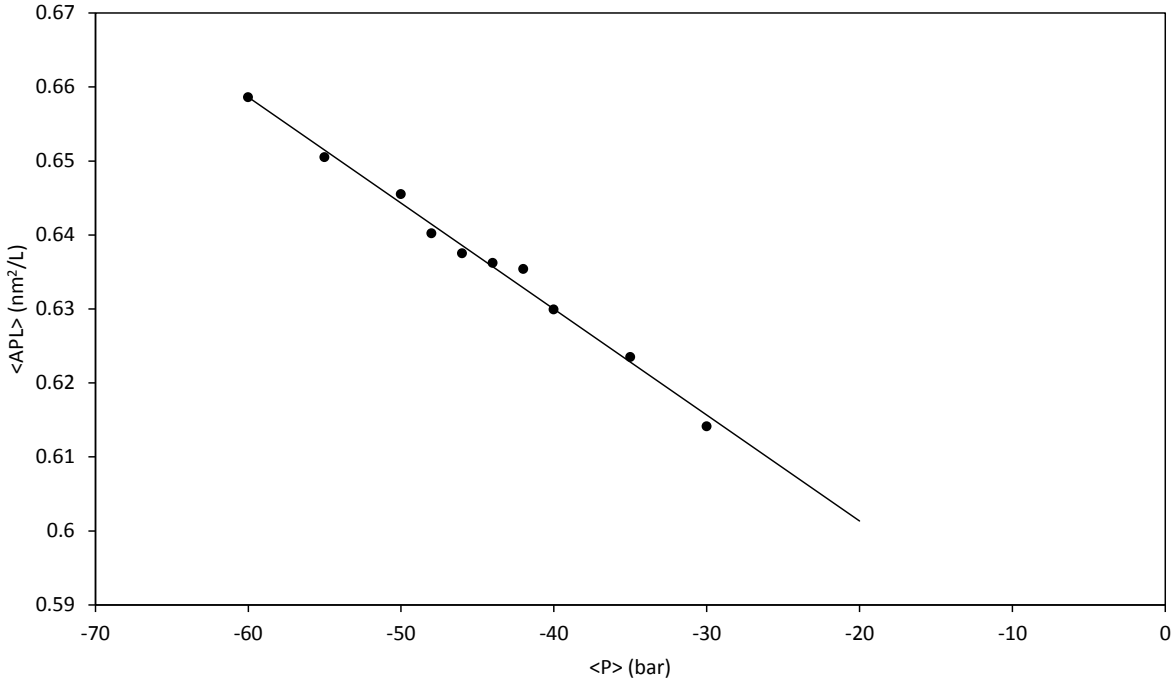


Figure 7.8: The Variation of Area per Lipid with External Pressure

values were chosen in order to give a 64ApL system for comparison with the NVT results. The variation of area per lipid and the structure factor are shown in figures 7.8 and 7.9. The average x/y dimensions were still around 12.80nm, but fluctuate with a standard deviation of 0.05nm

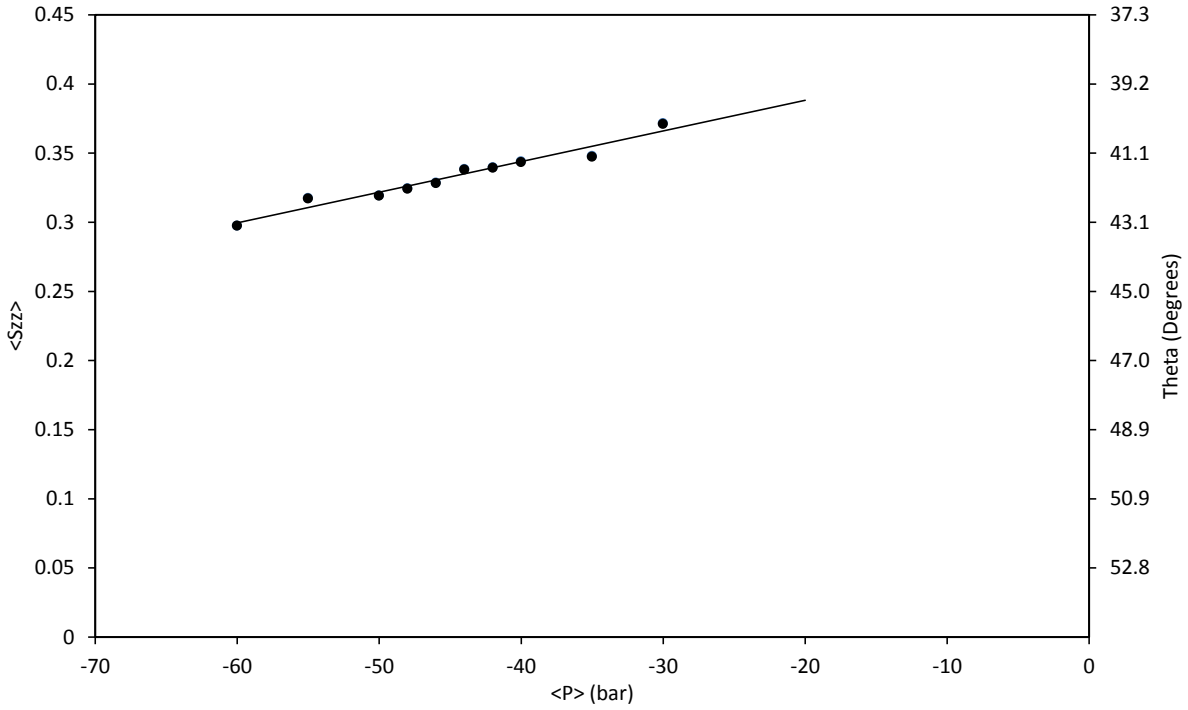


Figure 7.9: The Variation of Structure Factor with External Pressure

(0.5%). The value of the area per lipid (ApL) is therefore 64.0 ±0.2. The surface tension in the simulation was calculated to be 26.202 (±0.639) mN/m, which is comparable to that found in the lung during inhalation when the alveolus is expanded. Studies by Bangham [156] and others [157] suggest an upper range of around 25-30 mN/m.

Chapter 8

Results II - Interaction of Nanoparticles with Biomembranes

8.1 Bilayer NPT

The nanoparticles were placed above the membrane and allowed to diffuse into the tail region. Simulations were run for 50ns each and the center of mass of the nanoparticles monitored. The area per lipid (figure 8.1) and structure factor (figure 8.2) increase slightly as the nanoparticle enters.

8.1.1 Fullerene Nanoparticles

Upon starting the simulation the pristine fullerene (C_{60}) molecule is seen to rapidly enter the system and diffuse to an equilibrium position in the tail region where it remains for the rest of the simulation. Its center of mass resides in approximately the same position within the lipid tails (figure 8.3) throughout the simulation. The average positions after equilibration (relative to the water equimolar dividing surface (EMDS)) are 0.9712 $\pm$0.1532nm and 0.9761 $\pm$0.1451nm, putting them both around 0.5nm from the start of the interfacial headgroup region.

Features from the density profile are noted on the plots. The water equimolar diving surface (EMDS), the position of the start of the lipid tail atoms and the peak in the lipid head group density have been represented by straight lines on the graph. All nanoparticle trajectories are positioned relative to the equimolar dividing surface, which is therefore the zero on the z-axis.

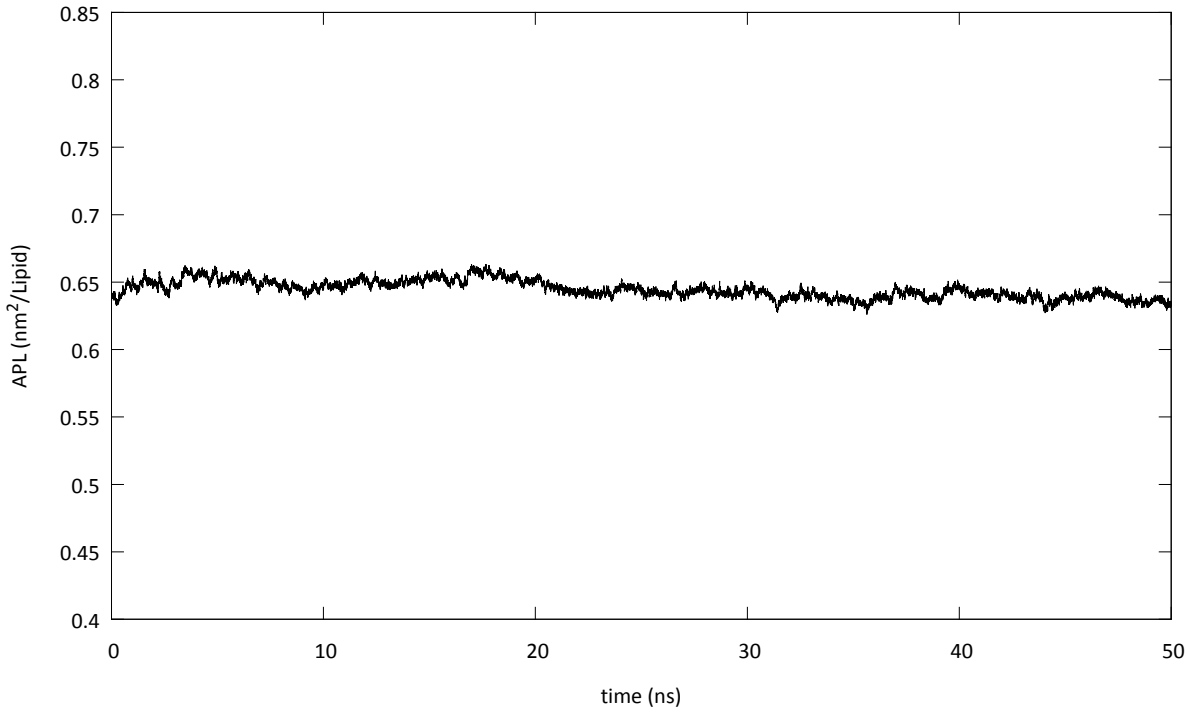


Figure 8.1: The Area per Lipid of the System during the Simulation

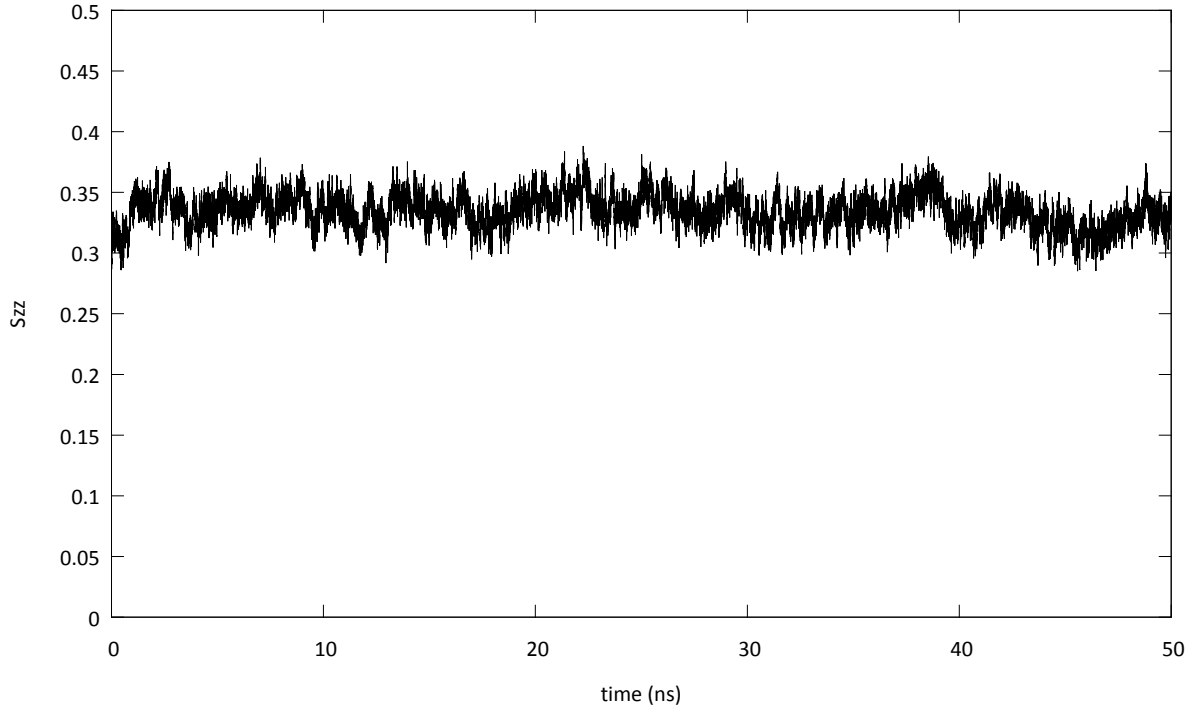


Figure 8.2: The Structure Factor of the System during the Simulation

The peak in the head group density is the line slightly above this point around z=0.3nm and the lipid tail/vacuum interface is marked by the line around 1.5nm above this.

The C_{60} nanoparticle possesses no charge and interacts via Van der Waals forces only. The

energy of the nanoparticle is also seen to be constant after entry (figure 8.4), averaging around -169.50 kJ/mol. The equilibrium position therefore is within the tail region. The lateral diffusion coefficient for the nanoparticle in this region is $0.0765 \times 10^{-9} \mathrm{m}^2\mathrm{s}^{-1}$.

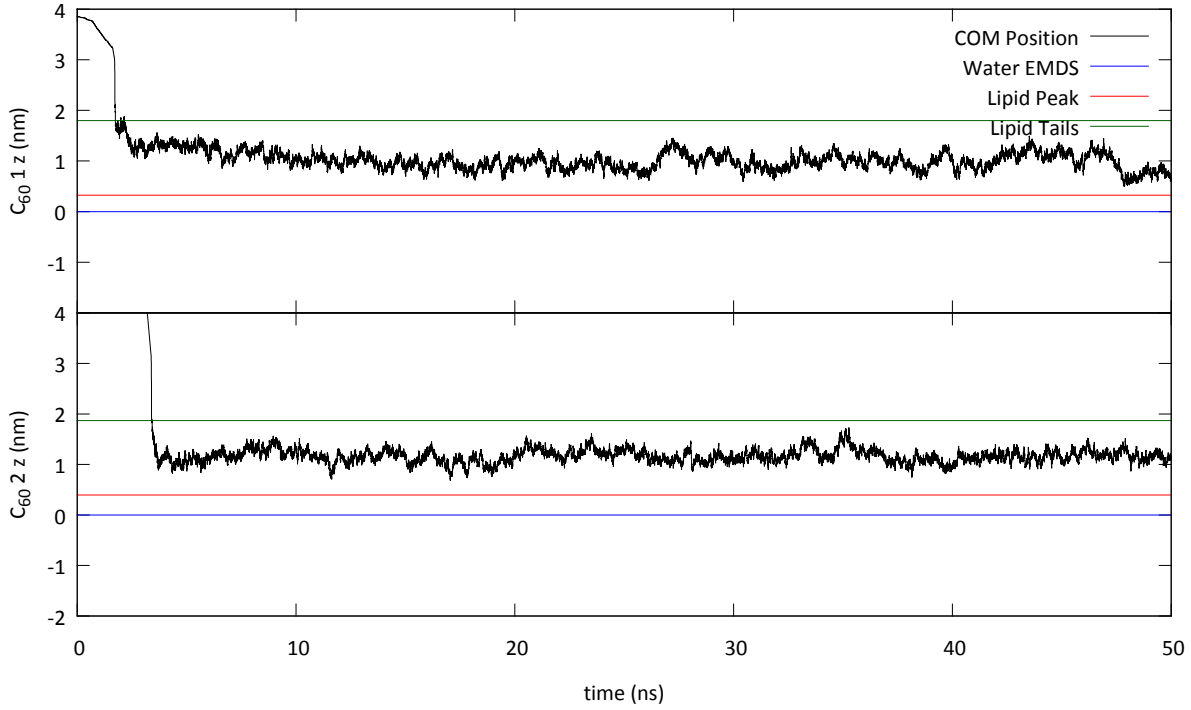


Figure 8.3: The Position of the Center of Mass of the C_{60} Nanoparticle

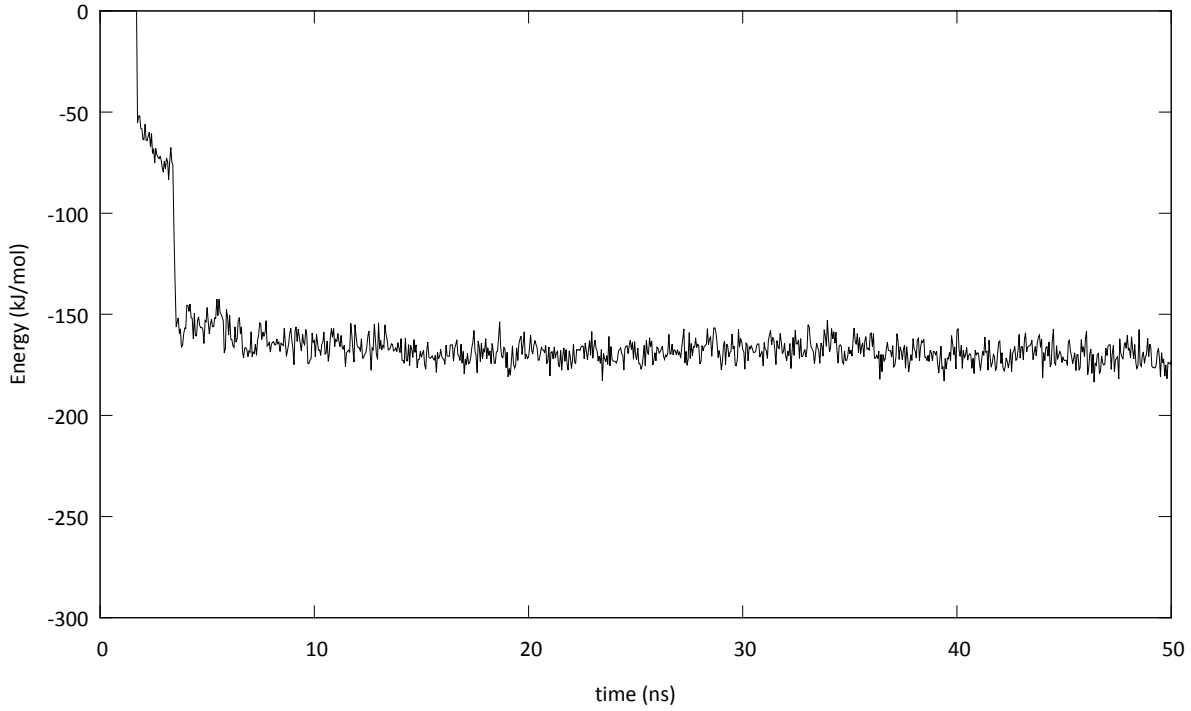


Figure 8.4: The Energy of the C_{60} Nanoparticle as a Function of Time

The hydroxylated fullerene is seen to sit further into the membrane, residing around the position of the peak in the head group density (figure 8.5). The nanoparticle in this case takes tens of nanoseconds to diffuse to an equilibrium position. The average positions after equilibration are 0.2421 ±0.1235nm and 0.06268 ±0.1401nm, both within the head group/water interface region of the monolayer.

Representation of the fluid (water/lipid) interface as a straight line does not necessarily give a clear image of the situation, so a more local picture has been obtained by measuring the types and numbers of atoms residing in the first shell around the nanoparticle. The numbers of water molecules and lipid atoms surrounding the nanoparticle have therefore been calculated. It is seen that as the nanoparticle sits at the interface, water molecules leave the bulk and totally surround the nanoparticle (both top and bottom, figure 8.6). The numbers seem to have equilibrated after 30ns. The lateral diffusion coefficient for the nanoparticle in this region is lower this time at $0.0568 \times 10^{-9} \mathrm{m^2 s^{-1}}$.

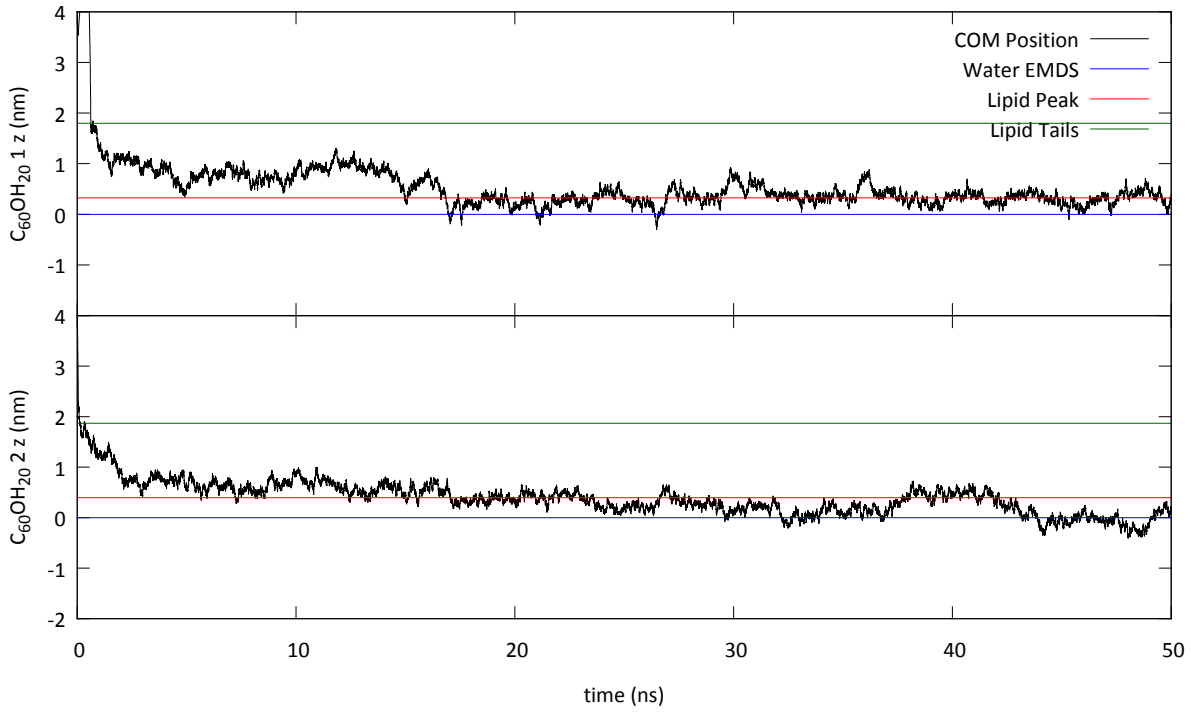


Figure 8.5: The Position of the Center of Mass of the $C_{60}(OH)_{20}$ Nanoparticle

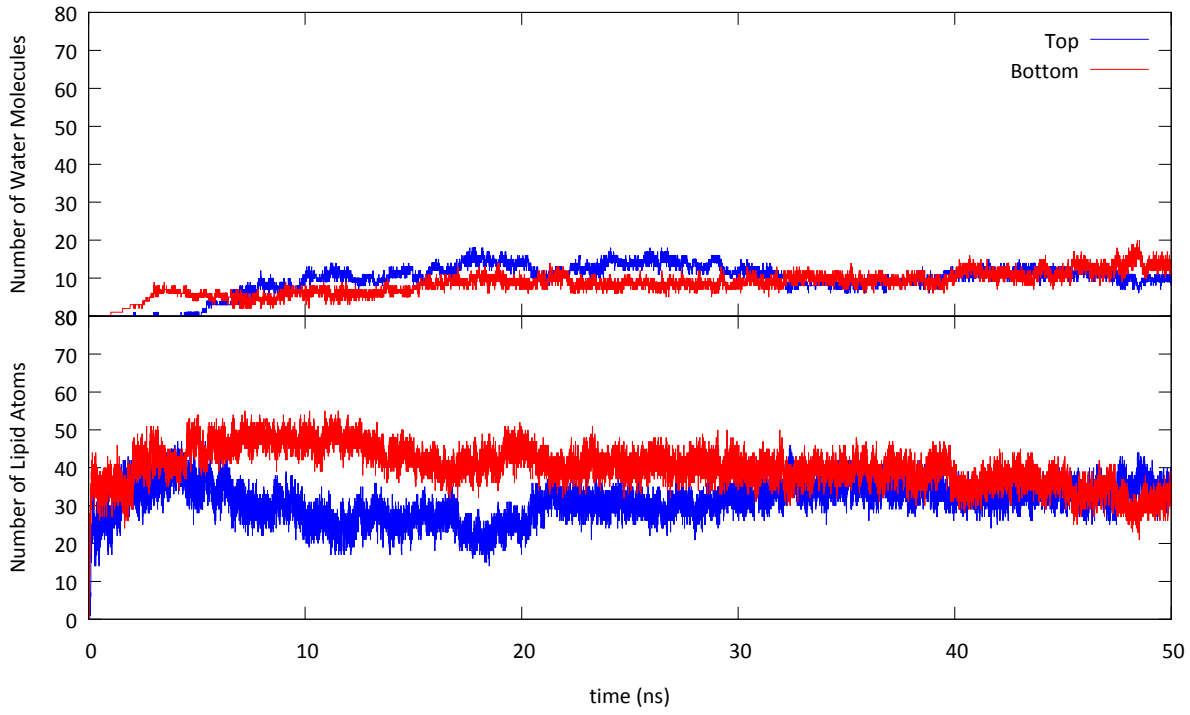


Figure 8.6: Number of Water Molecules and Lipid Atoms around the $C_{60}(OH)_{20}$ Nanoparticle as a Function of Time

8.1.2 Titanium Dioxide Nanoparticles - Potential I

r=0.6nm

The smallest TiO_2 nanoparticle with potential I is seen to behave similarly to the pristine fullerene, but sits slightly lower within the tail region (figure 8.7). The average positions of the two nanoparticles after equilibration are 0.7865 ±0.1561nm and 0.9939 ±0.1522nm.

r=1.5nm

The largest (r=1.5nm) nanoparticle behaves slightly differently. Due to its large size it can now span the entire monolayer. The center of mass position is similar to that of the r=0.6nm nanoparticle, but the edges of the nanoparticle extend well within the water layer, which allows the water to move around the nanoparticle edge, effectively bridging the layer. The entry of the nanoparticle into the layer is much slower and after 50ns, is still moving downwards. As can be seen in figure 8.10, the number of lipid atoms on the top half of the nanoparticle increases with time, this also corresponds to the center of mass of the nanoparticle moving downwards and a number of water molecules reaching the top half of the nanoparticle too, all resulting in

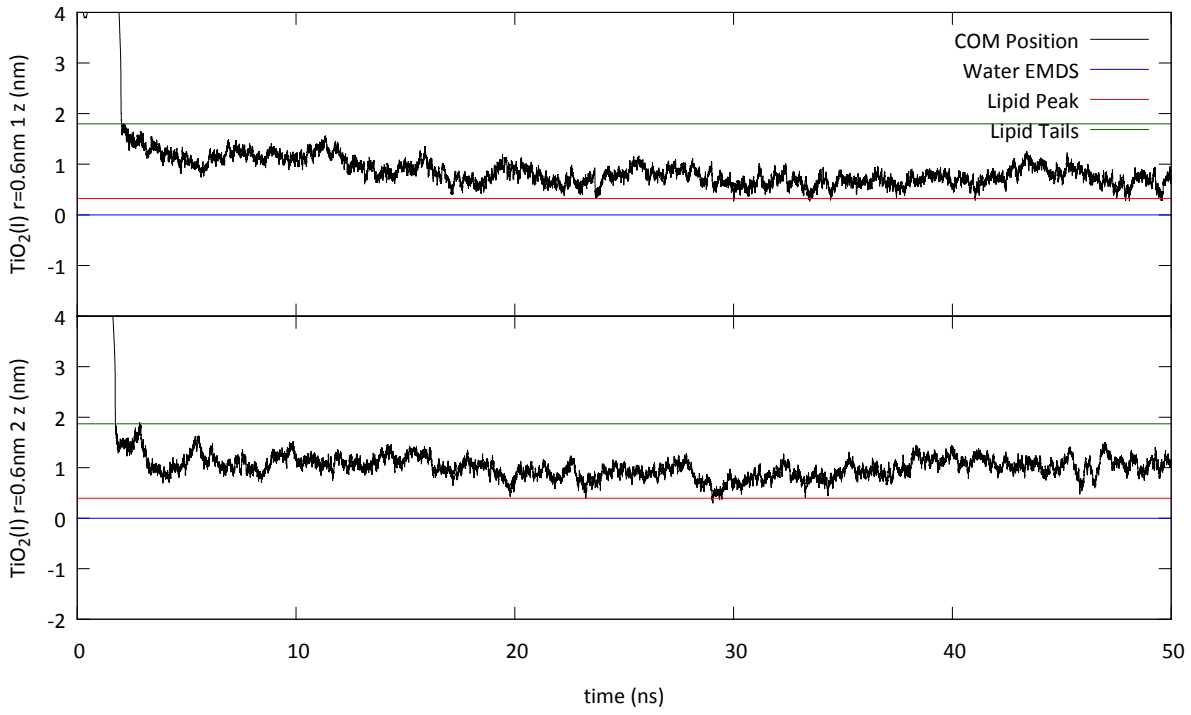


Figure 8.7: The Position of the Center of Mass of the r=0.6nm TiO_2 (I) Nanoparticle

a reduction in the amount of nanoparticle/vacuum interface on the top half. The total number of water molecules reaches 70 after 50ns.

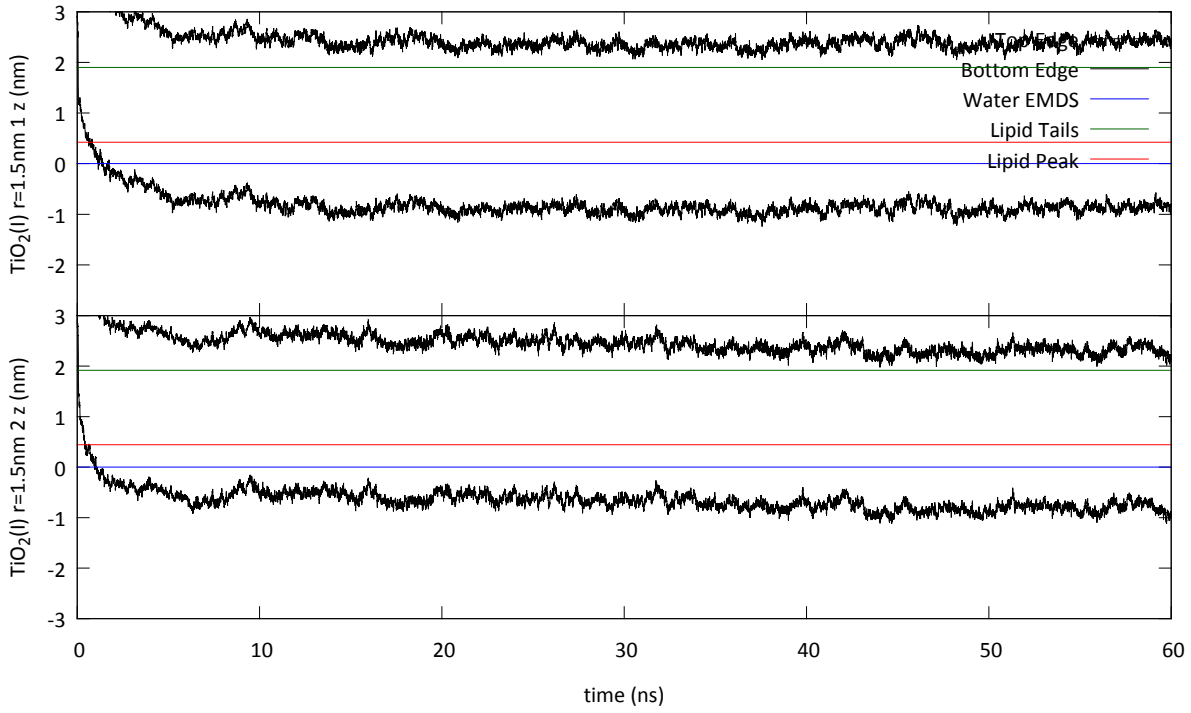


Figure 8.8: The Positions of the r=1.5nm TiO_2(I) Nanoparticle Edges

The rotation of the nanoparticle within the membrane has been calculated by measuring the θ

and ϕ angles of the nanoparticle axis with respect to that of the membrane. As can be seen in figure 8.9, there is some movement, but it is not particularly rapid once the nanoparticle has entered the membrane, nor does it only rotate in one direction. The standard deviations of the angles are $\theta = \pm 2.976°$ and $\phi = \pm 8.343°$.

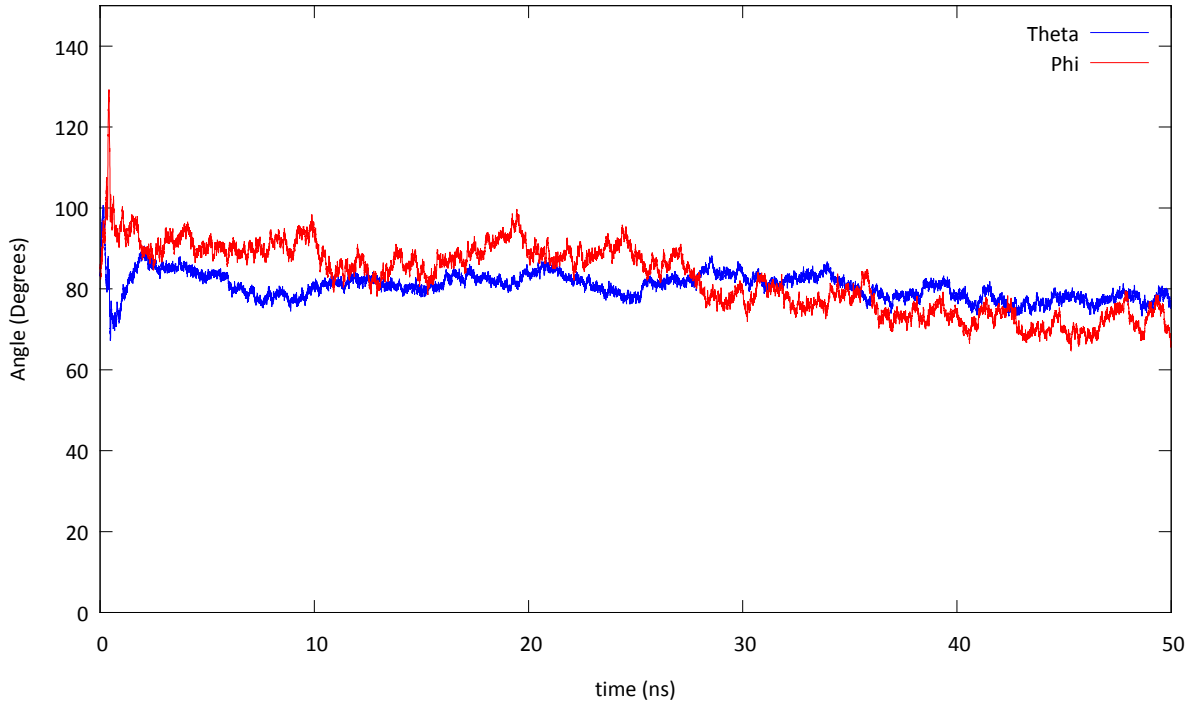


Figure 8.9: The Rotation of the r=1.5nm TiO_2 Nanoparticle

The structure factor of lipid tails as a function of distance from the center of the nanoparticle has also been calculated (figure 8.11). Closest to the nanoparticle some additional ordering is seen, relative to the bulk.

8.1.3 Titanium Dioxide Nanoparticles - Potential II

The same simulations were also carried out with the more hydrophillic potential II.

r=0.6nm

The smallest Titanium dioxide nanoparticle (figure 8.12) sits at the interface next to the water layer, closer than the previous model, but still does not completely enter the water phase. Again through monitoring the number and types of atoms surrounding the particle (figures 8.13 and 8.14), it can be seen that there are still lipid atoms surrounding the particle on both top/bottom

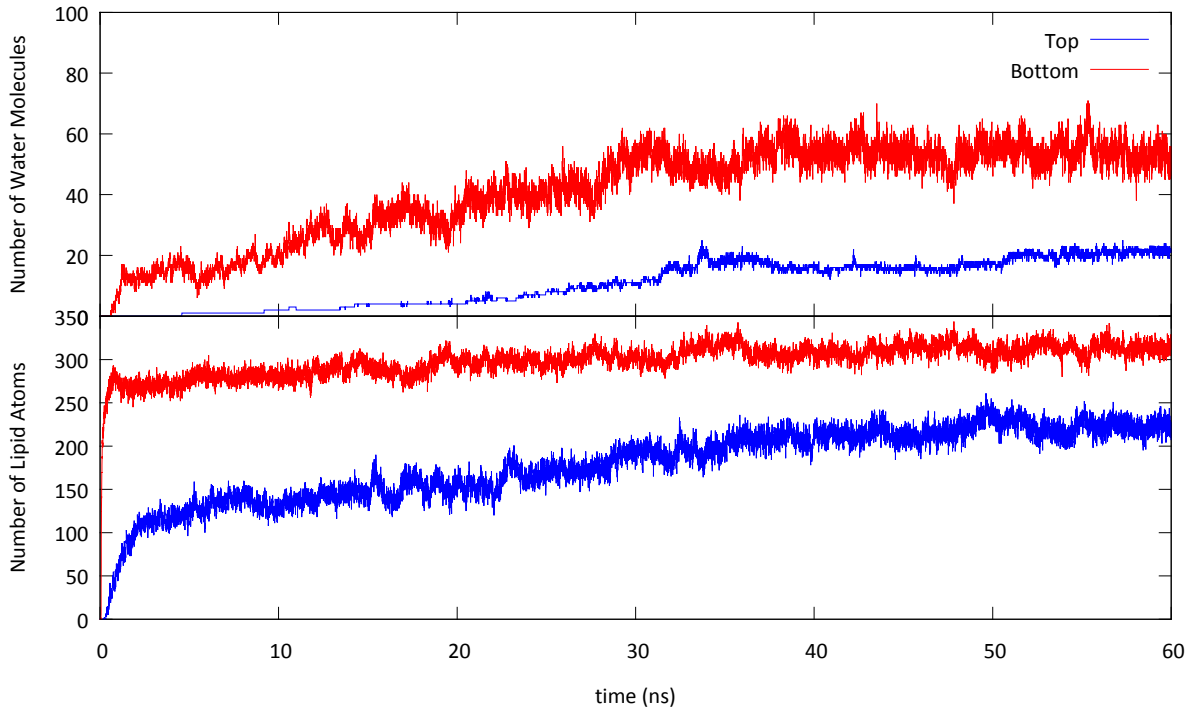


Figure 8.10: The Number of Water Molecules on the r=1.5nm TiO_2(I) Nanoparticle as a Function of Time

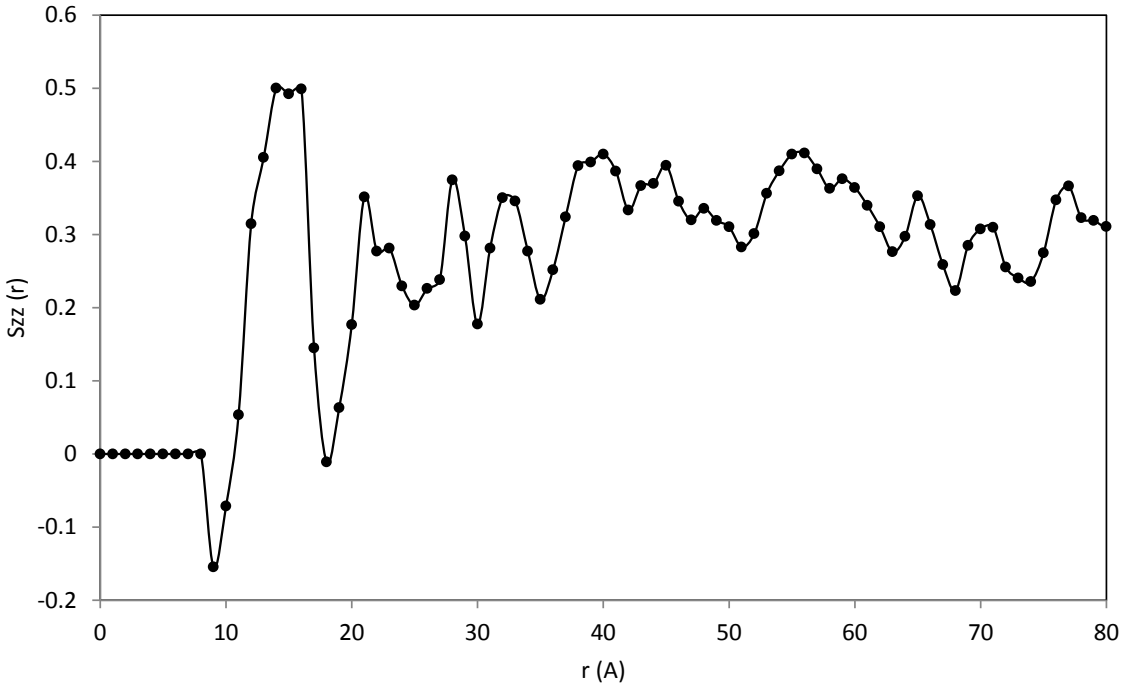


Figure 8.11: The Structure Factor Radially from the r=1.5nm TiO_2 Nanoparticle

at all times. The number of water molecules around the nanoparticle this time is much higher. The number of lipid atoms and water molecules are stable after 10ns in one case, 20ns in the

other. The average positions after equilibration are -0.2450 ±0.1609nm and 0.4415 ±0.1534nm.

As can be seen in figure 8.12 the first nanoparticle rapidly moves through the interfacial region at around t=18ns. This is accompanied by a sharp increase in the number of water molecules surrounding it plus a decrease in the number of lipid atoms Although this particle is below the normal position of the water equimolar dividing surface, locally it is still interfacially bound and surrounded by both lipid atoms as well as water molecules (figure 8.13). The lateral diffusion coefficient for the nanoparticle in this region is $0.0574\times10^{-9}\mathrm{m}^2\mathrm{s}^{-1}$, similar to the hydroxylated fullerene.

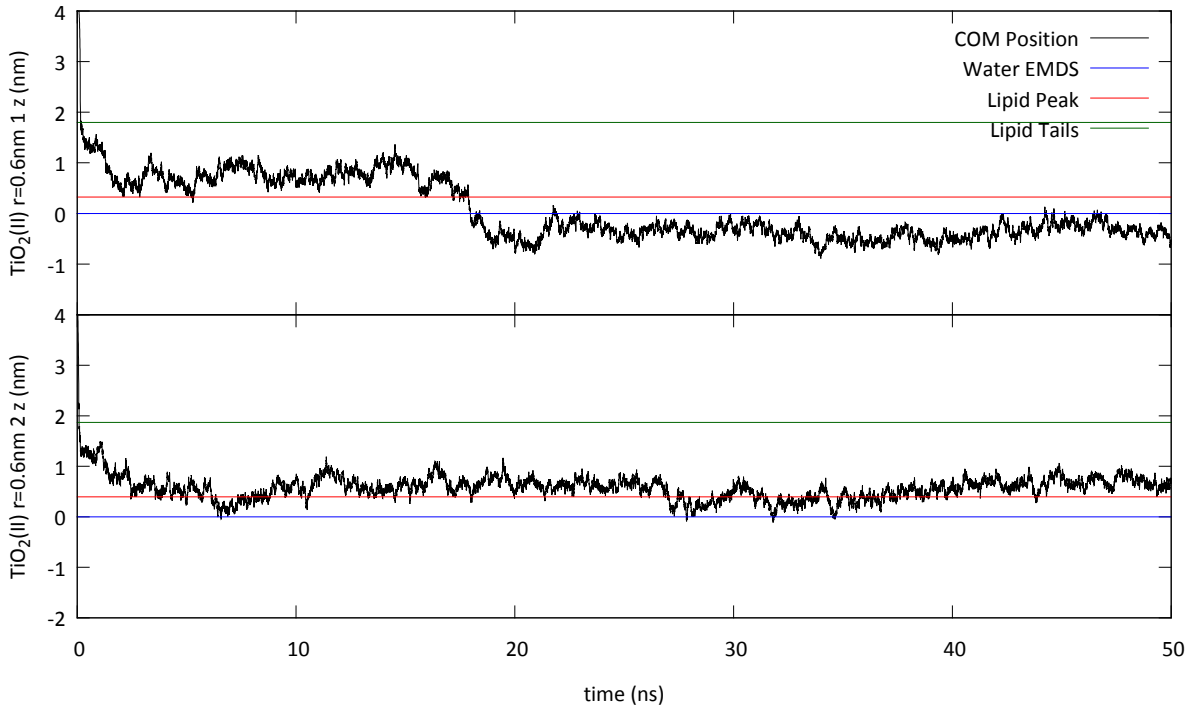


Figure 8.12: The Position of the Center of Mass of the r=0.6nm TiO_2(II) Nanoparticle

r=1.5nm

The largest Titanium dioxide particle again offers some interest. There are a much larger number of water molecules leaving the water phase and surrounding the nanoparticle, and this effect is much more rapid. In this case, relative to the smaller particle, the number of lipid atoms and water molecules surrounding the nanoparticle take more time to adjust. The bottom half becomes quickly covered in water molecules (around 250 total) but the top half only sees a gradual build-up to a similar number. The number of water molecules and lipid atoms do not stabilise until after 40ns in this case. These are figures 8.17 and 8.18. The lateral diffusion

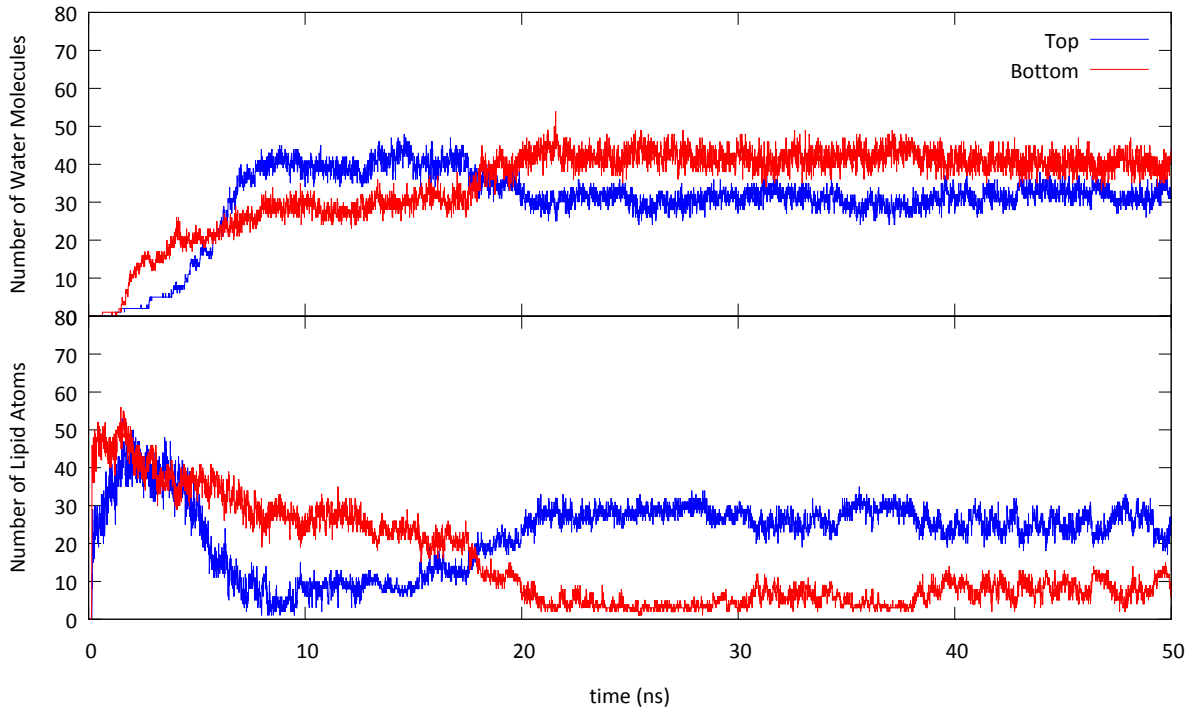


Figure 8.13: Number of Water Molecules and Lipid Atoms around the first r=0.6nm TiO_2(II) Nanoparticle as a Function of Time

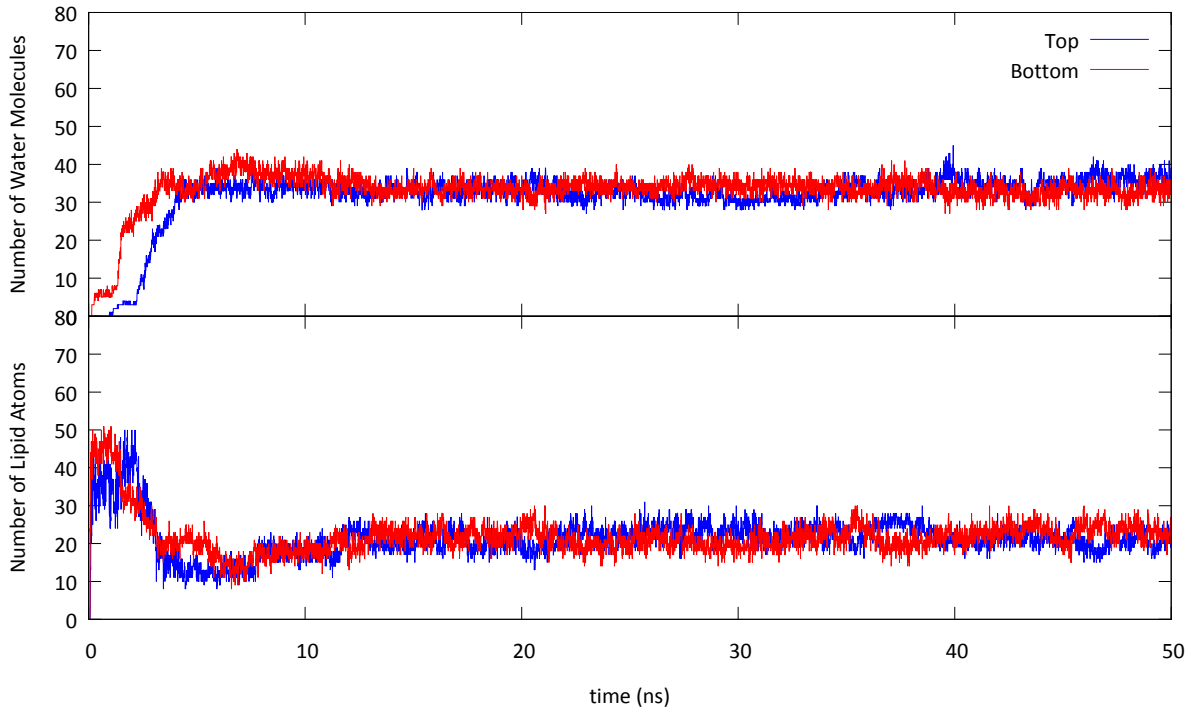


Figure 8.14: Number of Water Molecules and Lipid Atoms around the second r=0.6nm TiO_2(II) Nanoparticle as a Function of Time

coefficient for the nanoparticle is much lower this time at $0.0213\times10^{-9}m^2s^{-1}$, but is in line with that expected due to the increased size of the nanoparticle relative to the r=0.6nm one.

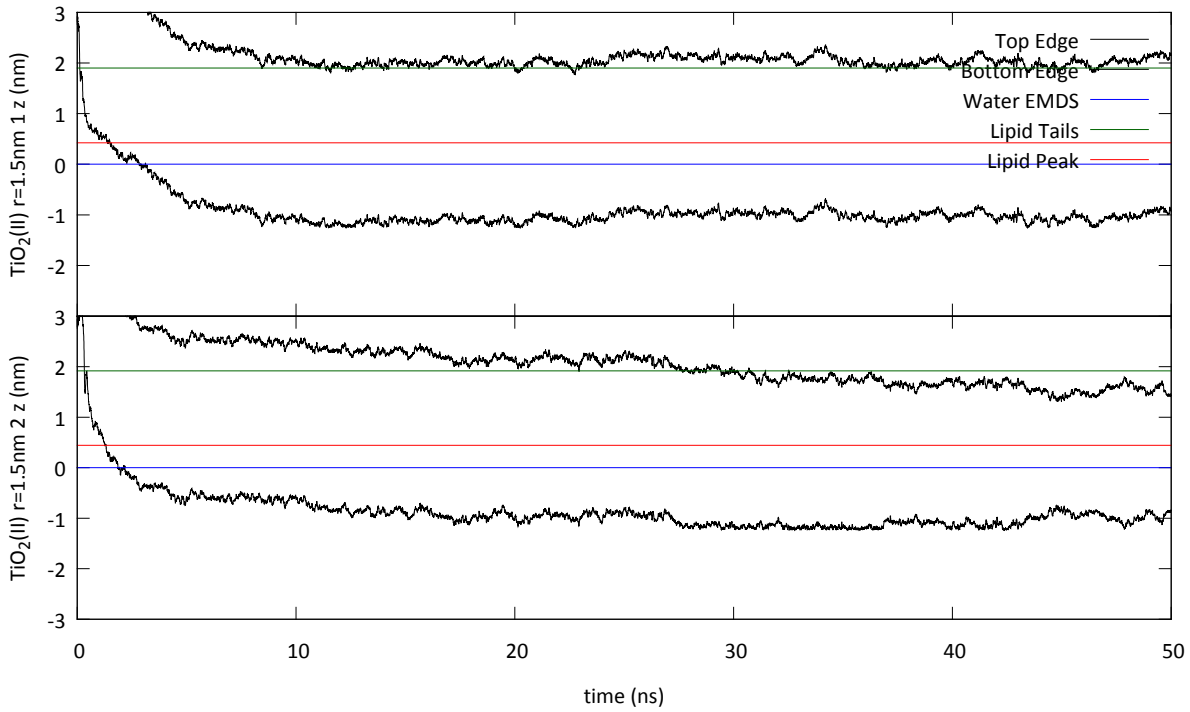


Figure 8.15: The Positions of the r=1.5nm TiO_2(II) Nanoparticle Edges

The wrapping of lipid tail atoms around the nanoparticle and the movement of water molecules to the top of the nanoparticle are shown in the picture below (figure 8.16). Only the molecules closest to the nanoparticle have been shown.

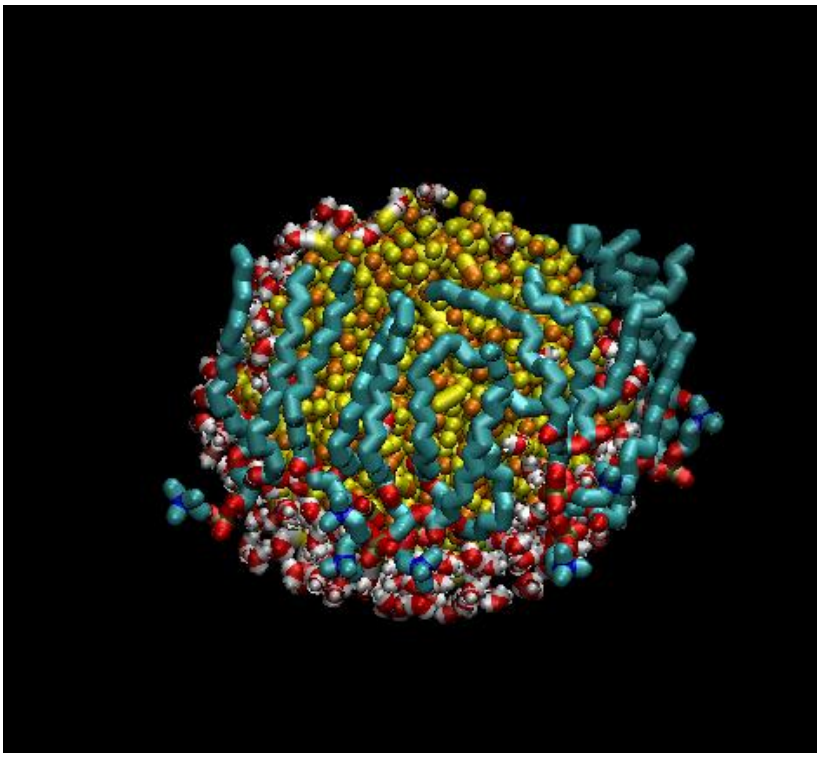


Figure 8.16: The r=1.5nm TiO_2(II) Nanoparticle in the Membrane

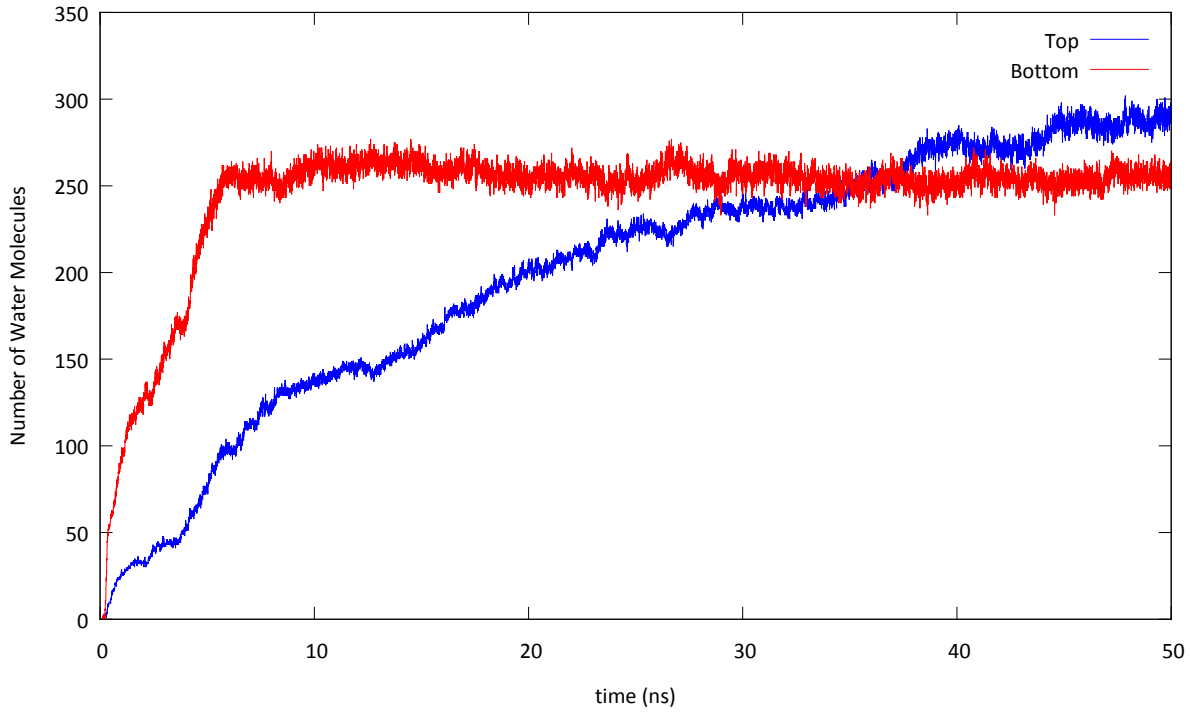


Figure 8.17: The Number of Water Molecules on the r=1.5nm TiO_2(II) Nanoparticle as a Function of Time

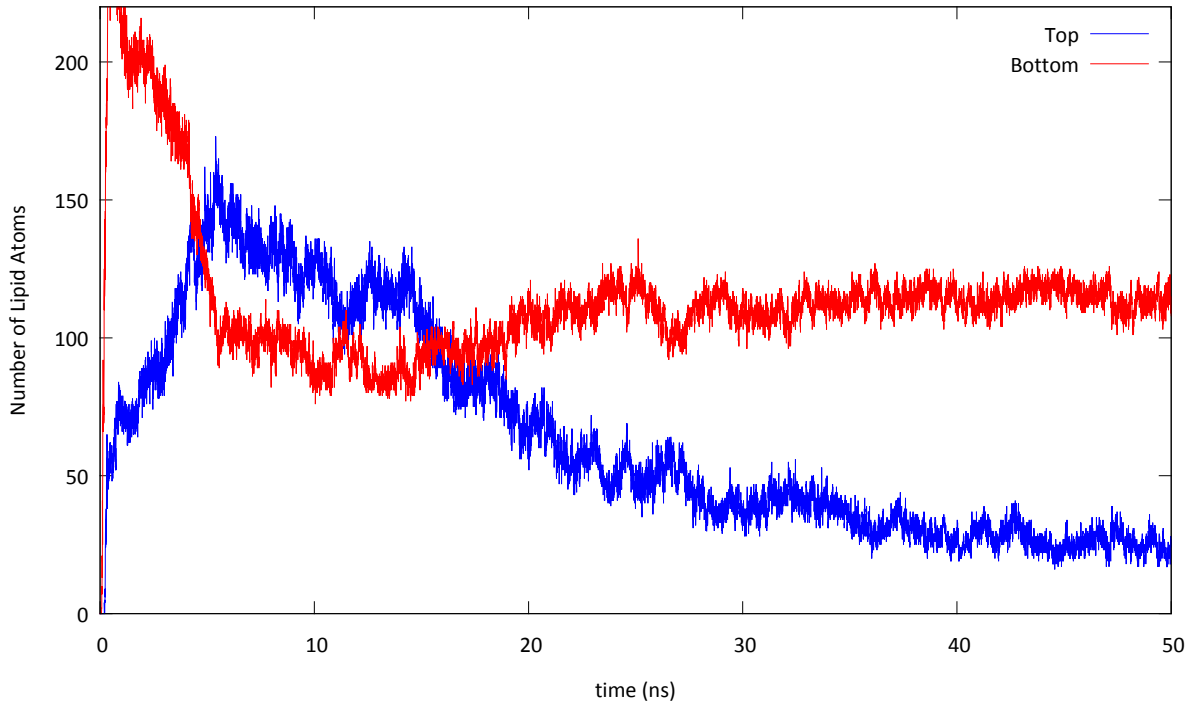


Figure 8.18: The Number of Lipid Atoms on the r=1.5nm TiO_2(II) Nanoparticle as a Function of Time

The density of water around the nanoparticle has been plotted two-dimensionally at several times to show how the water molecules form a continuous phase around the nanoparticle. In

figure 8.19 the situation is shown after 5, 15, 25 and 40ns. The z-axis and the r-axis are both defined relative to the center of mass of the nanoparticle.

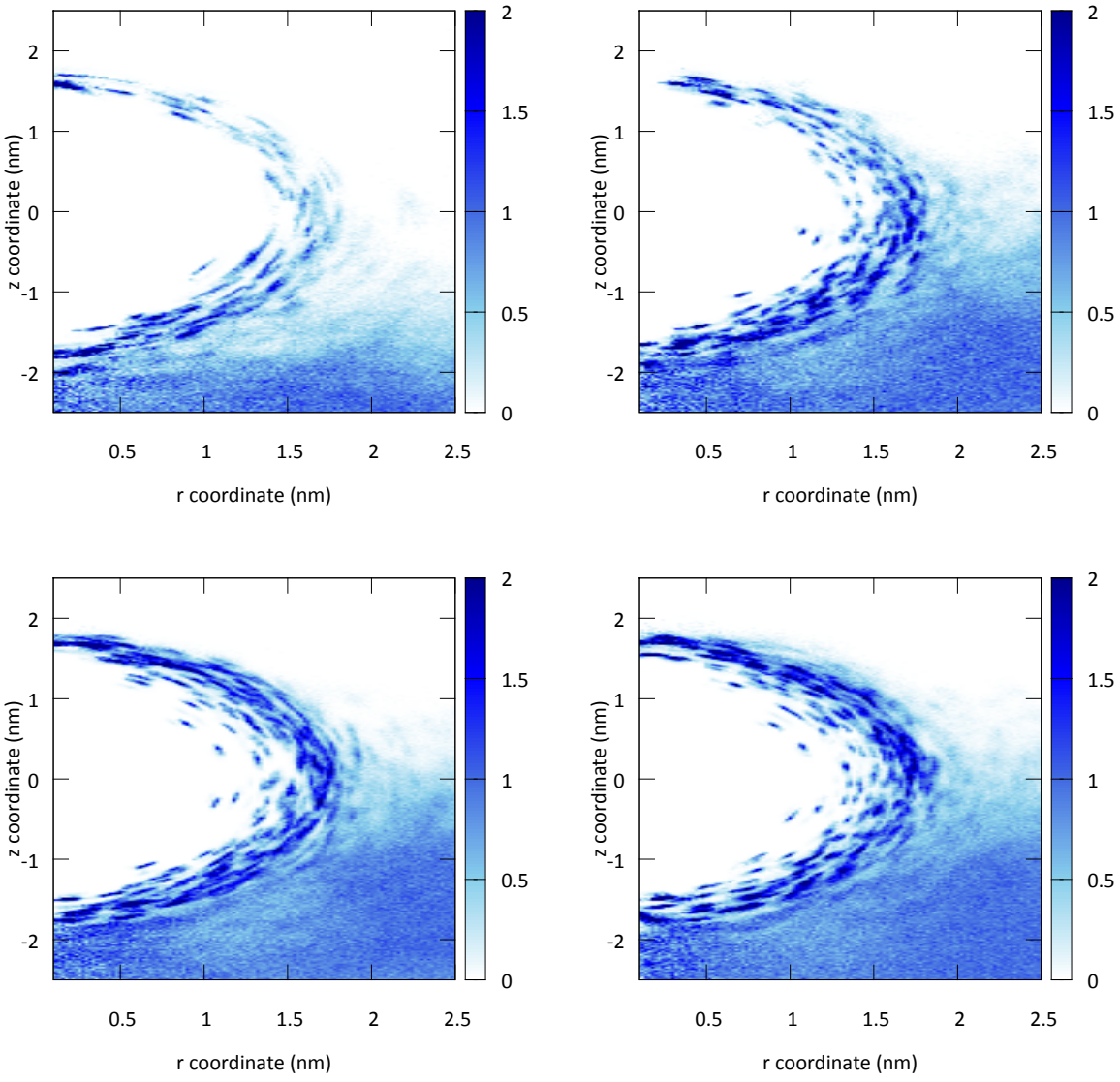


Figure 8.19: The 2D-Water Density Around the r=1.5nm TiO_2(II) Nanoparticle after 5, 15, 25 and 40ns

The trajectories of several individual water molecules have been followed as they interact with this nanoparticle. In picture 8.20 the trajectory one such water molecule takes around the nanoparticle is plotted. Both the r and z coordinates are relative to the center of the nanoparticle. A z coordinate of 0.0nm represents half-way up the z-axis of the nanoparticle and a radius of 1.8nm is approximately the radius of the first water shell around the nanoparticle. Thus when r and z meet (at around 1.8nm) the water molecule is at the top of the particle. In this case the molecule initially moves half-way up the side of the nanoparticle (to z=0.0nm, while maintaining

a constant r value of 1.8nm) and sits at the edge of the nanoparticle from t=5ns to t=10ns. It then leaves and later comes back to sit upon the top of the nanoparticle (z=1.8nm and r=1.8nm after t=20ns). Its trajectory is seen to be at a constant value of the radius, indicating it remains associated with the particle as it diffuses around. Diffusion coefficients for water molecules on the top and bottom half of the nanoparticle around the edge of the nanoparticle are calculated to be $0.0728\times10^{-9}\mathrm{m}^2\mathrm{s}^{-1}$ on the top half and $0.2590\times10^{-9}\mathrm{m}^2\mathrm{s}^{-1}$ for the bottom half. These are significantly reduced relative to the bulk (to around 10% of the value for the bottom and around 2.5% for the top).

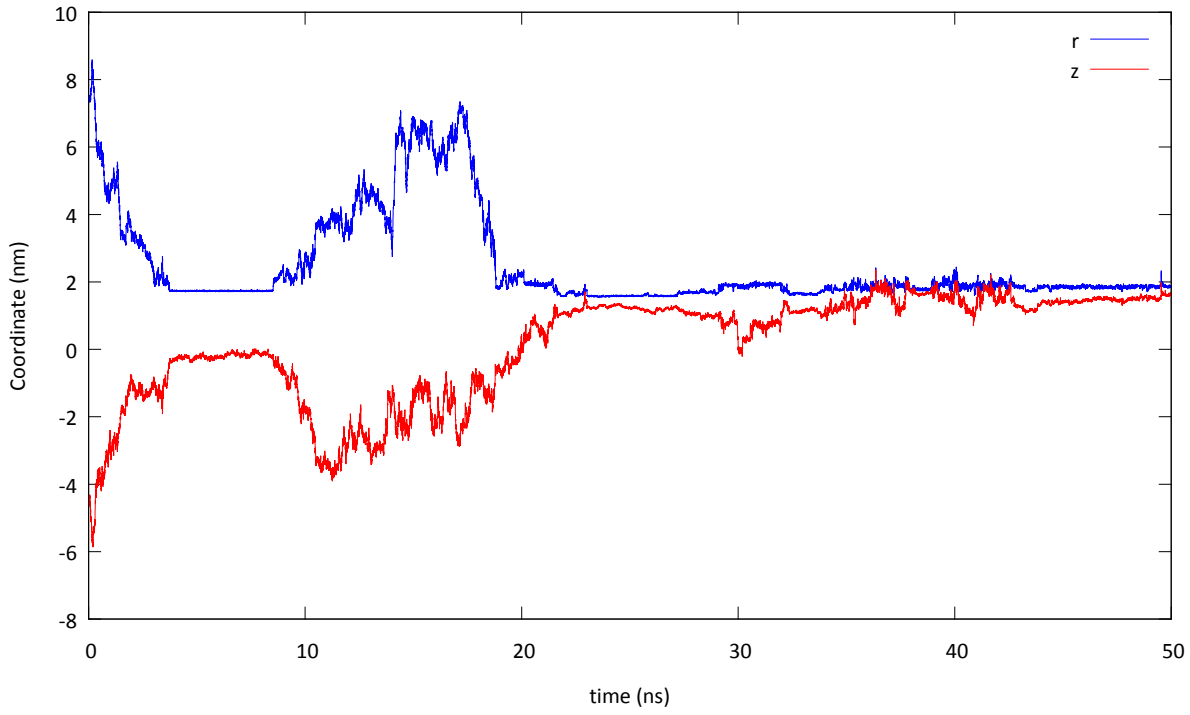


Figure 8.20: The Trajectory of a Water Molecule around the Largest TiO_2(II) Nanoparticle

Another plot is shown of the density along the z-axis, with the nanoparticle having entered, demonstrating the disruption caused to the membrane (figure 8.21). Some lipid atoms have been displaced downwards and the water phase now extends well within the lipid tail region.

The average positions of the smaller nanoparticles are summarised in table 8.1. They are averaged over the last 20ns of the simulation in most cases or once the particle has reached an equilibrium position.

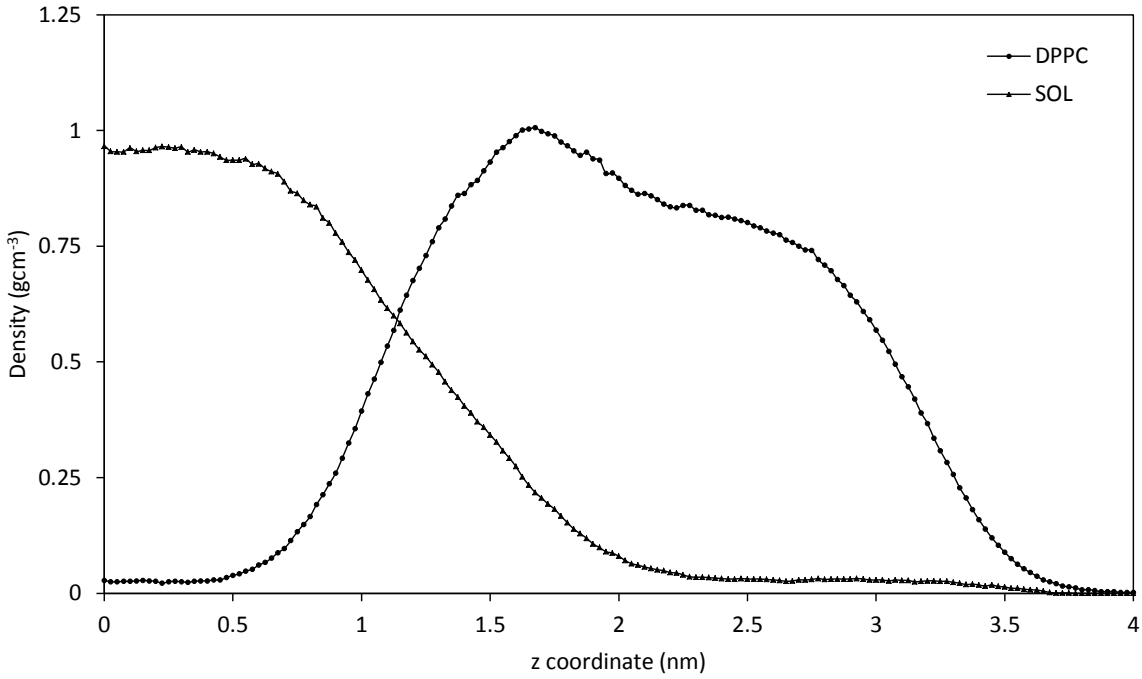


Figure 8.21: System Density Plot with the Effect of the r=1.5nm TiO_2(II) Nanoparticle

Particle	NP 1 Position (nm)	St. Dev. (nm)	NP 2 Position (nm)	St. Dev. (nm)
C_{60}	0.9712	0.1532	0.9761	0.1451
$C_{60}(OH)_{20}$	0.2421	0.1235	0.0627	0.1401
TiO_2(I) r=0.6nm	0.7865	0.1561	0.9939	0.1522
TiO_2(II) r=0.6nm	-0.2450	0.1609	0.4415	0.1534

Table 8.1: The Average Positions of the Nanoparticles

8.2 Monolayer Systems

In order to allow the nanoparticles to approach the layer from a different direction the bottom layer of the bilayer membrane was removed and additional water added. The external pressure was adjusted accordingly to again give a 64ApL system. A density profile along the z-axis for the new monolayer arrangement is shown in figure 8.22. The nanoparticles were this time placed on the water side of the membrane and allowed to enter again by diffusion.

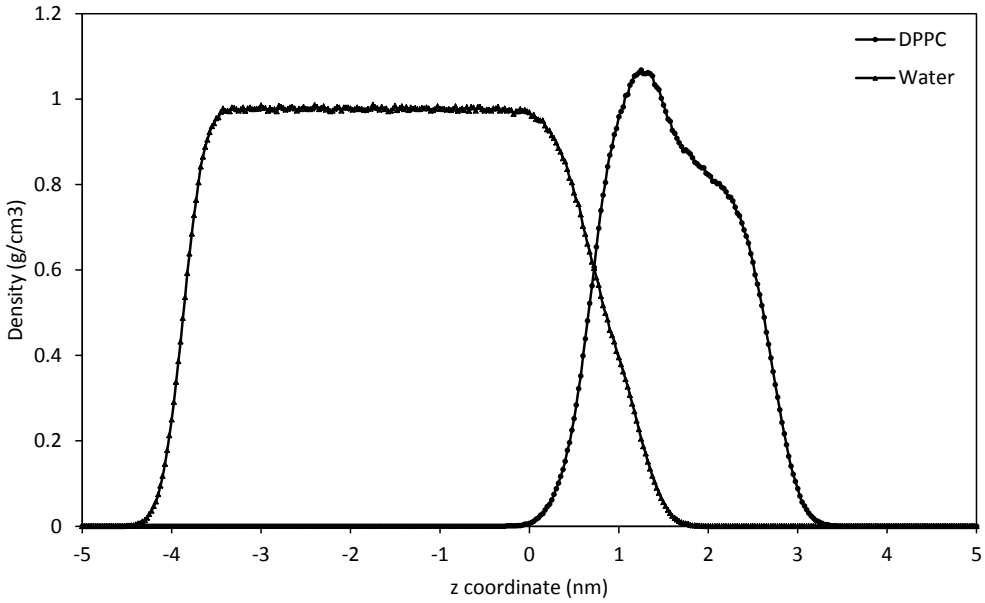


Figure 8.22: The Density Profile in the Monolayer System

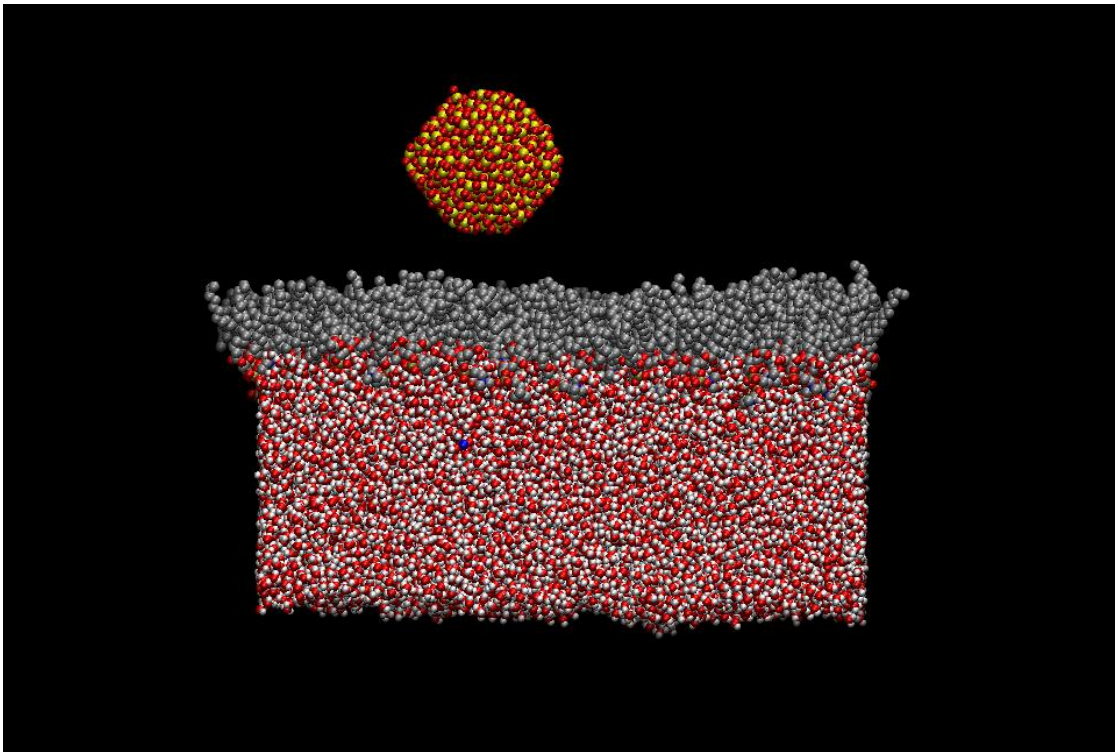


Figure 8.23: The Monolayer System with the Largest TiO_2 Nanoparticle

8.3 Approach of Nanoparticles through the Water Phase

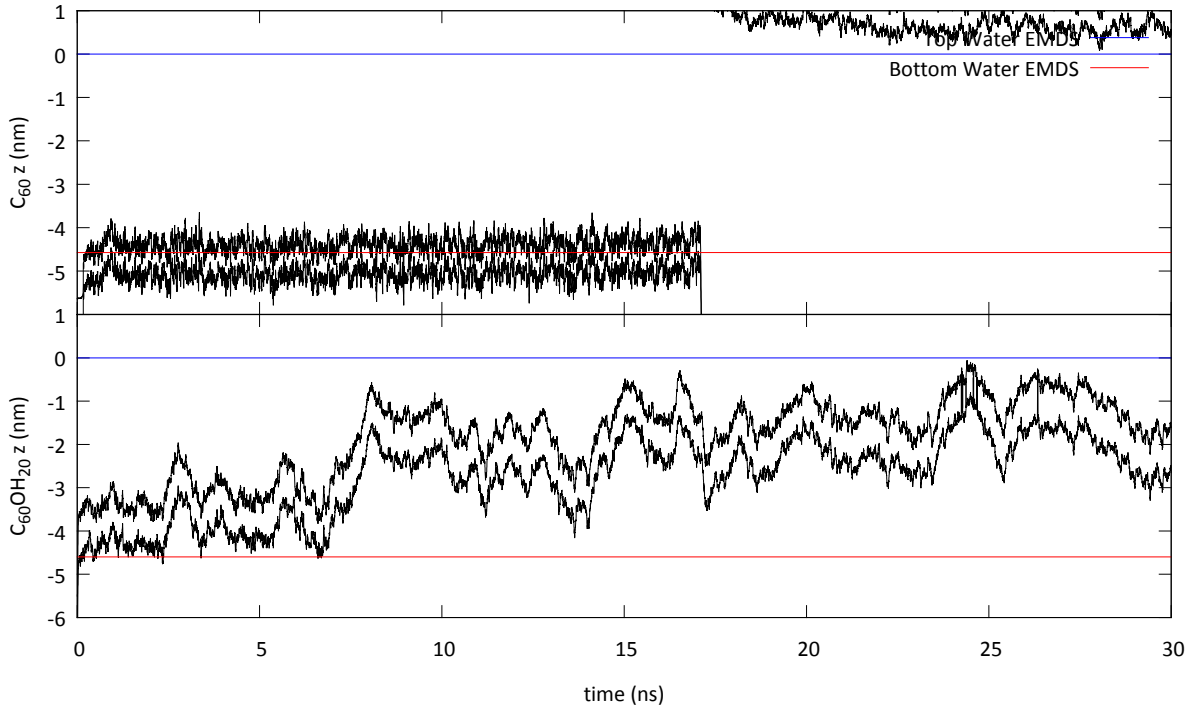


Figure 8.24: The Trajectories for the Fullerene Nanoparticles through the Water Layer

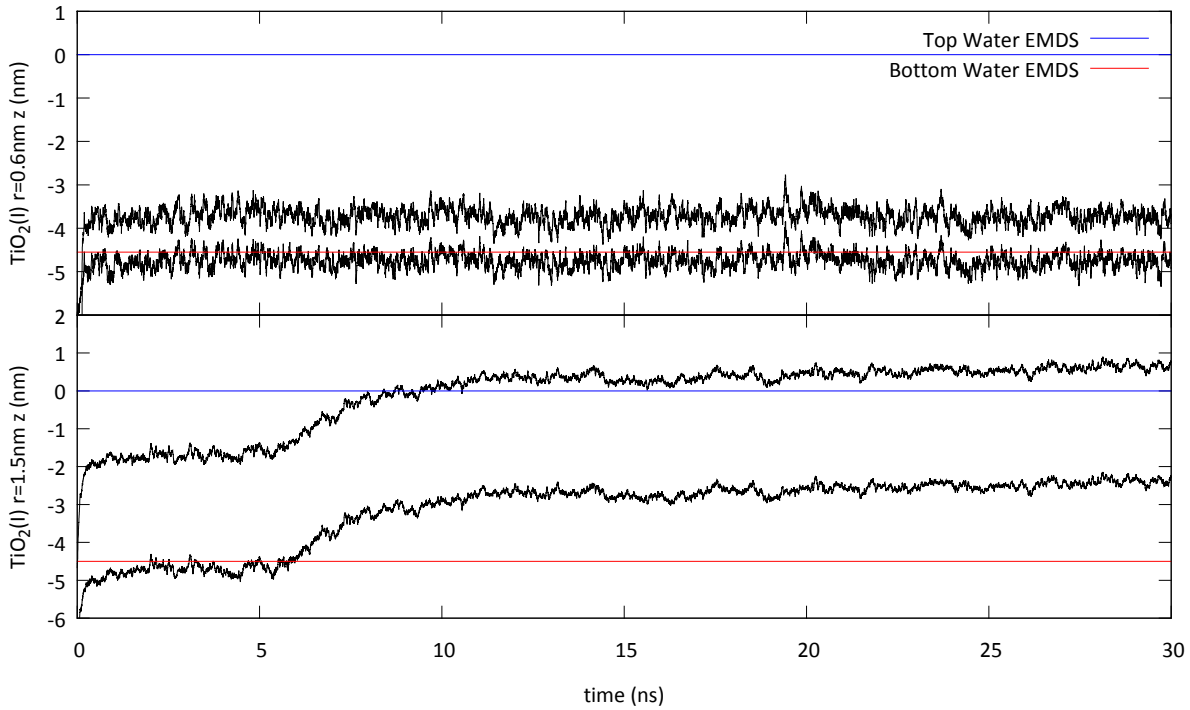


Figure 8.25: The Trajectories for the TiO_2 (I) Nanoparticles through the Water Layer

The trajectories of the different particles through the water phase are shown in figures 8.24, 8.25 and 8.29. None of the nanoparticles migrate to the interface except for the largest TiO_2(I)

one, which sits at the interface but does not breach it. The Van der Waals energy of the C_{60} molecule in the water phase is found to be -77.46 kJ/mol, much lower than that found in the preferred lipid tails region (-169.50 kJ/mol). The C_{60} nanoparticle sits at the water-vacuum interface for 18ns without fully entering before travelling to the other side of the simulation cell. The smallest TiO_2(I) particle shows a similar unwillingness to enter the water phase and sits at the interface. The other particles all sit within the water phase but there is no net migration one way or another, suggesting they are relatively stable in the water layer. This provides some evidence that once a particle crosses into the water from the other direction via the lipid phase it will stay there. Diffusion coefficients for the nanoparticle in the water phase were found to be $0.2943\times10^{-9}m^2s^{-1}$ for the $C_{60}(OH)_{20}$, $0.1372\times10^{-9}m^2s^{-1}$ for the r=0.6nm TiO_2(II) and $0.0442\times10^{-9}m^2s^{-1}$ for the r=1.5nm TiO_2 (II).

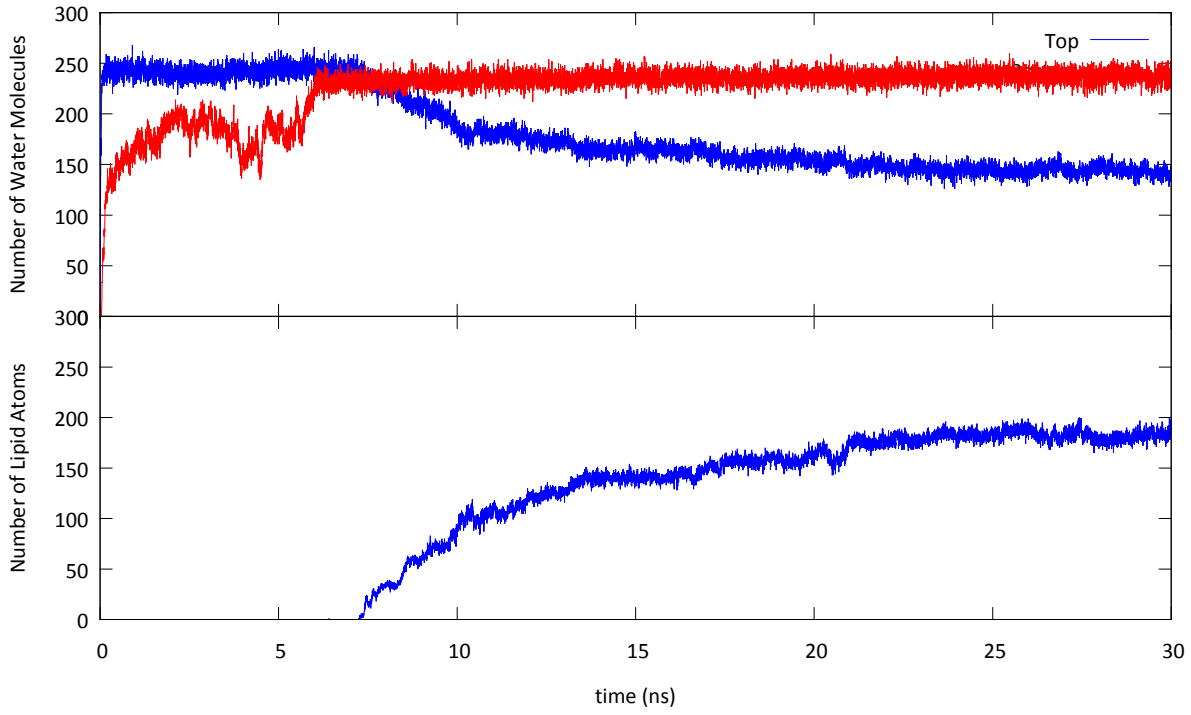


Figure 8.26: The Number of Water Molecules and Lipid Atoms Surrounding the r=1.5nm TiO_2(I) Nanoparticle as a Function of Time

As the largest TiO_2 (I) nanoparticle sits at the interface some further analysis was carried out. The number of water molecules and lipid atoms surrounding it are plotted in figure 8.26 and a 2-dimensional water density plot is shown in figure 8.27. Some of the water molecules on the top half are exchanged for those of the DPPC head group atoms.

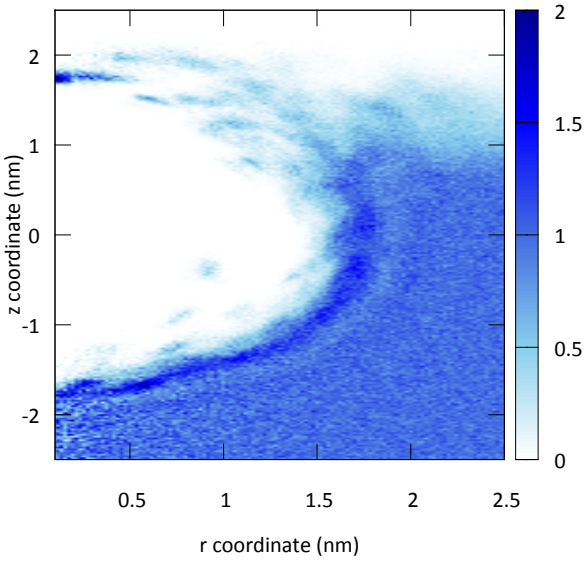


Figure 8.27: The 2D Water Density Surrounding the TiO_2(I) r=1.5nm Nanoparticle at the Interface

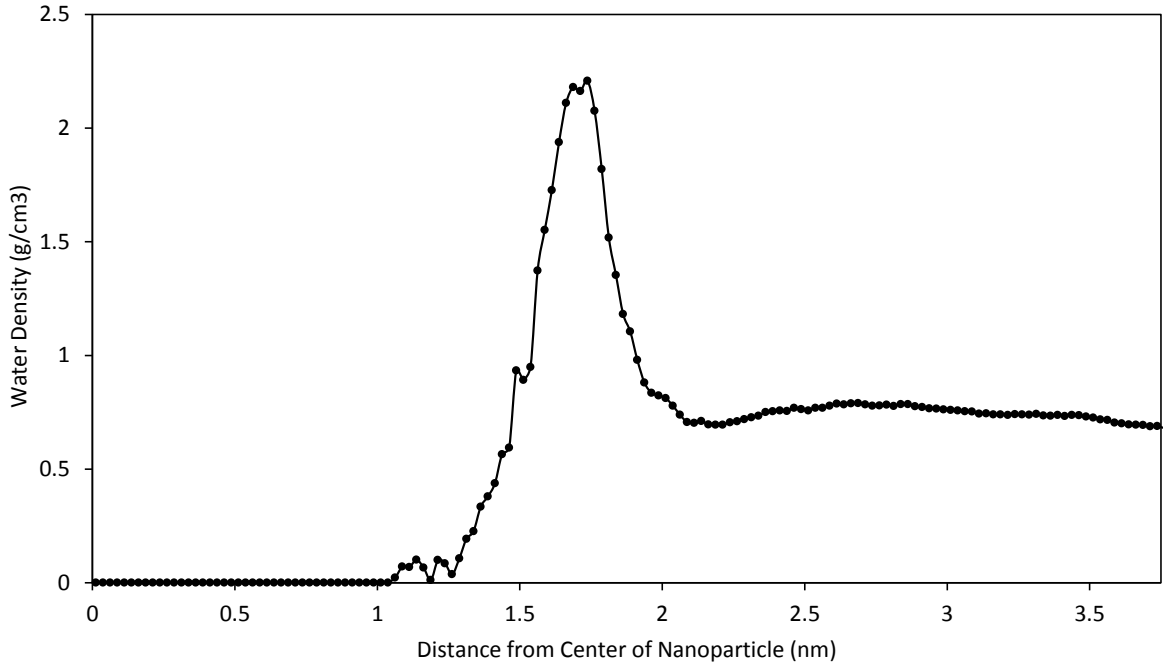


Figure 8.28: The Water Density Radially from the r=1.5nm Nanoparticle

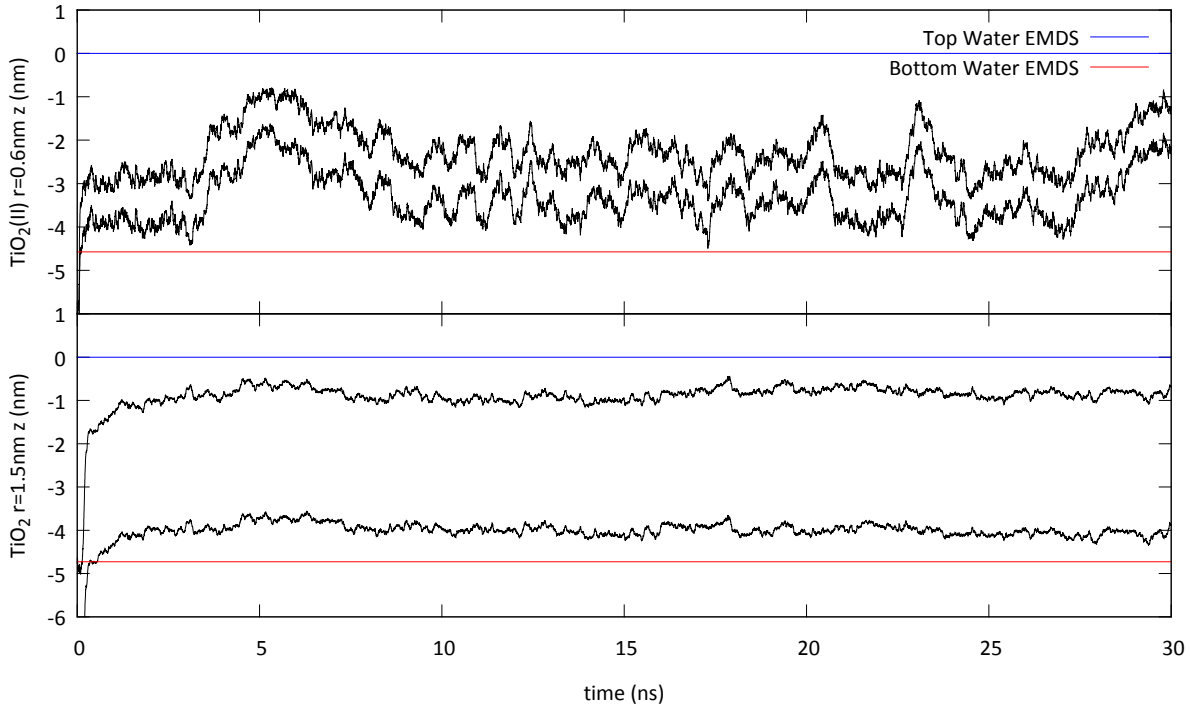


Figure 8.29: The Trajectories for the TiO_2 (II) Nanoparticles through the Water Layer

8.4 Energy/Force Measurements

Calculations were undertaken to measure the forces acting on and the energies of the nanoparticles at various points in the system, in order to further understand the results obtained in the previous section.

Energy calculations were made for the nanoparticles in each phase. An approximation of the energies experienced by the charged particles in each phase were calculated by using the direct Coulomb interaction, rather than the full Ewald sum due to the non-separability of the reciprocal space sum using GROMACS. The Coulomb energy was calculated directly to r=1.1nm and then shifted to zero over the next 0.3nm, giving a total of 1.4nm. In all cases the energies for the nanoparticles were more favourable in the equilibrium positions in the lipid phase found from the main simulations rather than in the water phase. For example the $C_{60}(OH)_{20}$ nanoparticle has a much higher energy (-2201.15kJ/mol) in the interfacial head-group region than in the water phase (-898.83kJ/mol). The effect of the spreading of water around the largest TiO_2 nanoparticle was also measured by taking points from the simulation where the nanoparticle was sitting at the interface initially after 15ns and then after 50ns when it was more hydrated. The energy at the equilibrium position was further lowered by this water spreading. These data are shown in table 8.2. The energy in the water phase relative to that of the nanoparticle in its equilibrium position in the lipid phase is shown in the last column.

Particle	Position	Energy (kJ/mol)	Relative To Eq.
C_{60}	Lipid (Eq.)	-169.50	1.00
C_{60}	Water	-77.46	0.46
$C_{60}(OH)_{20}$	Lipid (Eq.)	-2201.15	1.00
$C_{60}(OH)_{20}$	Water	-898.83	0.41
TiO_2(I) r=0.6nm	Lipid (Eq.)	-294.81	1.00
TiO_2(I) r=0.6nm	Water	-108.76	0.37
TiO_2(I) r=1.5nm	Lipid (Eq.)	-1052.48	1.00
TiO_2(I) r=1.5nm	Water	-671.50	0.56
TiO_2(II) r=0.6nm	Lipid (Eq.)	-1287.04	1.00
TiO_2(II) r=0.6nm	Water	-720.43	0.64
TiO_2(II) r=1.5nm	Lipid (Unhydr)	-6378.64	0.74
TiO_2(II) r=1.5nm	Lipid (Eq. Hydr)	-8568.67	1.00
TiO_2(II) r=1.5nm	Water	-4236.67	0.49

Table 8.2: The Energies for the Nanoparticles

Next, using a harmonic force the nanoparticles were dragged along the z-coordinate of the simulation cell from the vacuum side through the lipids to the water phase. The pulling rate was

0.005 nm per picosecond and the force constant applied was 400.0 kJmol^{-1}nm^{-2}. The particles were then frozen at several points along this ordinate and the average force at each position calculated. It is noted that the hydrophilic particles were found to extract lipid molecules from the interface and to retain them in their sphere of influence whilst dragged through the water phase, this effect was also noted previously [141, 142]. Several attempts were made to avoid this effect with different pulling rates/forces without success. The number of lipid atoms and water molecules surrounding the r=0.6nm TiO_2(I) nanoparticle during the dragging process are shown in figure 8.30. As can be seen there are lipid molecules pulled the length of the simulation cell by the nanoparticle. Water molecules though are less affected. The bottom half of the nanoparticle is considered to be that facing in the negative z direction.

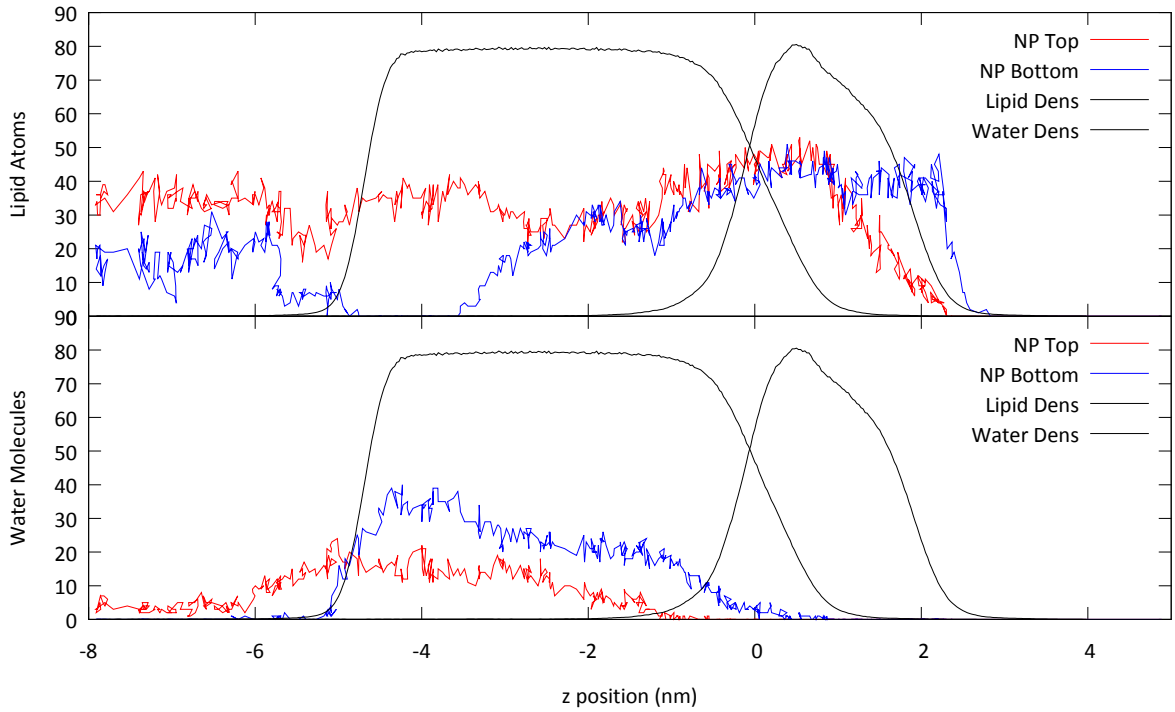


Figure 8.30: The Types of Particle Surrounding the r=0.6nm TiO_2(I) Particle During the Dragging Process

All the plots of the force are relative to the water equimolar dividing surface again (see figure 7.6 for the monolayer case). A negative force represents the nanoparticle being pulled towards the water phase (to negative z), positive being pushed back towards the vacuum side (to positive z). The equilibrium position (energy minimum) in the plots is therefore at the point where the force is zero. This corresponds in the $C_{60}(OH)_{20}$ system (figure 8.33) to z=0.5nm and to z=0.7nm for the r=0.6nm TiO_2(II) system (figure 8.35), both in the head-group region and for the r=0.6nm TiO_2(I) system (figure 8.34) at z=1.5nm, well within the tail region, reflecting

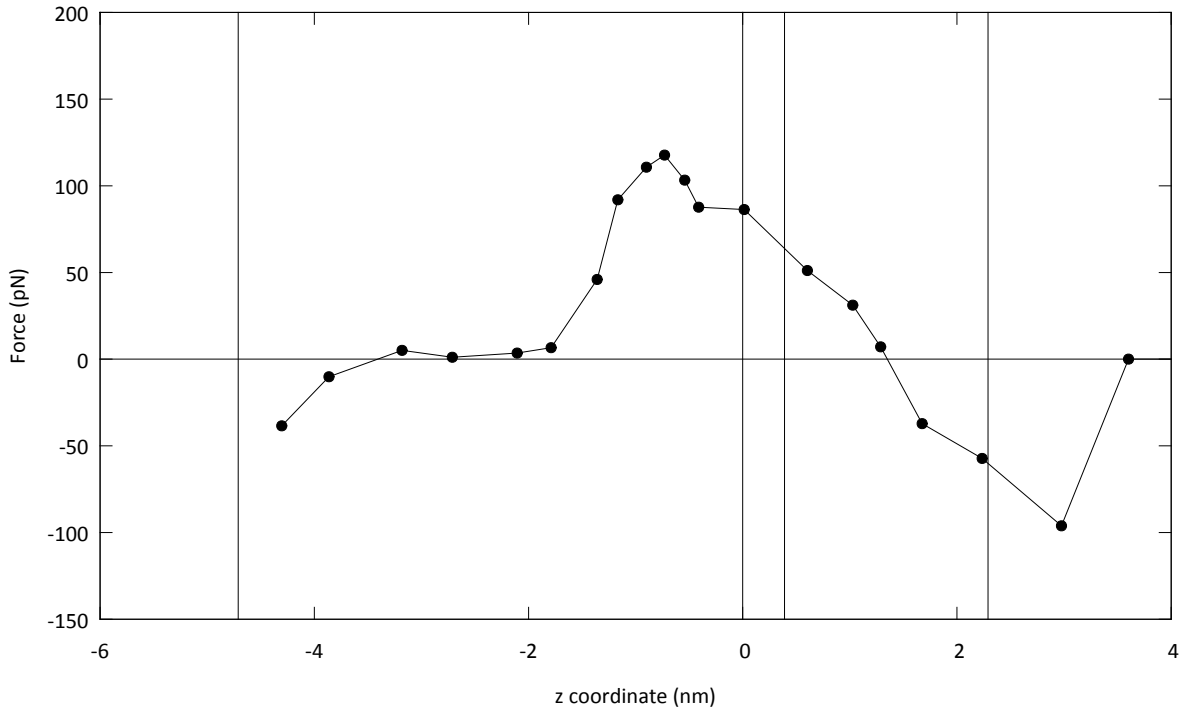


Figure 8.31: The Force Profile for the C_{60} Nanoparticle

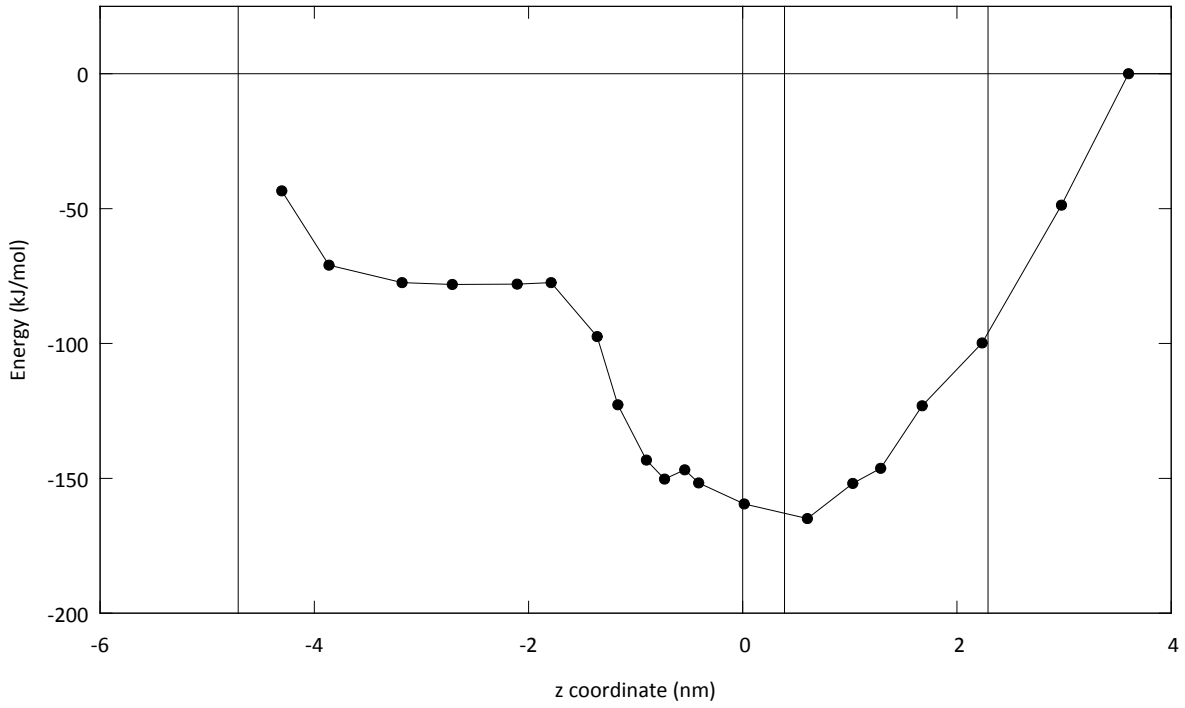


Figure 8.32: The Energy Profile for the C_{60} Nanoparticle

the difference in their hydrophilicities. These positions do not quite represent the long-time equilibrium positions attained during the main simulations, but those were run for 10-20 times longer. While the C_{60} particle from the force plot (figure 8.31) was found to have a minimum

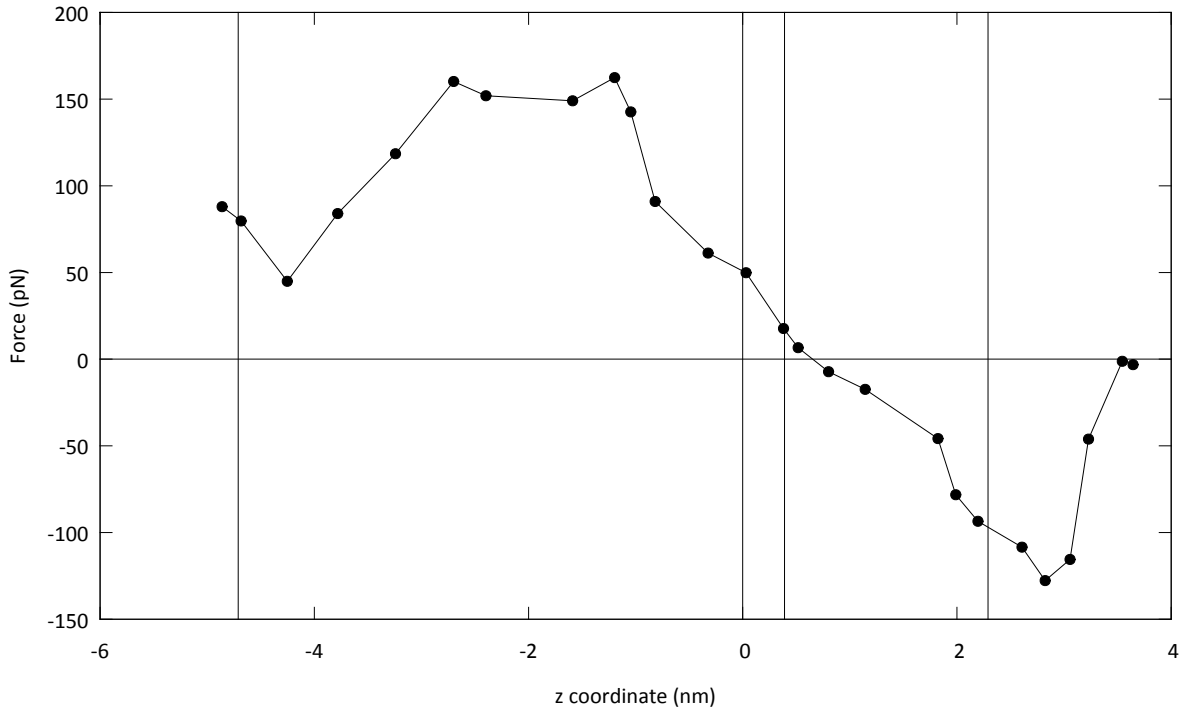


Figure 8.33: The Force Profile for the $C_{60}(OH)_{20}$ Nanoparticle

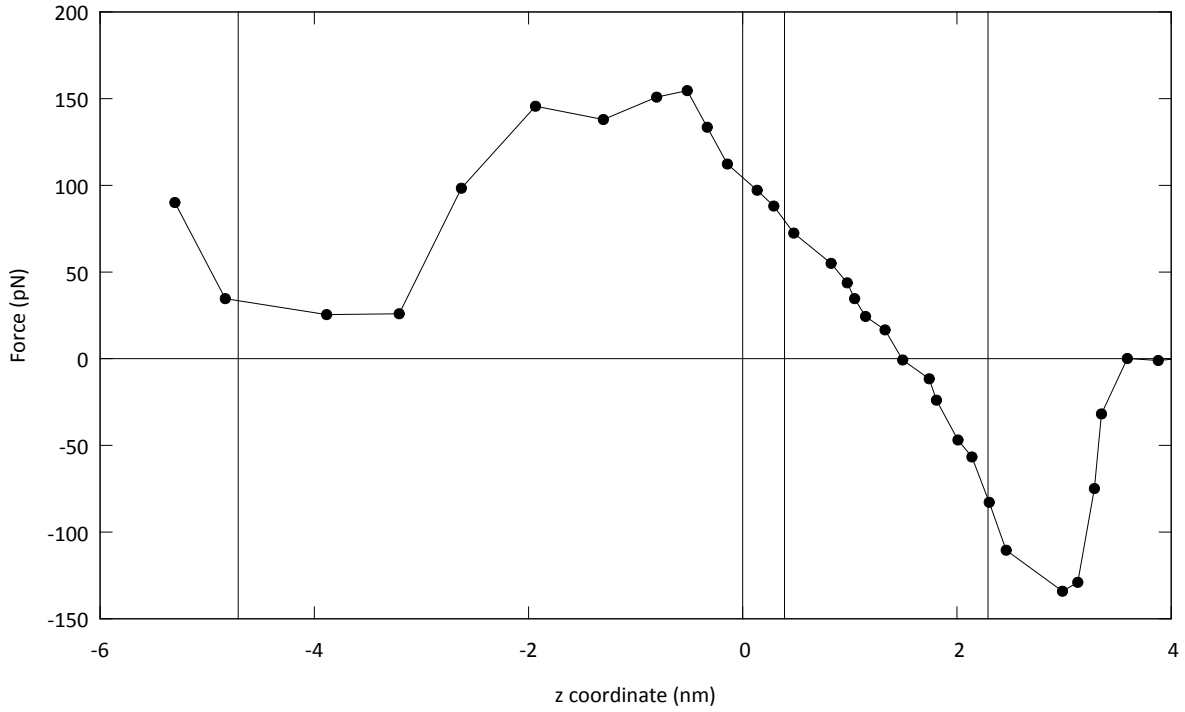


Figure 8.34: The Force Profile for the r=0.6nm TiO_2(I) Nanoparticle

at z=1.3nm, the energy profile suggests that the energy of the nanoparticle is stable throughout the interface. This effect could be due to the afore-mentioned extraction of lipids and it may also be showing that the increase in force is due to breaking intermolecular bonds between the lipid

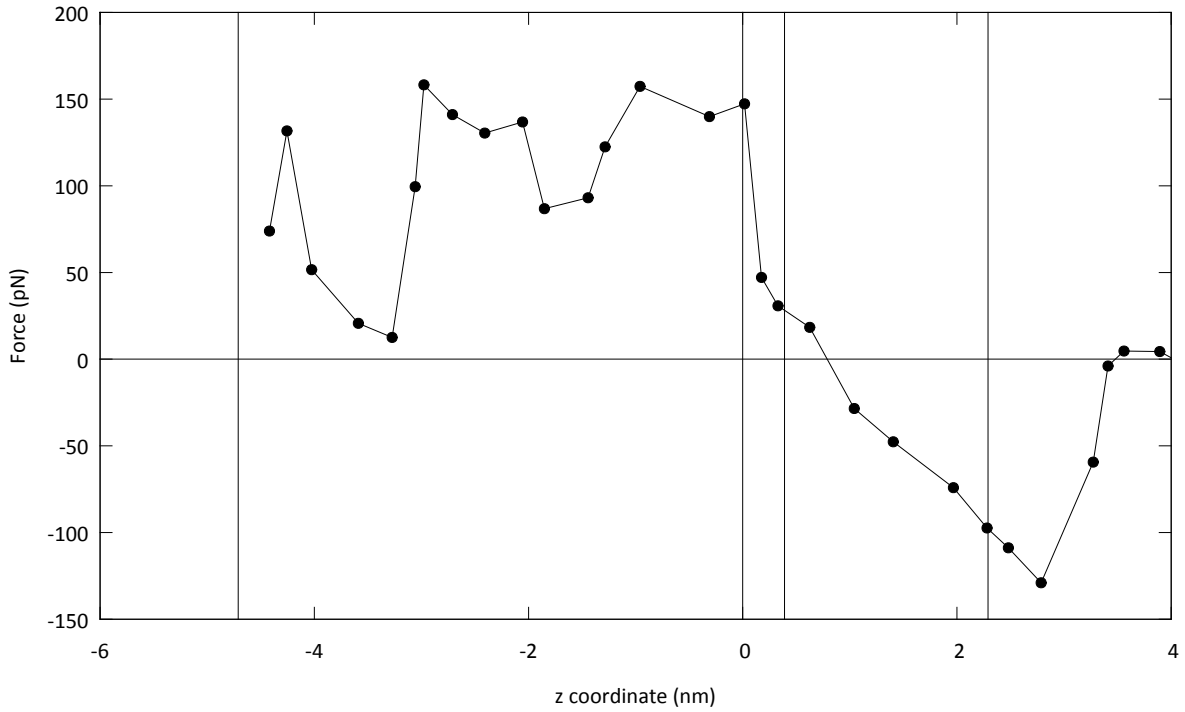


Figure 8.35: The Force Profile for the r=0.6nm TiO_2(II) Nanoparticle

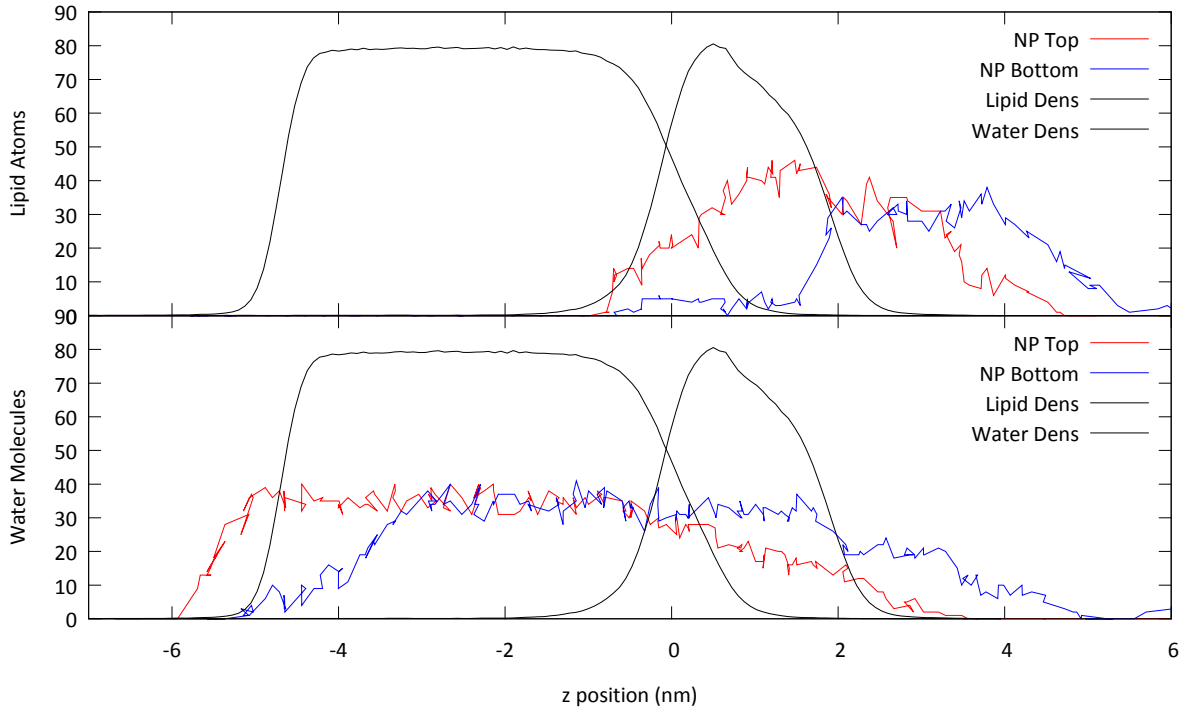


Figure 8.36: The Types of Particle Surrounding the r=0.6nm TiO_2(I) Particle During the Reversed Dragging Process

molecules as the nanoparticle passes through. Further simulations were carried out with the nanoparticle released once dragged across the membrane (rather than frozen as in the average force calculations above). Particles dragged across the interface and then released were found

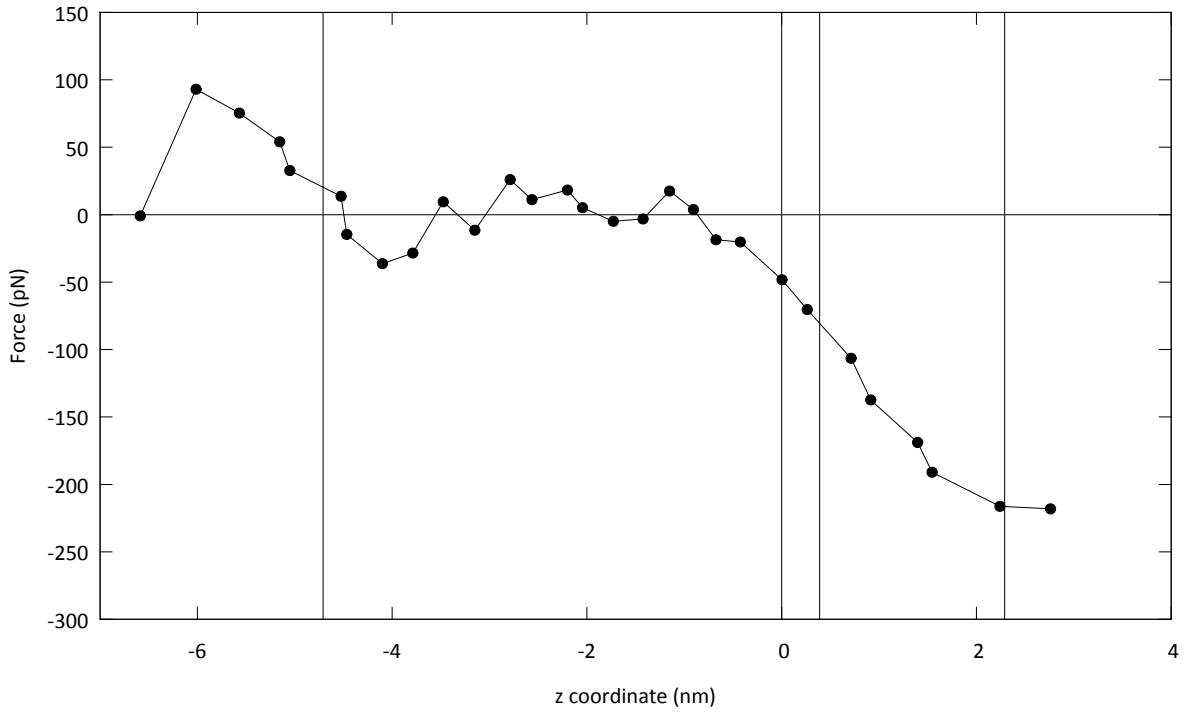


Figure 8.37: The Force Profile for the r=0.6nm TiO_2(I) Nanoparticle in the Reversed Direction

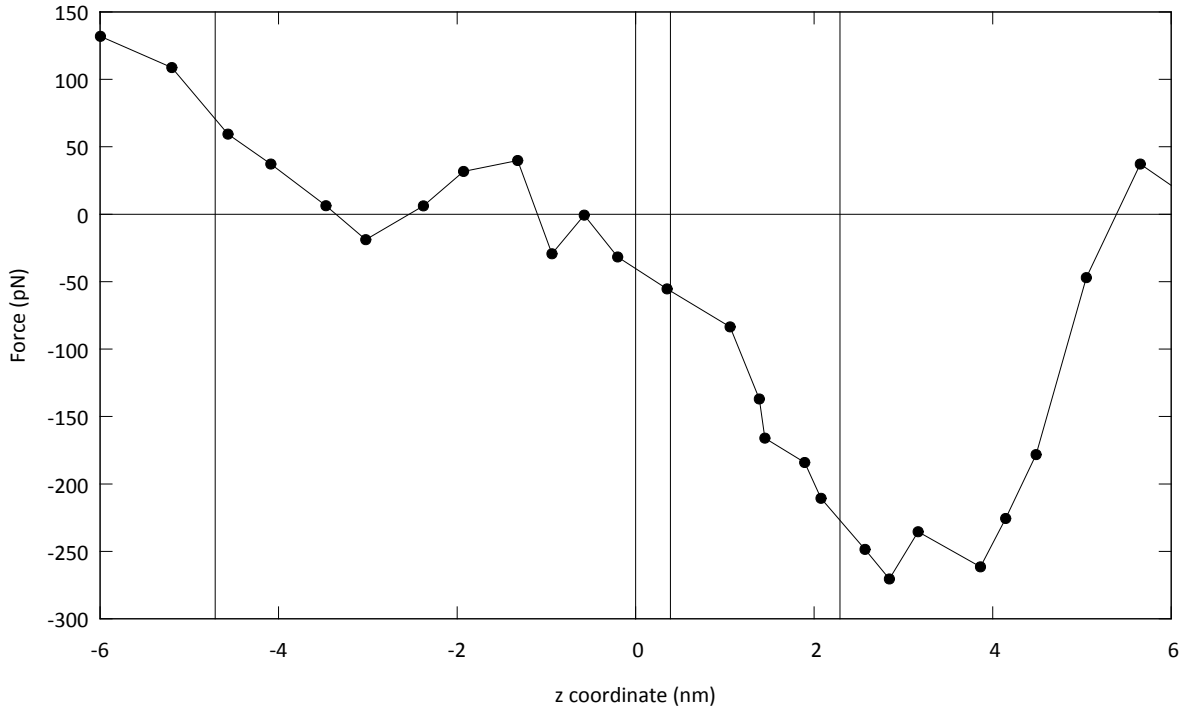


Figure 8.38: The Force Profile for the $C_{60}(OH)_{20}$ Nanoparticle in the Reversed Direction

to head back towards the interface as expected from the average force in the profile.

Some of the nanoparticles were also dragged in the opposite direction across the interface, from the water side. The number of lipid atoms and water molecules surrounding the r=0.6nm

TiO_2(I) nanoparticle during the dragging process in this reversed direction are again shown in figure 8.36. In these cases (figures 8.37 and 8.38) it is seen that the z position of the minimum is slightly lower than in the approach from the vacuum side. Again it seems that the lipid interface is acting as a barrier to the nanoparticle crossing as the force becomes repulsive and rises upon approach to it. It is also noted that the average force experienced in the water phase is fairly low, which could explain the nanoparticles remaining within the water phase rather than migrating to the interface. It also again provides some evidence that once across the membrane and free of the interface nanoparticles could stay across as found in some experimental cases.

All the force measurements suggest that there is a significant energy barrier to crossing the lipid interface ($> 10k_BT$). For the passage of the nanoparticle to occur, energy is required to vacate space within the head group region. The resistance of the DPPC lipid layer to the passage of the nanoparticles could represent the strong intermolecular bonding between the DPPC molecules. In reality the lipid layer is inhomogeneous and will have many different components, e.g. cholesterol or proteins which may introduce weakness into the layer through which nanoparticles may find it easier to pass.

Chapter 9

Conclusions

In this report, the flow and interfacial properties of a series of models of crystalline and amorphous surfaces have been comprehensively studied. In all the systems studied excellent agreement has been found for the calculation of relaxation times using both equilibrium and non-equilibrium methods and the corresponding slip lengths from each method show good agreement too. It is therefore concluded that using the relaxation time to characterise the interfacial dynamics has general applicability to nanoscale systems and offers distinct advantages compared to other methods.

It has been found that the macroscale assumption of stick boundary conditions is invalid on the nanoscale in most of these systems. The magnitudes of the slip velocities are found to be significant in some cases and can be as high as half of the peak velocities in the pore. The slip lengths in all but the PDMS systems are quite high relative to the pore widths leading to large flow enhancements in some cases. Significant flow enhancements though are only found for the smooth graphene surfaces and carbon nanotubes. The flow dynamics still follow that expected from a slip-modified version of the Hagen-Poiseuille law, but enhancements can be around 400 times that expected over a no-slip boundary condition.

It has also been shown that using the relaxation time and slip coefficient for the center of mass velocity, rather than Maxwell's coefficient for momentum accommodation at the wall, offers advantages when characterising the interfacial dynamics, due to the difficulties in obtaining consistent values for Maxwell's coefficient in condensed systems. Maxwell's model is very simple and was originally developed for gases not liquids – the wall-fluid collisions are more difficult

to define when amorphous surfaces are used and the influence of other fluid molecules on the collisions could be significant.

The flow of fluids over amorphous carbon surfaces was investigated. In experimental work it was found that flow in amorphous carbon nanopipes, as well as carbon nanotubes, is much higher than that expected through standard macroscale hydrodynamics, even up to 100nm. Equilibrium and non-equilibrium simulations have been shown to give consistent results for the relaxation times and slip coefficients across a wide range of systems with crystalline and amorphous surfaces. Across this sample of surfaces the slip coefficient is found to be inversely proportional to the roughness of the surface. Two different fluids, decane and water have also been tested and found to obey the equations. Proof that this method for predicting interfacial slip has wide applicability to many systems will help future simulation work and in the design of experimental systems.

PDMS is a very popular material in microfluidic devices and potentially useful in nanoscale devices. The discovery that nanoscale channels can be introduced into PDMS [49] shows that it is indeed possible to produce the pore widths used in this project in experimental conditions using this material. The model PDMS surfaces and oxidation process have already shown to give interfacial properties (e.g. contact angles) similar to a real experimental system [110]. The interfacial properties of the PDMS systems have been studied under both equilibrium conditions and under flow. All the data point to an increase in the interfacial friction upon oxidation. The tangential force experienced by the fluid increases as the number of oxidised sites in the surface increases. As the $-CH_3$ groups in the surface are replaced with –OH groups the surface becomes more hydrophilic as the water molecules interact more strongly with –OH than $-CH_3$. For the PDMS systems, unlike the carbon, very low slip coefficients and enhancements were found and the flow was essentially non-slip.

In this work it has been found though that the slip coefficients seen in the carbon nanopore simulations do not agree with those expected from the experimental work (flow enhancements are ten times lower). Flow rates and slip coefficients over crystalline nanotube/graphene surfaces are found to be much higher than the amorphous surfaces but are still somewhat lower than the corresponding flows seen in experiments (by a factor of between ten and a hundred), which suggests that again there is a disagreement between simulation and experiment. The lack of quantitative agreement between the two could be for many reasons such as the structure or

density of the surface being modelled incorrectly or due to the potential energy functions being inaccurate. If the simulations were wrong it could be due to oversimplifications made in the models of the surface or the potential, which are still classical in nature. Upon moving to a lower density surface (which also increased the roughness) the flow behaviour did not change dramatically. Changing the Lennard-Jones fluid-carbon interaction parameter only made a big difference to the slip coefficient upon extreme changes and the C-OW potential has to be made much more hydrophobic than that suggested by experimental calculation. Only small changes were noted when using either mobile or frozen surface atoms. Experimentally, a pressure is imposed and a flow rate measured. The expected flow rate is determined by equation 3.19 and possible sources of error in this calculation are in the radius determination or the number of pipes in the sample. The slip length (as calculated experimentally) is proportional to $1/N_{\text{pores}}$ and $1/r^3$ so underestimating these figures would give a larger calculated slip length than is actually the case, as would any leaks in the system. The difference could also be due to discrepancies between the experimental system and the model, e.g. adsorbed gases in the experiment, which are not being considered in the simulations.

Many parameters within the system have been altered to see if any greater enhancement could be achieved but only in extreme cases was a large effect noticed. Based on the lack of any substantial flow enhancements for any of these simulated systems and the fact that the potentials, which have been tested via contact angle measurements, would have to be greatly altered to achieve the experimental flow rates it is concluded along with previous studies for carbon nanotubes [23] that the experimental enhancements are likely to have been overestimated, possibly through the miscalculation of the flow parameters or the presence of gas bubbles lining the interface reducing interfacial friction. Further work in this area needs to be undertaken, both on the experimental and simulation sides to try to discover the source of these discrepancies. More recent experimental studies using different methodologies [158] also suggest that flow rates in the early studies are significantly over-estimated and there are possibly errors in the measuring methods. This has implications for the flow of fluids through nanoscale pores in devices as benefits due to miniaturisation could be outweighed by the additional complexities of producing devices at this scale.

There is currently a great interest in the effects of inhalation and the interactions of nanoparticles with lung tissues due to the implications in environmental toxicology. Dynamic effects at mem-

branes are important to understand and simulation work can help to shed light on them. The interaction of several types of nanoparticles with a biological membrane, based on the structure of a pulmonary surfactant layer, have been studied in this work. The nanoparticles were chosen as they are environmentally interesting - fullerenes are found in soot [60] and titanium dioxide is widely used industrially. The range and size of the nanoparticles examined have been extended compared to previous work and several hydrophilicities tested. The nanoparticles are all seen to rapidly diffuse into the tail region. Hydrophobic nanoparticles have been found to continue to reside in this location whereas hydrophilic ones have been shown to sit at the water/lipid head group interface. It is confirmed through studies of the energy of the nanoparticle in different positions, that they have reached their preferred locations. Through analysing the distribution of the numbers and types of each atom surrounding the nanoparticle it is found that no particles have entirely left the interfacial region and entered the water phase in the timescales employed here (<50ns). Therefore no nanoparticles are found to spontaneously diffuse across the surfactant layer and move freely within the water layer, which is found in some cases experimentally. A timescale of 2ms was predicted by Qiao [137] well beyond the range of these simulations.

In the case of the hydrophilic nanoparticles which sit at the interface, an interesting effect was found whereby mobile water molecules leave the bulk phase and spread round the surface of the nanoparticle. For the largest nanoparticles this creates a bridge across the interface, which could have useful applications, e.g. for the delivery of molecules to cells. This effect could be missed when using mesoscale methods such as coarse-grained models with no atomic scale resolution. That no particles are found to cross using these simplified systems yet do in experiments may suggest that another mechanism for crossing which is not being modelled adequately in the simulations may be responsible. The structure of real physiological lung membranes are far more complicated than those simulated here. The layer is in fact inhomogeneous with many different components and this could dramatically affect the interactions of nanoparticles with the tissue as could the perturbation caused by the lung membrane changing shape during breathing. Variations in the lung surface could provide areas where nanoparticles cross more easily.

9.1 Suggestions for Future Work

1. Look at different surface generation mechanisms (e.g. vapour deposition of fragments or diffusion of hydrocarbon components through an attractive tube) and analyse the effect on flow behaviour over these differently generated surfaces.

2. Analysis of the flow of ethanol through the tubes to enable further comparison with experimental results for the three fluids.

3. Simulation of larger pore width systems with water (nearer the d=42nm experimental amorphous systems).

4. Longer integration times and lower external force values for the flow through the nanopores.

5. Simulation of larger biomembrane systems and longer simulation times (several hundred nanoseconds).

6. Simulation of a wider variety of shapes and sizes of nanoparticles (e.g. Nanotubes or non-spherical Titanium dioxide fragments) and the effect of the shape on the interaction with the membrane.

7. The addition of more components to the surfactant layer, e.g. a greater variety of lipids or proteins which may alter the behaviour of nanoparticles at the interface.

Appendix A

Published and Submitted Papers

"Slip Boundaries in Nanopores"

M. Groombridge , M. Schneemilch and N. Quirke, Molecular Simulation, 37:12, 1023-1030 (2011)

Abstract: The flow of liquid water confined within slit pores formed from amorphous surfaces of carbon and polydimethylsiloxane (PDMS) has been investigated using molecular dynamics techniques. For PDMS (including plasma treated forms) the slip length is found to be very small, and there are essentially stick boundary conditions. The slip lengths for amorphous carbon surfaces are significant; however, they are much smaller than those measured experimentally for nanopipes. We show, for the first time, that the slip length can be predicted using the Sokhan-Quirke equation for amorphous surfaces using only equilibrium properties.

Nanoparticle Induced Water Bridging of Lung Surfactant Monolayers

M. Groombridge and N. Quirke

Chemistry Department, Imperial College, South Kensington, London SW7 2AZ, UK

Understanding how nanoparticles interact with biological barriers is key to many aspects of nanomedicine (including drug delivery) and environmental toxicology (for example related to lung diseases) yet this area is still poorly understood. Molecular simulation can play an important role in elucidating the fundamental processes by providing a molecular level description. Using molecular dynamics we follow the translocation of hydrophobic and hydrophilic engineered nanoparticles across a model pulmonary surfactant membrane and show, for the first time, how hydrophilic nanoparticles create a continuous water phase that bridges the membrane, linking the air and liminal phases.

1 Introduction

Inhaled particles have long been recognised as a health risk [1, 2]. There is particular concern where aerodynamic diameters are less than or equal to 100nm i.e. nanoparticles [3, 4, 5]. Fullerene-like structures are present in diesel and petrol soot [6, 7]. Mineral nanoparticles are widespread in the environment [8]. For singlet particles there is evidence that particles with diameters $>$10 nm deposit readily, largely by diffusion, in the airways and centriacinar, respiratory regions of the lung [9]. Those $<$10nm are found preferentially in the upper airways [10]. In susceptible subjects with existing heart and lung disease, there is an increased risk of morbidity and mortality [2]. Some of these effects have been attributed to translocated nanoparticles based on their potential effects on vascular function [11, 12].

Historically asbestos was discovered to have negative effects and carbon nanotubes are predicted to behave similarly. In-vivo experiments [13] have shown that nanotubes can induce a response similar to that of asbestos fibres. Carcinogenicity of asbestos fibres is found to be largest when exposed to longer ($> 20\mu$m) fibres because macrophages cannot engulf larger fibres. Radioactive particles have also been found to enter the bloodstream in humans when inhaled [14]. More recently, the negative effects of graphene nanoplatelets were reported [15]. The size and planar shape of the particles were predicted to possess unusual aerodynamic effects.

Ultrafine TiO_2 particles have been shown to cross airways and cellular membranes by nonphagocytic mechanisms (by diffusion or adhesive interactions) in lungs and in cultured cells [16] and that the toxic effect of TiO_2 increases as the particulate size decreases [17]. Despite many studies the exact nature of nanoparticle interaction with lung lining fluids, and their transport into and across biological membranes remains unclear. Note that some nanoparticles may degrade pulmonary surfactant but be non-toxic to e.g. bronchial epithelial cells [18] so any nanoparticle related toxic effects may have different mechanisms depending on the type of membrane and its function.

Most previous simulation work has focused on the interactions between a bilayer membrane and nanoparticles. Few studies have looked specifically to simulate a lung membrane. One such paper, published in 2008 [19] looked at the surfactant film interacting with a carbon fragment. NVT simulation work of the passage of fullerene C_{60} across a model lung surfactant layer has also previously been carried out [20]. C_{60} molecules enter the hydrophilic tail region of a lipid bilayer. C_{60} particles are seen to remain in the head group region for the duration of the simulation. These previous simulations have primarily focused on relatively small nanoparticles around the size of fullerenes [21]. In this work a much larger (diameter 3nm) particle has been simulated atomistically, as well as several smaller particles of experimental interest, in order to study some of the effects of nanoparticles at biological interfaces.

We have used molecular dynamics to simulate mineral and organic nanoparticles in contact with model lung surfactant barriers looking in particular at sub 100ns processes including translocation but before protein adsorption (corona formation [22, 23], or membrane protein stripping [18]) is likely to occur. We show how translocation varies with nanoparticle size and surface properties and, for the first time, that hydrophilic nanoparticles create a continuous water phase that bridges the surfactant layer due to nanoparticle wetting. The wetting of the nanoparticle has not been considered in previous model studies and is often ignored in mesoscale models [24], yet it changes the nature of the particle/membrane (lipid and protein) interaction.

2 Simulation Details

In the lungs, the surfaces of the alveoli are covered with a layer of surfactant which controls surface tension during breathing. This surfactant contains a large number of different proteins/phospholipids but the most common constituent is DPPC. We therefore use a simple model of the functional lung lining membrane comprising only DPPC lipids as we are not accessing timescales relevant to membrane proteins. All simulations were performed in the NPT ensemble using GROMACS [25] at a physiological temperature of 310K. The DPPC and SPC/E molecules were coupled separately to a Berendsen thermostat [26] and the nanoparticles were uncoupled. Lennard-Jones potentials were cut off at 1 nm and particle mesh Ewald summation (PME) [27] was used to calculate the electrostatic forces.

Two configurations were studied: one with two independent DPPC monolayers in air (represented by vacuum) separated by a water phase with the nanoparticles entering the DPPC from the air phase (above and below the condensed phase) and a single monolayer on a water phase with the nanoparticle entering from the air/water interface. The initial bilayer configuration was based on the popular bilayer configuration published by Berendsen and Tieleman [28]. The bilayer was inverted, reflected and vacuum introduced to obtain two monolayer leaflets in the xy plane, each comprising 256 lipids, with 14552 waters with a specific area of 64 ApL (System 1). A density profile along the z-axis is shown for this equilibrated system (figure 1). The monolayer system had one layer removed and extra water molecules added to give a total of 25800 waters (the dimensions are Lx=12.5, Ly=12.5 and Lz=18.0nm for both systems (System 2). Parameters for the DPPC model were taken from Berger [29]. The SPC/E model [30] was used for the water molecules. Ion concentrations were fixed at physiological levels (Na = 24, K = 8, Cl = 32). The water equimolar density (taken as the location of the water surface) is located at $\pm$1.25 nm, and the density of DPPC groups peaks at $\pm$1.68nm. The shoulder of the surfactant density corresponds to the location of the hydrophobic tails. A density profile along the z-axis for the new monolayer arrangement is also shown in figure 1.

In agreement with previous work on the effect of ions on DPPC membranes we find that the sodium ion concentration peaks in the head group region (between 1 and 2 nm, figure 1) with an excess of chlorine over potassium and sodium in the water phase leading to a small net positive charge at the lipid head group interface balanced by a small net negative charge in the water phase so that overall the system is neutral.

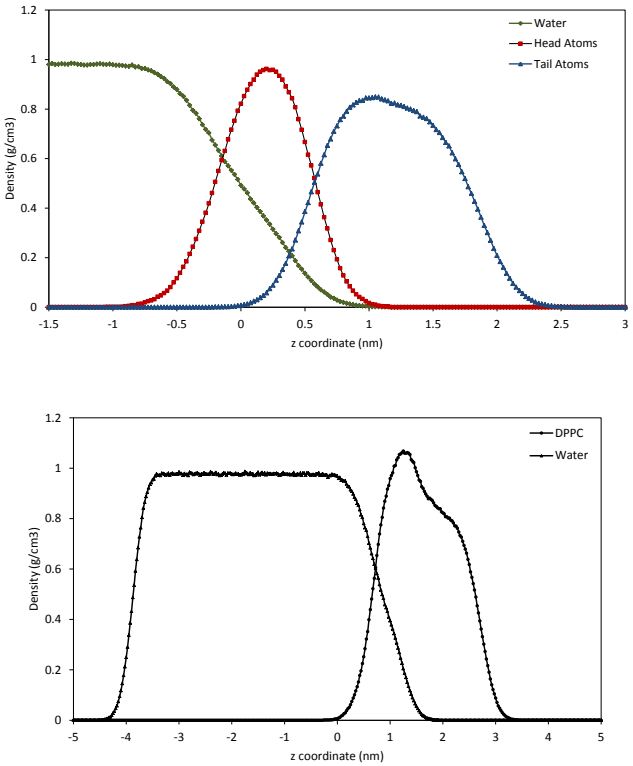


Figure 1: Density distributions for a) System 1 in the absence of nanoparticles and b) System 2

The external pressure values were chosen in order to give a 64ApL system for comparison with the NVT results. The surface tension in the simulation was calculated to be 26.202 ($\pm$0.639) mN/m, which is comparable to that found in the lung. Studies by Bangham [31] and others [32] suggest an upper range of around 25-30 mN/m during inhalation when the alveolus is expanded.

2.1 Nanoparticle Models

The fullerene (C_{60}) nanoparticle is modelled as a rigid sphere with a C-C bond length of 0.146nm. Functionalised nanoparticles were generated by adding hydroxyl groups at randomly chosen sites on the C_{60} molecule. We focus here on functionalised nanoparticles with 20 hydroxyl groups. All angles in the nanoparticle were fixed, as a result only the hydrogen atoms were able to move in relation to the rest of the molecule. The various interactions are therefore identical to those used by Qiao [33] except that here the SPC/E model was used. The C_{60}-lipid tail interaction was based on Werder et al [34].

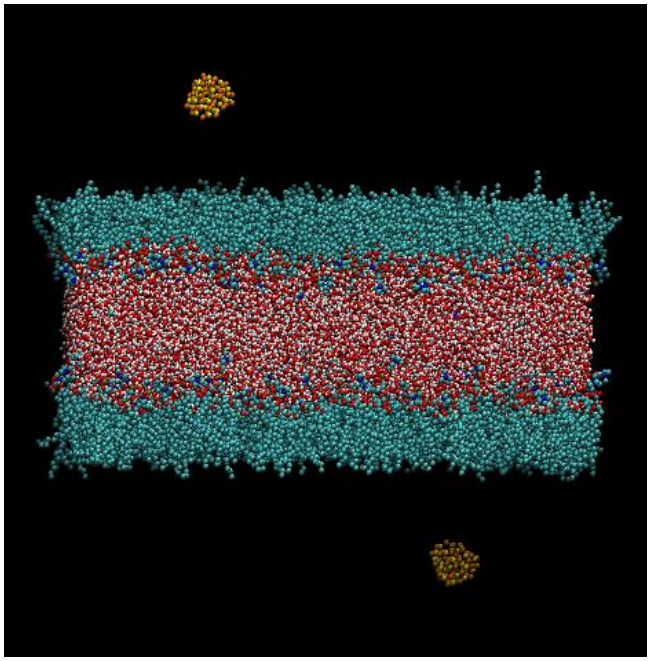


Figure 2: The Bilayer System with the Smallest TiO_2 Nanoparticles

Titanium Dioxide spheres at initial radii of 0.6nm, 1.0nm and 1.5nm were cut from a rutile lattice. They were then allowed to relax for 200ps to create an amorphous surface using potential parameters previously used in the study of TiO_2 nanoparticles [35]. The atoms were then fixed in position using constraints. Two different models were used for the Titanium Dioxide, one with the quantum mechanically determined partial charges used during the initial formation of the nanoparticles and the other with reduced partial charges to give a better agreement with the experimental contact angle [36]. These models give contact angles with water of around 45° and 75° respectively. UFF Lennard-Jones parameters [37] were chosen for the Van der Waals interactions. Lennard-Jones interactions with the lipid atoms were then determined using mixing-rules.

Nanoparticle properties are summarised in table 1.

3 Results

3.1 Fullerene Nanoparticles

Upon starting the simulation the pristine C_{60} molecule is seen to rapidly enter the system and diffuse to an equilibrium position in the tail region where it remains for the rest of the simulation. Its center of mass resides in the same position within the lipid tails (figure 3). The average positions after equilibration (relative to the water equimolar dividing surface (EMDS)) are 0.9712 $\pm$0.1532nm and 0.9761 $\pm$0.1451nm, putting them both around 0.5nm from the start of the interfacial headgroup region. Features from the density profile are noted on the plots. The water equimolar diving surface (EMDS), the position of the start of the lipid tail atoms and the peak in the lipid head group density have been represented on the graph. The C_{60} nanoparticle possesses no charge and interacts via Van der Waals forces only. The energy of the nanoparticle is also seen to be constant after entry, averaging around -169.50 kJ/mol. The equilibrium position therefore is within the tail region. The lateral diffusion coefficient for the nanoparticle in this region is $0.0765\times10^{-9}\mathrm{m}^2\mathrm{s}^{-1}$.

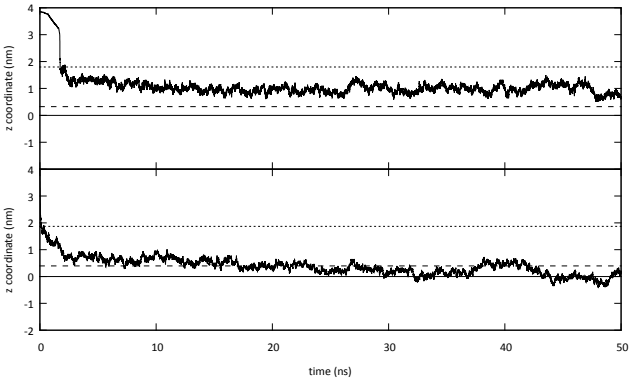


Figure 3: The Position of the Center of Mass of the C_{60} and $C_{60}OH_{20}$ Nanoparticles

The hydroxylated fullerene is seen to sit further into the membrane, residing around the position of the peak in the head group density (figure 3). The nanoparticle in this case takes tens of nanoseconds to diffuse to an equilibrium position. The average positions after equilibration are 0.2421 $\pm$0.1235nm and 0.06268 $\pm$0.1401nm, both within the head group/water interface region of the monolayer. Representation of the fluid (water/lipid) interface as a straight line does not necessarily give a clear picture, so a more local picture has been obtained by measuring the types and numbers of atoms residing in the first shell around the nanoparticle. The numbers of water molecules and lipid atoms surrounding the nanoparticle have therefore been calculated. It is seen that as the nanoparticle sits at the interface, water molecules leave the bulk and totally surround the nanoparticle. The numbers seem to have equilibrated after at a total of around 20 after 30ns. The lateral diffusion coefficient for the nanoparticle in this re-

Nanoparticle	Radius (nm)	Surface Area (nm^2)	Volume (nm^3)
TiO_2 Small	0.629	4.9718	1.0424
TiO_2 Large	1.543	29.9186	15.3882
C_{60}	0.351	1.5482	0.1811
$C_{60}(OH)_{20}$	0.525	3.4636	0.6061

Table 1: Nanoparticle properties. C_{60} radius was taken at the surface carbon atom centre of mass, for $C_{60}(OH)_{20}$, at the hydrogen atom, for the amorphous TiO_2, at 95% of the mass.

gion is lower this time at $0.0568\times10^{-9}m^2s^{-1}$.

3.2 Titanium Dioxide Nanoparticles - Potential I

The smallest TiO_2 nanoparticle with potential I is seen to behave similarly to the pristine fullerene, but sits slightly lower within the tail region (figure 4). The average positions of the two nanoparticles after equilibration are 0.7865 $\pm$0.1561nm and 0.9939 $\pm$0.1522nm.

The largest (r=1.5nm) nanoparticle behaves slightly differently. Due to its large size it can now span the entire monolayer. The center of mass position is similar to that of the r=0.6nm nanoparticle, but the edges of the nanoparticle extend well within the water layer, which allows the water to move around the nanoparticle edge, effectively bridging the layer. The entry of the nanoparticle into the layer is much slower and after 50ns is still moving downwards. The total number of water molecules reaches 70 after 50ns.

The rotation of the nanoparticle within the membrane has been calculated, by measuring the zenith and azimuth angles of the nanoparticle axis with respect to that of the membrane during the course of the simulation. There is some movement, but it is not particularly rapid once the nanoparticle has entered the membrane, nor does it only rotate in one direction. The standard deviations of the angles are $\theta = 2.976°$ and $\phi = 8.343°$.

3.3 Titanium Dioxide Nanoparticles - Potential II

The smallest Titanium Dioxide nanoparticle sits at the lipid/water interface (figure 4), but still does not completely enter the water phase. Again through monitoring the number and types of atoms surrounding the particle, it can be seen that there are still lipid atoms surrounding the particle on both top/bottom at all times. The number of water molecules around the nanoparticle this time is much higher. The number of lipid atoms and water molecules is stable after 10ns in one case, 20ns in the other. The average positions after equilibration are -0.2450 $\pm$0.1609nm and 0.4415 $\pm$0.1534nm. Although one is below the normal position of the equimolar dividing surface, locally it is still interfacially bound and surrounded by both lipid atoms as well as water molecules. The lateral diffusion coefficient for the nanoparticle in this region is $0.0574\times10^{-9}m^2s^{-1}$, similar to the hydroxylated fullerene.

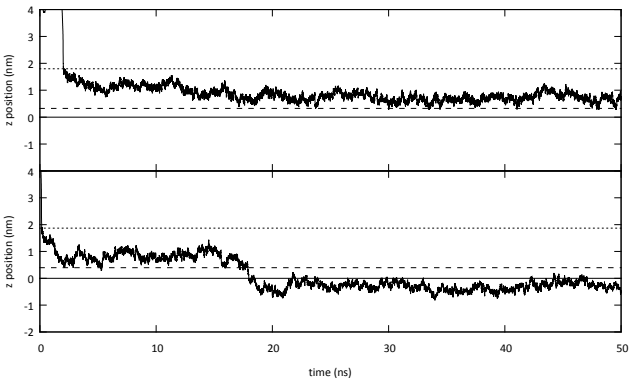


Figure 4: The Position of the Center of Mass of the r=0.6nm TiO_2 Nanoparticles (Potential I top, II bottom)

The largest TiO_2 particle, which is now more hydrophilic, is rapidly hydrated on entering the membrane. The positions of the top/bottom edges are plotted in figure 5. There are a much larger number of water molecules leaving the water phase and surrounding the nanoparticle, and this effect is much more rapid. In this case the number of lipid atoms and water molecules surrounding the nanoparticle take time to adjust. The bottom half becomes quickly covered in water molecules upon reaching the interface (around 250 molecules) but the top half sees a gradual build-up over 30ns to reach the same number. The number of water molecules and lipid atoms do not stabilise until after 40ns in this case. These are shown in figure 6. The lateral diffusion coefficient for the nanoparticle is much lower this time at $0.0213\times10^{-9}m^2s^{-1}$, but is in line with that expected

Particle	NP 1 Position (nm)	St. Dev. (nm)	NP 2 Position (nm)	St. Dev. (nm)
C_{60}	0.9712	0.1532	0.9761	0.1451
$C_{60}(OH)_{20}$	0.2421	0.1235	0.0627	0.1401
TiO_2(I) r=0.6nm	0.7865	0.1561	0.9939	0.1522
TiO_2(II) r=0.6nm	-0.2450	0.1609	0.4415	0.1534

Table 2: The Average Positions of the Nanoparticles

due to the increased size of the particle.

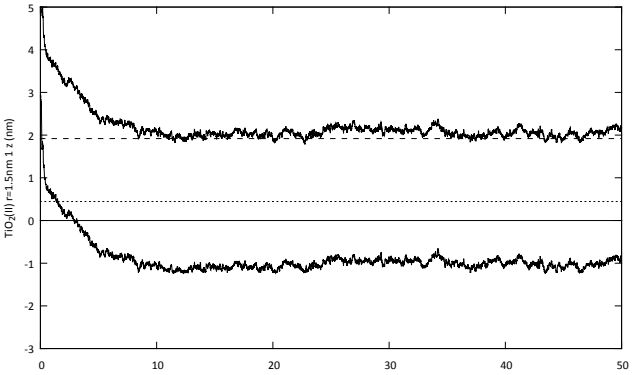


Figure 5: The Positions of the r=1.5nm TiO_2(II) Nanoparticle Edges

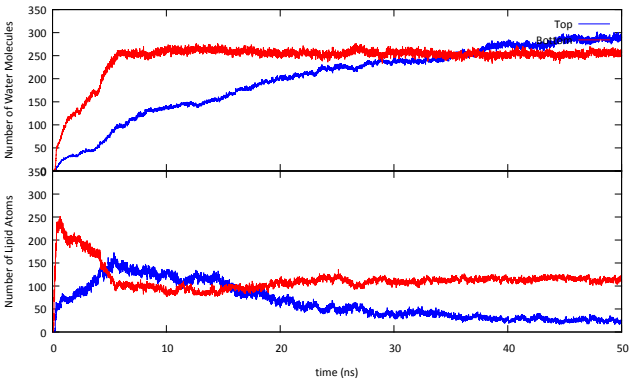


Figure 6: The Number of Water Molecules and Lipid Atoms on the r=1.5nm TiO_2(II) Nanoparticle as a Function of Time

The density of water around the nanoparticle has been plotted two-dimensionally at several times to show how the water molecules form a continuous phase around the nanoparticle. In figure 7 the situation is shown after 5, 15, 25 and 40ns. The z-axis and the r-axis are both defined relative to the center of mass of the nanoparticle.

The trajectories that some individual water molecules take around the nanoparticle have been tracked. In one example the molecule initially moves

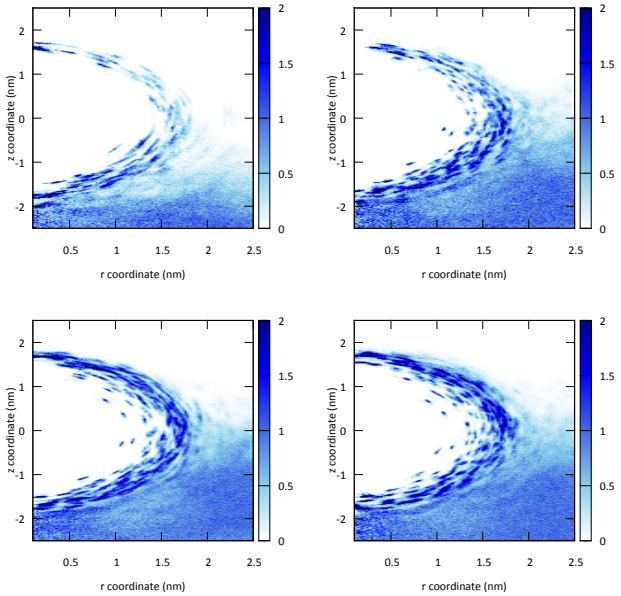


Figure 7: The 2D-Water Density Around the r=1.5nm TiO_2(II) Nanoparticle after 5, 15, 25 and 40ns

half-way up the side of the nanoparticle and sits at the edge of the nanoparticle, then leaves and later comes back to sit upon the top of the nanoparticle. Its trajectory is seen to be at a constant value of the radius, indicating it remains associated with the particle as it diffuses around. Diffusion coefficients for water molecules on the top and bottom half of the nanoparticle around the edge of the nanoparticle are calculated to be $0.0728\times10^{-9}\mathrm{m}^2\mathrm{s}^{-1}$ on the top half and $0.2590\times10^{-9}\mathrm{m}^2\mathrm{s}^{-1}$ for the bottom half. These are significantly reduced relative to the bulk water in the system, around 10% for the bottom and 2.5% for the top.

3.4 Monolayer Systems

Next nanoparticles were added to the monolayer configuration and allowed to enter the system through the water/air interface. None of the nanoparticles migrate to the interface except for the largest TiO_2(I) one, which sits at the interface but does not breach

it. The Van der Waals energy of the C_{60} molecule in the water phase is found to be -77.46 kJ/mol, much lower than that found in the lipid tails region (-169.50 kJ/mol). The C_{60} nanoparticle sits at the water-vacuum interface for 18ns before travelling to the other side of the simulation cell. The smallest TiO_2(I) particle shows a similar unwillingness to enter. The other particles all sit within the water phase but there is no net migration, suggesting they are relatively stable in the water layer. Diffusion coefficients for the nanoparticle in the water phase were found to be $0.2943\times10^{-9}m^2s^{-1}$ for the $C_{60}(OH)_{20}$, $0.1372\times10^{-9}m^2s^{-1}$ for the r=0.6nm TiO_2(II) and $0.0442\times10^{-9}m^2s^{-1}$ for the r=1.5nm TiO_2 (II). The largest TiO_2 (I) nanoparticle sits at the interface.

3.5 Energy/Force Measurements

Calculations were undertaken to measure the forces and energies needed for translocation of the nanoparticles across the membrane. Using a harmonic force the nanoparticles were dragged along the z-coordinate of the simulation cell from the vacuum side through the lipids to the water phase. The particles were frozen at several points along this coordinate and the average force at each position calculated over several nanoseconds. It is noted that the hydrophilic particles were found to extract lipid molecules from the interface and to retain them in their sphere of influence whilst dragged through the water phase, this effect was also noted previously [19, 20]. Several attempts were made to avoid this effect with different pulling rates/forces without success.

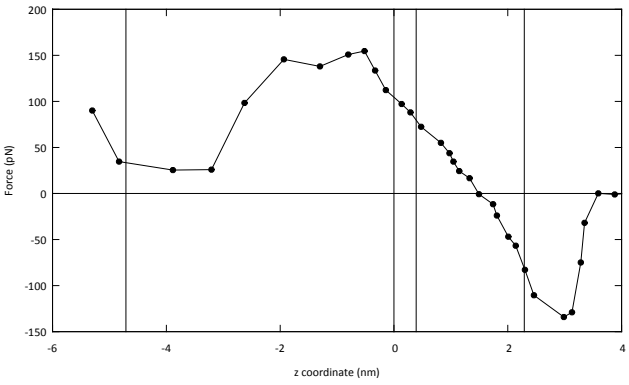


Figure 8: The Force Profile for the r=0.6nm TiO_2(I) Nanoparticle

All plots are relative to the water equimolar dividing surface again (see figure 1). A negative force represents the nanoparticle being pulled towards the water phase (to negative z), positive being pushed back towards the vacuum (to positive z). The minimum in the plots is at the point where the force is zero, which corresponds in the $C_{60}(OH)_{20}$ system to z=0.5nm and z=0.7nm for the r=0.6nm TiO_2(II) system, both in the head-group region and for the r=0.6nm TiO_2(I) system (figure 8) at z=1.5nm, well within the tail region, reflecting the difference in their hydrophilicities. These positions do not quite represent the long-time equilibrium positions attained during the main simulations, but those were run for 10-20 times longer. The C_{60} particle from the force plot was found to have a minimum at z=1.3nm.

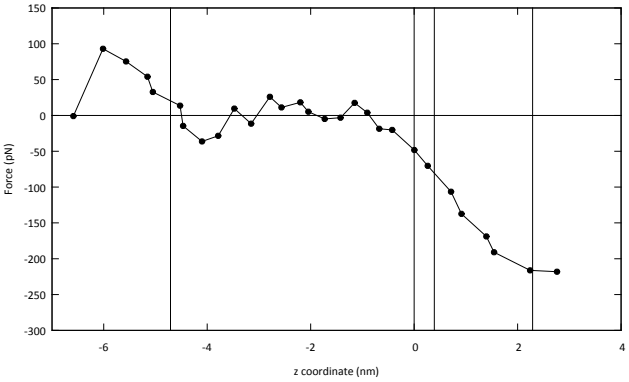


Figure 9: The Force Profile for the r=0.6nm TiO_2(I) Nanoparticle in the Reversed Direction

The nanoparticles were also dragged in the opposite direction across the interface, from the water side. In these cases it is seen that the z position of the minimum is slightly lower than in the approach from the vacuum side (figure 9). Again it seems that the DPPC interface is acting as a barrier to the nanoparticle crossing. It is also noted that the average force experienced in the water phase is fairly low, which could explain the nanoparticles remaining within the water phase rather than migrating to the interface in the monolayer systems.

All the force measurements suggest that there is a significant energy barrier. The resistance of the DPPC layer to the passage of the nanoparticles could represent the strong intermolecular bonding between the DPPC molecules. In reality the lipid layer is inhomogeneous and will have many different components, e.g. Cholesterol or Proteins which may introduce weakness into the layer through which nanoparticles may find it easier to pass.

Energy calculations were also made for the nanoparticles in each phase. An approximation of the energies experienced by the charged particles in each phase were calculated by using the direct Coulomb interaction, rather than the full Ewald sum

Particle	Position	Energy (kJ/mol)
C_{60}	Lipid	-169.50
C_{60}	Water	-77.46
$C_{60}(OH)_{20}$	Lipid	-2201.15
$C_{60}(OH)_{20}$	Water	-898.83
TiO_2(I) r=0.6nm	Lipid	-294.81
TiO_2(I) r=0.6nm	Water	-108.76
TiO_2(I) r=1.5nm	Lipid	-1052.48
TiO_2(I) r=1.5nm	Water	-671.50
TiO_2(II) r=0.6nm	Lipid	-1287.04
TiO_2(II) r=0.6nm	Water	-720.43
TiO_2(II) r=1.5nm	Lipid (Unhydr)	-6378.64
TiO_2(II) r=1.5nm	Lipid (Hydr)	-8568.67
TiO_2(II) r=1.5nm	Water	-4236.67

Table 3: The Energies for the Nanoparticles

due to the non-separability of the reciprocal space sum using GROMACS. The Coulomb energy was calculated directly to r=1.1nm and then shifted to zero over the next 0.3nm, giving 1.4nm total. In all cases the energies for the nanoparticles were lower in the equilibrium positions in the lipid phase found from the main simulations rather than the water phase. For example the $C_{60}(OH)_{20}$ nanoparticle has a much higher energy (-2201.15 kJ/mol) in the interfacial head-group region than in the water phase (-898.83 kJ/mol). The effect of the spreading of water around the largest TiO_2 nanoparticle was also measured by taking points from the simulation where the nanoparticle was sitting at the interface initially after 15ns and then after 50ns when it was more hydrated. The energy at the equilibrium position was further lowered by this water spreading. This data is shown in table 3.

4 Conclusions

There is currently a great interest in the effects of inhalation and the interactions of nanoparticles with lung tissues due to the implications in environmental toxicology. Dynamic effects at membranes are important to understand and simulation work can help to shed light on them. The interaction of several types of nanoparticles with a biological membrane, based on the structure of a pulmonary surfactant layer, have been studied in this work. The nanoparticles were chosen as they are environmentally interesting - fullerenes are found in soot [7] and titanium dioxide is widely used industrially. The range and size of the nanoparticles examined have been extended compared to previous work and several hydrophilicities tested. The nanoparticles are all seen to rapidly diffuse into the tail region. Hydrophobic nanoparticles have been found to continue to reside in this location whereas hydrophilic ones have been shown to sit at the water/lipid head group interface. It is confirmed through studies of the energy of the nanoparticle in different positions, that they have reached their preferred locations. Through analysing the distribution of the numbers and types of each atom surrounding the nanoparticle it is found that no particles have entirely left the interfacial region and entered the water phase in the timescales employed here (<50ns). Therefore no nanoparticles are found to spontaneously diffuse across the surfactant layer and move freely within the water layer. A timescale of 2ms was predicted by Qiao [33] well beyond the range of these simulations.

The nanoparticle may scavenge protein surfactant from membrane but this seems to occur on times scales up to an hour or more. Since the nanoparticle studies here translocate the membrane in 5 to 40 ns , this may be an indication that the protein absorption takes place after translocation to the membrane water interface, with membrane protein displacing the water phase around the nanoparticle.

In the case of the hydrophilic nanoparticles which sit at the interface, an interesting effect was found whereby mobile water molecules leave the bulk phase and spread round the surface of the nanoparticle. For the largest nanoparticles this creates a bridge across the interface, which could have useful applications, e.g. for the delivery of molecules to cells. This effect could be missed when using mesoscale methods such as coarse-grained models with no atomic scale resolution. The structure of real physiologi-

cal lung membranes are far more complicated than those simulated here. The layer is in fact inhomogeneous with many different components and this could dramatically affect the interactions of nanoparticles with the tissue as could the perturbation caused by the lung membrane changing shape during breathing. Variations in the lung surface could provide areas where nanoparticles cross more easily.

References

[1] M. Schwarz and T. King 5th ed., PMPH USA, 2011.

[2] W. Morgan and A. Seaton 3rd ed., Saunders, 1995.

[3] J. Schwartz, *Is There Harvesting in the Association of Airborne Particles with Daily Deaths and Hospital Admissions?*, Epidemiology 12 (2001), pp. 55–61.

[4] K. Donaldson, V. Stone, A. Clouter, L. Renwick, and W. MacNee, *UltraFine Particles*, Occupational and Environmental Medicine 58 (2001), pp. 211–216.

[5] J. Kaiser, *Mounting Evidence Indicts Fine Particle Pollution*, Science 307 (2005), p. 1858.

[6] T. Ishiguro, Y. Takatori, and K. Akihama, *Microstructure of Diesel Soot Particles Probed by Electron Microscopy*, Combustion and Flame 108 (1997), pp. 231–234.

[7] T. Lee, N. Yao, T. Chen, and W. Hsu, *Fullerene-like Carbon Particles in Petrol Soot*, Carbon 40 (2002), pp. 2275–2279.

[8] T. Tsao, Y. Chen, and M. Wang, *Origin, Separation and Identification of Environmental Nanoparticles: A Review*, Journal of Environmental Monitoring 13 (2011), pp. 1156–1163.

[9] H. Yeh, B. Muggenburg, and J. Harkema, *In-Vivo Deposition of Inhaled Ultrafine Particles in the Respiratory Tract of Rhesus Monkeys*, Aerosol Science and Technology 27 (1997), pp. 465–470.

[10] L. Zhao, S. Feng, and M. Go, *Investigation of Molecular Interactions Between Paclitaxel and DPPC by Langmuir Film Balance and Differential Scanning Colourimetry*, Journal of Pharmaceutical Sciences 93 (2004), pp. 86–98.

[11] K. Bagate, J. Meiring, M. Gerlofs-Nijland, R. Vincent, F. Cassee, and P. Borm, *Vascular Effects of Ambient Particulate Matter Instillation in Hypertensive Rats*, Toxicology and Applied Pharmacology 197 (2004), pp. 29–39.

[12] T. Nurkiewicz, D. Porter, M. Barger, V. Castranova, and M. Boegehold, *Particulate Matter Exposure Impairs Systemic Microvascular Endothelium-Dependent Dilation*, Environmental Health Perspectives 112 (2004), pp. 1299–1306.

[13] K. Kostarelos, *The Long and Short of Carbon Nanotube Toxicity*, Nature Biotechnology 26 (2008), pp. 774–776.

[14] A. Nemmar, P. Hoet, B. Vanquickenborne, D. Dinsdale, M. Thomeer, M. Hoylaerts, H. Vanbilloen, L. Mortelmans, and B. Nemery, *Passage of Inhaled Particles Into the Blood Circulation in Humans*, Circulation 105 (2002), pp. 411–414.

[15] A. Schinwald, F. Murphy, A. Jones, W. MacNee, and K. Donaldson, *Graphene-Based Nanoplatelets: A New Risk to the Respiratory System as a Consequence of their Unusual Aerodynamic Properties*, ACS Nano 6 (2012), pp. 736–746.

[16] M. Geiser, B. Rothen-Rutishauer, N. Kapp, S. Schurch, W. Kreyling, H. Sculz, M. Semmler, V. Hof, J. Heyder, and P. Gehr, *Ultrafine Particles Cross Cellular Membranes by Nonphagocytic Mechanisms in Lungs and in Cultured Cells*, Environmental Health Perspectives 113 (2005), pp. 1555–1560.

[17] H. Johnston, G. Hutchison, F. Christensen, S. Peters, S. Hankin, and V. Stone, *Identification of the Mechanisms that Drive the Toxicity of TiO_2 Particulates: the Contribution of Physicochemical Characteristics*, Particle and Fibre Toxicology 6 (2009), p. 33.

[18] Q. Fan, Y. Wang, X. Zhao, J. Loo, and Y. Zuo, *Adverse Biophysical Effects of Hydroxyapatite Nanoparticles on Natural Pulmonary Surfactant*, ACS Nano 5 (2011), pp. 6410–6416.

[19] S. Choe, R. Chang, J. Jeon, and A. Violi, *Molecular Dynamics Simulation Study of a Pulmonary Surfactant Film Interacting with a Carbonaceous Nanoparticle*, Biophysical Journal 95 (2008), pp. 4102–4114.

[20] M. Schneemilch and N. Quirke, *Molecular Dynamics of Nanoparticle Translocation at Lipid Interfaces*, Molecular Simulation 36 (2010), pp. 831–835.

[21] A. Makarucha, N. Todorova, and I. Yarovsky, *Nanomaterials in Biological Environment: A Review of Computer Modelling Studies*, European Biophysics Journal 40 (2011), pp. 103–115.

[22] I. Lynch, A. Salvati, and K. Dawson, *Protein-Nanoparticle Interactions: What Does the Cell See?*, Nature Nanotechnology 4 (2009), pp. 546–547.

[23] D. Dell'Arco, M. Lundqvist, C. Oslakovic, T. Cedervall, and S. Linse, *Modelling the Time Evolution of the Nanoparticle-Protein Corona in a Body Fluid*, PLoS One 5 (2010), p. e10949.

[24] M. Deserno, *Mesoscopic Membrane Physics: Concepts, Simulations and Selected Applications*, Macromolecular Rapid Communications 30 (2009), pp. 752–771.

[25] E. Lindahl, B. Hess, and D. SpoelVan der , *GROMACS 3.0: A Package for Molecular Simulation and Trajectory Analysis*, Journal of Molecular Modelling 7 (2001), pp. 306–317.

[26] H. Berendsen, J. Postma, W. Gunsterenvan , A. DiNola, and J. Haak, *Molecular Dynamics with Coupling to an External Bath*, Journal of Chemical Physics 81 (1984), pp. 3684–3690.

[27] T. Darden, D. York, and L. Pedersen, *Particle Mesh Ewald: An Nlog(N) Method for Ewald Sums in Large Systems*, Journal of Chemical Physics 98 (1993), pp. 10089–10092.

[28] D. Tieleman and H. Berendsen, *Molecular Dynamics Simulations of a Fully Hydrated Dipalmitoylphosphatidylcholine Bilayer with Different Macroscopic Boundary Conditions and Parameters*, Journal of Chemical Physics 105 (1996), pp. 4871–4880.

[29] O. Berger, O. Edholm, and F. Jahnig, *Molecular Dynamics Simulations of a Fluid Bilayer of Dipalmitoylphosphatidylcholine at Full Hydration, Constant Pressure and Constant Temperature*, Biophysics Journal 72 (1997), pp. 2002–2013.

[30] H. Berendsen, J. Grigera, and T. Straatsma, *The Missing Term in Effective Pair Potentials*, Journal of Physical Chemistry 91 (1987), pp. 6269–6271.

[31] A. Bangham, *Lung Surfactant: How it Does and Does Not Work*, Lung 165 (1987), pp. 17–25.

[32] F. Possmayer, K. Nag, K. Rodriguez, R. Qanbar, and S. Schurch, *Surface Activity in Vitro: Role of Surfactant Proteins*, Comparative Biochemistry and Physiology A 129 (2001), pp. 209–220.

[33] R. Qiao, A. Roberts, A. Mount, S. Klaine, and P. Ke, *'Translocation of C60 and its Derivatives Across a Lipid Bilayer'*, Nano Letters 7 (2007), pp. 614–619.

[34] T. Werder, J. Walther, R. Jaffe, T. Halicioglu, and P. Koumoutsakos, *On the Water-Carbon Interaction for Use in Molecular Dynamics Simulations of Graphite and Carbon Nanotubes*, Journal of Physical Chemistry B 107 (2003), pp. 1345–1352.

[35] P. Naicker, P. Cummings, H. Zhang, and J. Banfield, *Characterisation of Titanium Dioxide Nanoparticles Using Molecular Dynamics Simulations*, Journal of Physical Chemistry B 109 (2005), pp. 15243–15249.

[36] J.H. Park and N. Aluru, *Temperature-Dependent Wettability on a Titanium Dioxide Surface*, Molecular Simulation 35 (2009), pp. 31–37.

[37] A. Rappe, C. Casewit, K. Colwell, W. Goddard, and W. Skiff, *UFF, a Full Periodic Table Force Field for Molecular Mechanics and Molecular Dynamics Simulations*, Journal of the American Chemical Society 114 (1992), pp. 10024–10035.

Appendix B

Acknowledgments

Professor Nick Quirke for guidance throughout, helpful comments and also allowing me the freedom to follow my own interests.

Dr. Matt Schneemilch for providing some initial models and assistance.

Bibliography

[1] J. Kameoka, H. Craighead, H. Zhang, and J. Henion, *A Polymeric Microfluidic Chip for CE/MS Determination of Small Molecules*, Analytical Chemistry 73 (2001), pp. 1935–1941.

[2] G.B. Lee, S.H. Chen, G.R. Huang, W.C. Sung, and Y.H. Lin, *Microfabricated Plastic Chips by Hot Embossing Methods and their Applications for DNA Separation and Detection*, Sensors and Actuators B 75 (2001), pp. 142–148.

[3] Z. Fan, S. Mangru, R. Granzow, P. Heaney, W. Ho, Q. Dong, and R. Kumar, *Dynamic DNA Hybridisation on a Chip using Paramagnetic Beads*, Analytical Chemistry 71 (1999), pp. 4851–4859.

[4] I.K. Glasgow, H. Zeringue, D. Beebe, S. Choi, J. Lyman, N. Chan, and M. Wheeler, *Handling Individual Mammalian Embryos using Microfluidics*, IEEE Transactions on Biomedical Engineering 48 (2001), pp. 570–578.

[5] S. Yang, A. Undar, and J. Zahn, *A Microfluidic Device for Continuous, Real Time Blood Plasma Separation*, Lab on a Chip (2006).

[6] A. Van Der Berg, A. Grisel, E. Verney-Norberg, B. Van Der Schoot, M. Koudelha, and N. De Rooj, *On-wafer Fabricated Free-chlorine Sensor with ppb Detection Limit for Drinking-Water Monitoring*, Sensors and Actuators B 13 (1993), pp. 396–399.

[7] C.e.a. Luo, *A PDMS Microfluidic Device for Optical Detection of Protein Immunoassay Using Gold Nanoparticles*, Lab on a Chip 5 (2005), pp. 726–729.

[8] M. Morra, P. Occhiello, P. Humphrey, and D. Johnson, *On the Aging of Oxygen Plasma Treated Polydimethylsiloxane Surfaces*, Journal of Colloid and Interfacial Science 137 (1990), pp. 11–24.

[9] D. Eddington, J. Puccinelli, and D. Beebe, *Thermal Aging and Reduced Hydrophobic Recovery of Polydimethylslioxane*, Sensors and Actuators B 114 (2006), pp. 170–172.

[10] J. McDonald, D. Duffy, J. Anderson, D. Chui, H. Wu, O. Schueller, and G. Whitesides, *Fabrication of Microfluidic Systems in Poly(dimethylsiloxane)*, Electrophoresis 21 (2000), pp. 27–40.

[11] C. Effenhauser, G. Bruin, A. Paulus, and M. Ehrat, *Integrated Capillary Electrophoresis on Flexible Silicone Microdevices: Analysis of DNA Restriction Fragments and Detection of Single DNA Molecules*, Analytical Chemistry 69 (1997), pp. 3451–3457.

[12] N. Churaev Gordon and Breach (Amsterdam), 2000.

[13] V. Sokhan, D. Nicholson, and N. Quirke, *Fluid Flow in Nanopores: Accurate Boundary Conditions for Carbon Nanotubes*, Journal of Chemical Physics 117 (2002), pp. 8531–8539.

[14] A. Ziarani and A. Mohamad, *A Molecular Dynamics Study of Perturbed Poiseuille Flow in a Nanochannel*, Microfluid Nanofluid 2 (2005), pp. 12–20.

[15] S. Iijima, *Helical Microtubules of Graphitic Carbon*, Nature 354 (1991), pp. 56–58.

[16] P. Harris 1st ed., Cambridge, 2009.

[17] C. Jin, K. Suenaga, and S. IIjima, *Plumbing Carbon Nanotubes*, Nature Nanotechnology 3 (2008), pp. 17–21.

[18] G. Hummer, J. Rasaiah, and J. Noworyta, *Water Conduction Through the Hydrophobic Channel of a Carbon Nanotube*, Nature 414 (2001), pp. 188–190.

[19] S. Supple and N. Quirke, *Molecular Dynamics of Transient Oil Flows in Nanopores I : Imbibition Speeds for Single Walled Nanotubes*, Journal of Chemical Physics 121 (2004), pp. 8571–8579.

[20] A. Striolo, *The Mechanism of Water Diffusion in Narrow Carbon Nanotubes*, Nano Letters 6 (2006), pp. 633–639.

[21] S. Joseph and N. Aluru, *Why are Carbon Nanotubes Fast Transporters of Water?*, Nano Letters (2008).

[22] P. De Gennes, *On Fluid/Wall Slippage*, Langmuir 18 (2002), pp. 3413–3414.

[23] J. Thomas and A. McGaughey, *Reassessing Fast Water Transport Through Carbon Nanotubes*, Nano Letters 8 (2008), pp. 2788–2793.

[24] K. Falk, F. Sedlmeier, L. Joly, R. Netz, and L. Bocquet, *Molecular Origin of Fast Water Transport in Carbon Nanotube Membranes: Superlubricity versus Curvature Dependent Friction*, Nano Letters 10 (2010), pp. 4067–4073.

[25] E. Kotsalis, J. Walther, and P. Koumoutsakos, *Multiphase Water Flow Inside Carbon Nanotubes*, International Journal of Multiphase Flow 30 (2004), pp. 995–1010.

[26] G. Cao, Y. Qiao, Q. Zhou, and X. Chen, *Water Infiltration Behaviours in Carbon Nanotubes Under Quasi-Static and Dynamic Loading Conditions*, Molecular Simulation 34 (2008), pp. 1267–1274.

[27] D. Mattia and Y. Gogotsi, *Review: Static and Dynamic Behaviour of Liquids Inside Carbon Nanotubes*, Microfluid Nanofluid 5 (2008), pp. 289–305.

[28] X. Chen, G. Cao, A. Han, V. Punyamurtula, L. Liu, P. Culligan, T. Kim, and Y. Qiao, *Nanoscale Fluid Transport: Size and Rate Effects*, Nano Letters 8 (2008), pp. 2988–2992.

[29] Q. Zhang, K.Y. Chan, and N. Quirke, *Molecular Dynamics Simulation of Water Confined in a Nanopore of Amorphous Silica*, Molecular Simulation 35 (2009), pp. 1215–1223.

[30] Z. Insepov, D. Wolf, and A. Hassanein, *Nanopumping Using Carbon Nanotubes*, Nano Letters 6 (2006), pp. 1893–1895.

[31] M. Longhurst and N. Quirke, *Temperature-driven Pumping of Fluid through Single-Walled Carbon Nanotubes*, Nano Letters 7 (2007), pp. 3324–3328.

[32] E. Dujardin, T. Ebbesen, A. Krishnan, and M. Treacy, *Wetting of Single Shell Carbon Nanotubes*, Advanced Materials 10 (1998), pp. 1472–1475.

[33] M. Majumder, N. Chopra, R. Andrews, and B. Hinds, *Enhanced Flow in Carbon Nanotubes*, Nature 438 (2005), p. 44.

[34] J. Holt, H. Park, Y. Wang, M. Stadermann, A. Artyukhin, C. Grigoropoulos, A. Noy, and O. Bakajin, *Fast Mass Transport Through Sub-2-Nanometer Carbon Nanotubes*, Science 312 (2006), pp. 1034–1036.

[35] J. Cheng and N. Giordano, *Fluid Flow Through Nanometer-Scale Channels*, Physical Review E 65 (2002), p. 031206.

[36] B. Kim, S. Sinha, and H. Bau, *Optical Microscope Studies of Liquid Transport in Carbon Nanotubes*, Nano Letters 4 (2004), pp. 2203–2208.

[37] A. Poynor, L. Hong, I. Robinson, S. Granick, Z. Zhang, and P. Fenter, *How Water Meets a Hydrophobic Surface*, Physical Review Letters 97 (2006), p. 266101.

[38] D. Nicholson and S. Bhatia, *Fluid Transport in Nanospaces*, Molecular Simulation 35 (2009), pp. 109–121.

[39] S. Sinha, M. Rossi, D. Mattia, Y. Gogotsi, and H. Bau, *Induction and Measurement of Minute Flow Rates through Nanopipes*, Physics of Fluids 19 (2007), p. 013603.

[40] B. Kim, T. Murray, and H. Bau, *The Fabrication of Integrated Carbon Pipes with Sub-Micron Diameters*, Nanotechnology 16 (2005), pp. 1317–1320.

[41] T. Kyotani, L. Tsai, and A. Tomita, *Formation of Ultrafine Carbon Tubes by Using an Anodic Aluminium Oxide Film as a Template*, Chemistry of Materials 7 (1995), pp. 1427–1428.

[42] S. Joo, S. Choi, I. Oh, J. Kwak, Z. Liu, O. Terasaki, and R. Ryoo, *Ordered Nanoporous Arrays of Carbon Supporting High Dispersions of Platinum Nanoparticles*, Nature 412 (2001), pp. 169–172.

[43] T. Frauenheim, P. Balaudeck, U. Stephan, and G. Jungnickel, *Atomic Structure and Physical Properties of Amorphous Carbon and its Hydrogenated Analogs*, Physical Review B 48 (1993), pp. 4823–4834.

[44] G. Che, B. Lakshmi, C. Martin, E. Fisher, and R. Ruoff, *Chemical Vapour Deposition Based Synthesis of Carbon Nanotubes and Nanofibres Using a Template Method*, Chemistry of Materials 10 (1998), pp. 260–267.

[45] M. Whitby, L. Cagnon, M. Thanou, and N. Quirke, *Enhanced Fluid Flow Through Nanoscale Carbon Pipes*, Nano Letters 8 (2008), p. 2632.

[46] M. Whitby, L. Cagnon, M. Thanou, and N. Quirke, *Enhanced Fluid Flow Through Nanoscale Carbon Pipes (Erratum)*, Nano Letters 9 (2009), p. 2802.

[47] J. Jang, S. Ko, and Y. Kim, *Dual Functionalised Polymer Nanotubes as Substrates for Molecular Probe and DNA Carrier Applications*, Advanced Functional Materials 16 (2006), pp. 754–759.

[48] X. Zhao, Y. Xia, and G. Whitesides, *Soft Lithographic Methods for Nano-fabrication*, Journal of Materials Chemistry 7 (1997), pp. 1069–1074.

[49] F. Hua, Y. Sun, A. Gow, M. Meitl, L. Bilhaut, L. Rotkina, J. Wang, P. Geil, M. Shim, and J. Rogers, *Polymer Imprint Lithography with Molecular Scale Resolution*, Nano Letters 4 (2004), pp. 2467–2471.

[50] M. Chaudhury and G. Whitesides, *How to Make Water Run Uphill*, Science 256 (1992), pp. 1539–1541.

[51] D. Bodas, J. Rauch, and C. Khan-Malek, *Surface Modification and Aging Studies of Addition-Curing Silicone Rubbers by Oxygen Plasma*, European Polymer Journal 44 (2008), pp. 2130–2139.

[52] M. Schrlau, E. Falls, B. Ziober, and H. Bau, *Carbon Nanopipettes for Cell Probes and Intracellular Injection*, Nanotechnology 015101 (2008), p. 101.

[53] Y. Gogotsi, N. Naguib, and J. Libera, *In Situ Chemical Experiments in Carbon Nanotubes*, Chemical Physics Letters 365 (2002), pp. 354–360.

[54] Z. Li, W. Yan, and S. Dai, *Surface Functionalisation of Ordered Mesoporous Carbons*, Langmuir 21 (2005), pp. 11999–12006.

[55] A. Verma and F. Stellacci, *Effect of Surface Properties on Nanoparticle-Cell Interactions*, Small 6 (2010), pp. 12–21.

[56] W. Morgan and A. Seaton 3rd ed., Saunders, 1995.

[57] K. Kostarelos, *The Long and Short of Carbon Nanotube Toxicity*, Nature Biotechnology 26 (2008), pp. 774–776.

[58] A. Nemmar, P. Hoet, B. Vanquickenborne, D. Dinsdale, M. Thomeer, M. Hoylaerts, H. Vanbilloen, L. Mortelmans, and B. Nemery, *Passage of Inhaled Particles Into the Blood Circulation in Humans*, Circulation 105 (2002), pp. 411–414.

[59] A. Schinwald, F. Murphy, A. Jones, W. MacNee, and K. Donaldson, *Graphene-Based Nanoplatelets: A New Risk to the Respiratory System as a Consequence of their Unusual Aerodynamic Properties*, ACS Nano 6 (2012), pp. 736–746.

[60] T. Lee, N. Yao, T. Chen, and W. Hsu, *Fullerene-like Carbon Particles in Petrol Soot*, Carbon 40 (2002), pp. 2275–2279.

[61] M. Geiser, B. Rothen-Rutishauer, N. Kapp, S. Schurch, W. Kreyling, H. Sculz, M. Semmler, V. Hof, J. Heyder, and P. Gehr, *Ultrafine Particles Cross Cellular Membranes by Nonphagocytic Mechanisms in Lungs and in Cultured Cells*, Environmental Health Perspectives 113 (2005), pp. 1555–1560.

[62] Q. Fan, Y. Wang, X. Zhao, J. Loo, and Y. Zuo, *Adverse Biophysical Effects of Hydroxyapatite Nanoparticles on Natural Pulmonary Surfactant*, ACS Nano 5 (2011), pp. 6410–6416.

[63] L. Creuwels, L. Van Golde, and H. Haagsman, *The Pulmonary Surfactant System: Biochemical and Clinical Aspects*, Lung 175 (1997), pp. 1–39.

[64] S. Shelley, J. Balis, J. Paciga, C. Espinoza, and A. Richman, *Biochemical Composition of Adult Human Lung Surfactant*, Lung 160 (1982), pp. 195–206.

[65] C. Navier, *Memoire Sur les Lois du Mouvement des Fluides*, Memoires de l'Academie des Sciences 6 (1822), pp. 389–440.

[66] K. Travis, B. Todd, and D. Evans, *Departure from Navier-Stokes Hydrodynamics in Confined Liquids*, Physical Review E 55 (1997), pp. 4288–4295.

[67] B. Todd and D. Evans, *Temperature Profile for Poiseuille Flow*, Physical Review E 55 (1997), pp. 2800–2807.

[68] K. Travis and K. Gubbins, *Poiseuille Flow of Lennard-Jones Fluids in Narrow Slit Pores*, Journal of Chemical Physics 112 (2000), pp. 1984–1994.

[69] P. Thompson and M. Robbins, *Origin of Stick-slip Motion in Boundary Lubrication*, Science 250 (1990), p. 792.

[70] Y. Zhu and S. Granick, *Limits of the Hydrodynamic No-Slip Boundary Condition*, Physical Review Letters 88 (2002), p. 106102.

[71] J. Maxwell, *On Stresses in Gases Arising From Inequalities in Temperature*, Philosophical Transactions of the Royal Society of London 170 (1879), p. 231.

[72] R. Feres and G. Yablonski, *Knudsen's Cosine Law and Random Billiards*, Chemical Engineering Science 59 (2004), pp. 1541–1556.

[73] G. Arya, H. Chang, and E. Maginn, *Molecular Simulations of Knudsen Wall-Slip: Effect of Wall Morphology*, Molecular Simulation 29 (2003), pp. 697–709.

[74] G. Arya and H. Chang, *Knudsen Diffusivity of a Hard Sphere in a Rough Slit Pore*, Physical Review Letters 91 (2003), p. 026102.

[75] V. Sokhan, D. Nicholson, and N. Quirke, *Transport Properties of Nitrogen in Single Walled Carbon Nanotubes*, Journal of Chemical Physics 120 (2004), pp. 3855–3863.

[76] V. Sokhan and N. Quirke, *Interfacial Friction and collective Diffusion in Nanopores*, Molecular Simulation 31 (2004), p. 217.

[77] V. Sokhan and N. Quirke, *Slip Coefficients in Nanoscale Pore Flow*, Physical Review E 78 (2008), p. 015301(R).

[78] L. Bocquet and J. Barrat, *Hydrodynamic Boundary Conditions, Correlation Functions and Kubo Relations for Confined Fluids*, Physical Review E 49 (1994), pp. 3079–3092.

[79] P. Thompson and S. Troian, *A General Boundary Condition for Liquid Flow at Solid Surfaces*, Nature 389 (1997), pp. 360–362.

[80] A. Martini, H. Hsu, N. Patankar, and S. Lichter, *Slip at High Shear Rates*, Physical Review Letters 100 (2008), p. 206001.

[81] Y. Zhu and S. Granick, *Rate-Dependent Slip of Newtonian Liquid at Smooth Surfaces*, Physical Review Letters 87 (2001), p. 096105.

[82] A. Martini, A. Roxin, R. Snurr, Q. Wang, and S. Lichter, *Molecular Mechanisms of Liquid Slip*, Journal of Fluid Mechanics 600 (2008), pp. 257–269.

[83] R. Voronov, D. Papavassiliou, and L. Lee, *Slip Length and Contact Angle over Hydrophobic Surfaces*, Chemical Physics Letters 441 (2007), pp. 273–276.

[84] D. Huang, C. Sendner, D. Horinek, R. Netz, and L. Bocquet, *Water Slippage versus Contact Angle : A Quasiuniversal Relationship*, Physical Review Letters 101 (2008), p. 226101.

[85] T. Qian, X.P. Wang, and P. Sheng, *Hydrodynamic Slip Boundary Condition at Chemically Patterned Surfaces : A Continuum Deduction from Molecular Dynamics*, Physical Review E 72 (2005), p. 0022501.

[86] N. Priezjev and S. Troian, *Influence of Periodic Wall Roughness on the Slip Behaviour at Liquid/Solid Interfaces*, Journal of Fluid Mechanics 554 (2006), pp. 25–46.

[87] P. Thompson and M. Robbins, *Shear Flow Near Solids : Epitaxial Order and Flow Boundary Conditions*, Physical Review A 41 (1990), pp. 6830–6837.

[88] M. Tuckerman, J. Alejandre, R. Lopez-Rendon, A. Jochim, and G. Martyna, *A Liouville-Operator Derived Measure Preserving Integrator for Molecular Dynamics Simulations in the Isothermal-Isobaric Ensemble*, Journal of Physics A: Mathematical 39 (2006), pp. 5629–5651.

[89] S. Nose, *A Molecular Dynamics Method for Simulations in the Canonical Ensemble*, Molecular Physics 52 (1984), pp. 255–268.

[90] W. Hoover, *Canonical Dynamics: Equilibrium Phase-Space Distributions*, Physical Review A 31 (1985), pp. 1695–1697.

[91] S. Nose and M. Klein, *Constant Pressure Molecular Dynamics for Molecular Systems*, Molecular Physics 50 (1983), pp. 1055–1076.

[92] J. Powles, S. Murad, and P. Ravi, *A New Model for Permeable Micropores*, Chemical Physics Letters 188 (1992), pp. 21–24.

[93] M. Cole, D. Velegol, H. Kim, and A. Lucas, *Nanoscale van der Waals Interactions*, Molecular Simulation 35 (2009), pp. 849–866.

[94] J. Lennard-Jones, *Cohesion*, Proceedings of the Physical Society 43 (1931), pp. 461–482.

[95] A. Toukmaji and J. Board, *Ewald Summation Techniques in Perspective: A Survey*, Computer Physics Communications 95 (1996), pp. 73–92.

[96] I. Yeh and M. Berkowitz, *Ewald Summation for Systems with Slab Geometry*, Journal of Chemical Physics 111 (1999), pp. 3155–3162.

[97] J. Rychaert, G. Ciccotti, and H. Berendsen, *Numerical Integration of the Cartesian Equations of Motion of a System with Constraints*, Journal of Computational Physics 23 (1977), pp. 327–341.

[98] H. Anderson, *Rattle: A Velocity version of the Shake Algorithm for Molecular Dynamics Calculations*, Journal of Computational Physics 52 (1983), pp. 24–34.

[99] B. Todd and P. Daivis, *Homogeneous Non-Equilibrium Molecular Dynamics Simulations of Viscous Flow: Techniques and Applications*, Molecular Simulation 33 (2007), pp. 189–229.

[100] J. Irving and J. Kirkwood, *The Statistical Mechanical Theory of Transport Processes. IV: The Equations of Hydrodynamics*, Journal of Chemical Physics 18 (1950), pp. 817–829.

[101] R. Kubo, *Statistical-Mechanical theory of Irreversible Processes I*, Journal of the Physical Society of Japan 12 (1957), pp. 570–586.

[102] S. Hess and D. Evans, *Computation of the Viscosity of a Liquid from Time Averages of Stress Fluctuations*, Physical Review E 64 (2001), p. 011207.

[103] G.J. Guo, Y.G. Zhang, and Y.J. Zhao, *Comment on 'Computation of the Viscosity of a Liquid from Time Averages of Stress Fluctuations'*, Physical Review E 67 (2003), p. 043101.

[104] S. Yongli, S. Minhua, C. Weidong, M. Congxiao, and L. Fang, *The Examination of Water Potentials by Simulating Viscosity*, Computational Materials Science 38 (2007), pp. 737–740.

[105] I. Hanasaki and A. Nakatani, *Fluidised Piston Model for Molecular Dynamics Simulations of Hydrodynamic Flow*, Modelling and Simulation in Materials Science and Engineering 14 (2006), pp. S9–S20.

[106] J. Li, D. Liao, and S. Yip, *Coupling Continuum to Molecular-Dynamics Simulation: Reflecting Particle Method and the Field Estimator*, Physical Review E 57 (1998), pp. 7259–7267.

[107] J. Tersoff, *Empirical Interatomic Potential for Carbon with Applications to Amorphous Carbon*, Physical Review Letters 61 (1988), pp. 2879–2882.

[108] E. Neyts, A. Bogaerts, R. Gijbels, J. Benedikt, and M. Van De Sanden, *Molecular Dynamics Simulations for the Growth of Diamond-Like Carbon Films From Low Kinetic Energy Species*, Diamond and Related Materials 13 (2004), pp. 1873–1881.

[109] B. Coasne, S. Jain, L. Naamar, and K. Gubbins, *Freezing of Argon in Ordered and Disordered Porous Carbon*, Physical Review B 76 (2007), p. 085416.

[110] M. Schneemilch and N. Quirke, *Effect of Oxidation on the Wettability of Poly(dimethylsiloxane) Surfaces*, Journal of Chemical Physics 127 (2007), p. 114701.

[111] J. Smith, O. Borodin, and G. Smith, *A Quantum Chemistry Based Force Field for Poly(dimethylsiloxane)*, Journal of Physical Chemistry B 108 (2004), pp. 20340–20350.

[112] J. Hirvi and T. Pakkanen, *Molecular Dynamics Simulations of Water Droplets on Polymer Surfaces*, Journal of Chemical Physics 125 (2006), p. 144712.

[113] H. Berendsen, J. Grigera, and T. Straatsma, *The Missing Term in Effective Pair Potentials*, Journal of Physical Chemistry 91 (1987), pp. 6269–6271.

[114] P. Mark and L. Nilsson, *Structure and Dynamics of the TIP3P, SPC and SPC/E Water Models at 298K*, Journal of Physical Chemistry A 105 (2001), pp. 9954–9960.

[115] E. Sanz, C. Vega, F. Abascal, and L. MacDowell, *Phase Diagram of Water from Computer Simulation*, Physical Review Letters 92 (2004), p. 255701.

[116] B. Hess, *Determining the Shear Viscosity of Model Liquids from Molecular Dynamics Simulations*, Journal of Chemical Physics 116 (2002), pp. 209–217.

[117] P. Mark and L. Nilsson, *Structure and Dynamics of Liquid Water with Different Long-Range Interaction Truncation*, Journal of Computational Chemistry 23 (2002), pp. 1211–1219.

[118] A. Harasima, *Molecular Theory of Surface Tension*, Advances in Chemical Physics 1 (1957), pp. 203–237.

[119] J. Kirkwood and F. Buff, *The Statistical Mechanical Theory of Surface Tension*, Journal of Chemical Physics 17 (1949), pp. 338–343.

[120] F. Chen and P. Smith, *Simulated Surface Tensions of Common Water Models*, Journal of Chemical Physics 126 (2007), p. 221101.

[121] S. Supple and N. Quirke, *Short Range United Atom Potentials for Alkanes: Decane and Nonane*, Molecular Simulation 29 (2003), pp. 77–82.

[122] W. Price, H. Ide, and Y. Arata, *Self-Diffusion of Supercooled Water to 238K using PGSE NMR Diffusion Measurements*, Journal of Physical Chemistry A 103 (1999), p. 448.

[123] D. Gomez-Diaz and J. Navaza, *Surface Behaviour of Aqueous Solutions of Pyrrolidine and Piperidine*, Journal of Chemical Engineering Data 49 (2004), p. 1406.

[124] H. Ertl and F. Dullien, *Self-Diffusion and Viscosity of Some Liquids as a Function of Temperature*, AIChE Journal 19 (1973), pp. 1215–1223.

[125] H. Iloukhani, J. Dezali-Sameti M. Basini-Parsa, and S. Azizian, *Studies of Dynamic Viscosity and Gibbs Energy of Activation of Binary Mixtures of Methylcyclohexane with n-Alkanes at Various Temperatures*, Journal of Molecular Liquids 126 (2006), p. 117.

[126] D. Gomez-Diaz, J. Mejuto, J. Navaza, and A. Rodriguez-Alvarez, *Viscosities, Densities, Surface Tensions and Refractive Indices of 2,2,4-Trimethylpentane + Cylcohexane + Decane Ternary Liquid Systems at 298K*, Journal of Chemical Engineering Data 47 (2002), p. 872.

[127] T. Werder, J. Walther, R. Jaffe, T. Halicioglu, and P. Koumoutsakos, *On the Water-Carbon Interaction for Use in Molecular Dynamics Simulations of Graphite and Carbon Nanotubes*, Journal of Physical Chemistry B 107 (2003), pp. 1345–1352.

[128] W. Smith, C. Yong, and P. Rodger, *"DLPOLY : Application to Molecular Simulation"*, Molecular Simulation 28 (2002), p. 385.

[129] W. Humphrey, A. Dalke, and K. Schulten, *VMD - Visual Molecular Dynamics*, Journal of Molecular Graphics 14 (1996), pp. 33–38.

[130] J.L. Barrat and L. Bocquet, *Influence of Wetting Properties on Hydrodynamic Boundary Conditions at a Fluid/Solid Interface*, Faraday Discussions 112 (1999), pp. 119–127.

[131] M. Jazdzewska, M. Sliwinska-Bartkowiak, A. Beskrovnyy, S. Vasilovskiy, S. Ting, K. Chan, L. Huang, and K. Gubbins, *Novel Ice Structures in Carbon Nanopores: Pressure Enhancement Effect of Confinement*, Physical Chemistry Chemical Physics 13 (2011), pp. 9008–9013.

[132] J. Stawiskowska, *AFM Measurement Data*, Unpublished Work (2008).

[133] M. Bojan and W. Steele, *Interactions of Diatomic Molecules with Graphite*, Langmuir 3 (1987), pp. 1123–1127.

[134] C. Lopez, S. Nielson, B. Ensing, P. Moore, and M. Klein, *Structure and Dynamics of Model Pore Insertion into a Membrane*, Biophysical Journal 88 (2005), pp. 3083–3094.

[135] J.A. Garate, N. English, and J. MacElroy, *Static and Alternating Electric Field and Distance-Dependent Effects on Carbon Nanotube-assisted Water Self-Diffusion Across Lipid Membranes*, Journal of Chemical Physics 131 (2009), p. 114508.

[136] D. Bemporad, J. Essex, and C. Luttman, *Permeation of Small Molecules through a Lipid Bilayer: A Computer Simulation Study*, Journal of Physical Chemistry B 108 (2004), pp. 4875–4884.

[137] R. Qiao, A. Roberts, A. Mount, S. Klaine, and P. Ke, *'Translocation of C60 and its Derivatives Across a Lipid Bilayer'*, Nano Letters 7 (2007), pp. 614–619.

[138] L. Monticelli, E. Salonen, P. Ke, and I. Vattulainen, *Effects of Carbon Nanoparticles on Lipid Membranes: A Molecular Simulation Perspective*, Soft Matter 5 (2009).

[139] J. Lin, H. Zhang, Z. Chen, and Y. Zheng, *Penetration of Lipid Membranes by Gold Nanoparticles: Insights into Cellular Uptake, Cytotoxicity and their Relationship*, ACS Nano 4 (2010), pp. 5421–5429.

[140] K. Yang and Y.Q. Ma, *Computer Simulation of the Translocation of Nanoparticles with Different Shapes Across a Lipid Bilayer*, Nature Nanotechnology 5 (2010), pp. 579–583.

[141] S. Choe, R. Chang, J. Jeon, and A. Violi, *Molecular Dynamics Simulation Study of a Pulmonary Surfactant Film Interacting with a Carbonaceous Nanoparticle*, Biophysical Journal 95 (2008), pp. 4102–4114.

[142] M. Schneemilch and N. Quirke, *Molecular Dynamics of Nanoparticle Translocation at Lipid Interfaces*, Molecular Simulation 36 (2010), pp. 831–835.

[143] A. Makarucha, N. Todorova, and I. Yarovsky, *Nanomaterials in Biological Environment: A Review of Computer Modelling Studies*, European Biophysics Journal 40 (2011), pp. 103–115.

[144] E. Egberts, S. Marrink, and H. Berendsen, *Molecular Dynamics Simulation of a Phospholipid Membrane*, European Biophysics Journal 22 (1994), pp. 423–436.

[145] O. Berger, O. Edholm, and F. Jahnig, *Molecular Dynamics Simulations of a Fluid Bilayer of Dipalmitoylphosphatidylcholine at Full Hydration, Constant Pressure and Constant Temperature*, Biophysics Journal 72 (1997), pp. 2002–2013.

[146] M. Matsui and M. Akaogi, *Molecular Dynamics Simulation of the Structural and Physical Properties of the Four Polymorphs of TiO2*, Molecular Simulation 6 (1991), pp. 239–244.

[147] D. Collins and W. Smith, *Evaluation of TiO2 Force Fields*, Daresbury Laboratory Technical Report 96 (1996).

[148] P. Naicker, P. Cummings, H. Zhang, and J. Banfield, *Characterisation of Titanium Dioxide Nanoparticles Using Molecular Dynamics Simulations*, Journal of Physical Chemistry B 109 (2005), pp. 15243–15249.

[149] J.H. Park and N. Aluru, *Temperature-Dependent Wettability on a Titanium Dioxide Surface*, Molecular Simulation 35 (2009), pp. 31–37.

[150] A. Rappe, C. Casewit, K. Colwell, W. Goddard, and W. Skiff, *UFF, a Full Periodic Table Force Field for Molecular Mechanics and Molecular Dynamics Simulations*, Journal of the American Chemical Society 114 (1992), pp. 10024–10035.

[151] D. Tieleman and H. Berendsen, *Molecular Dynamics Simulations of a Fully Hydrated Dipalmitoylphosphatidylcholine Bilayer with Different Macroscopic Boundary Conditions and Parameters*, Journal of Chemical Physics 105 (1996), pp. 4871–4880.

[152] E. Lindahl, B. Hess, and D. SpoelVan der , *GROMACS 3.0: A Package for Molecular Simulation and Trajectory Analysis*, Journal of Molecular Modelling 7 (2001), pp. 306–317.

[153] H. Berendsen, J. Postma, W. Gunsterenvan , A. DiNola, and J. Haak, *Molecular Dynamics with Coupling to an External Bath*, Journal of Chemical Physics 81 (1984), pp. 3684–3690.

[154] T. Darden, D. York, and L. Pedersen, *Particle Mesh Ewald: An Nlog(N) Method for Ewald Sums in Large Systems*, Journal of Chemical Physics 98 (1993), pp. 10089–10092.

[155] S. Pandit, D. Bostick, and M. Berkowitz, *Molecular Dynamics Simulation of a Dipalmitoylphosphatidylcholine Bilayer with NaCl*, Biophysical Journal 84 (2003), pp. 3743–3750.

[156] A. Bangham, *Lung Surfactant: How it Does and Does Not Work*, Lung 165 (1987), pp. 17–25.

[157] F. Possmayer, K. Nag, K. Rodriguez, R. Qanbar, and S. Schurch, *Surface Activity in Vitro: Role of Surfactant Proteins*, Comparative Biochemistry and Physiology A 129 (2001), pp. 209–220.

[158] X. Qin, Q. Yuan, Y. Zhao, S. Xie, and Z. Liu, *Measurement of the Rate of Water Translocation through Carbon Nanotubes*, Nano Letters 11 (2011), pp. 2173–2177.